DESIGN, DEVELOPMENT AND CHARACTERISATION OF A NOVEL BUILDING INTEGRATED PHOTOVOLTAIC CONCEPT FOR ENERGY COLLECTION AND PASSIVE SOLAR SHADING

Vincent O'Brien

BEng (Hons)

Faculty of Art, Design and the Built Environment of the University of Ulster

Thesis submitted for the degree of Doctor of Philosophy

December 2020

I confirm that the word count of this thesis is less than 100,000 words

Contents

Figures

Tables

Acknowledgements

The author would like to take this opportunity to express gratitude to everyone who provided help and support during this protracted period of study. Special thanks are extended to the staff and students of the Centre for Sustainable Technologies at Ulster University as well as the Applied Solar Energy and Energy Storage research teams at the Universitat de Lleida, who's support throughout the process was invaluable and greatly appreciated.

The author also takes great pleasure in acknowledging the contributions of a number of individuals from Prof Neil Hewitt, Director of the Centre for Sustainable Technologies, who provided additional funding for the development of the proof of concept prototype, to Dr Aggelos Zacharopoulos and Dr Mervyn Smyth, thesis supervisors, and finally, Prof Daniel Chemisana Villegas without whom this project would have faltered on more than one occasion.

Finally, I would like to thank my family and friends for their continued and unwavering support in all things academic or otherwise.

Abstract

This thesis takes a broad approach to building integrated solar collection and presents a novel solution which attempts to address a diverse range of physical, technical and aesthetic barriers to the implementation of these technologies. The thesis presents a detailed literature review which leads to the design of a novel, modular, solar window for building integration applications. Comparable in size and scale to a double-glazed window, the design conceals the dark absorber material from non-perpendicular viewpoints, provides solar shading and electrical energy generation for 80 minutes either side of solar noon while at the same time allowing natural lighting to be conveyed into the building outside of the selected concentration period. The system was also designed to be flexible enough to be adapted to various window aperture sizes and orientations.

In developing this innovative system, a number of refractive selectively concentrating line axial lenses were designed with a ratio of collector area to absorber area of 2:1 and an acceptance half angle range of solar noon ±20 degrees, with any light incident on the collector outside of that range being allowed to enter the building. A range of solutions was then optically modelled and evaluated.

A final 5 degree defocused fast Fresnel lens design was selected for manufacture, based on its optical performance and a number of key manufacturing constraints, to allow the proof of concept collector to be fabricated. The system was then evaluated experimentally and characterised under real world test conditions in Lleida, Spain. The comparative analysis experimentally validated the optical design and highlighted an increase in energy generation of ~75 % at a perpendicular incidence angle, compared to a baseline design without a concentrating refractive element.

Finally, the annual performance of the developed collector was simulated using historical weather data for Athens, Greece at four architectural integration orientations in order to more fully understand the electrical generation potential of the prototype solution. An annual energy collection of 768 $kWhm^{-2}yr^{-1}$ for an atrium roof (38^{o} slope) and an East-West absorber alignment was the most effective final design with a 9% increase in energy collection versus the baseline design.

NOTES ON ACCESS TO CONTENTS

"I hereby declare that for 2 years following the date on which the thesis is deposited in the Research Office of the University of Ulster, the thesis shall remain confidential with access or copying prohibited. Following expiry of this period I permit

1. the Librarian of the University to allow the thesis to be copied in whole or in part without reference to me on the understanding that such authority applies to the provision of single copies made for study purposes or for inclusion within the stock of another library.
2. the thesis to be made available through the Ulster Institutional Repository and/or EThOS under the terms of the Ulster eTheses Deposit Agreement which I have signed.

IT IS A CONDITION OF USE OF THIS THESIS THAT ANYONE WHO CONSULTS IT MUST RECOGNISE THAT THE COPYRIGHT RESTS WITH THE UNIVERSITY AND THEN SUBSEQUENTLY TO THE AUTHOR ON THE EXPIRY OF THIS PERIOD AND THAT NO QUOTATION FROM THE THESIS AND NO INFORMATION DERIVED FROM IT MAY BE PUBLISHED UNLESS THE SOURCE IS PROPERLY ACKNOWLEDGED."

Nomenclature

^0C	Degrees Celsius
A	Ampere
A_{eff}	Effective absorber area
B^{3+}	Boron
C	Celsius
C	Concentration
c	Speed of light in a vacuum
cm	Centimetre
E	East
e^-	Electron
E_A	Acceptor level
E_C	Conduction band
E_D	Donor level
E_G	Energy gap
E_V	Valence band
f	Focal length
FF	Fill factor
G	Radiative power density (radiation)/ generation rate (photovoltaics)
h^+	Holes
I	Current
i	Incident radiation
I	Intensity
I_0	Dark Current
I_{01}	Dark Current in the quasi-neutral region

I_{02}	Dark Current in the space charge region
I_{MPP}	Current at Maximum Power Point
I_{SC}	Short circuit current
I_{SCD}	Short circuit current in the depletion region
I_{SCN}	Short circuit current in the n-type region
I_{SCP}	Short circuit current in the p-type region
K	Kelvin
K	Proportionality constant, extinction coefficient or attenuation index
kT	Thermal voltage of a cell
L	Optical path length
m	Metre
m2	Square metre
mm	Millimetre
M_{PP}	Maximum power point
mV	Millivolt
n	Ideality factor (semiconductors)/ refractive index (optics)
N	North
N	Photon flux
nm	Nanometre
O	Optical Axis
P	Point
P^{5+}	Phosphorus
P_{in}	Power input to a cell
P_{MMP}	Power at Maximum Power Point
q	Charge on an electron

R	Maximum distance from the optical axis
r	Reflection
$r_{\parallel}$	Parallel component of the unpolarized light
$r_{\perp}$	Perpendicular component of the unpolarized light
R_S	Series resistance
R_{SH}	Shunt resistance
s	Distance travelled
S	South
Si^{4+}	Silicon
T	Maximum steady state temperature
v	Speed of light in a medium
V	Volt/Voltage
V_{MPP}	Voltage at Maximum Power Point
V_{OC}	Open circuit voltage
W	Watt (Power)/ West (orientation)
Wm^{-2}	Watts per meter squared
x	Distance
x	Prism width
z	Height of prism

Abbreviations

2D	2-dimensional
3D	3-dimensional
AA	angular acceptance
AM 0	Air Mass 0
AM 1.5	Air Mass 1.5
AM	Air Mass
ASTM	American Society for Testing and Materials
AU	Astronomical Unit
BIPV	Building Integrated Photovoltaic
CdTe	Cadmium Telluride
CFFLAB	conventional fast Fresnel lens augmented baseline
CIBSE	Chartered Institution of Building Services Engineers
CNC	Computer Numerical Control
CO_2	Carbon Dioxide
CPC	Compound parabolic concentrators
$Cu(InGa)Se_2$	Copper Indium Gallium Selenium
DFFL	defocused fast Fresnel lens
DFFLAB	defocused fast Fresnel lens augmented baseline
EREC	European Renewable Energy Council
EU	European Union
EU28	28-member states of the European Union
FF	Fill factor
FiTs	Feed in Tariffs

GW_{el}	Gigawatts of electricity
HEPA	High-Efficiency Particulate Air
IEA	International Energy Agency
IV or I-V	Current-Voltage
kWh/kWp	Kilowatt-hour per kilowatt-pence
$kWhm^{-2}yr^{-1}$	Kilowatts hours per metre squared per annum
NREAP	National Renewable Energy Action Plan
OE	Optical Efficiency
PFA	Pulverised Fuel Ash
PMMA	Poly(methyl methacrylate)
ppm	parts per million
PV	Photovoltaic
P-V	Power-Voltage
PVT	Photovoltaic-thermal
RC	resistance-capacitance
ROCs	Renewable Obligation Certificates
ROHS	restriction of the use of hazardous substances
RR	refraction-refraction
RX	refraction-reflection
RXI	refraction-reflection-total internal reflection
SMS	Simultaneous multiple surface
TIR	Total internal reflection
TIR-R	Transmission-total internal reflection-refraction-refraction
TWh	Terawatt hours
TX	Copper/Constantan

UK	United Kingdom
USA	United States of America
UV	Ultraviolet
VAT	Value Added Tax
WBGU	Wissenschaftlicher Beirat der Bundesregierung Globale Umweltveränderungen (German Advisory Council on Climate Change)
WW1	World War 1
WW2	World War 2
XRI	reflection-refraction-total internal reflection
XX	reflection-reflection

Greek

α	Absorption coefficient
α_s	Solar altitude angle
β	Slope of the collector plane
γ	Surface azimuth angle
γ_s	Solar azimuth angle
η	Cell efficiency
θ	Angle of incidence
Θ_c	Half acceptance angle
θ_z	Zenith angle
σ	Steffan-Boltzman constant
τ	Refraction
τ_r	Total reflection losses from transmitted light
Ψ	Acceptance half angle
Ω	Ohms

Introduction

1 Introduction

Anthropogenic climate change as a result of the emission of greenhouse gases and the security of fuel supplies are two of the biggest issues facing the developed world today. The use of solar energy has the potential to alleviate mankind's reliance on fossil fuels both in terms of electrical and thermal energy supply. Major long-term reductions in CO_2 emissions and improvements in energy self-sufficiency can be made by promoting the implementation of solar energy systems within domestic, office and small commercial buildings relatively quickly. This recognition has led to a flurry of increasingly strict policy changes to building regulations and the initiation of a number of renewable incentive schemes like capital grants, VAT reductions, loans, renewable obligation certificates (ROCs) and feed-in tariffs (FiTs) for example. Despite these incentives there are still a number of barriers to the widespread implementation of solar energy systems and the most prevalent of these are economic and aesthetic barriers. This chapter briefly summarises; some of the main policy drivers which have been put in place to tackle these energy challenges, identifies the potential of the solar energy resource along with the current state of the world markets for both solar thermal and photovoltaic technologies and highlights the barriers to the implementation of the existing solar technologies. The chapter concludes by stating the aim of the research carried out in this thesis and identifies the objectives necessary for the successful completion of that aim.

1.1 Policy Drivers

"DONE at Paris this twelfth day of December two thousand and fifteen" – a somewhat unassuming line of text making up the second paragraph of Article 29 in the Paris Agreement just above the list of 189 signatories (Anon, 2015a). The agreement was drafted during the 21st session of the Conference of the Parties, commonly referred to as COP21, and gave birth to the first ever legally binding global framework to avoid dangerous climate change. At its crux the agreement aims to "reach global peaking of greenhouse gas emissions as soon as possible", holding the increase in global average temperature to well below 2 °C and pursuing efforts to limit it to 1.5 °C above pre-industrial levels. The conditions for the entry into force for the Agreement were met on the 5th of October 2016 and the Agreement entered into force 30 days later (4th November 2016, Anon, 2016).

Steffen et al (2018) further reinforce the need for governments worldwide to invest heavily in preventing an average global temperature rise in excess of 1.5 to 2 ^{o}C, a level at which the earth would be irreversibly moved out of its stable (in terms of global climate) zone and into a

'Hothouse Earth' climate zone where global temperatures and sea levels would rise and large areas of the earth would become uninhabitable. Figure 1-1 shows the impact of anthropogenic climate change on the Earth's climate as it has transitioned into the Anthropocene, a geological age in which mankind's impact on the environment is described. The policy documents described in this section are a part of the 'Earth System stewardship' identified in Figure 1-1, which are designed to reduce the impact of human emissions and biosphere degradation and guide the climate back into the 'Stabilised Earth' zone.

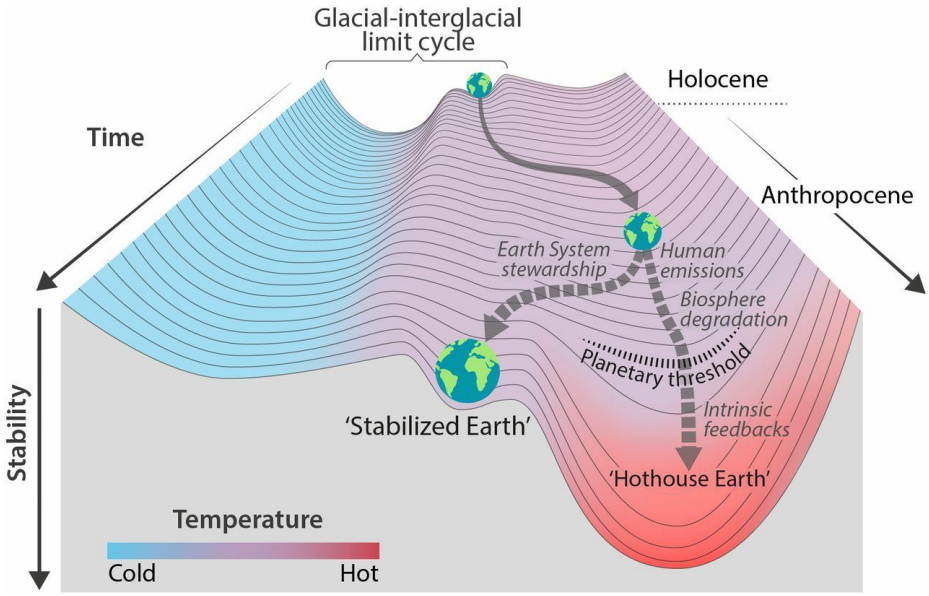

Figure 1-1 – Stability landscape showing the pathway of the Earth System out of the Holocene and thus, out of the glacial–interglacial limit cycle to its present position in the hotter Anthropocene.

(Steffen et al, 2018)

As a direct consequence of the Paris Agreement the European Union released Directive (EU) 2018/844, amending Directive 2010/31/EU on the energy performance of buildings (commonly referred to as the EPBD) and Directive 2012/27/EU on energy efficiency. Of specific note was the commitment stated in paragraph 6 to "reach the long-term greenhouse gas emission goal and that decarbonise the building stock, which is responsible for approximately 36 % of all CO_2 emissions in the Union, by 2050." (Anon, 2018a). This commitment trickles down the responsibility for developing short, medium and long term national milestones, actions and strategies on energy efficiency to each on the member states.

More locally, and based on the advice published in the May 2019 report by the committee on climate change "Net Zero – The UK's contribution to stopping global warming" (Anon, 2019a),

the UK government signed the Climate Change Act 2008 (2050 Target Amendment) Order 2019 (Anon, 2019b) into law, committing the UK to a target of reducing greenhouse gas emissions by at least 100% of 1990 levels (net zero) by 2050.

These strategic areas of action call for legally binding large scale changes in the way in which energy is created and utilized at both large and small scale levels and rapid changes can be made at a commercial and domestic level relatively quickly. The targets to reduce CO_2 emissions from these sources have led to a wide scale initiative to increase the prevalence of energy efficiency and renewable technologies leading to substantial market growth within this sector; incentives which, based on the document 'Transforming our world: the 2030 Agenda for Sustainable Development' (Anon, 2015b) and thanks to the adoption of the Paris Agreement (Anon, 2015a), look set to continue into the foreseeable future.

1.2 Potential and Market Opportunities of Solar Energy

Within the context of seminal solar energy literature, Rabl (1985) is popularly quoted as saying the solar radiation incident on the earth's surface is approximately 8×10^{16} W which is more than 10,000 times the present world energy consumption. However, more recent estimations by the European Renewable Energy Council suggest the potential of the solar energy resource to meet 2,850 times the 2010 global energy needs (EREC, 2010) based on research carried out by the German Advisory Council on Climate Change (the WBGU) or a solar potential worldwide of 1098 exajoules per year (Dupont et al, 2020). These impressive statistics indicate that solar energy has by far the largest potential, of any renewable energy resource, to meet all of mankind's energy requirements however, this isn't the whole picture. As a result of the intermittent nature of solar energy and its uneven distribution across the earth's surface, solar energy supply is too inconsistent to fully meet mankind's energy needs reliably or without the use of various additional energy storage technologies. Despite these major drawbacks, solar energy has been successfully implemented across the globe for centuries to alleviate the costs (both fiscal and environmental) associated with various fuel sources and has been particularly prevalent during periods of fuel scarcities or high fuel costs. Florida, USA in the 1920s is a prime example of the viability of solar energy to meet thermal energy demands in the presence of high fossil fuel energy costs. Butti and Perlin (1981) explain that during the post WW1 population boom in Florida the market for basic solar water heaters, with a payback period of just 2 years in some cases, flourished as the alternative water heating technologies of that era were more costly and less reliable. After dozens of patents and thousands of installations the solar energy market in Florida peaked in 1941 with a reported 80% of new buildings having solar water heaters and approximately half the population of Miami using solar energy.

The solar energy boom ended almost as quickly as it began. With WW2 embargos on the non-military use of copper and the post war increases in the cost of copper and labour solar energy became progressively less cost effective when compared with a cheaper post WW2 electricity supply.

1.3 Global Market

This section examines the current global market for both solar thermal and photovoltaic technologies in an attempt to aid in understanding the overall application and usage of solar energy worldwide.

1.3.1 Solar thermal

The market for solar energy is once again showing a healthy rise with 652.9 million m^2 of new thermal capacity installed in 2016 (Weiss and Spörk-Dür, 2019). In addition to the financial benefits available as a result of variable fuel costs this increase in the use of renewable energies is supported by worldwide government grants and the public's will to reduce CO_2 emissions and militate against anthropogenic climate change.

Worldwide, annual solar thermal energy yields amounted to 51 TWh in 2000 and 388 TWh in 2017 (Figure 1-2). The main growth markets for solar thermal technologies have traditionally been and continue to be China and Europe, which accounted for 84.5% of the overall new collector installations in 2017 (Weiss and Spörk-Dür, 2019).

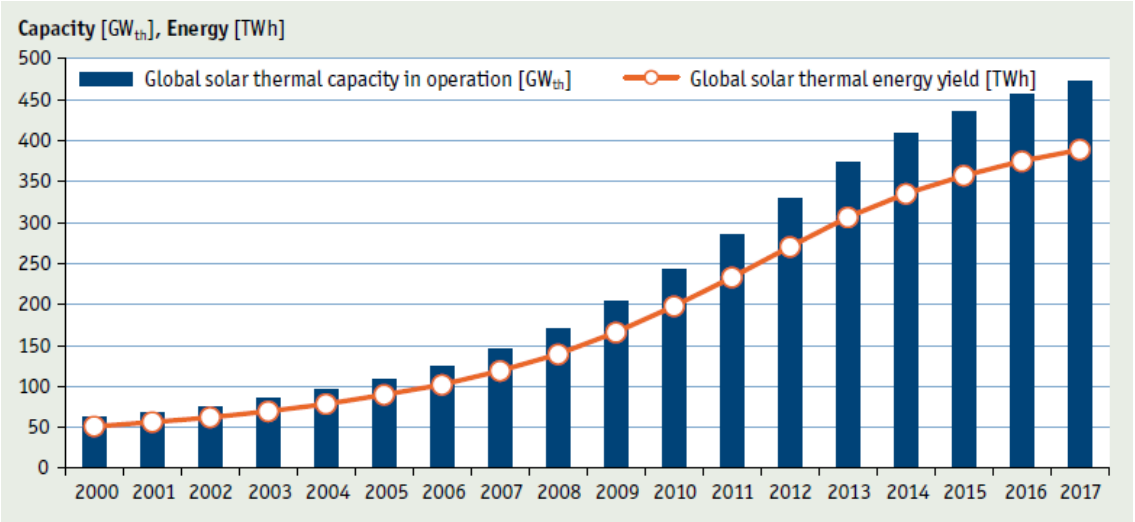

Figure 1-2 – Global solar thermal capacity in operation and annual energy yields 2000 – 2017 (Weiss and Spörk-Dür, 2019)

Globally, the breakdown of the types of newly installed solar thermal technology is dominated by evacuated tube collectors with 79.4% of the total market share and primarily driven by Chinese installations. Flat plate collectors come in a distant second with a 17.4% market share and finally unglazed and air collectors make up the remainder with 3.1% and 0.1%, respectively (Weiss and Mauthner, 2015). Curiously the European market share highlights a higher preference to flat plat collectors over evacuated tube collectors with a 74.9% to 23.4% market split (respectively) almost entirely inverting the global trend. The final significant observation across the global statistics is the prevalence of unglazed water collectors in the United States of America and neighbouring Canada. The biggest area of application for solar technologies in these regions tends to be for heating outdoor swimming pools.

1.3.2 Photovoltaic

The world market for PV has shown a rapid growth similar to that of the solar thermal market. Europe was the dominant force in this market until China began ramping up installed capacity in 2011, establishing itself as the world's largest solar market by 2016 (Figure 1-3).

The initial European dominance in the PV demand began to flatten out as the market was impacted by two major factors: a reduction in the available financial support for installed capacity and EU28 National Renewable Energy Action Plan (NREAP) targets being met for a large proportion of the member states. The NREAP targets for the EU28 constituent states highlight their 2020 commitments in terms of electrical generation from solar energy. The Global Market Outlook for Solar Power 2017 - 2021 (Anon, 2017) has shown that by underestimating the potential contribution of PV technologies, those targets have been met for the majority of the EU countries in the period covering 2014 to 2015.

With the on-going uncertainty over fuel prices and the EU commitment to increasing the overall percentage of energy supplied from renewable sources to 20% by 2020 under the European Renewable Directive (EU, 2009), the Paris Agreement (Anon, 2015a) and the announcement of a climate emergency in 2019 a resurgence in the rapid growth of the solar market is expected within the next decade, particularly in a European context, in order to meet these targets and with the aid of the new financial incentives. The economic viability of these systems will also promote their usage as traditional fossil fuel costs are expected to increase over the coming years after a period of artificially deflated oil prices making renewable energy alternatives a much more viable option once again, especially in the imminent 'greening' of the global economy.

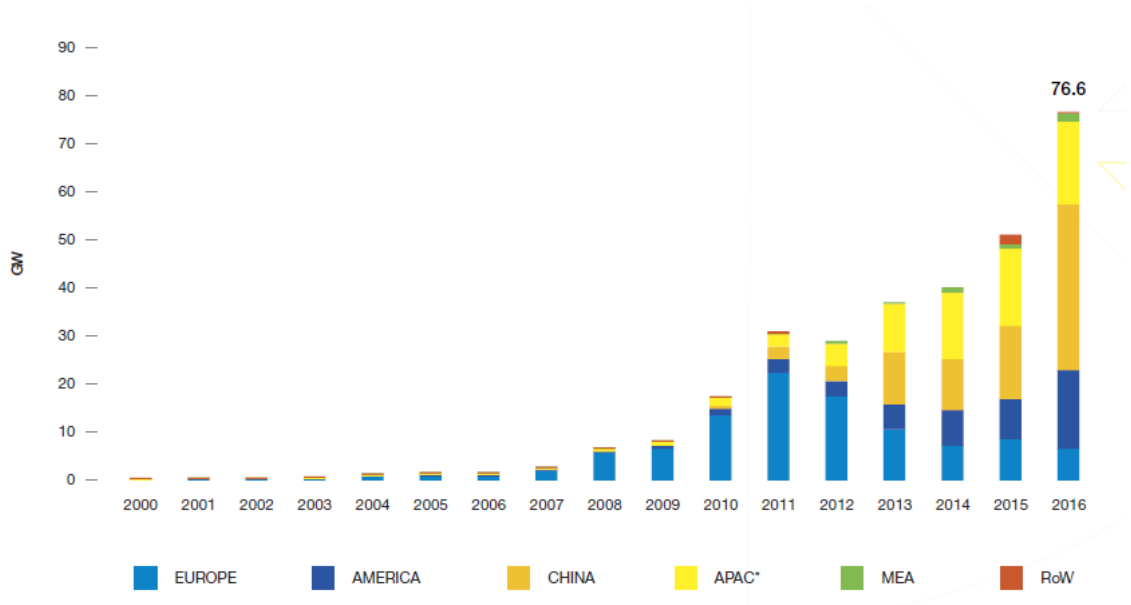

(a)

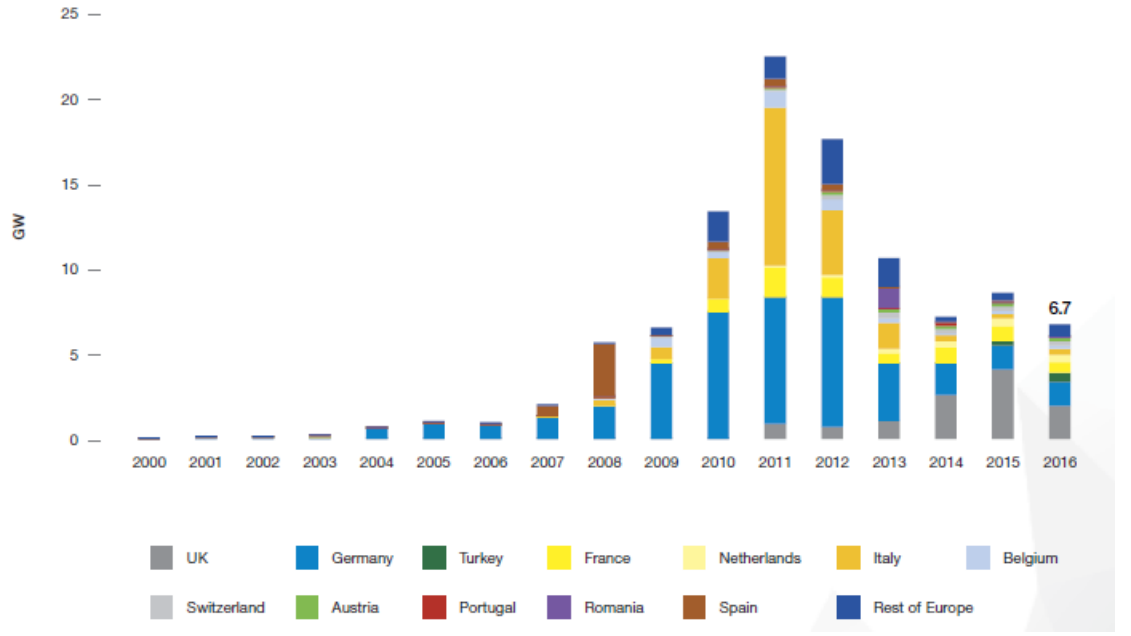

(b)

Figure 1-3 - Historical development of cumulative PV power installed in GW_{el} for: a) the global and b) European markets

(Anon, 2017)

1.4 Barriers to the implementation of solar technologies

The integration of solar energy collection technologies within an architectural context can be divided into five categories to describe the level of their impact (Kaan and Reijenga, 2004; Luque and Hegedus, 2011):

- applied invisibly,
- added to the design,
- adding to the architectural image,
- determining architectural image, and
- leading to new architectural concepts.

Of the levels of impact listed, the first two categories are by far the most common in today's built environment and it is those levels of impact which are the greatest physical and aesthetic barriers to the integration of solar technologies within the build environment due to the limitations in space to apply solar technologies invisibly and the aesthetic impact of adding solar technologies at either a late stage in the design of a new building or within a retrofit context. The level of architectural integration of a solar technology within a building is directly related to the perceived aesthetic impact and appeal of the system being considered and a group of architects working within the International Energy Agency's (IEA) Task 7 working group on photovoltaic power systems in the built environment developed a list of criteria by which to judge the aesthetic qualities of building integrated photovoltaic systems. Those criteria are as follows (van Mierlo and Oudshoff, 1999; Reijenga, 2000; Kaan and Reijenga, 2004):

- natural integration,
- designs that are architecturally pleasing,
- good composition of colours and materials,
- dimensions that fit the gridula, harmony, composition,
- PV systems that match the context of the building,
- well-engineered design, and
- use of innovative design.

Luque and Hegedus (2011) clarify the meaning of these criteria for non-architects as follows:

- Natural integration. This means that the PV system seems to form a logical part of the building. The system adds the finishing touch to the building. The PV system does not have to be that obvious. In renovation situations the result should look as though the PV system was there before the renovation.
- Architecturally pleasing. The design has to be architecturally pleasing. The building should look attractive and the PV system should noticeably improve the design. This is a very subjective issue, but there is no doubt that people find some buildings more pleasing than others.
- Good composition of colours and materials. The colour and texture of the PV system should be consistent with other materials.
- Fit the gridula, harmony and composition. The dimensions of the PV system should match the dimensions of the building. This will determine the dimensions of the modules and the building grid lines used (grid = modular system of lines and dimensions used to structure the building).
- Matching the context of the building. The entire appearance of the building should be consistent with the PV system used. In a historic building, a tile-type system will look better than large modules. A high-tech PV system, however, would look better in a high-tech building.
- Well-engineered. This does not concern the waterproofing or reliability of the construction. However, it does concern the elegance of the details. Did the designer pay attention to details? Has the amount of material been minimized? These considerations will determine the influence of the working details.
- Innovative design. PV systems have been used in many ways, but there are still countless new ways to be developed. This is all the more reason to consider this criterion as well.

In addition to these aesthetic criteria for the implementation of building integrated solar technologies three additional barriers to the implementation of solar technologies have been provided by the IEA's Task 47 working group on solar renovation of non-residential buildings and they are as follows (Salvesen, 2015):

- economic factors such as investment costs and maintenance costs,
- technical knowledge factors such as lack of knowledge among decision makers and architects, and
- a general reluctance to "new" technologies.

All of these factors identify an opportunity to examine the academic literature and existing technologies within the area of building integrated solar technologies to seek out a gap in the knowledge base in which to make a contribution to the field of building integrated solar energy systems and to develop novel solar energy collection systems, inspired by these criteria, specifically designed for integration within a building.

1.5 Thesis aims and objectives

The aim of this thesis was to develop and examine the potential of novel, innovative building integrated solar energy systems which address some of the subjective and aesthetic architectural concerns mentioned in this chapter. This research aim was met through the completion of the following research objectives:

- The first and most fundamental objective of the thesis was to carry out an extensive and detailed literature review of all relevant past and present work on building integrated solar energy collection systems by utilizing seminal works in the field along with appropriate English language journal articles on the subject to identify the nature and direction of the gap in the knowledge base.
- The second objective was to carry out the optical design, development and simulation of a novel building integrated solar energy collection system. This was achieved through the evaluation of the collector's optical performance in terms of the developed systems ability to collect energy and the characterisation of the energy distribution across the absorber plane during the collection period. The output from this objective was the physical refractive lens used on the proof of concept collector.
- The third objective was the design and manufacture of the prototype solar collector for a programme of real world outdoor experimental tests.
- Fourth was carrying out the outdoor experimental programme and presenting an analysis of the collector's performance as a means to experimentally validate the theoretical mathematical models generated during the optical design phase.
- The fifth objective was a comparison between the theoretical (mathematical) and experimental optical and electrical performance of the novel collection system and the discussion of the potential practical applications of the developed system in terms of building integration.
- Finally, an extrapolated prediction of the annual performance of the system under four different building integration alignments, façade and atrium integration with North-South and East-West absorber alignments, has been presented before closing out the thesis with a series of conclusions and recommendations which were drawn from the development of the novel solar energy collection system.

1.6 Chapter Summary

This chapter has introduced the rationale behind the need to continuously develop innovative and alternative renewable energy technologies to assist in meeting mankind's energy requirements. It has summarised some of the more important policy drivers for moving away from a society heavily reliant on fossil fuels and has identified the potential of solar energy technologies as a real option to help fill the gap in power generation both in terms of available energy and of financial opportunities. It has also highlighted that, although solar energy has the greatest potential of all of the renewable resources to fully meet mankind's energy requirements, significant barriers to the implementation of solar technologies still exist within the context of the built environment. The chapter concludes with a specific research aim 'the development and evaluation of the potential for a novel, innovative building integrated solar energy collection systems' and lists the research objectives necessary to accomplish that aim.

Literature Review

2 Literature Review

2.1 Introduction

This chapter begins by looking at the energy available from the sun in a general context and introduces some of the key terms used in the description of passive and active solar energy collection. Next, a brief description of the main technologies available for active solar energy collection are presented before focusing specifically on PV technologies and the options for integrating those technologies within the built environment. At this stage a detailed investigation into solar concentrating systems is presented focusing primarily on the development of nonimaging refractive lenses and identifying any limitations in the existing system designs. Finally, after identifying a significant knowledge gap in the subject area, a design brief has been included to identify how the work presented in this thesis intends to provide an innovative contribution to that knowledge gap.

2.1.1 The Solar Resource

The sun is, directly or indirectly, the source of most terrestrial energy. It is responsible for generating the winds, producing chemical energy through photosynthesis and, in conjunction with the moon, governing hydraulic changes within all of the water bodies on earth. It is essential to almost all forms of life on planet earth with the exception of a handful of extremophiles which, as resilient as they are, would have struggled to develop in a world without the sun.

The sun itself is a sphere of intensely hot gaseous matter with a diameter of 1.39×10^9 m which is fuelled by nuclear fusion and provides an effective blackbody temperature of 5777 K (Duffie and Beckman, 2006). As this description implies despite the physical complexities of the Sun as shown in Figure 2-1 it can be viewed in simplistic terms as a source of energy created by the fusion of Hydrogen particles in a very large nuclear reactor.

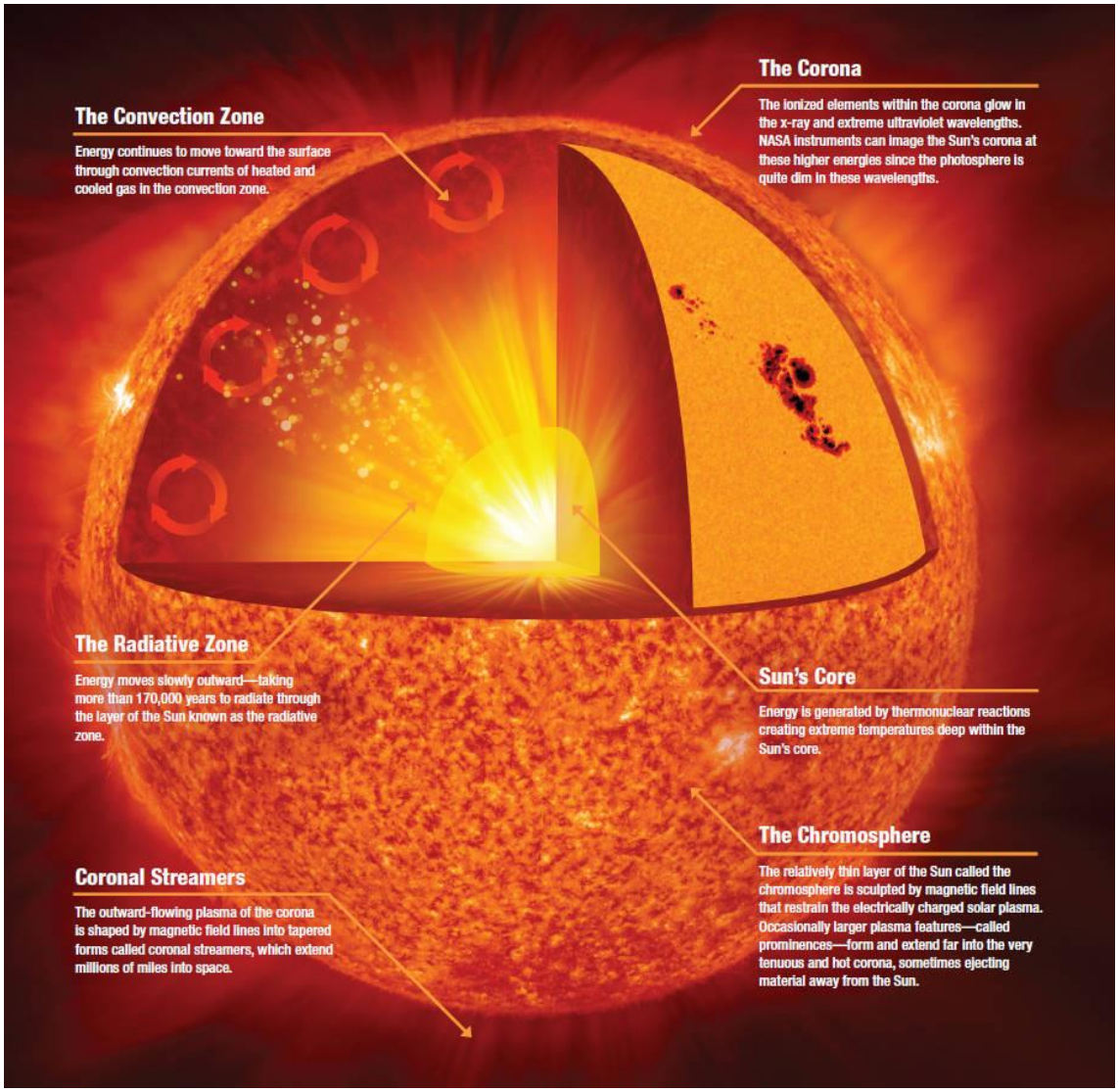

Figure 2-1 – Anatomy of the Sun

(NASA, 2020)

2.1.2 The Solar Constant

Despite the numerous geometric variations between the earth and the sun and the varying cycles in solar output an internationally recognised solar constant has been derived. Duffie and Beckman (2006) define this solar constant as follows: "the energy from the sun, per unit time, received on a unit area of surface perpendicular to the direction of propagation of the radiation, at a mean earth-sun distance, outside of the atmosphere". This solar constant has been defined as 1367 Wm^{-2} (Duffie and Beckman, 2006) at a mean earth-sun distance of 1 astronomical unit (AU = 1.496 x 10^{11} m) and, despite an actual variation of ±3.4% throughout the year (ASTM, 2003), it is essentially assumed to be unvarying (Wenham et al, 2007).

2.1.3 The Solar Spectrum

The energy incident upon the earth from the sun is a compilation of a variety of different wavelengths of light. Figure 2-2 shows how solar irradiance varies with wavelength across the spectrum outside of the earth's atmosphere (AM 0) and on a surface normal to the sun, tilted towards the equator, at sea level on a clear day at a latitude of 41.81° (AM 1.5).

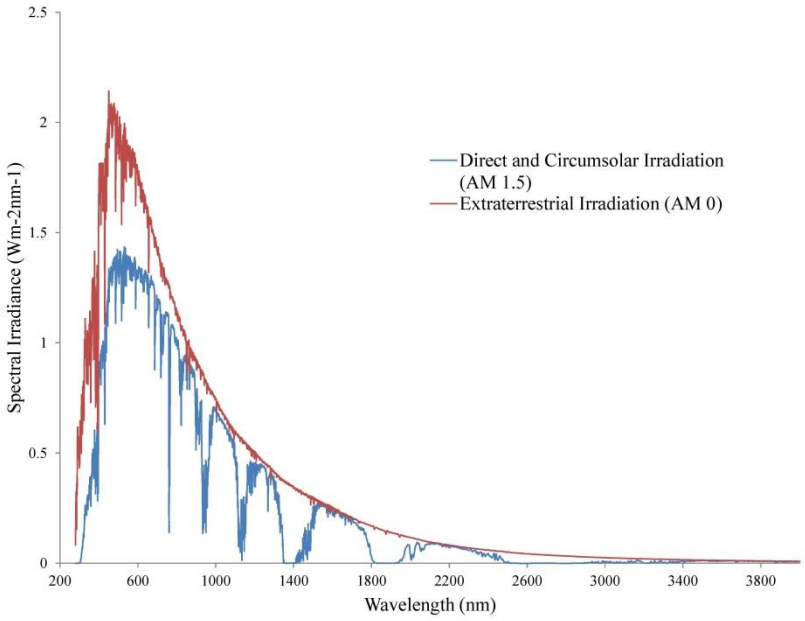

Figure 2-2 – Variation of Spectral Irradiance against wavelength at AM 0 and AM 1.5 (Created from the data presented in ASTM: G173 – 03, 2003)

The significance of an AM 1.5 standard spectrum dates back to the early resurgence in solar energy research in the late 60s and early 70s when the majority of the contributions where coming from Northern America, Europe and Japan and a latitude of 41.81° connects all three regions.

Duffie and Beckman (2006) explain that the variations between the two profiles shown in Figure 2-2 are directly related to Raleigh scattering and the susceptibility of certain wavelengths to absorption in the atmosphere.

2.1.4 Solar Geometry

As a result of the transient nature of solar energy capture a set of angles were introduced by Benford and Bock (1939) to define the orientation of a collector plane and the position of the sun relative to that plane. Figure 2-3 presents a pictorial representation of some of these angles.

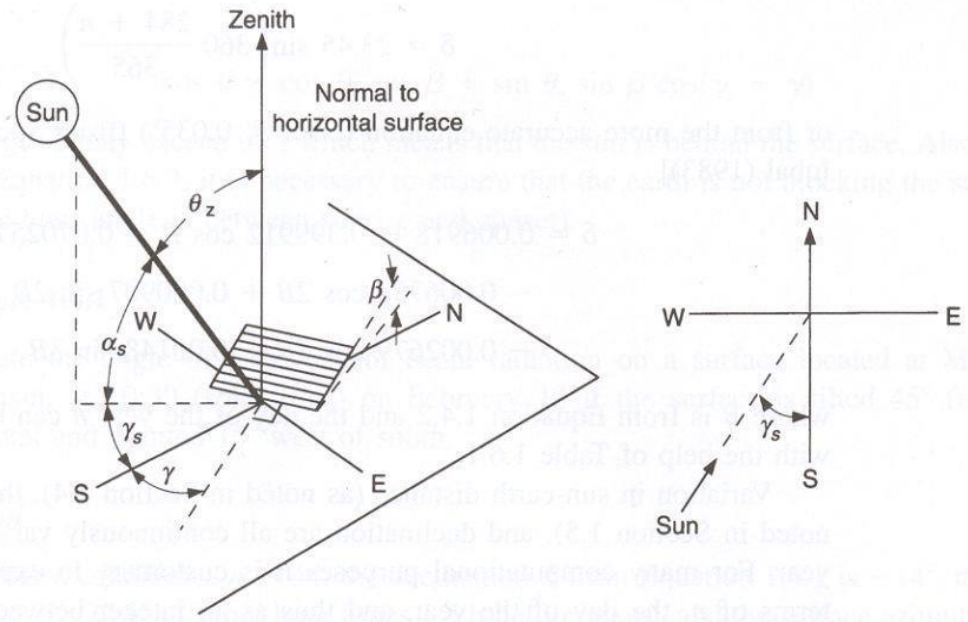

(a) (b)

Figure 2-3 – Sketches depicting the terminology used for describing the reference geometry for solar energy collection systems

(Duffie and Beckman, 2006)

The following angular descriptions have been adapted from Duffie and Beckman (2006) and are used throughout this thesis (Figure 2-3 (a)):

The angle between the collector plane and the horizontal is referred to as its slope and is identified by the Greek letter β. A β value of 90 degrees signifies a vertically mounted collection plane.

The angle of incidence (θ) is the angle between the normal to the collector plane and the incident beam of light.

The surface azimuth angle (γ) can be described as the horizontal angular deviation, of a given incidence beam of light, as the sun traverses the sky from the angle made by an incident beam at the meridian. By definition, at the local meridian γ is equal to zero.

The angle created between the zenith (the normal to the earth's surface at the collector's position i.e. the vertical axis) and the angle of an incident beam of light is referred to as the zenith angle (θ_z). The complimentary angle to the zenith angle is known as the solar altitude angle and is represented by α_s.

Finally, the solar azimuth angle (γ_s) can be described as the angular displacement, from the south, of the projection of beam radiation on the horizontal plane (Figure 2-3 (b)). The collector plane itself is described as being aligned in one of two distinctive orientations; either north-south or east-west. A north-south alignment may be thought of as an upright or vertical collector and an east-west alignment describes a horizontally aligned system. The optimum tilt angle for a flat plate collector can be roughly generalized as the latitude of the site minus 20° (CIBSE, 2009) although this is highly dependent on the type of collector and the geographical location and characteristics of the site.

2.1.5 Theoretical Maximum Solar Energy Collection

In order to accurately evaluate the potential of solar collection it is useful to create a baseline to compare the performance of developed systems against. The baseline in this case is the maximum steady state temperature available for collection (T) by a perfect unit area blackbody absorber and is defined by Equation 2-1.

$$\sigma T^4 = G \qquad \text{Equation 2-1}$$

Where, G is the radiative power density incident upon the absorber and σ is the Steffan-Boltzman constant.

Given that the peak energy density of incident solar radiation at the earth's surface is approximately 1100 Wm^{-2} (Duffie and Beckman, 2006) this results in an equilibrium temperature for the absorber of 373 K or approximately 100 °C which is ideal for numerous heating and cooling applications within buildings (Winston et al, 2005).

However, in real life applications it is not possible to achieve this ideal absorber temperature because of a number of factors which impinge upon collector performance ranging from insufficient absorber materials to transient levels of insolation from hour to hour, day to day and year to year at the earth's surface.

2.1.6 Solar Energy Capture

Incident solar radiation has been, and continues to be, utilized by mankind in a number of passive and active ways. The following section differentiates between the two types of energy capture and briefly describes a few of the systems used in each case.

2.1.6.1 Passive Solar Energy Capture

The concept of passive solar energy capture takes advantage of both the natural heat and light from the sun without the use of any parasitic power requirements to lower the heating, cooling and/or electrical lighting demands of a building. This well-established field dating back to classical Greek designs is primarily based around the orientation of buildings to the sun and has been expanded more recently to include the use of thermal mass systems like Trombe walls for example.

2.1.6.1.1 Daylighting

Daylighting is perhaps the most obvious form of passive solar energy capture. Allowing sunlight to penetrate into a building not only reduces the electrical energy requirements from artificial lighting but, when properly managed, also promotes wellbeing by regulating serotonin production within the body which has been proven to ease the effects of depression and reduce the symptoms associated with sick building syndrome relating to artificial lighting (headaches, eye strain, etc). The continued prevalence of sun spaces like solariums, atria and conservatories throughout the centuries is testament to the perceived benefits and enjoyment associated with natural lighting. An historical overview charting the development of solar architecture and technologies has been published by Butti and Perlin (1981).

2.1.6.1.2 Space Heating

In its most basic form a passive heating system is one in which the sun's radiant energy is converted to heat upon absorption by the building (Goswami et al, 2000). Put simply, the building elements themselves act as the solar energy collector, relinquishing the energy into the building in the late afternoon or in periods of reduced insolation as the temperature inside the heated spaces drops below the surface temperature of the walls, floors and windows.

Selectively orientating the larger window openings towards the equator with low zenith angle shading allows for increased passive solar gains and lowers heat losses from the non-equatorial façade in winter while preventing excessive heat gains in the summer from the exposed equatorial façade. The combined effects of this simple adjustment to the building's layout are a reduction in heating energy requirements in the winter and a reduction in cooling energy requirements in the summer.

2.1.6.1.3 Passive Ventilation

Solar energy can be used to aid in passive ventilation by utilizing a process known as the stack effect. The stack effect is created as a result of solar energy warming air within a building or a specifically designed cavity. The heated air, having a lower density than the surrounding air, then rises entraining cooler air into the void it has left.

2.1.6.2 Active Solar Energy Capture

Duffie and Beckman (2006) describe active solar heating systems as systems which use collectors to heat a [working] fluid, storage units to store solar energy until needed and distribution equipment to provide the solar energy to the heated spaces in a controlled manner. Although the description by Duffie and Beckman is based on thermal systems the same reasoning can be applied to solar electrical or photovoltaic systems too.

2.1.6.2.1 Electrical Solar Energy Capture

Although there are large scale systems available, like solar tower power plants, which pass a working fluid, superheated by solar energy, through a turbine to create electricity the most common and widespread form of solar electrical power generation comes from photovoltaic systems. The captured solar energy is converted to electricity by taking advantage of the photovoltaic effect (referred to in some literature as the photoelectric effect) which was first discovered by Alexander-Edmund Becquerel in 1839. Becquerel found that when exposing some materials to light they created an electrical current and it is this principle which underpins today's photovoltaic technologies.

2.1.6.2.2 Thermal Solar Energy Capture

Duffie and Beckman (2006) define a solar [Thermal] collector as a "special kind of heat exchanger that transforms solar radiant energy into heat" and Rabl (1985) identifies that the most important and most expensive single component of an active solar thermal energy system is the collector field which is responsible for the thermal conversion of captured solar energy. According to the report by Weiss and Mauthner (2015) the most common types of active solar thermal systems globally are; unglazed, glazed and evacuated tube collectors.

2.1.6.3 Hybrid Passive/Active Solar Energy

In reality most buildings which have installed a solar energy collection system can be considered as hybrid as they will, intentionally or unintentionally, employ some aspects of passive and active solar energy capture and this leads to the concept of the solar house (Goswami et al, 2000). A solar house utilizes both active and passive solar energy capture to reduce the overall energy requirements of the building.

2.1.7 Section Summary

This section has given a general introduction to solar energy; the consistency and magnitude of the resource, its availability, composition and the terminology used to describe how it interacts with collector planes. The section has also briefly introduced the various ways in which solar energy can be captured and used to meet the needs of the built environment. From the information presented in this section it is clear that, ideally, a building integrated solar collector would contribute in both active and passive ways to the building it's installed into and this concept will be carried through the rest of this chapter and into the collector design.

2.2 Active Solar Energy Collection Systems

The previous section has identified the inherent benefits of combining active and passive solar energy capture into the built environment. The purpose of this section is therefore to examine typical active solar energy collectors and to evaluate their suitability to incorporate aspects of passive solar energy collection too. This section covers four main groupings; solar thermal energy collection, solar electrical (photovoltaic) energy collection, photovoltaic-thermal (PVT) energy collection and concentrating solar energy collection. The operating principle for each type of systems is briefly explained with the focus remaining on shortlisting one type of system with the potential for adapting its absorber plane to incorporate some form of passive solar energy collection.

2.2.1 Solar Thermal

There are numerous variations in the design of solar thermal collection systems available however this section will focus on the three most common; unglazed, glazed and evacuated tube collectors. Figure 2-4 graphically presents the typical efficiencies and applications of the most common types of active solar thermal systems.

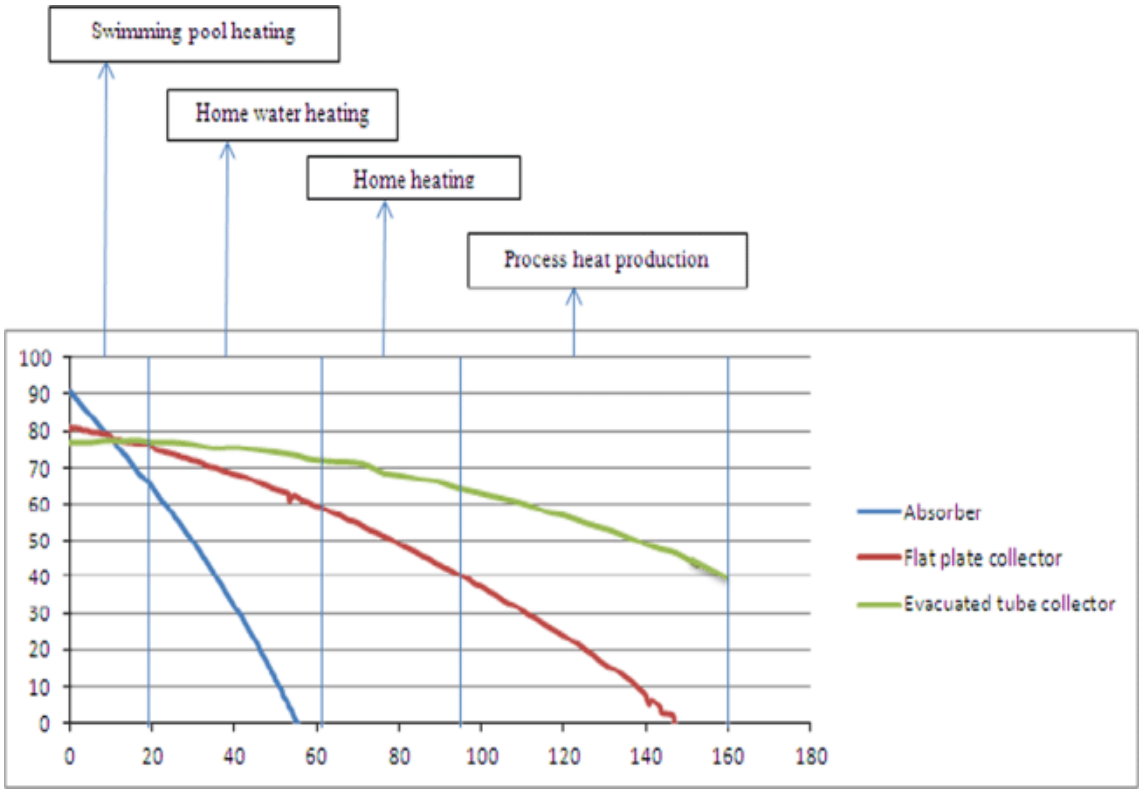

Figure 2-4 – Typical efficiencies and applications for the most common type of active solar thermal collectors

(Gaur, 2018)

2.2.1.1 Unglazed Solar Thermal Collectors

Unglazed collectors are commonly used in low temperature applications such as pool heating (Figure 2-4) and require large collector areas. This type of collector is most prevalent in Australia and the United States of America (Weiss and Mauthner, 2015). They are relatively basic flat plate collectors comprised of an absorber material which, in addition to having high absorbance of the incident radiation, should also have low emissivity, good thermal conductivity, and be stable thermally under temperatures encountered during operation and stagnation (Norton, 1992).

2.2.1.2 Glazed Solar Thermal Collectors

Glazed solar thermal collectors use one or more glazed panes to minimise upward heat losses from the absorber surface. Glazed flat plate collectors are commonly used in a variety of applications, heating air for space heating and water for low temperature hot water distribution systems (domestic hot water for example).

Both unglazed and glazed flat plate collectors have similar components. Figure 2-5 illustrates the construction of a generic flat plate glazed collector. Note the extensive insulation below the absorber plate used to prevent heat loss through the system.

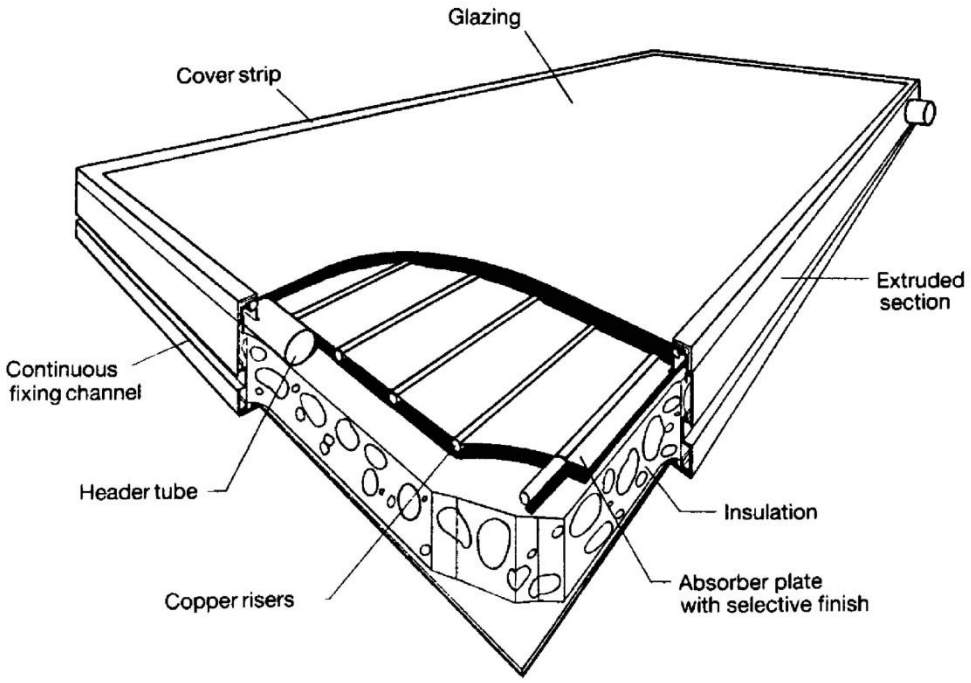

Figure 2-5 – Typical water-heating flat-plate collector panel

(Norton, 1992)

2.2.1.3 Evacuated Tube Solar Thermal Collectors

Evacuated tube solar thermal collectors come in various formats, primarily varying on how the absorbed solar energy is transferred into the working fluid in the manifold (direct flow, heat pipe etc.). Figure 2-6 shows a generic layout of a heat pipe evacuated tube solar collector complete with the evacuated tube, collector plate, evaporator and the condenser located in the manifold containing the fluid flow. This type of collector reduces heat losses from radiation and convection by enclosing a selectively coated low emissivity absorber surface within a vacuum.

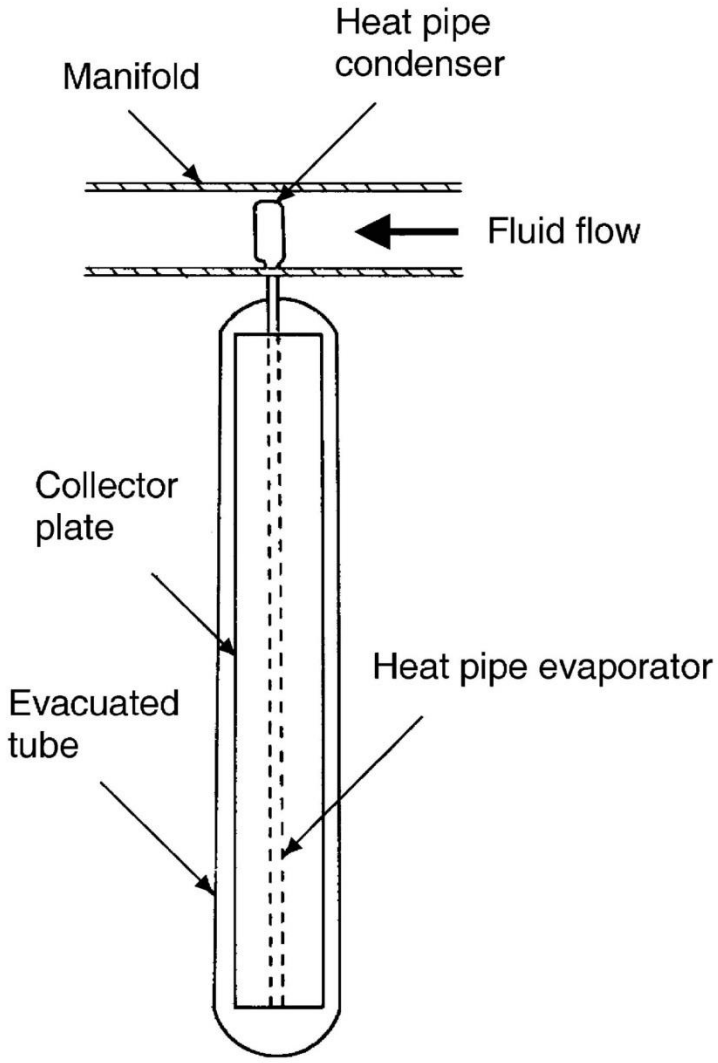

Figure 2-6 – Pictorial view of an evacuated tube collector

(Kalogirou, 2004)

2.2.2 Photovoltaics

Photovoltaic (PV) collectors are modular systems built from semiconductor cells. The cells are combined into modules and the modules in turn are used to construct collector arrays. This section focuses on providing a brief overview of the physical descriptions for PV cells, modules and arrays.

2.2.2.1 Cells

As alluded to in the previous section, PV cells operate by taking advantage of the photovoltaic effect Becquerel discovered in 1839. In his simple photoelectrochemical experiment shown in Figure 2-7 (a) he discovered that when certain materials are exposed to light they generate electricity. Within 50 years of this discovery William Adams and Richard Day had demonstrated that a solid body, a selenium tube, exposed to light can produce electrical energy (Figure 2-7 (b)).

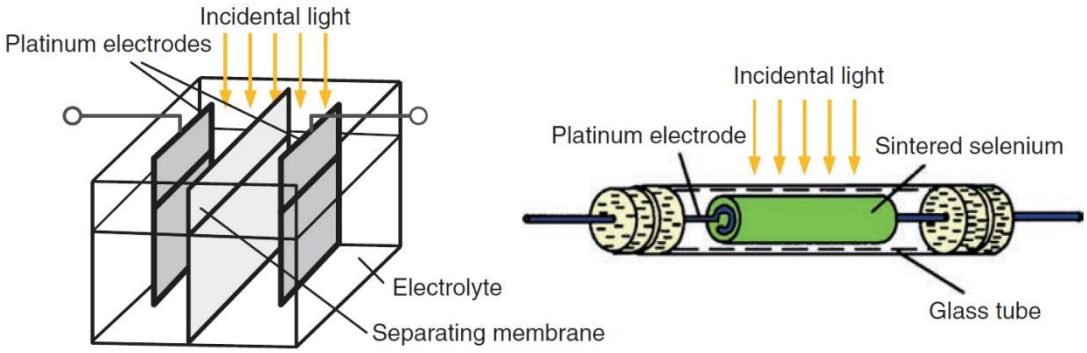

(a) (b)

Figure 2-7 – The History of the Solar Cell – (a) Becquerel's electrochemical experiment and (b) Adams and Day's Solar Cell

(Mertens, 2014)

The next significant step forward came in 1916 with the development of the Czochralski method, named after Polish Chemist Jan Czochralski, for growing high quality single semiconductor crystals. However, it wasn't until 1954 that the first silicon solar cell, the 'Bell Cell', was presented to the public. This cell, with a functional p-n junction, laid the foundations for most of the solar cell technologies available today (Figure 2-8).

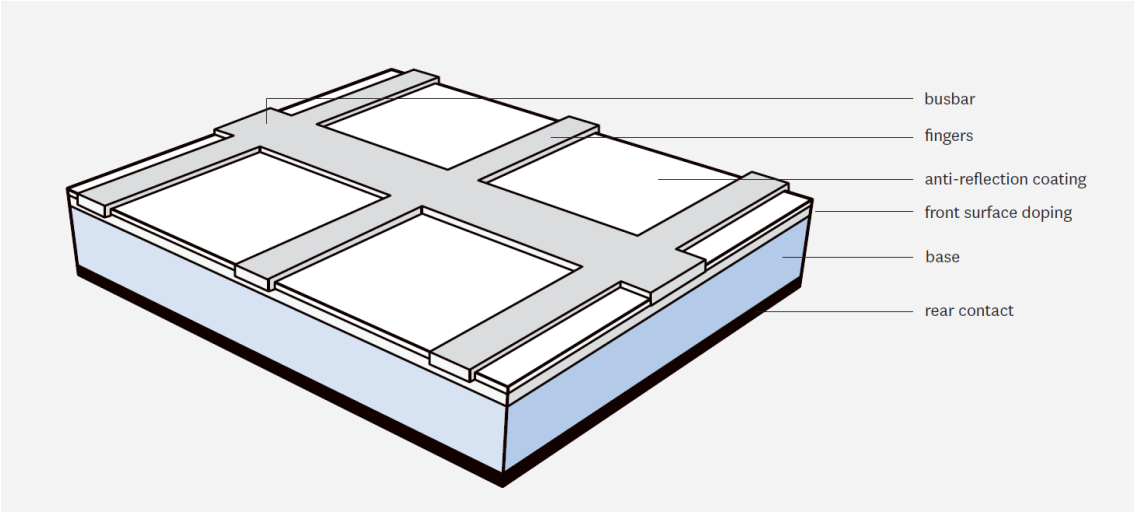

Figure 2-8 - Basic design of a crystalline silicon solar cell

(Roberts and Guariento, 2009)

Figure 2-9 gives a chronological insight into the various categories of cell development alongside the evolution of their respective conversion efficiencies to highlight the scope and speed of PV cell development.

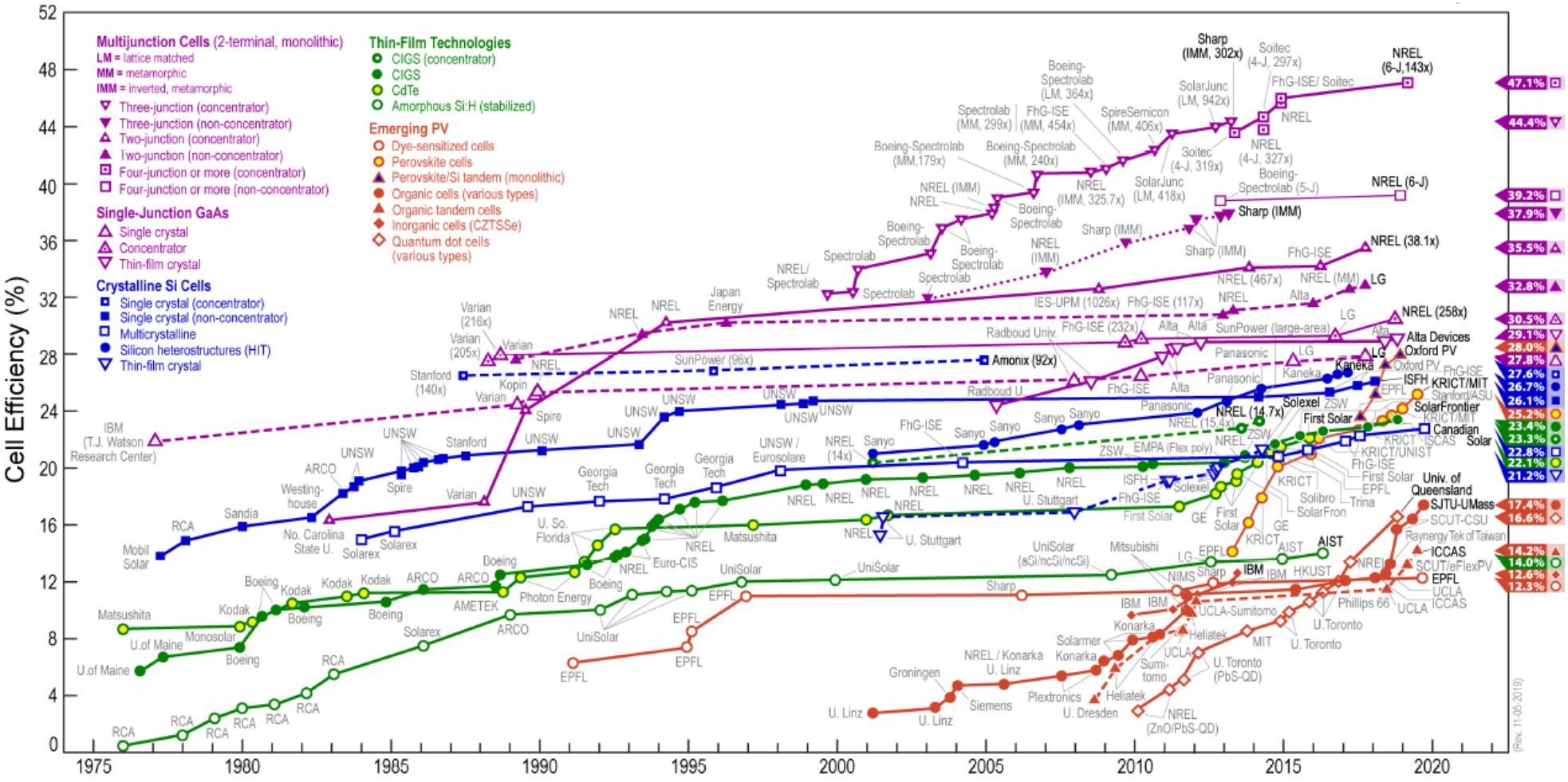

Figure 2-9 – Evolution of PV cell classes and efficiencies

(NREL, 2020)

2.2.2.2 Modules and Arrays

PV modules are a collection of individual cells connected together electrically to cover a larger surface area and to generate a larger electrical output than a single cell. Figure 2-10 shows how a typical PV module is constructed and Figure 2-11 shows the very first 8 cell solar module produced by the Bell Laboratory in 1954 which demonstrates just how far PV technologies have come in the last 66 years.

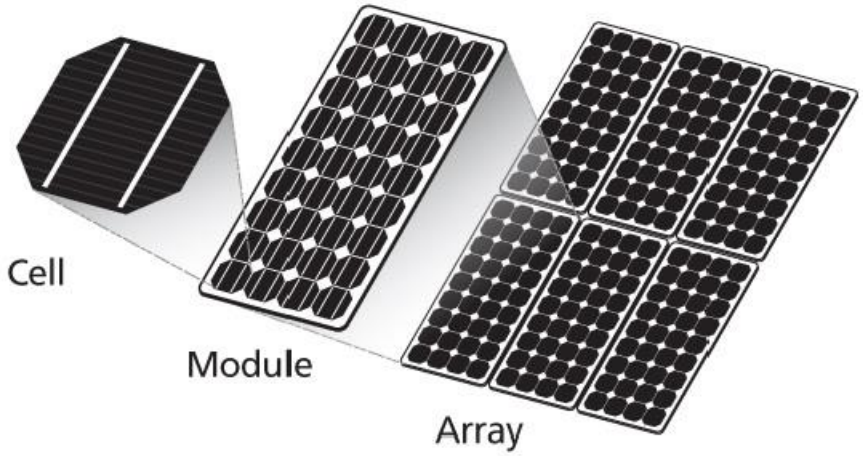

Figure 2-10 – Relationship between solar cells, modules and arrays

(Anon, 2018b)

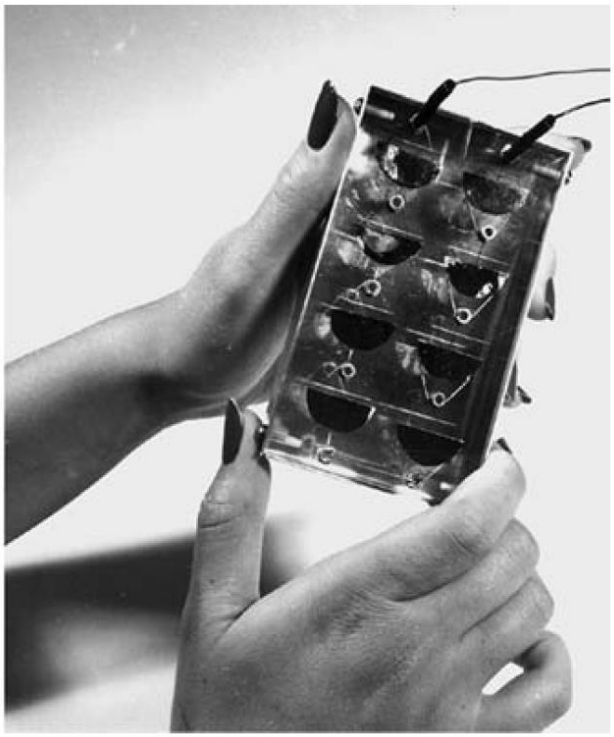

Figure 2-11 – The first 8 cell solar module

(Mertens, 2014)

A PV array is a collection of individual solar modules designed to be a power generator for a specific installation (Figure 2-10). There are a number of specific challenges associated with combining cells into modules and modules into array the most significant of which is non-uniform illumination leading to either shading or hotspots, both of which have a detrimental impact on the performance of the complete array.

2.2.3 PVT

The relatively low conversion efficiency of the solar energy captured by the selective absorber material used in the most common types of PV cell leads to a build-up of heat at the absorber surface. PVT collectors, generally flat plate designs, increase the efficiency of PV collectors by converting a portion of the addition captured energy into useable heat for space or water heating by warming air or water. Figure 2-12 shows the typical features of a flat plate PVT collector.

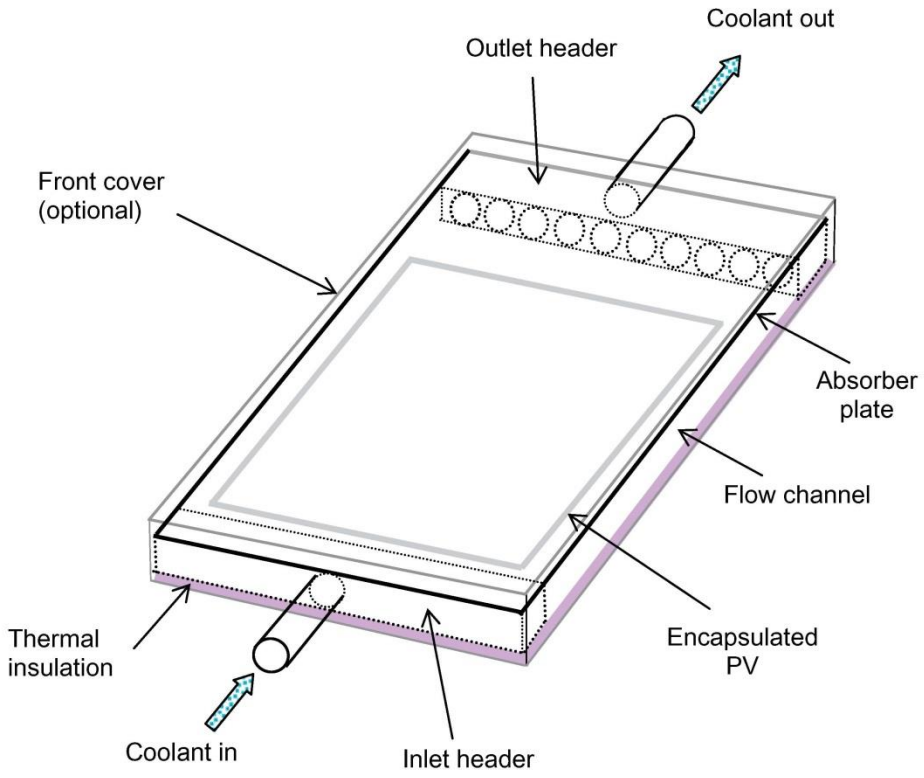

Figure 2-12 – Main features of a flat plate PVT collector

(Chow, 2009)

2.2.4 Concentrating Solar Energy Collectors

As a result of the relatively low energy density of incident solar energy and high capital cost of the collector field (absorber) a variety of concentration methods have been investigated throughout academic literature, mostly focussing on variations of the Compound Parabolic Concentrator (CPC) technologies introduced by Winston (1974) for thermal applications and on concentrating lenses based around the domed Fresnel lens and Simultaneous Multiple Surface (SMS) techniques refined by Leutz and Suzuki (2001) and Miñano et al (2003) respectively for photovoltaic applications. These systems, whether stationary or tracking, are designed to focus incident solar energy for a predetermined pair of acceptance angles on to an absorber surface, increasing the amount of energy available for conversion into electricity or heat without increasing the amount of expensive absorber material. The main issue encountered with solar concentrating technologies is that the cost of manufacturing the concentration elements is often prohibitive and offsets any saving gained from reducing the absorber area.

2.2.5 Section Summary

From the information presented within this section a modular PV array with a solar window design combining active energy collection, passive solar shading and natural lighting appears to be the most logical system to develop for a building integrated solar collector based on the subjective and aesthetic concerns outlined in Chapter 1. However, this section has also highlighted the potential for incorporating some form of cost effective solar concentrating element into the modular design to allow a certain amount of control over how and when the energy is collected.

2.3 PV Technologies and Building Integration

2.3.1 Introduction

This section is dedicated to the description of PV technologies and how those technologies are integrated into elements within the built environment. The section, which is composed of two parts, begins by introducing the main types of PV technologies available and how they have developed over time. Once the various PV cell options have been put in context, in terms of their level of development and typical output, the operating principals used in the most common types of PV cell will be introduced. The operating principals discussed are not comprehensive and are included solely to aid understanding of the work presented later in the thesis. After PV cell operating principals have been described the effects of connecting the cell together into modules are introduced, drawing the first half of the section to a close. The interconnection of PV modules into PV arrays is excluded from this section as it extends beyond the scope of the research presented here.

The second theme in this section defines the term building integration for PV modules and presents a sample of the options available for integrating PV within building envelopes using a variety of published works on the topic.

The section then concludes by briefly summarising the information presented and identifying the most appropriate type of building integrated module for development within this thesis, again focusing on the criteria presented by Luque and Hegedus (2011) in Chapter 1.

2.3.2 Introduction to PV cells

Semiconductor solar cells are fundamentally quite simple devices. Semiconductors have the capacity to absorb light and to deliver a portion of the energy of the absorbed photons to carriers of electrical current – electrons (e^-) and holes (h^+) (Gray, 2011). However solar cell technologies have evolved, and continue to evolve, in a number of ways to meet the demands of a variety of different applications.

There are a number of variations in the construction of the PV cells readily available on the market, each with their own specific pros and cons which primarily result in a trade-off between cell cost and cell performance. The following summaries are not intended to be comprehensive in their description but instead will serve as a brief introducing the main technologies available.

2.3.2.1.1 Crystalline Silicon Solar cells

There are two main varieties of crystalline silicone solar cells based on the processes developed by Czochralski; single crystalline (monocrystalline) and multicrystalline cells. Between them they constitute more than 85% of the PV market (Luque and Hegedus, 2011). The multicrystalline cells were introduced in the 1980s as a cheaper alternative to the more expensive single crystalline cells. However, due to issues with quality and efficiency of the final cell, those savings were never realised. Figure 2-13 shows that the performance of crystalline silicone cells has remained largely unchanged for 30 years.

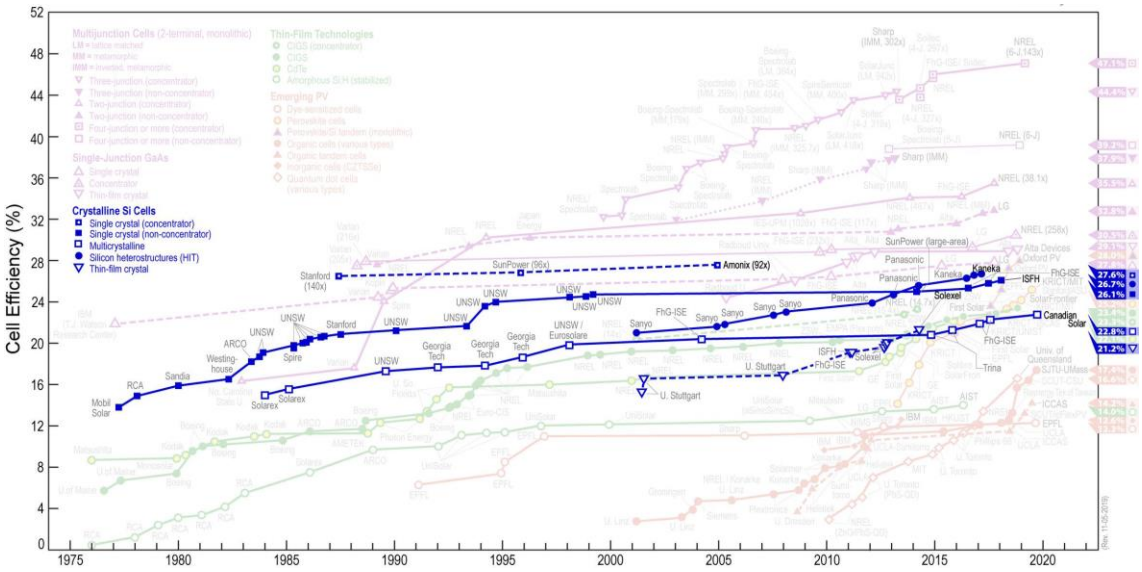

Figure 2-13 – Efficiency growth in Crystalline Silicone Solar Cells

(NREL, 2020)

2.3.2.1.2 Thin film Silicon Solar Cells

Thin film silicon solar cells have been extensively investigated for three reasons; material availability, performance and cost. The PV industry has been reliant on the semiconductor industry for a long time and as such they both compete for the same materials, this has led to periods of shortages in silicon for PV production. As a direct consequence of this thin film cells have been seen to be a more efficient way of using silicon, thus minimising the impact of these shortages. The second reason for investigating thin film cells is performance. One of the biggest barriers to the widespread adoption of thin film cells is conversion efficiency, which has been significantly lower than Crystalline Silicon cells. However, the efforts in developing thin film

cells are beginning to close the gap (Figure 2-14). Finally, although significant strides are being made, the cost of thin film cells in terms of kWh/kWp is still unattractive.

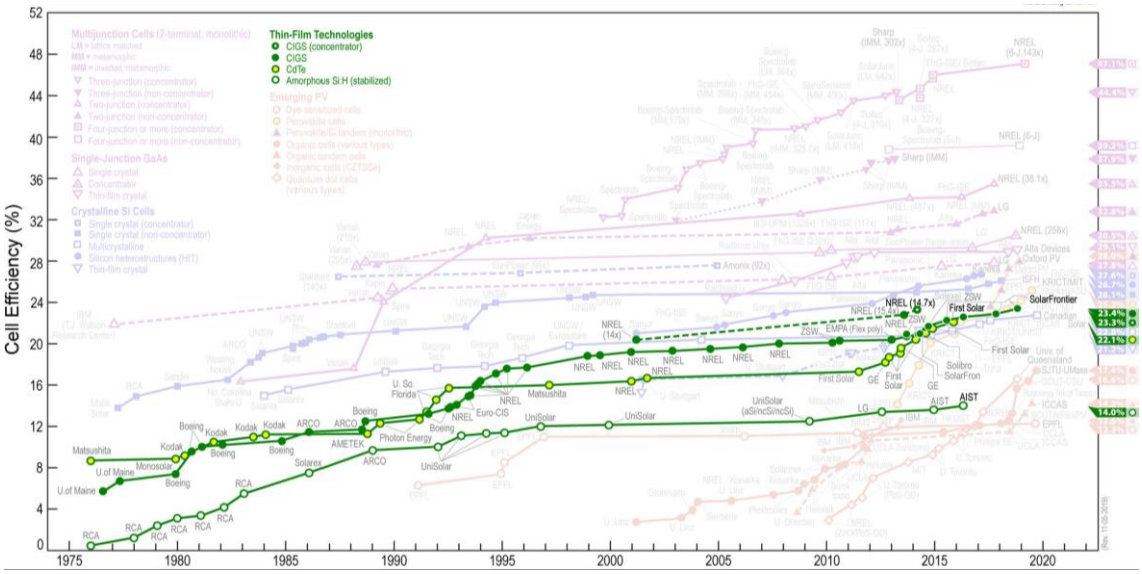

Figure 2-14 – Efficiency growth in thin film Silicone Solar Cells

(NREL, 2020)

2.3.2.1.3 High efficiency III-V multijunction Solar Cells

Tandem or composite solar cells are high efficiency cells which combine a number of solar cells layered on top of each other. The benefits of using this format are based around the collection efficiency for collectors with high concentration ratios and efficiencies of up to 47.1% have been confirmed in approved test lab conditions (Figure 2-15). These cells have the highest conversion efficiencies of any of the cell discussed however the main barrier to the widespread adoption of this solution is cost. In general, the costs of using multijunction solar cells are prohibitive for most applications.

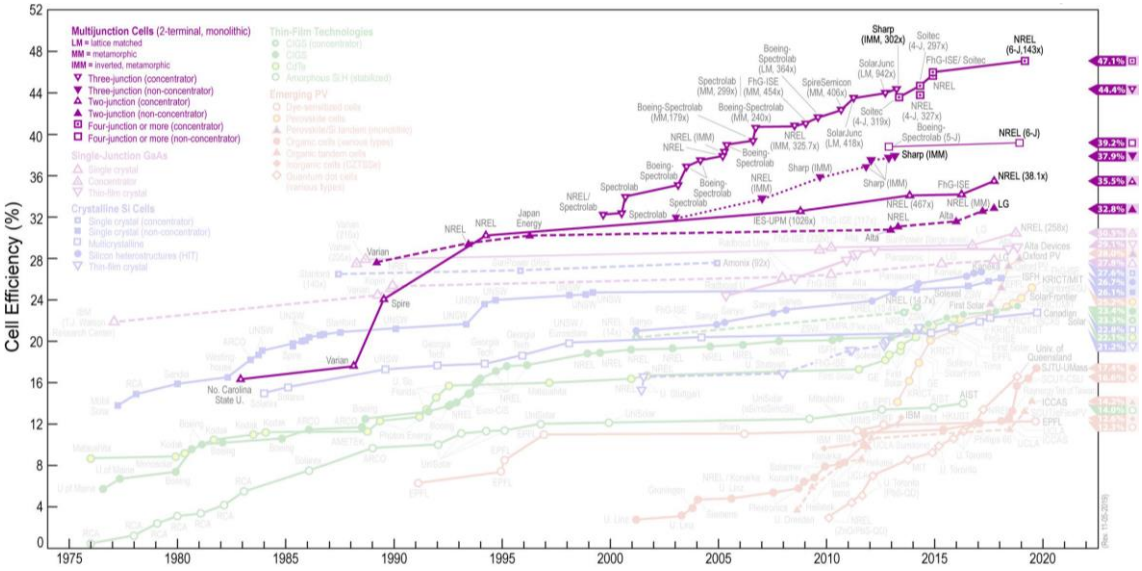

Figure 2-15 – Efficiency growth in multijunction Solar Cells

(NREL, 2020)

2.3.2.1.4 Amorphous Silicon Solar Cells

Amorphous silicon cells are non-crystalline cells generally grown by deposition from gases or plasma. They are relatively cheap to manufacture when compared to crystalline cell growth however their efficiencies tend to be quite low. One of the most interesting idiosyncrasies of these cells is the Staebler-Wronski effect which sees a degradation in cell efficiency over the first 1000 hours of exposure to light at which point the cells conversion efficiency stabilises.

2.3.2.1.5 Cu(InGa)Se_2 Solar Cells

Cu(InGa)Se_2-based solar cells have often been touted as being among the most promising of solar cell technologies for cost-effective power generation (Shafarman and Stolt, 2011). Developed as part of the work carried out by Bell Laboratories, the potential for this type of cell was recognised early on. The challenge for this solution was the development of the manufacturing processes necessary to achieve large scale production and, despite a significant amount of progress in this area, the production quality of Cu(InGa)Se_2 cells have failed to live up to the promise of the laboratory samples tested.

2.3.2.1.6 Cadmium Telluride (CdTe) Solar Cells

Thin-film cadmium telluride (CdTe) solar cells are the basis of a significant technology advancement with major commercial impacts on solar energy production. Large-area monolithic thin film modules demonstrate long-term stability, competitive performance, and the ability to attract production-scale capital investments (McCandless and Sites, 2011). There are a number of technical barriers for this technology to overcome in order to challenge crystalline silicon cells, not least of which are the concerns over using Cadmium in the manufacturing process and the damage to the environment caused by Cadmium toxicity. These concerns have led to the inclusion of Cadmium in European Directive 2011/65/EU on the restriction of the use of hazardous substances (ROHS Recast) in electrical and electronic equipment (Anon, 2011).

2.3.2.1.7 Dye Sensitised Solar Cells

Dye Sensitised Solar Cells are photoelectrochemical cells and are in essence a modern-day equivalent of the cell used in Becquerel's experiment almost 200 years ago. This technology has significant potential however it lacks maturity at present and the main challenges which it will need to overcome are the relatively low efficiencies, the chemical complexities and the long-term stability of the cells in operation.

2.3.3 PV technology

Within this sub-section the terminology and physical operating principles of PV cell technologies are introduced. Throughout this chapter, and the thesis as a whole, the terms PV cell(s) and solar cell(s) are used interchangeably with the same meaning. Before delving into the physics behind the performance of PV cells it is prudent to first take a look at the raw material used throughout the most prevalent technologies; Silicon. The Silicon atom (Figure 2-16) is comprised of a nucleus containing 14 neutrons and 14 protons surrounded by 14 electrons across 3 shells. The inner two shells are fully populated but the outer shell, the M-shell, contains four valence electrons which are necessary in the creation of covalent bonds between other atoms. It is this valence electron structure which allows the atoms to form the regular crystalline lattice necessary for the growth of semiconductor wafers.

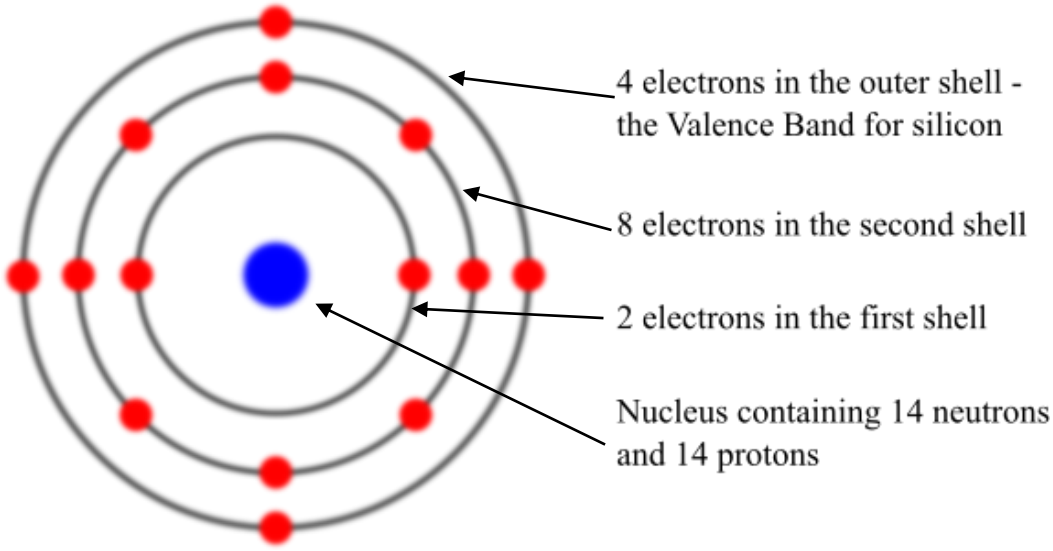

Figure 2-16 – The Bohr Model of a silicon atom

2.3.3.1 Crystalline Silicon solar cells and p-n junctions

In 1950 William Shockley laid the theoretical groundwork for modern solar cells by describing the function of the p-n junction; a metallic junction created at the boundary of two doped layers of silicon. In this section the creation, characteristics and function of a p-n junction will be discussed but first the anatomy of a simple solar cell will be described. Figure 2-17 shows a simplistic view of the conversion of a portion of incident sunlight into electrical energy. A solar cell is essentially a semiconductor diode sandwiched between two electrical contacts; a metal contact on the back of the cell and a metal grid on the top. The grid structure allows sunlight to fall between the metal contacts into the semiconductor material. An antireflective coating is also added to the top of the cell, between the contacts of the metal grid, to maximise the amount of incident solar radiation. The obvious imbalance in the volume of doped materials is to allow sunlight to penetrate through the thinner n-doped region into the depletion zone between the layers where the electron – hole pairs are generated.

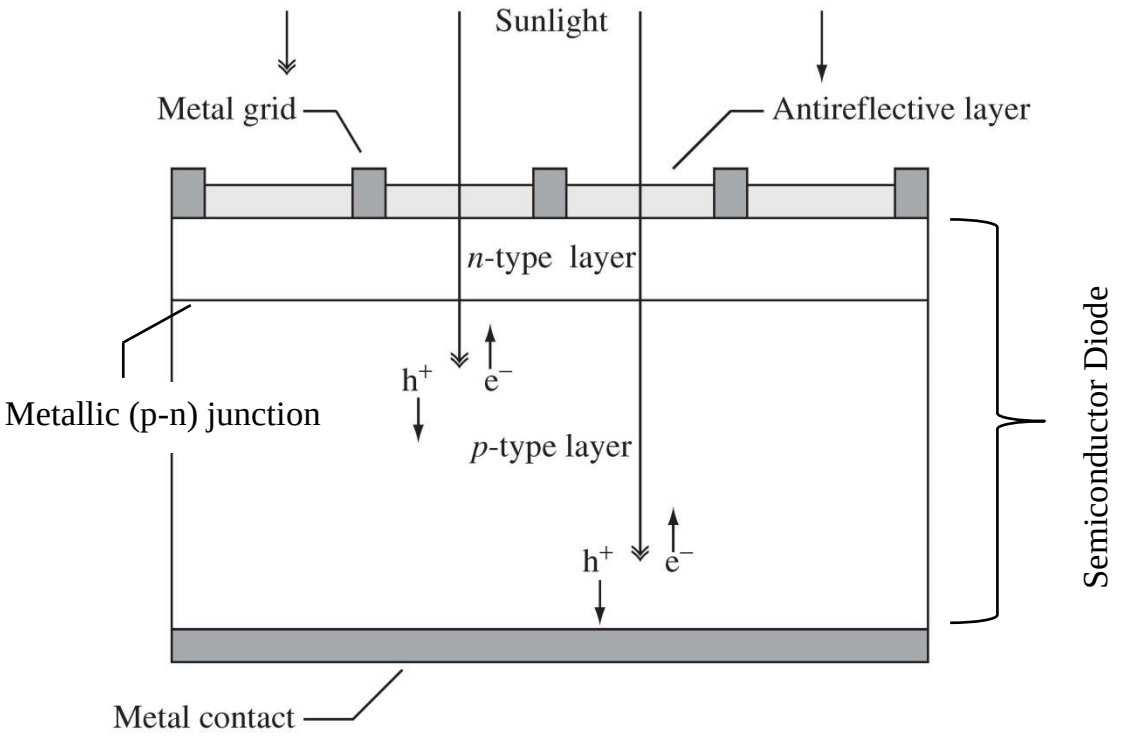

Figure 2-17 – A schematic of a simple conventional solar cell showing the creation of electron – hole pairs

(Adapted from Gray, 2011)

As the name indicates a semiconductor wafer, manufactured solely from silicon, is a relatively poor conductor of electricity. In order to improve the ability of the silicon crystals to conduct electrons the raw silicon crystals are doped with a material which has either one extra valent electron (n-doping) or one less valent electron (p-doping). Figure 2-18 shows a 2-dimensional depiction of all three states; undoped, n-doped and p-doped. In practice the doping densities are very low: For instance, only every hundred-thousandth silicon atom is replaced by a doping atom. Yet the conductivity of the material can be increased by many factors of 10 (Mertens, 2014).

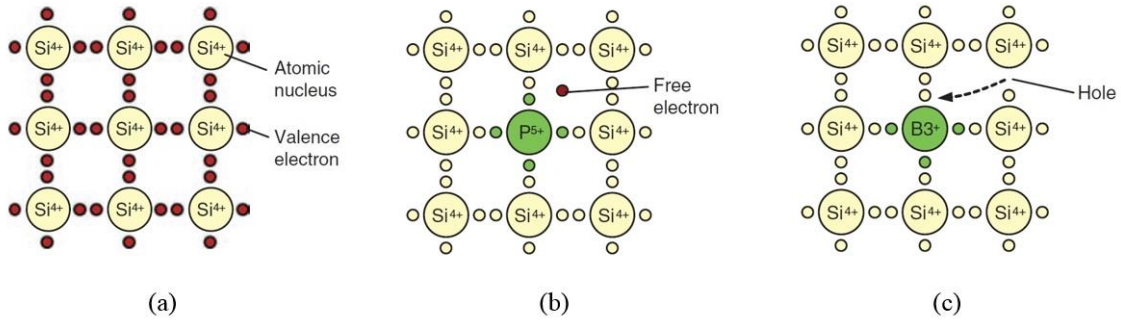

Figure 2-18 – 2-D images of undoped and doped silicon crystal structures: (a) undoped Silicon, (b) n-doped silicon with Phosphorus, (c) p-doped silicon with Boron

(Adapted from Mertens, 2014)

By combining the p and n-doped semiconductor layers a diode is formed around the metallic junction which is essential for the functionality of solar cells. This diode can be either forward or reverse biased depending on the electrical field applied. For solar cells the connection is forward biased, meaning the anode connection is located on the p-doped electrical contact and the cathode is mounted on the n-doped metal grid. Reversing this connection would prevent the cells from operating effectively.

The main advantage of this configuration is that the semiconductor material is capable of carrying current much more readily because of the higher number of available intrinsic carriers. The final physical consideration in the doping process is that both the p and n-doped layers are doped evenly. Practically, uneven doping can and does occur, the main consequence of which is a lowering of the overall intrinsic carrier concentration and the layer with the lowest doping concentration tends to be more dominant in defining the cell's performance characteristics.

When the p and n layers are joined together a depletion zone is created on either side of the p-n junction (the space charge region in Figure 2-19). The n-doped material is rich in excess free electrons, which are not chemically bound to the atomic structure, and electrons will naturally

gravitate to the lowest available energy level. Across the p-n junction the p-doped material is rich in holes for the free electrons to inhabit and so the excess electrons drift and diffuse across the junction into the p-doped material creating a negatively charged region in the n-doped material. The migration of holes using the same method creates a positively charged region in the n-doped material. Hole mobility is lower than that of the electron. For holes to gain mobility it is necessary that electrons move one after the other to free spaces, which occurs much slower than the movement of a free electron in a crystal (Mertens, 2014). If no external influences are applied this process will tend to equilibrium as an insulating electrical field is formed in the depletion zone, repelling like charges from crossing the p-n junction.

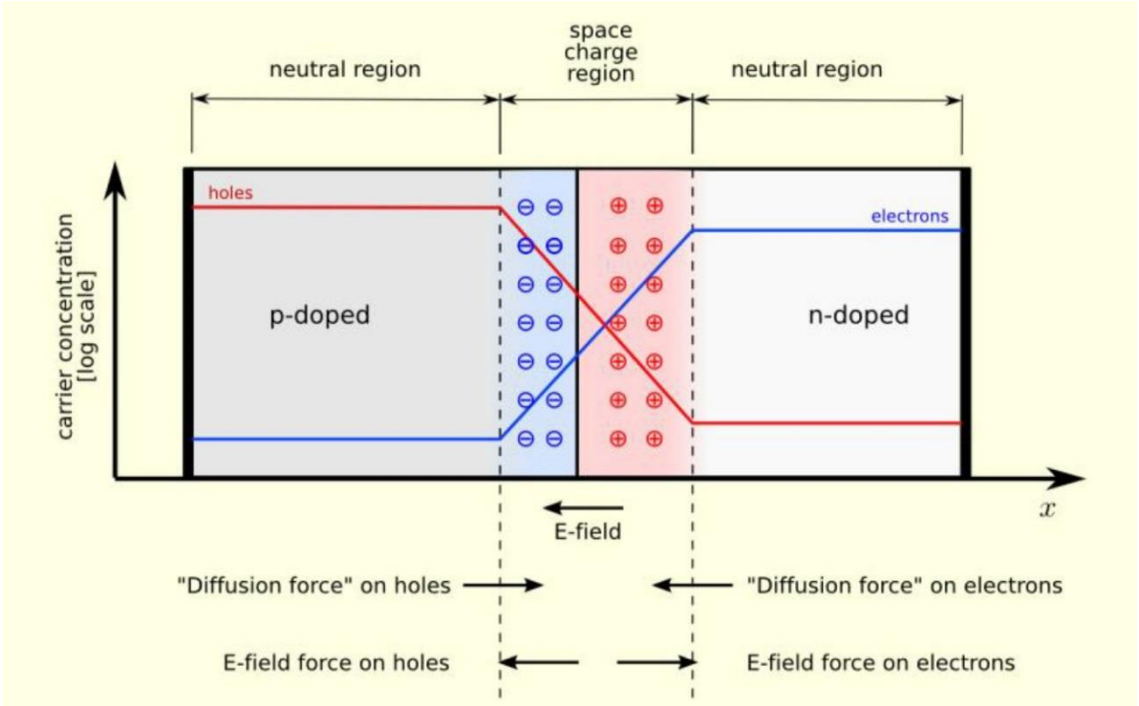

Figure 2-19 – Simplified sketch of a p-n junction and energy band structure (Markvart, 1994)

A final advantage of doping silicon for solar applications is the impact the doped regions have on the enegy gap (E_G) between the conduction (E_C) and valence (E_V) bands. The addition of excess electrons and holes creates two new levels within the original energy gap; the acceptor level (E_A) and the donor level (E_D) (Figure 2-20). This reduction in the energy gap between the conduction and valence band facilitates increases the ability of the material to conduct electrical energy.

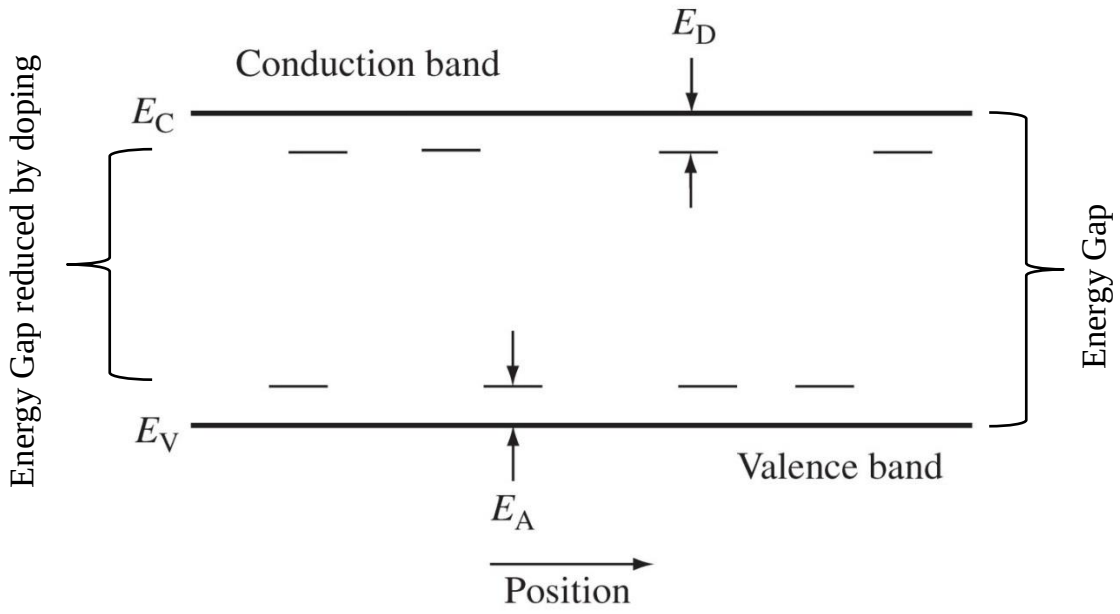

Figure 2-20 – Simplified energy band structure for a doped semiconductor

(Adapted from Gray, 2011)

Gray (2011) states that the nonuniform spatial distribution of these states reinforces the concept that these are localised states. This statement essentially describes the relationship between the energy gap (or band gap in some literature) and the doping concentration. Slotboom and de Graaff (1976) investigated the effects of band gap narrowing and concluded that excessive band gap narrowing as a result of this mechanism has a negative effect on solar cell performance.

2.3.3.2 Light absorption and recombination in semiconductors

The excitation of an electron directly from the valence band (which leaves a hole behind) to the conduction band is called fundamental absorption. Both the total energy and momentum of all particles involved in the absorption process must be conserved (Gray, 2011).

It should be noted that it is not possible to convert all of the incident solar energy to electrical energy. Only incident photons with an energy exceeding the band gap between the valence and conductions bands are successful in creating an electron-hole ($e^- h^+$) pair. Figure 2-21 shows a simplified model of the light absorption and recombination process for a solar cell.

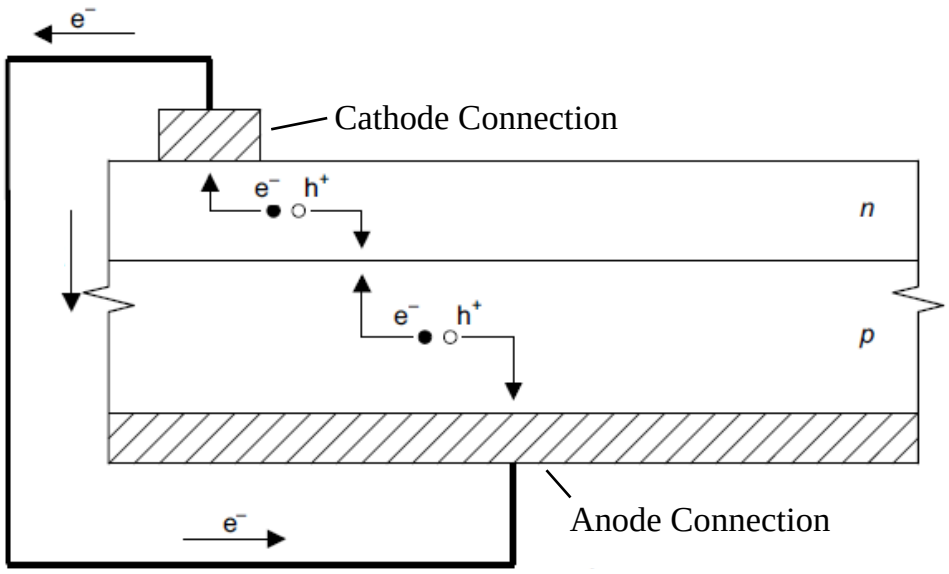

Figure 2-21 – Simplified model showing the absorption of light in PV cells

(Adapted from Wenham et al, 2007)

When an incident photon of the correct magnitude provides an electron with enough energy to escape its chemical bond an electron-hole pair is formed. Once formed the electron migrates towards the cathode connection and the hole migrates towards the anode. This process creates a potential difference across the cell as the electron is attracted to the anode through the circuit. The electron then flows along the electrical connections (across a load if present). On reaching the anode it recombines with the hole equalising the charge within the semiconductor material.

2.3.3.3 Generation rate

The generation rate (G) of electron-hole pairs per unit volume can be calculated using the formula:

$$G = \alpha N e^{-\alpha x} \qquad \text{Equation 2-2}$$

Where, N is the photon flux (photons per unit area per second), α is the absorption coefficient, and x is the distance from the surface (Wenham et al, 2007).

2.3.3.4 Characterising the performance of solar cells

Solar cell performance is generally characterised by plotting a cell's current against its voltage in an I-V Curve (Figure 2-22), written as 'IV curve' in some literature. This allows the cell's performance to be described as a function of a number of key metrics:

- Short circuit current
- Open circuit voltage
- Maximum power point
- Fill factor
- Cell efficiency

These metrics have been developed over time to provide insight into the quality of a solar cell's construction and output.

Within this section a brief description of the main metrics will be outlined including a summary of the significance they play in providing clarity on the underlying physics at play.

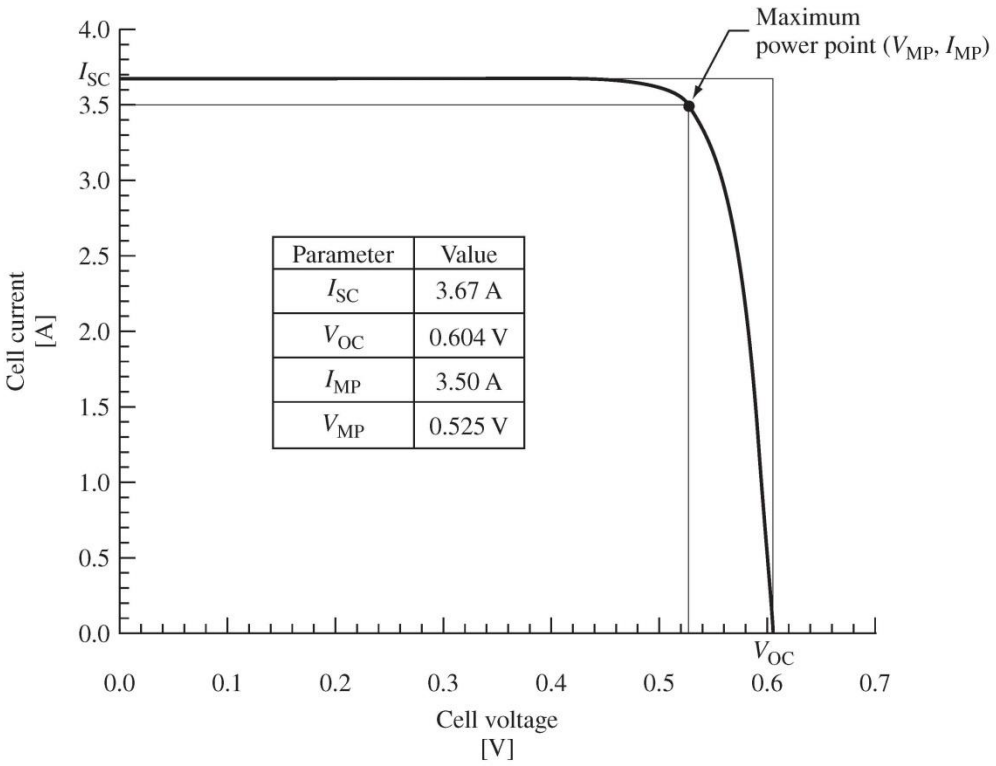

Figure 2-22 – Typical I-V curve for a PV cell

(Gray, 2011)

2.3.3.4.1 Short circuit current (I_{SC}) and Open circuit voltage (V_{OC})

The two limiting parameters used to characterise the output of solar cells for given irradiance, operating temperature and area are (Adapted from Shockley & Queisser, 1961):

1. Short circuit current (I_{SC}) – the maximum current, at zero voltage. Ideally, if the voltage is equal to zero, then the short circuit current is equal to the light generated current. This assumes that dark current (I_0), current generated in the absence of illumination, is zero. Short circuit current is directly proportional to the intensity of the available light.
2. Open circuit voltage (V_{OC}) – the maximum voltage, at zero current. The value of V_{OC} increases logarithmically with increased sunlight. This characteristic makes solar cells ideally suited to battery charging (Wenham et al, 2007)

Gray (2011) defines the short circuit current (Equation 2-3) as a sum of the contributions from the three regions: the n-type region (I_{SCN}), the depletion region (I_{SCD}) and the p-type region (I_{SCP}).

$$I_{SC} = I_{SCN} + I_{SCD} + I_{SCP}$$ Equation 2-3

From this equation the current (I) generated by a solar cell can be inferred using the following equation:

$$I = I_{SC} - I_{o1}\left(e^{qV/kT} - 1\right) - I_{o2}\left(e^{qV/2kT} - 1\right)$$

Equation 2-4

Where, I_{o1} and I_{o2} are defined as function so the dark saturation currents due to recombination in the quasi-neutral and space charge regions, respectively (Gray, 2011).

As the description by Shockley & Queisser (1961) implies, open circuit voltage is the potential difference across the solar cell (between the cathode and anode contacts) when no load is applied. Wenham et al (2007) describe open circuit voltage using the following equation:

$$V_{OC} = \frac{nkT}{q}\ln\left(\frac{I_L}{I_o} + 1\right)$$ Equation 2-5

Where, kT is the thermal voltage of the cell, n is an ideality factor (a number between 1 and 2 which is used to describe the recombination characteristics within a diode, this factor typically increases as the current decreases) and q is the charge on an electron.

2.3.3.4.2 Maximum power point (M_{PP})

The maximum power point (M_{PP}) is the point on an I-V curve where the solar cell is producing its maximum power output. As shown in Figure 2-22, this maximum output can be described within the graph as the largest area which can be defined under the I-V curve. In order to clarify the position of the maximum power point it is often common to see a power against voltage (P-V) curve alongside an I-V plot.

2.3.3.4.3 Fill factor (FF)

The fill factor (FF) is a measure of the junction quality and series resistance of a cell (Wenham et al, 2007) and can be defined as follows:

$$FF = \frac{P_{MPP}}{V_{OC}I_{SC}} = \frac{V_{MPP}I_{MPP}}{V_{OC}I_{SC}} \qquad \text{Equation 2-6}$$

Graphically, in terms of the I-V curve for a typical solar cell presented in Figure 2-22, the closer the fill factor is to unity the larger the area under the curve becomes signifying a higher quality/lower loss cell construction.

2.3.3.5 Effect of temperature on cell performance

As the temperature of a silicon solar cell increases a number of things happen (Figure 2-23). The most notable of which is that the fill factor is reduced as the open circuit voltage decreases. A small increase in short circuit current can also be seen as a side effect of band gap shrinkage.

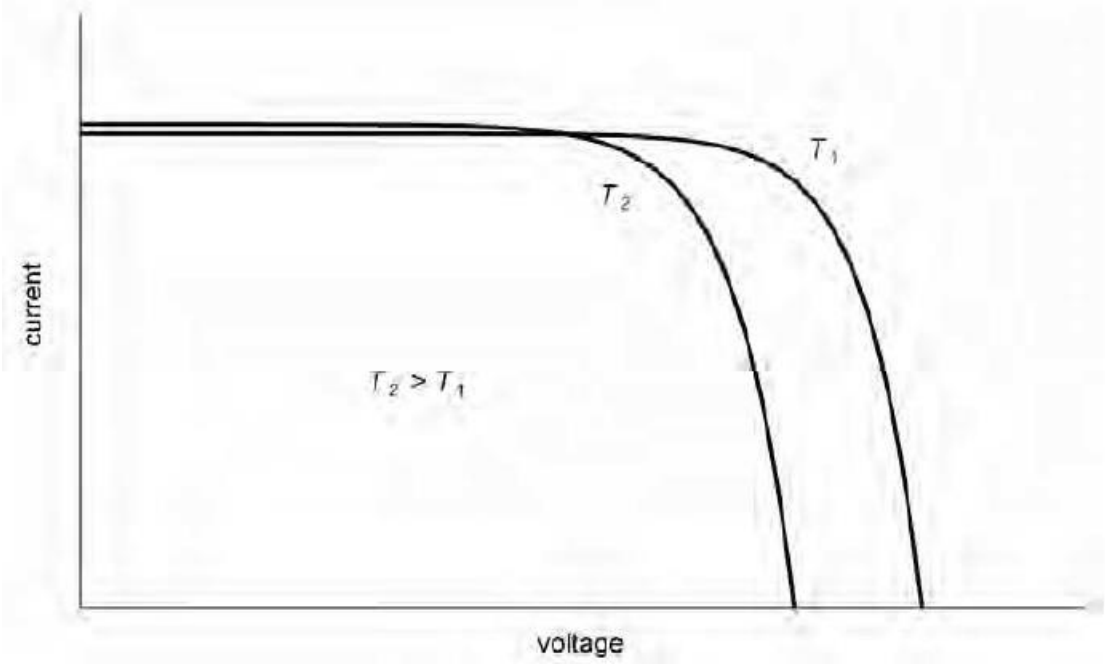

Figure 2-23 – The effect of temperature on the I-V characteristics of a solar cell (Wenham et al, 2007)

2.3.3.6 Cell efficiency (η)

A variety of ways to measure solar cell efficiency have been presented in academic literature from collection efficiency and conversion efficiency through to the electrical efficiency of cells, modules and arrays. Throughout all of them the concept can be summarised by the simple power in over power out ratio presented in Equation 2-7. For the purposes of this introduction to PV technology this is sufficient enough to aid understanding without adding any unnecessary complications.

$$\eta = \frac{P_{MPP}}{P_{in}} = \frac{FF.V_{OC}.I_{SC}}{GA_{eff}} \qquad \text{Equation 2-7}$$

Where; GA_{eff} is the global incident radiation (G) multiplied by the effective absorber area (A_{eff}) power input (P_{in}) to the cell.

Gray (2011) provides an indication of the theoretical maximum efficiency of a solar cell as a function of the semiconductor's band gap at AM 1.5 (Figure 2-24). This calculated efficiency assumes an impractical zero loss light absorption under uniform, non-concentrated solar illumination. However, a later acknowledgement is made that the actual maximum theoretical efficiency for a solar cell is approximately 30% (Gray, 2011).

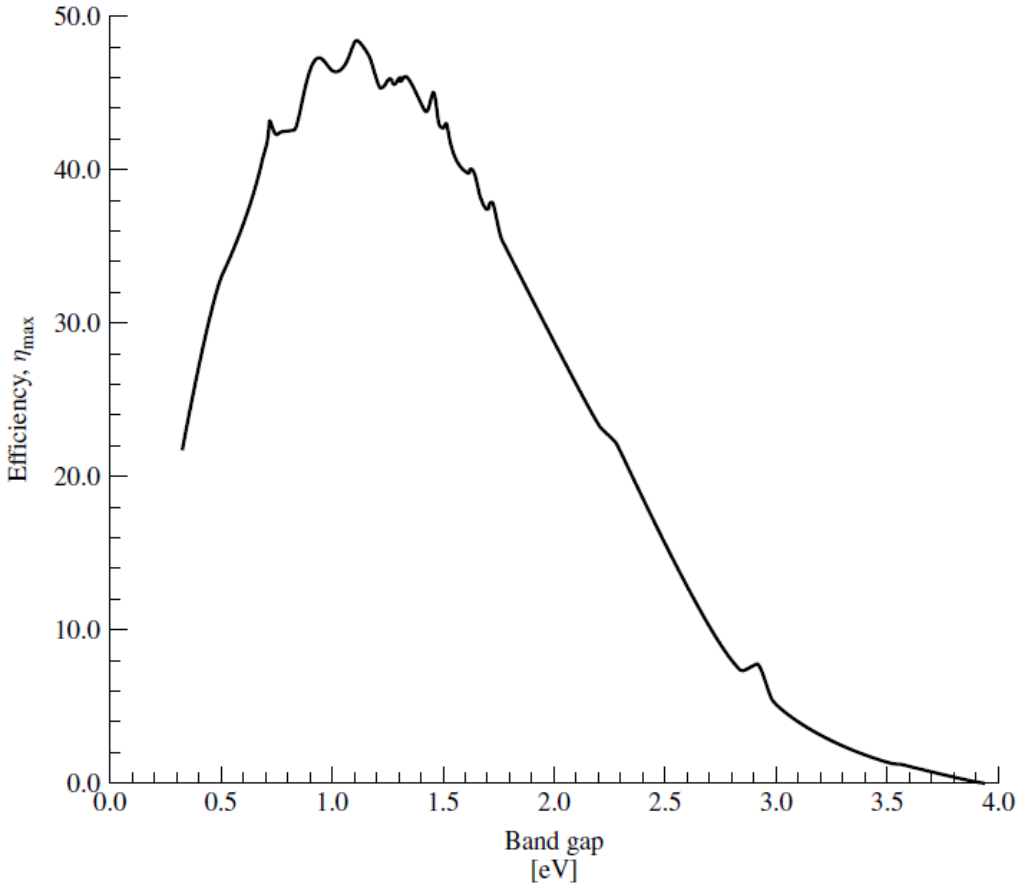

Figure 2-24 – Theoretical maximum efficiency as a function of semiconductor band gap for an AM 1.5 global spectrum

(Gray, 2011)

2.3.3.7 Connecting cells and modules

When combining solar cells into modules there are two options; the cells can be connected in series or in parallel. There are positive and negative aspects associated with each type of cell integration method. The practicalities and consequences of the two circuit designs, including the losses associated with both options, are introduced and described in this section.

2.3.3.7.1 Series Circuits

Connecting solar cells in series has an additive effect on the potential difference across the cell but doesn't effect the current produced. This increase in the voltage produced comes at the cost of introducing losses as a result of series resistance (R_S). The impact of increasing series resistance can be seen in Figure 2-25 and Wenham et al (2007) categorises the major contributors to the series resistances losses as:

- the bulk resistance of the semiconductor material
- the metallic contacts and interconnections
- carrier transport through the top diffused layer
- contact resistance between the metallic contacts and the semiconductor.

2.3.3.7.2 Parallel (shunt) Circuits

In contrast to the series circuits, connecting solar cells in parallel has an additive effect on the current but doesn't effect the potential difference between the cathode and anode. Parallel circuits also suffer losses from increased resistance in the system, in this case shunt resistance (R_{SH}). Wenham et al (2007) explains that shunt resistance is a consequence of non-idealities and impurities near the p-n junction which leads to localised shorting, particularly near the cell edges. The impact of increasing shunt resistance within a solar module can be seen in Figure 2-26.

In reality a module may be influenced by both series and shunt resistance and given that the maximum power point is the product of both current and voltage it is clear that any additional resistance created within the module will have a detrimental impact of the collector's performance.

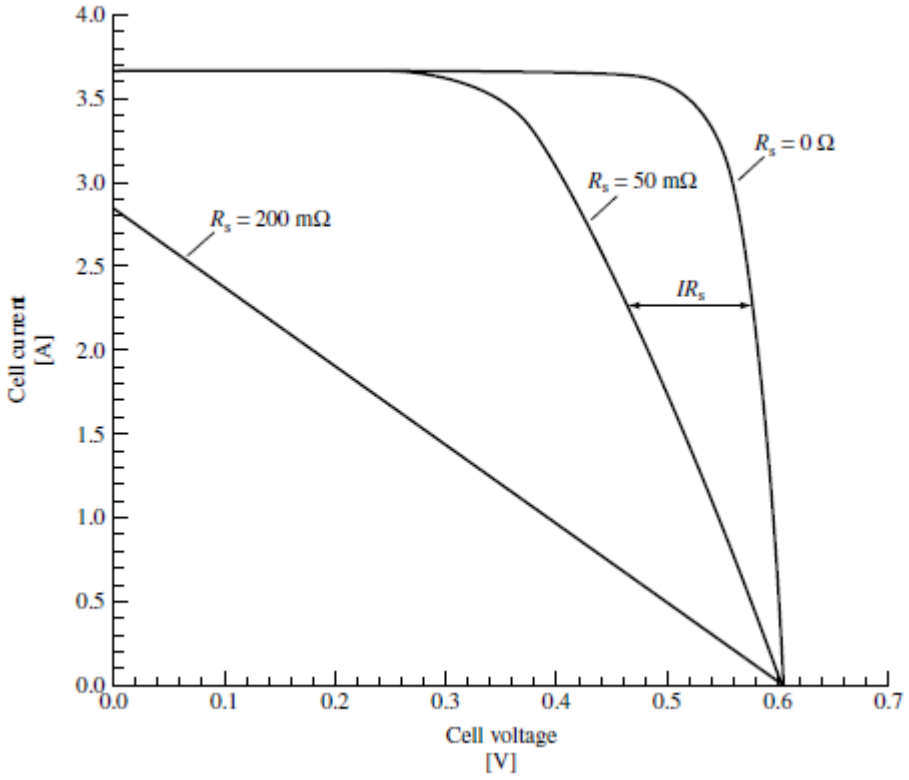

Figure 2-25 – Series losses in PV modules and arrays

(Gray, 2011)

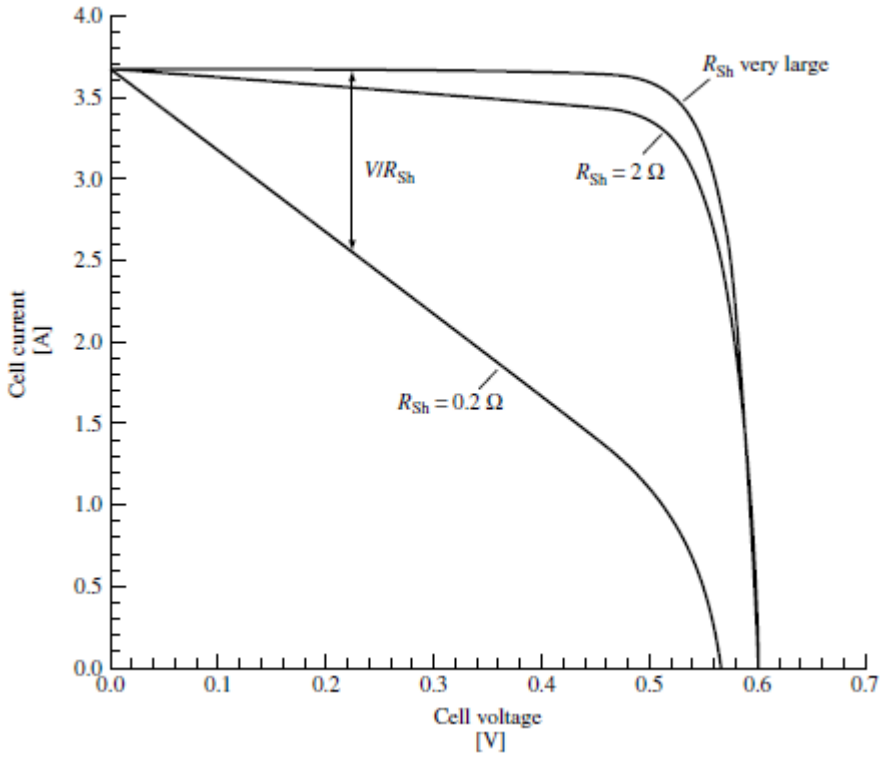

Figure 2-26 – Parallel (shunt) losses in PV modules and arrays

(Gray, 2011)

2.3.4 Section Summary

This section has introduced the fundamental concepts describing the operation of a PV cell from the anatomy of the base material and the solar cell structure, through to the metrics used in characterising PV cell performance and culminating in some of the considerations useful in scaling up the collector area from a single cell to a solar collection module. This basic introduction into what PV technology is and how it operates will allow for a more informed understanding of how these technologies interact with various elements of the concept developed and the built environment as a whole..

2.3.5 Building Integration of PV Systems

One of the main themes of this thesis is the building integration of solar collectors. However, within the wider academic literature the term building integration has also been used to describe systems which are building mounted too. For clarification, within this section the term building integration refers to collectors which form part of the building envelope and building mounted collectors are external additions fixed to the building envelope. The following section provides examples of the various options available for incorporating PV systems within the built environment. The purpose of this section is to evaluate those options in order to highlight the potential for developing an active building integrated PV collector with the additional benefits of passive solar shading and the transmission of natural light into the building.

Thomas (2003) states that there are three basic design options available for integrating PV systems into buildings:

- Roof based systems
- Façade systems
- Sunshades and sunscreens

Each of these options will now be introduced and discussed, beginning with roof mounting and finishing on PV augmented brise-soleil (sunshades with active PV collection). All of the systems discussed in this section represent the first two of the categories for integrating solar energy collection technologies within an architectural context described by Kaan and Reijenga (2004) and Luque and Hegedus (2011). These categories, the most common in today's built environment, cover solar collection systems which are either applied invisibly or added to the design.

2.3.5.1 Methods for combining PV modules with roofs

Roof based PV systems are the most common type of PV installation and the inclusion of PV modules on a roof has a number of attractions. Thomas (2003) identifies three of these attractions for roof-based PV systems as:

- They are often free from over-shadowing
- The roof slope can be selected for higher performance
- It may be easier to integrate PVs aesthetically and functionally into a roof than a wall

There are two categories of roof-based PV systems; roof mounted and roof integrated. The following subsections present generic examples of each type.

2.3.5.1.1 Roof Mounted

Figure 2-27 presents an example of a generic roof mounted PV array. The array is normally orientated to a position which optimises the amount of light incident upon it with the aid of an A-frame support. This type of system is more common in buildings with large flat roofs.

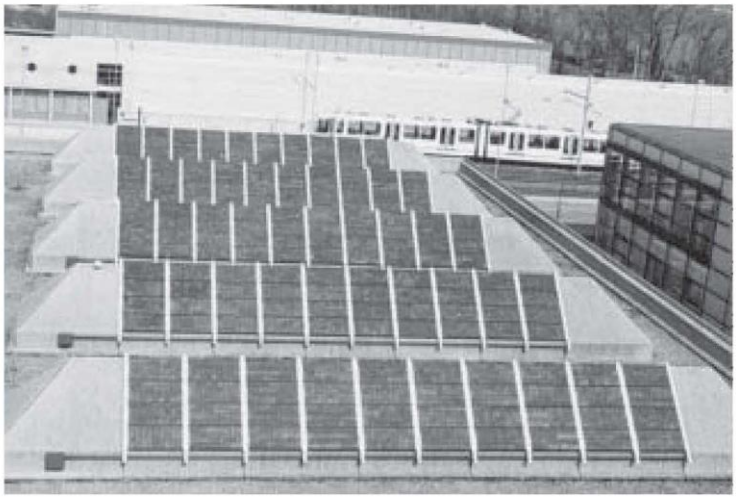

Figure 2-27 – Roof mounted PV panels in a typical saw-toothed formation

(Thomas, 2003)

This type of installation can also be adapted for sloped roofs by replacing the A-frame with an externally mounted fixing frame attached to the outside of the building envelope.

2.3.5.1.2 Roof Integrated

There are a number of options available for integrating PV modules into inclined roofs. The two most common types of roof integrated PV systems are; roof integrated panels and roof integrated tiles. Roof integrated panel systems (Figure 2-28) replace sections of the roofing material with the PV modules which results in a flush finish to the roof's appearance.

Figure 2-28 – Inclined roof with integrated PV panels

(Thomas, 2003)

In a similar concept to the roof integrated panel system, PV tiles can also be incorporated into the roofing structure. The PV tiles (Figure 2-29) are used instead of regular roofing tiles giving a similar, if darker, aesthetic appearance to the original roof appearance.

Figure 2-29 – Inclined roof with integrated PV tiles

(Thomas, 2003)

A more innovative use of PV for inclined roofs is the atrium example shown in Figure 2-30. This concept dedicates a proportion of the glazed area of the atrium roof to PV cells allowing solar

energy captured passively to be used for daylighting while at the same time providing an element of shading against overheating and glare.

Figure 2-30 – PV cells integrated into atrium glazing

(Thomas, 2003)

2.3.5.2 Methods of combining PV modules with Façades

Thomas (2003) identifies façades as having “significant potential” for incorporating PV systems and that much of PV cladding can be considered to be panes of glass to which PV cells are applied and as such add to the extensive experience already accessible on glazed façades. The following subsections present examples of the two main types of façade systems; façade mounted and façade integrated solar collector systems.

2.3.5.2.1 Façade Mounted

As with the roof mounted systems, façade mounted PV modules are a bolt-on addition to the building and are attached to the exterior of the building envelope. A generic example of a building mounted PV array has been presented in Figure 2-31.

Figure 2-31 – Vertical building mounted PV array

(Thomas, 2003)

2.3.5.2.2 Façade Integrated

Figure 2-32 and Figure 2-33 show examples of façade integrated PV modules on a vertical and an inclined façade, respectively. The systems shown in the figures provide prime examples of the ways in which the integration of PV modules into the building envelope are designed to blend into the gridular structure of building façades. Figure 2-32 shows the integration of PV modules in a vertical façade where the modules form integral components of the building envelope. Figure 2-33 shows the same concept applied to an inclined façade with the rows of PV modules forming aesthetic breaks in the building's façade.

Figure 2-32 – Vertical building integrated PV modules

(Thomas, 2003)

Figure 2-33 – Inclined wall with building integrated PV modules

(Thomas, 2003)

2.3.5.3 Sunshades and sunscreens

The final design option is the incorporation of PV modules into sunshades and sunscreens. Although these systems can be integrated into the building envelope they are most commonly mounted additions to the exterior surfaces. Brise-soleil are building elements which are specifically designed to passively assist in the control of solar gains within a building. They are sized to create a shadow over glazed surfaces during the summer months when the sun is higher in the sky and to allow light into the building during the winter to provide passive heating and light when the sun is at a lower angle of incidence. The following examples show how PV modules can be incorporated with glazed façades (Figure 2-34), as sunscreens around apartments (Figure 2-35) and as moveable shading devices (Figure 2-36).

In the first example (Figure 2-34) the façade mounted PV modules have been angled to create two additional benefits; the PV modules have been tilted to a more efficient angle for energy collection and shading from internal solar energy gains at higher angles of incidence (i.e. around solar noon during the summer months) has been created for the building.

Figure 2-34 – PV modules on an inclined wall

(Thomas, 2003)

Fixed sunshades, like those shown in Figure 2-35, create a more prominent shading effect and the inclusion of PV modules on or into the shading element is used to convert the solar energy blocked by the sunscreen into electricity for use within the building, harvesting the unwanted solar gain.

Figure 2-35 – Fixed sunshades

(Thomas, 2003)

Finally, the inclusion of moveable sunscreens (Figure 2-36) provides a number of additional features; the PV modules can be orientated to maximise output, the amount of shading can be adjusted and it can “enhance architectural interest” (Thomas, 2003).

Figure 2-36 – Moveable sunshades

(Thomas, 2003)

2.3.5.4 Novel Concentrating and Selective Collection Building Mounted and Integrated PV Systems

In addition to the most common types of building mounted and integrated PV systems a number of novel solar energy collection systems have been explored, most notably by Tripanagnostopoulos et al (2007), Chemisana and Rosell (2011) and Tripanagnostopoulos (2014).

Tripanagnostopoulos et al (2007) introduce the concept of using a Fresnel lens in combination with PV and PVT absorbers (Figure 2-37) as a means to control solar gains and comfort levels within a building. The concept employed in the study utilized the selective collection characteristics of a linear concentrating Fresnel lens to divert excess energy from the sun over a given period (depending on orientation) to the absorber plane of an active solar energy collector, converting the surplus incident solar energy to useful energy in the form of hot water and/or electricity.

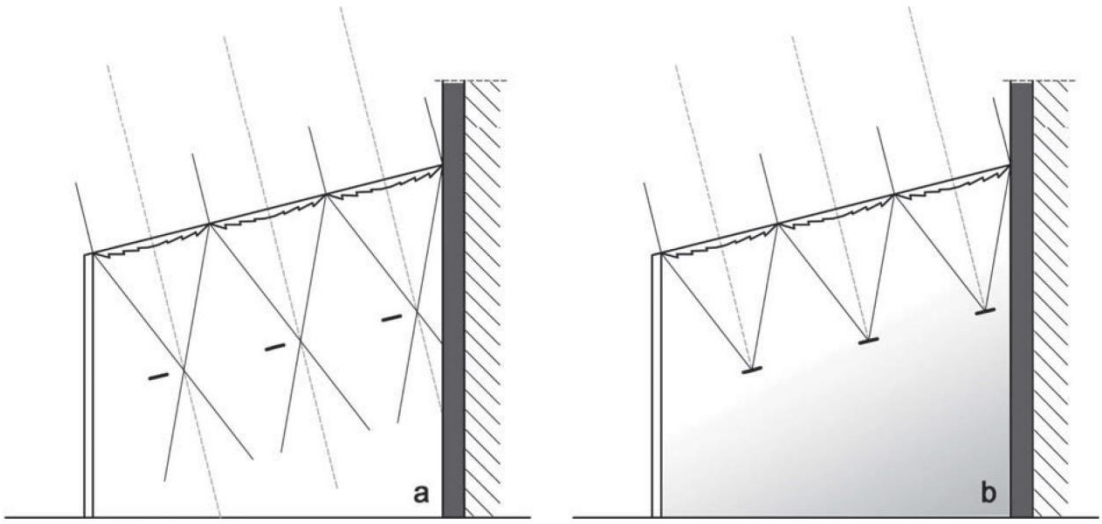

Figure 2-37 – Lighting effect of the Fresnel lens system to a building sunspace with, (a) absorber out of focus and no shading effect and (b) on focus with shading effect

(Tripanagnostopoulos et al, 2007)

This concept presented by Tripanagnostopoulos et al (2007) employs both passive and active solar energy collection, utilising the collected incident energy for electric and thermal energy production while at the same time adding an element of control over natural lighting and internal gains within the building.

Chemisana and Rosell (2011) examined the potential of a transmissive Fresnel reflector (Figure 2-38) design to match the needs of building integrated solar collectors. The developed collector incorporated aspects of solar collection with solar shading and concentrated sunlight onto a static receiver.

Figure 2-38 – 3D image of the transmissive Fresnel reflective concentrating collector (Chemisana and Rosell, 2011)

In a 2014 review of new designs for building integrated solar energy systems Tripanagnostopoulos identified a Fresnel lens system which could not only be used as a solar energy conversion system but also as a solar control system for building, an atrium in this case (Figure 2-39). The review expanded on the idea that the concentrator design could be used to allow sunlight to be transmitted into the building during periods of low intensity solar radiation, maintaining natural lighting within the building's interior.

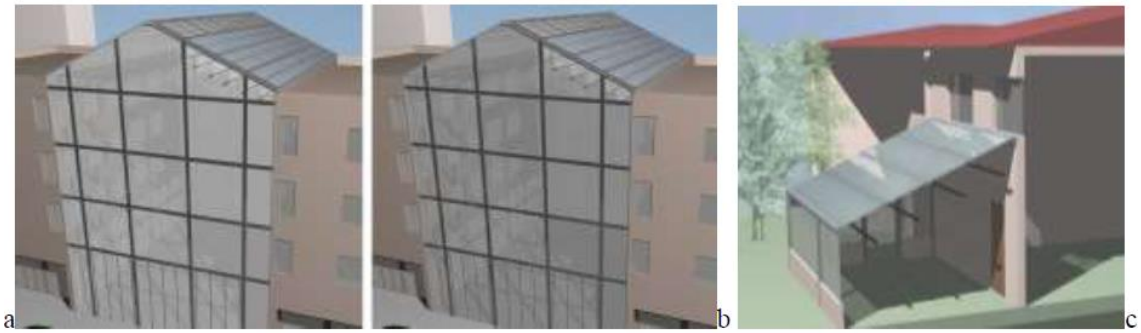

Figure 2-39 – Examples of Fresnel lens integration within buildings

(Tripanagnostopoulos, 2014)

This concept of the solar collection elements having more than one function within the building is a key consideration for the next generation of collector design. Another more recent approach to both active solar energy collection and passive control of solar gains has been the inclusion of semi-transparent organic photovoltaic cells (Yan et al, 2013; Lucera et al, 2017 and Moreno et al 2019). These systems have a high level of inherent flexibility due to the nature of the organic material used however organic photovoltaic cells have a relatively low conversion efficiency and, like the work presented in this thesis, the designs are at a largely conceptual stage. Of specific note in relation to the work presented in this thesis are the design concepts presented by Moreno et al (2019). Moreno et al (2019) presents four separate glazing configurations which included different combinations of ethylene tetrafluoroethylene (ETFE) foils and organic photovoltaic (OPV) cells (Figure 2-40), essentially seeking to achieve a multifunctional collector using an alternative approach.

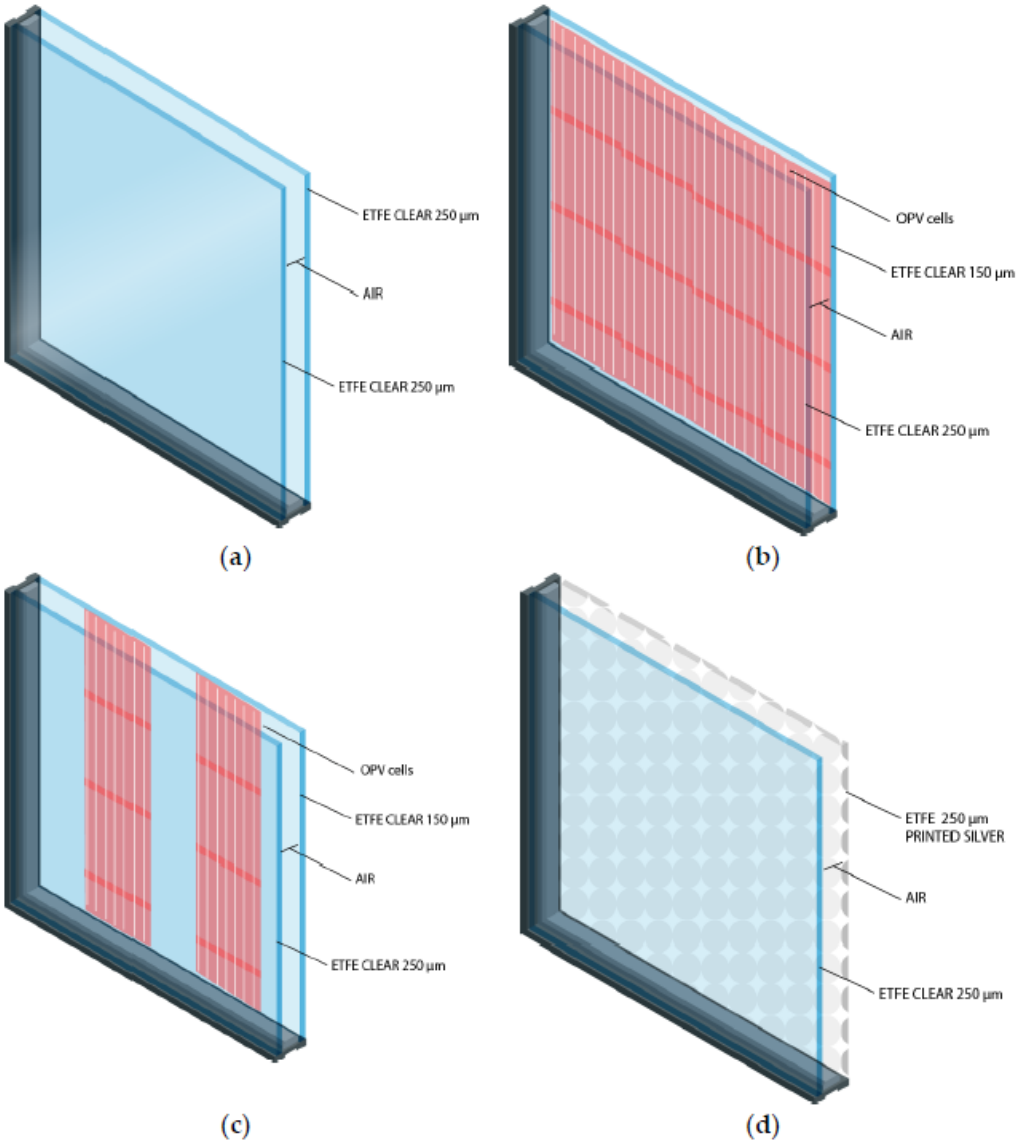

Figure 2-40 –Studied configurations: (a) ETFE + ETFE; (b) ETFE + OPV/ETFE; (c) ETFE + OPV(50%)/ETFE; (d) ETFE + ETFE-

(Moreno et al, 2019)

2.3.6 Section Summary

There are a wide range of options available for the integration of PV systems, both on and within a building, however to meet the criteria (gridular and aesthetic) requiremented by Luque and Hegedus (2011) in Chapter 1 the development of a modular solar window configuration, similar to the atrium system presented in Figure 2-30, which combines active electrical solar energy collection with both natural lighting and passive shading during peak times would be beneficial. The ideal design would be a thin version of the system described by Tripanagnostopoulos et al (2007) which could be readily integrated into new or existing building envelopes as a modular element similar to a window (for façade integration) or skylight (for inclined roof integration).

2.4 Solar Concentrating and Selective Collection

The previous sections have identified two challenges for the module design; ideally, in addition to active solar energy collection and conversion, the developed module would allow passive solar energy collection via daylighting and it would incorporate some form of cost-effective concentration to increase the energy available for conversion at the absorber plane during periods of peak solar gain. To tackle these challenges requires the design and incorporation of some form of solar energy concentrating lens utilising either single or multiple refractive changes in the trajectory of the light incident upon the solar collector over a predetermined collection period. This section is therefore devoted to the concepts of solar energy concentration and the selective collection of light and focuses on the options available for designing a refractive element for building integrated solar energy collection.

2.4.1 Introduction to Solar Concentrating Concepts

To avoid confusion throughout this thesis the terms solar concentration is used to describe the activity of a solar collector to increase the energy density of incident solar radiation onto an absorber plane. Selective collection on the other hand is the portion of daily solar radiation targeted by the solar collector and is generally describe as a function of the acceptance half angle or the timebound period that the acceptance half angle represents.

2.4.2 Imaging Concentration

The traditional approach to imaging solar concentration using parabolic and circular concentrators used the Lens Makers' Formula (Equation 2-8) and was based around the concept of reproducing an image of the sun, albeit with high levels of aberration in most cases, onto the absorbing surface. Imaging concentration is constrained by the sine condition derived from the laws of Gaussian optics (Equation 2-9). These two formulae were derived for systems with small object and image sizes.

The Lens Makers' Formula:

$$\frac{1}{f} = \frac{1}{i} + \frac{1}{o} \qquad \text{Equation 2-8}$$

Where the aperture ratio (f-value) is limited by the Abbe's sine condition:

$$n_1 y_1 sin\gamma_1 = n_0 y_0 sin\gamma_0 \qquad \text{Equation 2-9}$$

2.4.2.1 Development of Imaging Solar Concentrating Energy Collection

Developed by Augustin Jean Fresnel in 1822 Fresnel lenses were traditionally used in lighthouses to project a small light source up to 30 km out to sea (Leutz and Suzuki, 2001). The system was highly advantageous at the time as it considerably reduced the amount of glass required, and therefore weight of, a convex lens of the same specification and was easier to manufacture than the Buffon lens (Figure 2-41). However, it wasn't until the 1940s and early 1950s and the arrival of new low cost plastics with high optical performances that additional uses of the Fresnel technique began to be investigated (Johnson, 1942; Miller et al, 1951; Boettner and Barnett, 1951) eventually leading to the investigation of their suitability for solar applications in the 1970s (Rainhart and Schimmel, 1974; Collares-Pereira et al, 1977; James and Williams, 1978; O'Neill, 1978). Towards the end of the 1970s research into refractive lenses began to focus more on nonimaging concentrating techniques and applications however further theoretical investigations into the derivation of the optimum prism profile (Tver'yanovich, 1984), chromatic overlapping for multiple junction photovoltaic cells (O'Neill, 2000a) and space based applications (O'Neill, 2000b) continued to be published up to the beginning of the new millennium.

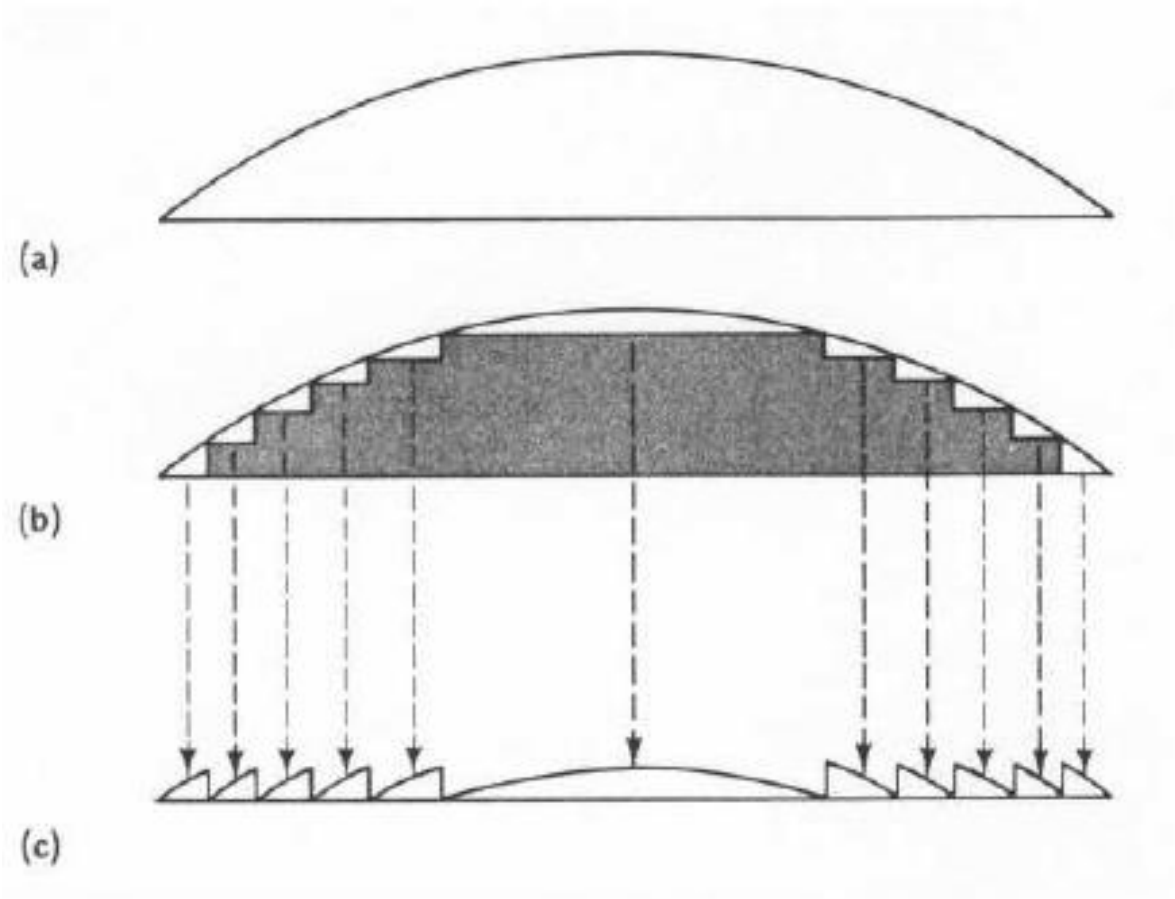

Figure 2-41 – (a) Convex lens, (b) Buffon lens, and (c) Fresnel lens

(Chemisana, 2009)

2.4.3 Nonimaging Concentration

O'Gallagher and Winston (1983) briefly describe traditional imagining concentration as achieving concentration by making a small image of the sun as with a burning glass. Conversely, nonimaging or anidolic concentrating collectors combine some of the characteristics of light pipes and some of the properties of traditional image forming optics but with very large aberrations so they do not reproduce a discernible image of the light source at the focal point of the convergent rays (Winston et al, 2005).

2.4.3.1 Nonimaging Reflective Concentrators

The first parabolic reflective concentrating system, then called a light funnel (Figure 2-42), was designed by Hinterberger and Winston (1966) to increase the efficiency of a light coupler for threshold Čerenkov counters.

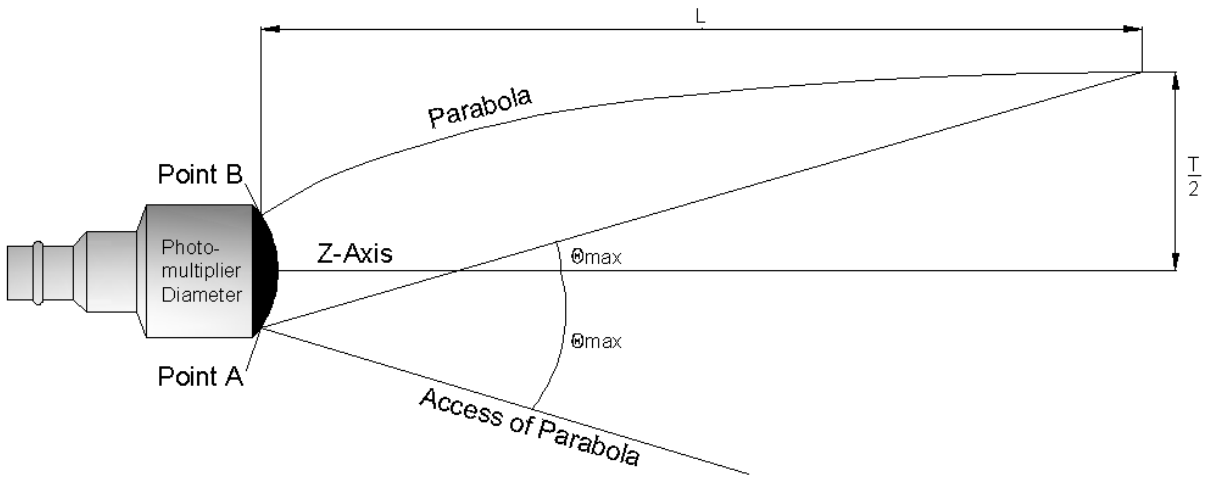

Figure 2-42 – Sketch of a $Q_{max} = 16^{o}$ light funnel

(Reproduced from: Hinterberger and Winston, 1966)

The Čerenkov gas counters of that era experienced optical losses of 66% (Hinterberger and Winston, 1966) and in an attempt to improve efficiency a light funnelling system was developed using a Monte Carlo technique ray tracing technique which increased the optical efficiency of the system to 78% (assuming a reflectivity of 90%).

Although Winston and Hinterberger built the theoretical foundations of compound parabolic concentrators (CPCs) during the late 1960s the use of CPCs for solar concentration wasn't suggested until 1974 (Winston, 1974). Winston (1974) described a novel concentrator based on previous designs as an ideal cylindrical light collector for solar concentration and goes on to state that the ideal light collector is a non-imaging reflecting wall light channel that concentrates a divergent beam by the maximum allowed by phase space conservation.

Since the emergence of CPCs a significant amount of work has been carried out in optimizing these systems investigating the uses of various absorber shapes and sizes, the effects of truncating the length of the parabolas, convection suppression techniques and asymmetry etc. However, despite the relative maturity of this technology in terms of theoretical development and the understanding of variations in CPC design CPCs have not made a significant impact on the small scale domestic or commercial solar collector markets.

2.4.3.2 Nonimaging Refractive Concentrators

In 1979 Collares-Pereira (Collares-Pereira, 1979) and Kritchman et al (1979a; 1979b) began examining the theoretical principles necessary to apply the proven nonimaging reflective techniques to refractive lenses including the relatively new concept of bi-focal refractive concentrators (Kritchman et al, 1979a). The theoretical development of nonimaging lenses continued throughout the 1980s (Lorenzo, 1981; Kritchman, 1984; Lorenzo and Luque, 1981; Lorenzo and Luque, 1982; Luque, 1989), 1990s (Yoshioka et al, 1994a; Yoshioka et al, 1994b; Leutz et al, 1999) and the early 2000s (Leutz et al, 2000a; Leutz et al, 2000b) and the first realistic prototypes began to emerge towards the start of the new millennium (Terao et al, 2000; Miñano et al, 2005). The first prototypes quickly created two parallel streams of research into refractive concentration; the domed nonimaging techniques derived by the team led by Ralf Leutz developed linear lenses (Figure 2-43) with angular acceptances comparable to those of compound parabolic concentrator, the leading type of reflective concentrator, and the simultaneous multiple surface (SMS) technique developed by the team led by Juan Carlos Miñano which focused on high concentration ratios and a more uniform flux distribution on the absorber. Both systems were initially only considered for photovoltaic systems however the angular tolerance of the SMS technique is generally lower than that of the domed lenses and requires the addition of a mechanical tracking system to produce a viable output. As a consequence of the increased angular tolerance of the nonimaging domed designs advances have been made in tailoring the global shape of the lenses (Ries and Leutz, 2003) and optimizing the internal facets (Leutz and Ries, 2003; Berger, 2003). Subsequent developments have examined the use of totally internal reflective microstructures as light guides to improve the flux distribution across the absorber (Leutz and

Ries; 2003b), the optimization of the ƒ-number for highly concentrating systems (500X+) (Lin et al, 2005), the effects of stress on the lens both during manufacture and operation (Leutz et al, 2009) and new lens fabrication techniques (Nachmias et al, 2009). More recently these systems have begun to be integrated into thermal and combined photovoltaic thermal systems either as single stage tracking systems (Zhai et al, 2010) or as multistage stationary collectors (Chemisana, 2009).

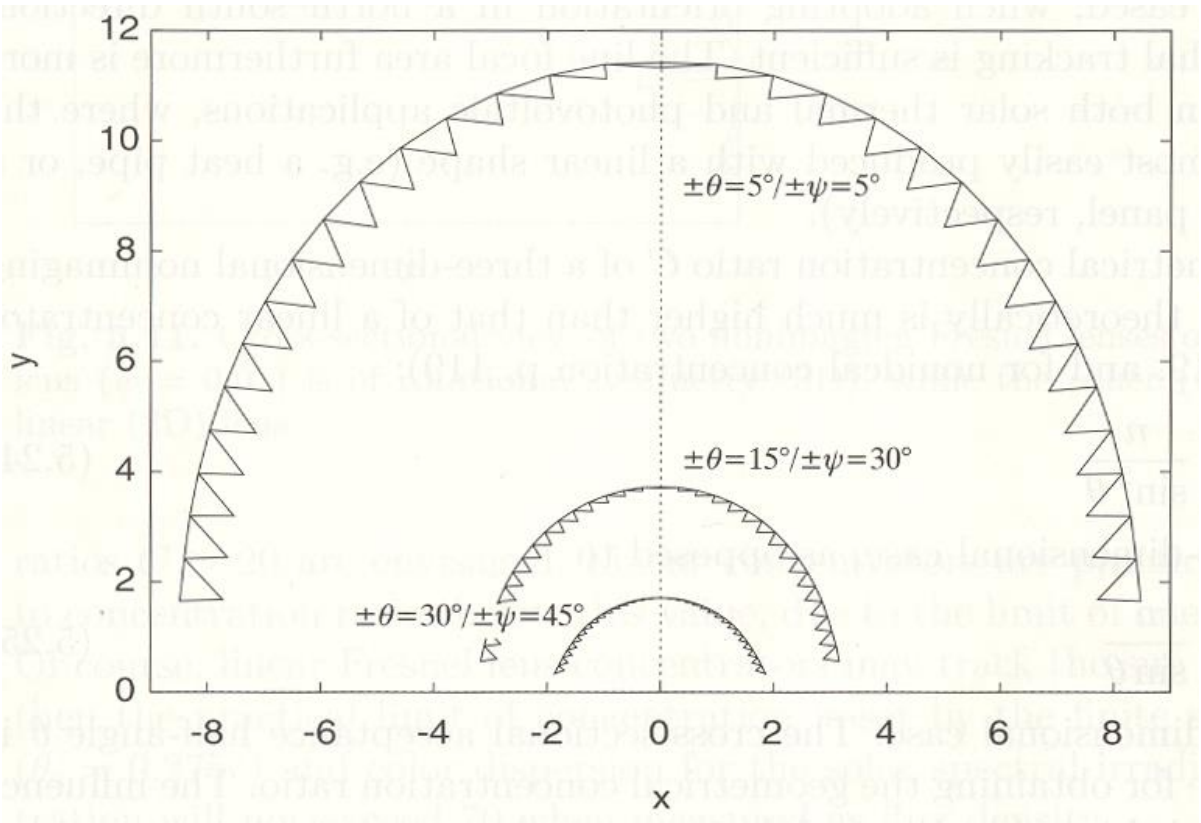

Figure 2-43 – Optimum nonimaging domed Fresnel lenses with various cross-sectional (θ) and perpendicular (ψ) acceptance half angle pairs and their associated geometries.

(Miñano et al, 2003)

2.4.3.3 The Development of SMS Refractive Lenses

The development of the SMS technique has run in parallel to the nonimaging domed techniques developed by Leutz and has continued to be developed both practically and experimentally since it began in the early 1990s. The SMS technique has resulted in a number of new nonimaging concentrating lenses designed exclusively for photovoltaic applications namely; the RR concentrator, the XR concentrator, the RX concentrator, the XX concentrator (not discussed), the

RXI concentrator, the XRI concentrator and the TIR-R concentrator (Miñano et al, 2003). Where; R is refraction, X is reflection, T is transmission and I is total internal reflection.

2.4.3.3.1 RR Lenses

The RR concentrating lens was the first to be developed (Miñano and González, 1991; Miñano and González, 1992) and has a strong resemblance to traditional imaging techniques as it uses the well-established concepts of focusing a bundle of rays through an oval refractive surface. The RR concentrator creates a set of two refractive surfaces which transform a predefined bundle of rays as shown in Figure 2-44.

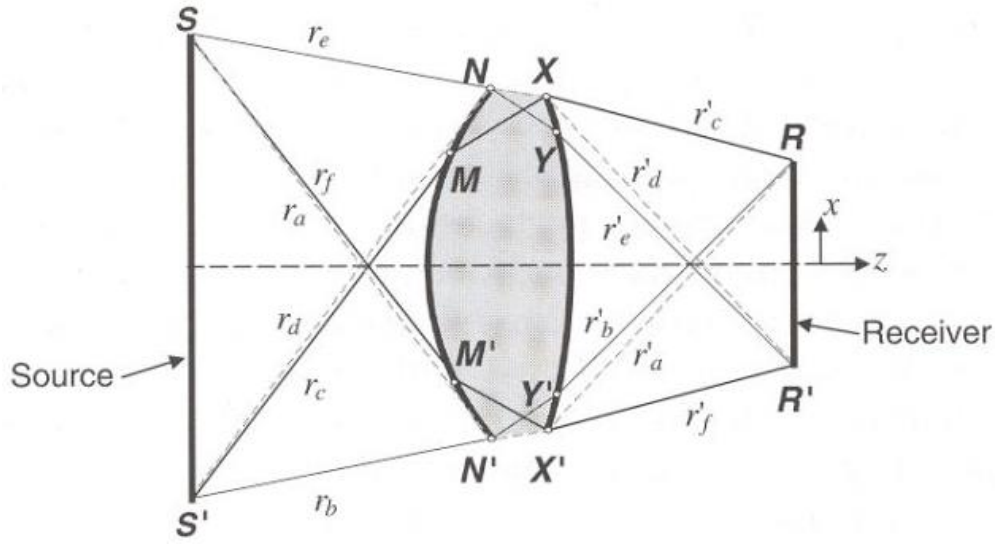

Figure 2-44 – Conceptual design of the RR Lens

(Winston et al, 2005)

2.4.3.3.2 XR and RX Lenses

Both the XR (Winston et al, 2005) and RX (Miñano et al, 1995a) lenses replace one of the working refractive transforming surfaces with a reflective surface creating a thinner concentrator profile and both systems encapsulate the absorber material in a refractive medium (Figure 2-45). This encapsulation led to a number of practical issues including manufacturing, overheating and electrical connection as the absorber faced inwards towards the direction of concentration. Despite the improved flux distribution over the absorber area as a result of these practical issues

these lens configurations weren't widely publicised in terms of solar concentration after the initial conceptual phase although they have been successfully employed in imaging applications.

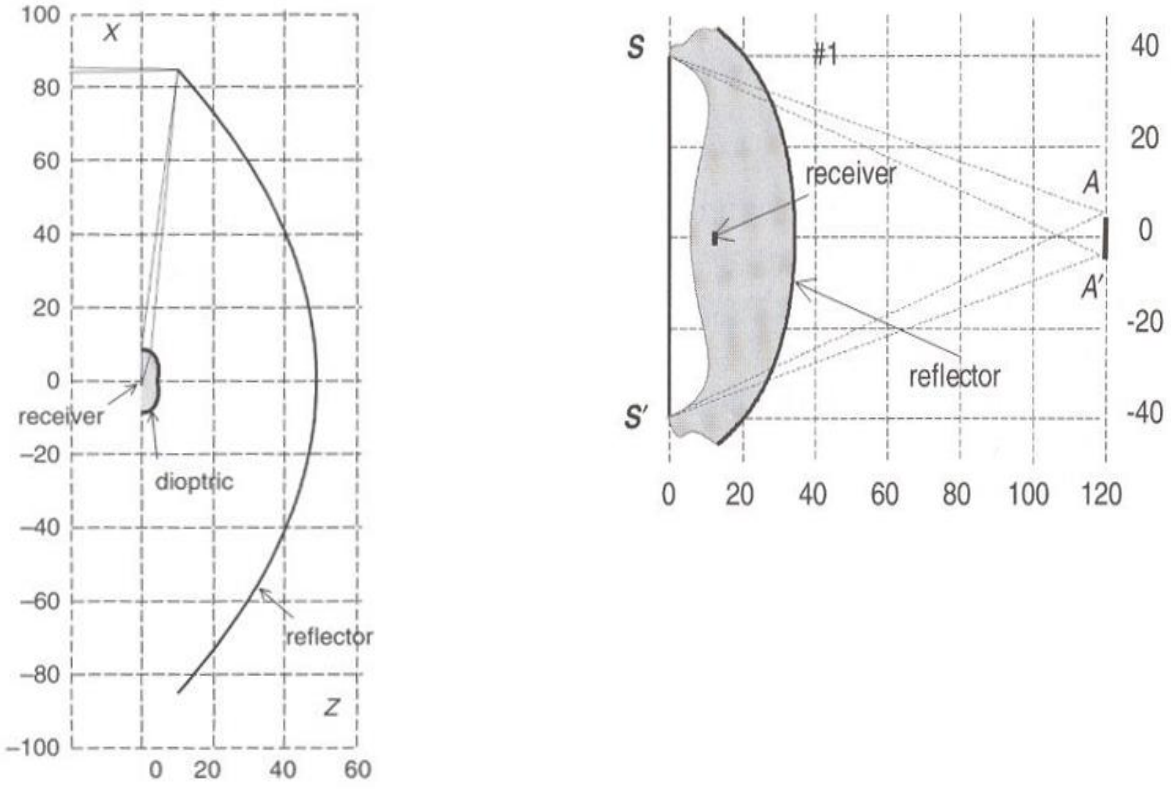

(a) (b)

Figure 2-45 – Conceptual design of the XR (a) and RX (b) Lenses

(Winston et al, 2005)

2.4.3.3.3 RXI and XRI Lenses

The RXI (Miñano et al, 1995b) and the XRI (Winston et al, 2005) lenses (Figure 2-46) attempted to rectify the issues discovered during the manufacturing phase of the earlier lenses and the addition of the I in their designation indicates that the incident ray bundle is transformed by the entry aperture twice differentiating these concentrating lenses from their predecessors. Despite the progress made with this generation of lenses in reducing the mechanical tracking constraints, a new set of manufacturing issues emerged in the form of fixing the front and back mirrors as well as the electrical connection and heat sink legacy issues inherited from the previous generation (Terao et al, 2000).

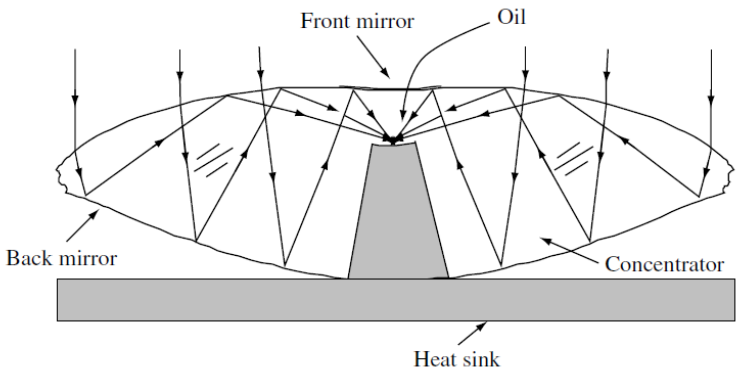

(a)

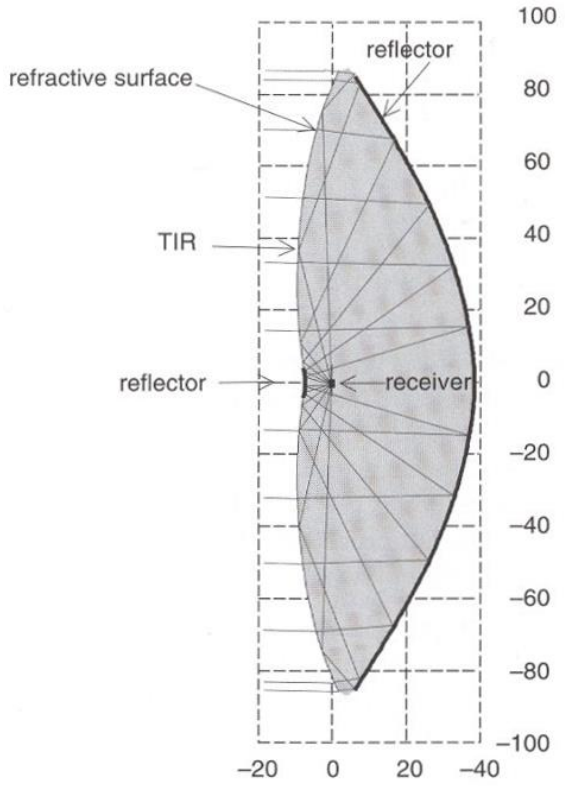

(b)

Figure 2-46 – Conceptual design of the RXI (a) and XRI (b) Lenses

(Winston et al, 2005)

2.4.3.3.4 TIR-R Lenses

The TIR-R lens (Terao et al, 2000; Mulligan et al, 2000) combines a primary TIR lens (Figure 2-47) with a secondary refractive lens which improves the uniformity of the flux distribution across the absorber surface (Alvarez et al, 2001). The TIR-R lens reduces both the profile thickness of the concentrator and reduces the material required however a more complex manufacturing process must be employed to produce the more complex geometry necessary for this design. As with the manufacture of any concentrator utilizing relatively small prisms on the working surface the lens become more prone to manufacturing errors like prism tip rounding (Leutz and Suzuki, 2001; Terao et al, 2000; Winston et al, 2005).

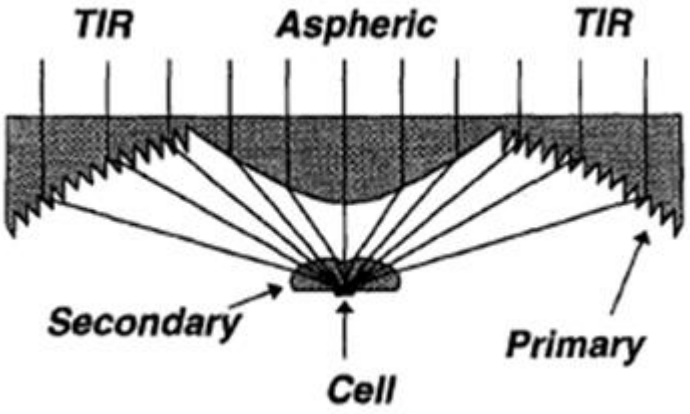

Figure 2-47 – Conceptual design of the TIR-R Lens

(Winston et al, 2005)

In addition to the issues mentioned previously all of the SMS refractive lenses have relatively large, thick optical profiles in comparison with both their focal length and the absorber size of the designed system which makes their use in large scale thermal applications prohibitive.

2.4.3.3.5 Novel applications of SMS Lenses

Additional investigations into the SMS techniques have examined the imaging and off-axis imaging illumination potential of this technique (Parkyn et al, 2003; Dross et al, 2004; Miñano et al, 2009) and the theoretical development of this method continues to be expanded and refined up to the present day (Benítez et al, 2004; Calero et al, 2006; Muñoz et al, 2008). The development of newer multi-focal and multi-zonal methods (Lui et al, 2009; Vázquez-Molini et al, 2009) and

free form v-groove reflectors (Grabovičkic et al, 2009) based in part on the SMS technique has begun however, as yet these systems are still too immature to fully explore with any real certainty.

2.4.4 Summary of Solar Concentrating Concepts

Within this section an extensive range of solar concentrating concepts has been discussed and reviewed. Conventional concentrating elements used for solar energy collection have traditionally suffered because the cost of the concentrating element generally offsets any savings seen as a result of the reduction in absorber area required. The body of knowledge in this area is such that it allows for the development and evaluation of a novel fast acting Fresnel lens. The key advantage in developing this type of technology is that, when hard tooled, the mass-produced cost of the developed lens can be relatively low compared to conventional concentrating elements.

2.5 Design Brief

Having completed an extensive investigation into the literature available on this topic it is clear that the potential exists to design, develop and characterise a novel photovoltaic collector for façade and/or atrium integration. The developed module should be relatively thin, allowing the cost of the collector to be partially offset by the cost of the building element it's replacing and would ideally incorporate some form of selective collection to convert the excess solar gains either side of solar noon into useful electrical energy for the building. It should also attempt to conform with the criteria outlined by Luque and Hegedus (2011) and allow natural light into the building.

2.6 Chapter Summary

This chapter has presented solar energy collection in terms of available resource and the main terminology used in the description and characterisation of solar systems. A series of active solar energy collection systems have been introduced and the physical characteristics and operating principals of PV technologies have been explained in detail. An overview has been presented describing how these technologies can be integrated within the built environment and a range of solar concentrating technologies has also been investigated at length. The chapter has culminated in a design brief which identifies a large gap in the existing body of knowledge and provides a clear direction for the development of a novel building integrated photovoltaic module for active energy collection and passive solar shading.

Optical Design

3 Optical Design

3.1 Introduction

In this chapter the major topics discussed include; component selection, the optical design and evaluation of the developed systems and component optimization. The component selection portion of this chapter builds upon the information presented in the literature review and states the specific characteristics of the materials chosen for the prototype design and the advantages of using those materials over similar suitable materials.

The optical design section charts the progression of the lens design from the performance of a traditional imaging refractive lens to the development of the finalized non-imaging refractive design focusing on the development of the design methodology, issues encountered and the optical performance analysis of the finalized systems using 2D and 3D ray tracing to generate optical maps identifying angular acceptance and optical efficiency. Finally, the flux density across the absorber will be mapped to highlight the distribution of energy across the absorber surface.

3.2 Optical evaluation methodology

In order to determine the suitability of an optical design it is necessary to have a means by which to evaluate the predicted performance of the design within its specified operational parameters. Since the trail-and-error manufacture and manual evaluation of a large number of potential lenses is both fiscally prohibitive and time consuming, the most appropriate method of generating and evaluating a large number of optical systems quickly and cost effectively is through the creation of a mathematical model of the optical systems and quantifying the behaviour of light through them. In the case of this thesis; the lenses were designed in Microsoft Excel, created and evaluated using a ray tracing software called Eazee (Zacharopoulos, 2001) and the post-processing and display output was carried out using Tecplot 10, a visualisation software for technical data.

3.3 Ray tracing theory and the fundamental concepts of geometric optics

Before beginning to examine the performance of Eazee in detail it is prudent to first identify some of the fundamental concepts in geometric optics used in the design of optical systems and utilized by ray tracing software. This section will therefore briefly introduce some of the basic concepts defining the behaviour of light as it propagates through a homogeneous absorbing material.

3.3.1 Huygens' Construction

Huygens' Principle, first put forward by Christian Huygens in 1690, suggests that each element of a wave-front may be regarded as the centre of a secondary disturbance which gives rise to spherical wavelets and that the position of the wave-front at any later time is the envelope of all such wavelets (Born and Wolf, 2002). This spherical expansion travels at the same speed and frequency as the primary wave-front and each point on the new wave-front has the same phase. This construction by Huygens underlies all of the optical work, both imaging and non-imaging, undertaken in the design of solar optics and culminates in three rules which must be obeyed when designing a concentrating system:

The 2D limitation for solar concentration,

$$C = \frac{n}{sin\theta_c} \qquad \text{Equation 3-1}$$

the 3D limitation for solar concentration,

$$C = \frac{n^2}{sin^2\theta_c} \qquad \text{Equation 3-2}$$

and an f-number equal to or above a lower limit of

$$f - number \geq \frac{1}{2} \qquad \text{Equation 3-3}$$

all provide a framework for the successful design of solar concentrators using the principles of Hamiltonian optics in which the optical system is simplified using a purely mechanical description of light; excluding the additional complications of diffraction and interference by working within the boundaries of Huygens' Principle to ensure the maintenance of phase-space or étendue.

Where; C is the limit of concentration, n is the refractive index of the medium and θ_c is the half acceptance angle (the extreme angle of an incident bundle of rays extending from perpendicular to θ_c; Figure 3-1).

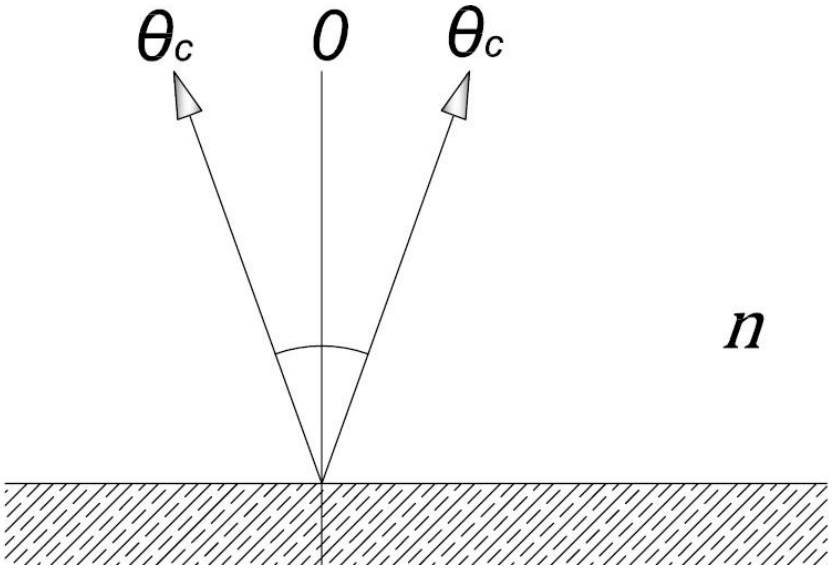

Figure 3-1 – Diagram denoting the definition of a half acceptance angle as the angle between the optical axis (O) and the edge of the incident bundle of rays

3.3.2 Paraxial or Gaussian Approximation

Light rays incident outside the Earth's atmosphere arrive almost parallel to each other (±0.275º) as a combined result of three main factors:

- the differential in size between the Earth and the Sun,
- the distance between the Earth and the Sun, and
- the inverse square law governing the propagation of light.

As a result of this minor divergence from parallel incident rays it is common for solar collection and concentrating systems to be designed using ray tracing techniques which utilize a paraxial approximation, simplifying the systems using Gaussian optics by assuming that all direct incident rays are completely parallel to the optical axis between the simulated Lambertian light source and the collector.

3.3.3 The Principle of Fermat

The principle of Fermat, also known as the principle of the shortest optical path states that "the optical length

$$\int_{P_1}^{P_2} n\, ds \qquad \text{Equation 3-4}$$

of an actual ray between any two points P_1 and P_2 is shorter than the optical length of any other curve which joins these two points and which lies in a certain regular neighbourhood of it" (Born and Wolf, 2002). This definition by Born and Wolf, simply states than in a homogeneous material of constant refractive index (n), a ray of light will take the shortest optical path between any two given points.

3.3.4 Propagation of light in a homogenous medium

With the principle of Fermat defining the optical path length (L) between any two points in a given homogenous medium it is possible to describe how light will propagate within that medium by the following relationship:

$$L = ns \qquad \text{Equation 3-5}$$

Where, the refractive index (n) is defined as the ratio of the speed of light in a vacuum (c) to the speed of light in the medium (v) (Equation 3-6) and s is the distance travelled in the medium.

$$n = \frac{c}{v} \qquad \text{Equation 3-6}$$

This relationship allows for the prediction of the path of a ray through an optical medium (Winston et al, 2005).

3.3.5 Propagation of light in an absorbing medium

The absorption of radiation in a dielectric medium can be described by Bouguer's law, which is based on the assumption that the absorbed radiation is proportional to the local intensity I in the medium and the distance (x) the radiation has travelled in the medium (Duffie and Beckman, 2006):

$$dI = -IK\,dx \qquad \text{Equation 3-7}$$

Where K is the proportionality constant, sometimes called the extinction coefficient or attenuation index, which is assumed to be constant across the solar spectrum (Duffie and Beckman, 2006) however, it should be noted that this assumption begins to breakdown as the frequency of light tends towards the resonant frequency of the material (Born and Wolf, 2002).

Integrating along the actual path length (Figure 3-2) in the medium yields:

$$\tau_a = \frac{I_{transmitted}}{I_{incident}} = \exp\left(-\frac{KL}{cos\theta_2}\right)$$ Equation 3-8

Where, the subscript a is a reminder that only absorption losses have been considered (Duffie and Beckman, 2006).

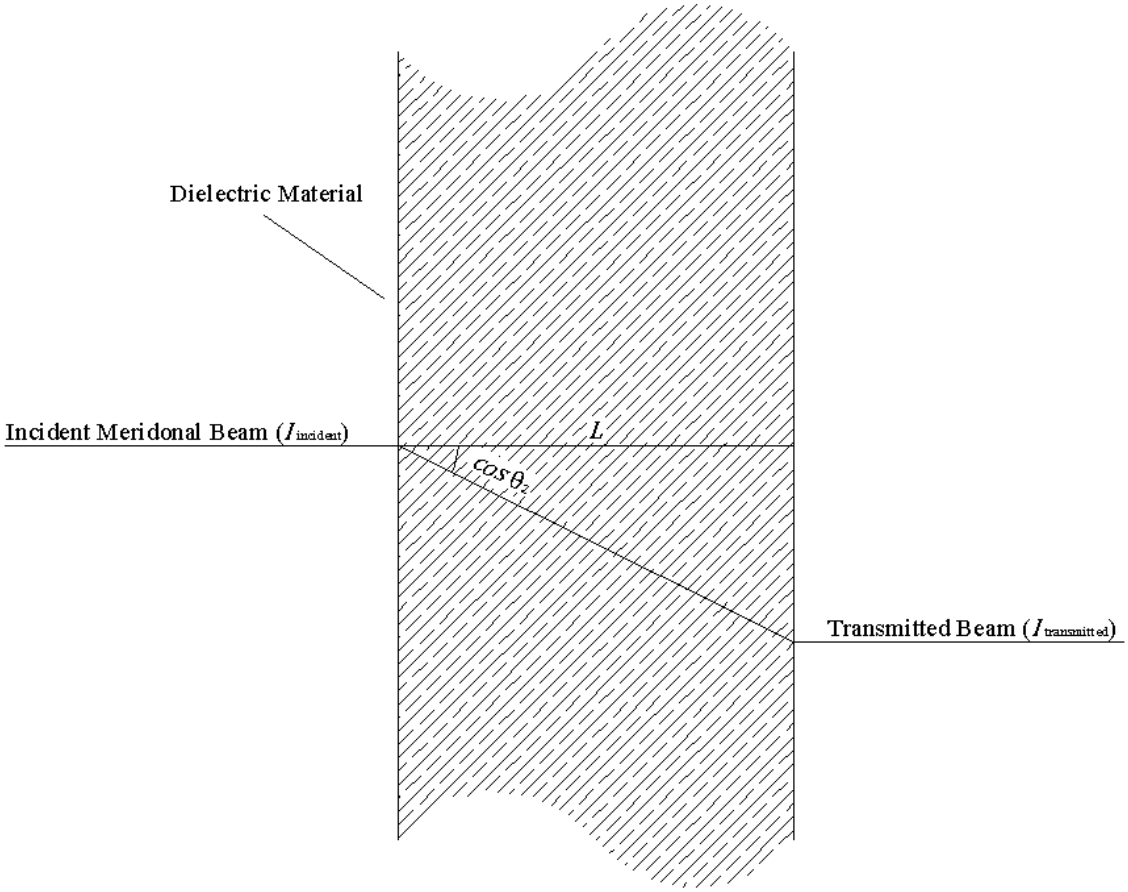

Figure 3-2 – Diagram depicting absorption in a dielectric medium

3.3.6 Laws of Reflection and Refraction

Having described the way in which light behaves in a given material it is important to identify what happens as incident light encounters the boundary or surface of another material. This interaction is dependent upon, and is affected by, the angle of incidence and the type of material encountered. The relationship between incident (***i***), reflected (***r***) and transmitted (refracted (***τ***)) light is fairly intuitive and is governed by the relationships shown in Figure 3-3.

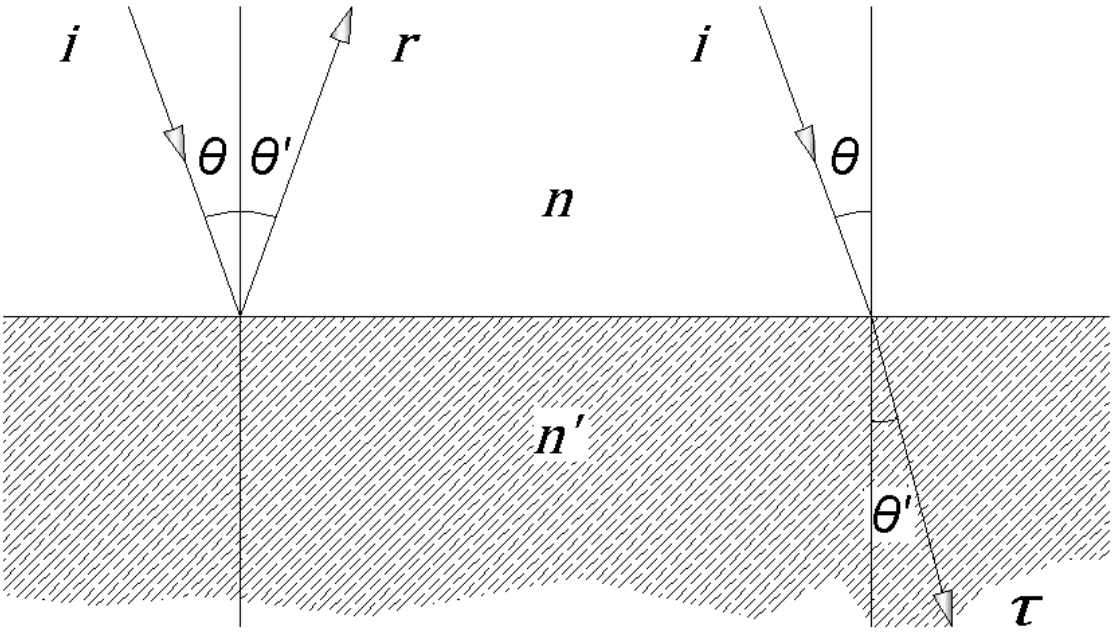

Law of Reflection:

$$\theta = \theta'$$

Snell's Law of Refraction:

$$nsin\theta = n'sin\theta'$$

Figure 3-3 – A Schematic of the Laws of Reflection and Refraction

These relationships infer that, about the normal to the surface, the angle of incidence (θ) is equal to the angle of reflection (θ') and that the angle of the transmitted ray (θ') is dependant on the refractive index of the secondary medium (n').

The incidence angle at which light can no longer pass through the boundary interfaces into, and out of, a material with a higher refractive index is known as the critical angle of total internal reflection (TIR) and is defined by using an incident angle of 90°. Leutz and Suzuki (2001) show that by substituting the maximum incidence angle of 90° into Snell's Law of Refraction the critical angles, for an air ($n = 1$) to acrylic ($n' = 1.49$) interface, at which all light rays with be totally internally reflected at are all the incidence angles less than or equal to 0.671° and greater than or equal to 42.16°.

The refractive index is also a function of the wavelength of the incident light. This variation in refractive index creates a normal dispersion pattern with the refractive index decreasing as the wavelength increases. This relationship has been described by Hartmann's formula as follows:

$$n = n_0 + \frac{C}{(\lambda - \lambda_0)}$$ Equation 3-9

Where; n, λ_0 and C are constant characteristics of the material which have been measured experimentally (Oshida, 1961; Leutz and Suzuki, 2001).

3.3.7 Propagation of light through a dielectric medium

For unpolarized light incident on a smooth surface the following expressions have been derived by Fresnel as an extension of Snell's Law of Refraction (Duffie and Beckman, 2006):

$$r_{\perp} = \frac{\sin^2(\theta' - \theta)}{\sin^2(\theta' + \theta)}$$ Equation 3-10

$$r_{\parallel} = \frac{\tan^2(\theta' - \theta)}{\tan^2(\theta' + \theta)}$$ Equation 3-11

$$r = \frac{I_r}{I_i} = \frac{r_\perp + r_\parallel}{2}$$ Equation 3-12

Where $r_\perp$ represents the perpendicular component of the unpolarized light, $r_\parallel$ represents the parallel component and θ and θ' are the angles of incidence and refraction as shown in Figure 3-4.

For most solar applications the incident radiation passes through a pane of an absorbing medium, generally glass or Perspex, which has two interfaces therefore these interactions begin to become slightly more complex. In the case of a medium with zero or negligible absorption, the reflection losses through the medium can be derived by summing the reflective losses at each interface (Figure 3-4) using the following relationships by splitting the unpolarized light into its perpendicular and parallel components:

$$\tau_\perp = (1 + r_\perp)^2 = \sum_{n=0}^{\infty} r_\perp^{2n} = \frac{(1 - r_\perp)^2}{1 - r_\perp^2} = \frac{1 - r_\perp}{1 + r_\perp}$$ Equation 3-13

$$\tau_\parallel = (1 + r_\parallel)^2 = \sum_{n=0}^{\infty} r_\parallel^{2n} = \frac{(1 - r_\parallel)^2}{1 - r_\parallel^2} = \frac{1 - r_\parallel}{1 + r_\parallel}$$ Equation 3-14

At a normal incidence angle the parallel and perpendicular components are equal and the following expression can be used to approximate the total reflection losses from the transmitted light (τ_r):

$$\tau_r = \frac{1}{2}\left(\frac{1 - r_\parallel}{1 + r_\parallel} + \frac{1 - r_\perp}{1 + r_\perp}\right)$$ Equation 3-15

Where, the subscript r is a reminder that only reflective losses have been considered (Duffie and Beckman, 2006).

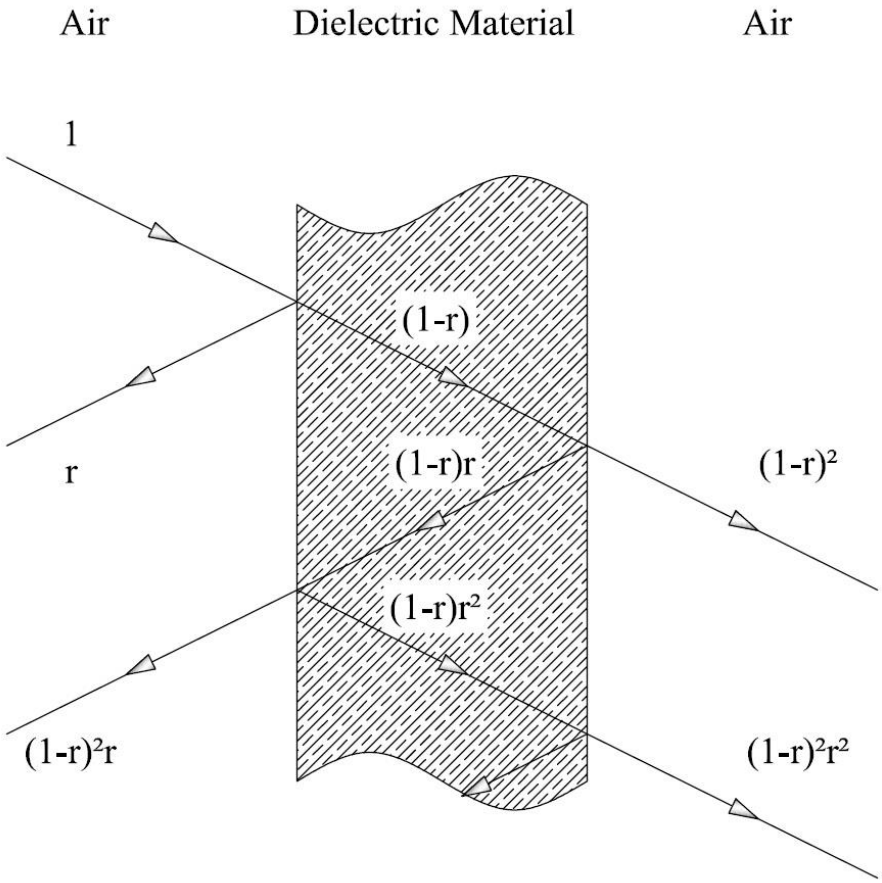

Figure 3-4 – Multiple reflections in a slab of non-absorbing material

In a single absorbing medium the transmittance, reflectance and absorption of light is more commonly calculated by ray tracing software utilizing Equation 3-8, Equation 3-13 and Equation 3-14 however they can also be calculated by using the net radiation method described by Howell et al (2010).

3.4 Ray tracing using Eazee

Like many other ray tracing software packages Eazee utilizes vector algebra to transform the inbound and outbound Hamiltonian paraxial rays of a simulated Lambertian light source about an interface using the principles outlined earlier in this chapter and based on the inputted characteristics of the proposed design. The simulation begins by evenly distributing a unit of energy across the opening aperture (Lambertian source) then at each consecutive interface Eazee calculates both the magnitude (energy) and direction of the resultant rays as a function of their condition before a given transformation and the inputted physical characteristic of the interface encountered.

3.4.1 Design and evaluation variables and assumptions

The design and optical evaluation of the lenses in Microsoft Excel and Eazee respectively, required a number of variables to be identified and defined in relation to the dimensions and performance of the materials used before work could begin. These criteria were then carefully maintained throughout the range of lens evaluations and are shown below in Table 3-1.

Table 3-1 - Eazee simulation variables

Variable	Specifications		
	Glazing	Lens	Absorber
x (microns)	950000	190000	95000
y (microns)	1000000	1000000	1000000
z (microns)	3000	750	400
Refractive Index	1.49	1.49	N/A
Extinction coefficient (m^{-1})	4	4	N/A
Extinction coefficient (micron)	0.000004	0.000004	N/A
Absorption (%)	N/A	N/A	100
Maximum cutting depth (microns)	N/A	375	N/A

In addition to the general specifications of the materials as described in Table 3-1, Leutz and Suzuki (2001) also provide additional information in relation to the performance of PMMA in solar applications which is not readily available in the technical specification sheets given by suppliers. Of specific interest in the design of a solar collector primarily constructed from PMMA are the discrepancies in refractive index as a result of; variations in the wavelength of the incident light, the temperature of the material and the relative humidity of the surrounding environment.

Table 3-2 - Variations in refractive index with wavelength

Material	n_D	n_F	n_C	$n_F - n_C$
Vacuum	1.000	1.000	1.000	1.000
Air	1.000	1.000	1.000	1.000
PMMA	1.493	1.485	1.495	0.009

Where:

Designation	D	F	C
Wavelength (nm)	589.29	486.13	656.27
Spectral Source	Sodium	Hydrogen	Hydrogen
Spectral Colour	Yellow	Blue	Red

(Adapted from Leutz and Suzuki, 2001)

Table 3-2 quantifies how the refractive index of PMMA varies depending on the wavelength of the incident light resulting in a 0.009 deviation across the visible spectrum. The Eazee software package doesn't factor multiple wavelengths of light into its calculations so to compensate for this, the effect of the 3 wavelengths described in Table 3-2 where evaluated as a function of their variations in the refractive index of the PMMA and compiled by overlaying the 2-dimensional ray trace files in Tecplot to create a composite image of the behaviour of the lens across the various wavelengths which represent the beginning, middle and end of the visible spectrum of light. The resultant simulation confirmed that the variation in refractive index had a negligible impact on the underlying vector algebra and that using a single value (1.49) was sufficient for the optical design.

Figure 3-5 shows the variations in the performance of PMMA across a larger solar spectrum ranging from the shorter ultraviolet to the longer infrared wavelengths of light. Of particular interest for simulating the optical performance of a 0.75 mm lens across the visible spectrum is that, despite more significant variations in the transmittance of solar energy above a wavelength of 1 μm, for the range of wavelengths under examination the transmittance of solar energy through a 1 mm PMMA lens is constant allowing the developed optical models to be simplified and standardised for all of the simulations.

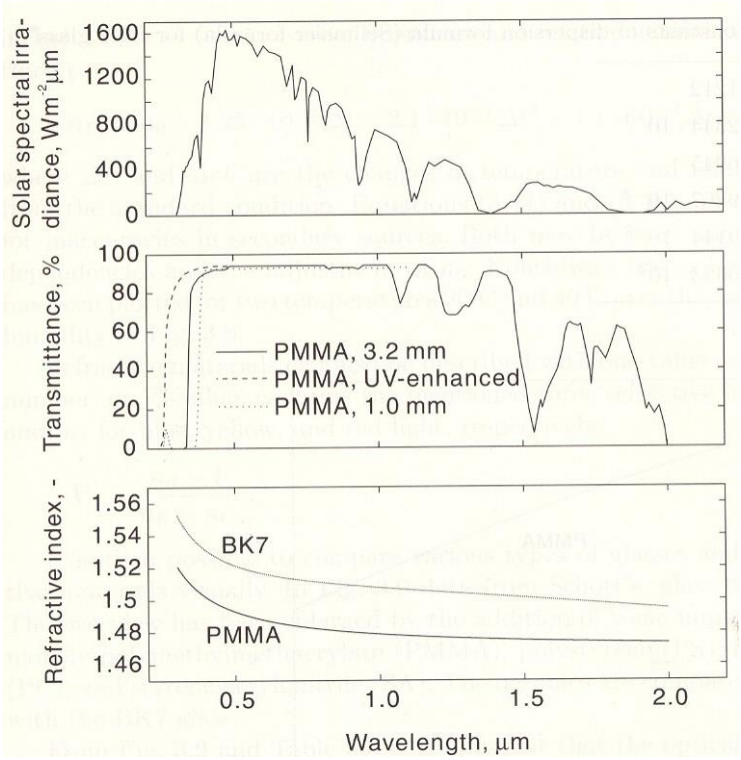

Figure 3-5 - The effect of spectral irradiance on the transmission and refractive index of PMMA

(Leutz and Suzuki, 2001)

Figure 3-6 identifies a constant decrease in the refractive index of PMMA as the temperature of the material increases. This variation in refractive index causes a problem for accurately simulating the optical performance of the designed collector in that the temperature of the collector, the cavity and the materials are not accounted for in the model design. Intuitively, as the collector is exposed to solar energy the temperature both on its surfaces and in its cavity will increase beyond that of the surrounding ambient temperature in proportion to the intensity of the incident solar energy and the length of the exposure. The significance of this is that, at any given time after the first rays arrive at the collector, the refractive index of the PMMA lens could be at any point between 1.493 and ~1.48, the upper limit of in terms of the lens designed operating conditions (100 ^{o}C). However, when put into context the importance of this refractive index 'drift' is minimal due to the nonimaging characteristics of the designed systems, resulting in a minor adjustment of the refractive index from 1.493 (glass point -7 ^{o}C) to a more realistic 1.49 (an assumed ambient temperature of ~ 25 ^{o}C).

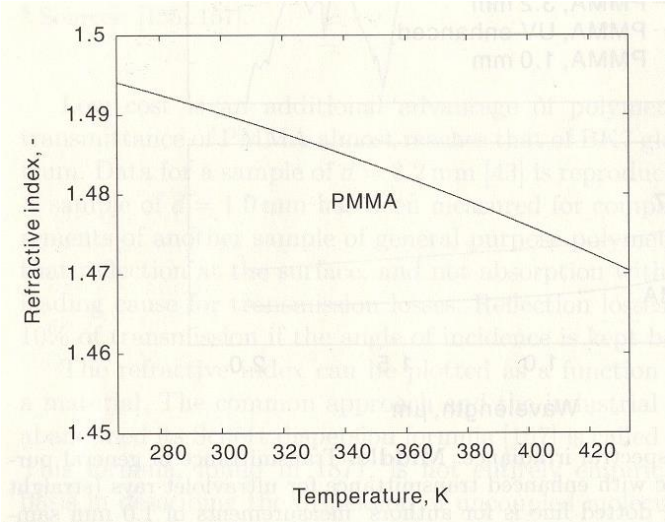

Figure 3-6 - The temperature dependence of the refractive index of PMMA at the wavelength of yellow light (D-line = 589.29 nm) between the glass point and melting point of PMMA at 266 K (-7 ^{o}C) and 433 K (160 ^{o}C), respectively.

(Leutz and Suzuki, 2001)

Figure 3-7 highlights the effect of relative humidity and temperature on the refractive index of PMMA and, like the effects shown in Figure 3-6, the significance of this drift in refractive index is minimal. The developed lenses of the collector are solely exposed to an enclosed cavity with a minimal liquid or vapour water content and as such as the temperature increases, despite the fact that the air can hold more water, the overall amount of water in the system cannot increase beyond its initial level making the effects of relative humidity negligible.

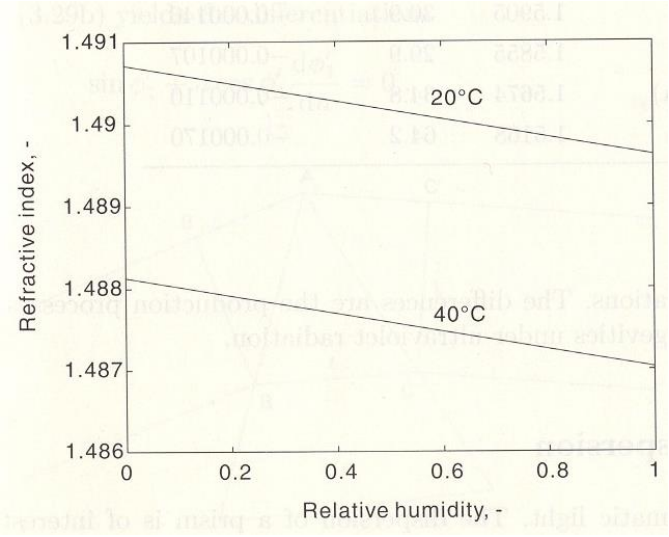

Figure 3-7 - Dependence of the refractive index of PMMA on relative humidity and temperature.

(Leutz and Suzuki, 2001)

Finally, the absorber was assumed to be a perfect blackbody absorber, absorbing 100 per cent of all incident energy with no reflections back into the collector cavity.

3.4.2 Eazee simulation criteria

The optical model was constructed of an outer optical pane, an optical lens, an absorber and an inner pane of glazing. The outer optical pane, a 3 mm pane of PMMA, and the 0.75 mm optical lens were combined into one single element assuming a negligible effect from any bonding agent needed to combine the two components. The second optical element in the system was the absorber. The absorber profile was constructed in two distinct configurations; a single absorber configuration and a multiple absorber configuration. The single absorber configuration created a single absorber for the lens under evaluation and the multiple absorber configuration evaluated the individual lens performance in terms of all of the absorbers in the modular system. The transmission of light into the building was evaluated by offsetting the absorber components, from their original positions, to the areas where the transmitted light would pass through the inner glazing of the collector. The final optical element in the system was the inner glazing lens. Like the outer lens, the inner lens was a 3 mm pane of PMMA directly behind the absorber material. The enclosing top, bottom and side boundaries were excluded in order to simplify the optical model by allowing light incident on those surfaces to escape the system and thus evaluating the collector solely in terms of the lens performance.

A constant 500 rays were traced through all of the collector configurations to provide an accurate representation of the lens performance and the output was described in terms of two variables; angular acceptance and optical efficiency.

The angular acceptance (AA) of the system is the fraction of the light incident on the collector, in terms of percentage, which is transmitted through the collectors' entrance aperture and the optical efficiency (OE) is the percentage of incident light which strikes the absorber.

The absorber flux profiles were created by utilizing a similar process, however two fundamental differences in the simulations were made; the number of rays was increased from 500 to 5000 in order to ensure a higher accuracy from the simulation, as a visualisation of the individual rays was not necessary for the absorber flux output, and the absorber area was split into 100 individual components to create a high resolution map of the Hamiltonian energy flux distribution.

There are a total of four different types of output files; a ray trace file, an absorber flux profile, a 2-dimensional optical map and a 3-dimensional optical map.

When presented in Tecplot 10, the ray trace output file is a visual representation of the transmission of the light rays through the collector, the absorber flux profile is a graphical display of the Hamiltonian distribution of energy on the absorber surface and the 2-dimensional optical map is a graphic profile of the collectors' performance across a range of incidence angles.

The 3-dimensional optical maps were used in conjunction with an additional piece of software to visualize the collectors' performance at various orientations and tilt angles using historical meteorological data to predict the actual energy output in terms of kilowatts hours per metre squared per annum ($kWhm^{-2}yr^{-1}$) and provide a graphical display of the collectors' performance each day of the simulated year (presented separately in Chapter 6).

3.4.3 Limitations of the ray tracing using Eazee

As with any simulation software Eazee has built-in limitations on what it can achieve when evaluating a design. With respect to the designed systems those limitations are as follows:

- Double coordinate errors

Two identical sets of consecutive x and z coordinates prevent the Eazee simulations from running and as a result of this great care had to be taken in the lens prism design to ensure the minimum prism height was kept above 1 micron. Although this inherent limitation in the software may be thought of as an issue with other optical systems, the inability to simulate a lens comprising of one or more prisms with a height of less than 1 micron ensured a stricter adherence to the manufacturing tolerances of the designed systems.

- Single refractive index

Eazee also has a limitation in its ability to simulate multiple refractive elements with different physical properties. As a result of this the glazing and lens material were chosen with identical properties in terms of extinction coefficients and refractive indices. However, during the optical simulations the effect of Tensol 70, the Perspex cement (n = 1.49), was assumed to be negligible.

- Temperature variations

The ambient temperature, the temperature of the materials within the optical model and the effects of temperature on those materials are not taken in to account. These variables were managed through the selection of the refractive index for the simulations.

- Single wavelength simulations

As previously mentioned, Eazee was incapable of simulating multiple wavelengths of incident light simultaneously. However, the effect of multiple wavelengths has already been discussed and was addressed through the selection of the refractive index. Profiling the chromatic aberration of the transmitted light into the building was not considered during the optical design.

- Resolution of the historical meteorological data

The historical meteorological data was only available at 1-hour intervals (15^{o} in terms of incidence angle) and as such, although the simulated performance may be representative for the different collector profiles, the accuracy of the output may not be fully reliable.

3.5 Optical design criteria

Winston et al (2005) identifies some of the main factors influencing the design of concentrators for solar energy use and they are as follows:

1. Cost and ease of manufacture on an appropriate scale
2. Extent of guidance required for following the sun
3. Durability and maintenance
4. Required working temperature of absorber
5. Preferred geometry of absorber in relation to the mode of utilization of the energy
6. Susceptibility to contamination and durability under ultraviolet irradiation

Thomas et al (1999) expand on these criteria by adding that building integrated PV systems have the following advantages:

1. No additional requirement for land
2. The [capital] cost of the PV wall or roof can be offset against the cost of the building element it replaces
3. Power is generated on site and replaces electricity that would otherwise be purchased at commercial rates
4. Connecting to the grid means that the high cost of storage is avoided and security of supply is ensured

With Strong and Lloyd Jones (2001) adding the very emotive benefit of “providing building owners with a highly visible public expression of their environmental commitment”.

In addition to these factors, and within a building integration context, acceptable aesthetics, high system performance and a viable economic payback are also required for a system to be implemented in a real-world context.

With these basic concepts forming the basis of the design parameters, this section describes the design process for both the concentrating lens and the absorber and the selection on the materials used for a building integrated solar collector with an additional passive daylighting and solar shading aspects.

3.6 Collector designs

The design concept was to take a comprehensive look at the optical and architectural criteria outlined within this subject area and to create a novel, modular, solar window for building integration. Comparable in scale to a double-glazing unit the collector would conceals the black absorber material where possible, harvest solar energy during peak periods, conveys some aspect of natural lighting into the building's interior and be flexible enough to be adapted to various window aperture sizes and orientations. To achieve this objective a number of collectors were designed; a simplistic baseline design, a conventional fast Fresnel lens augmented baseline (CFFLAB) design and a range of defocused fast Fresnel lens augmented baseline (DFFLAB) designs. Including the baseline collector, dozens of collector configurations were designed and evaluated encompassing 12 different lens resolutions, 12 different levels of defocus with the absorber area taking up no more than half of the inner glazed area and 2 different types of modularisation methods were considered.

3.6.1 Baseline design

The cheapest and easiest way to meet the main desired criteria is to simply include strips of photovoltaic cells on the inner glazing pane in the cavity of a double-glazed window unit, congruous with the approach taken by Moreno et al (2019) but using traditional, cost effective and commercially available multicrystalline PV cells instead of organic PV cells. This design would collect, after considering reflective and absorption losses, just under half of the total energy incident on the outer glazing pane and transmit the remainder of the energy into the building in the form of natural lighting (Figure 3-8). However, as previously mentioned the appearance of a black absorber material on building exteriors is a barrier to the implementation of building integrated solar collectors and is therefore not the ideal solution for the concept under development but it does serve as a baseline by which to compare the performance of the developed collectors.

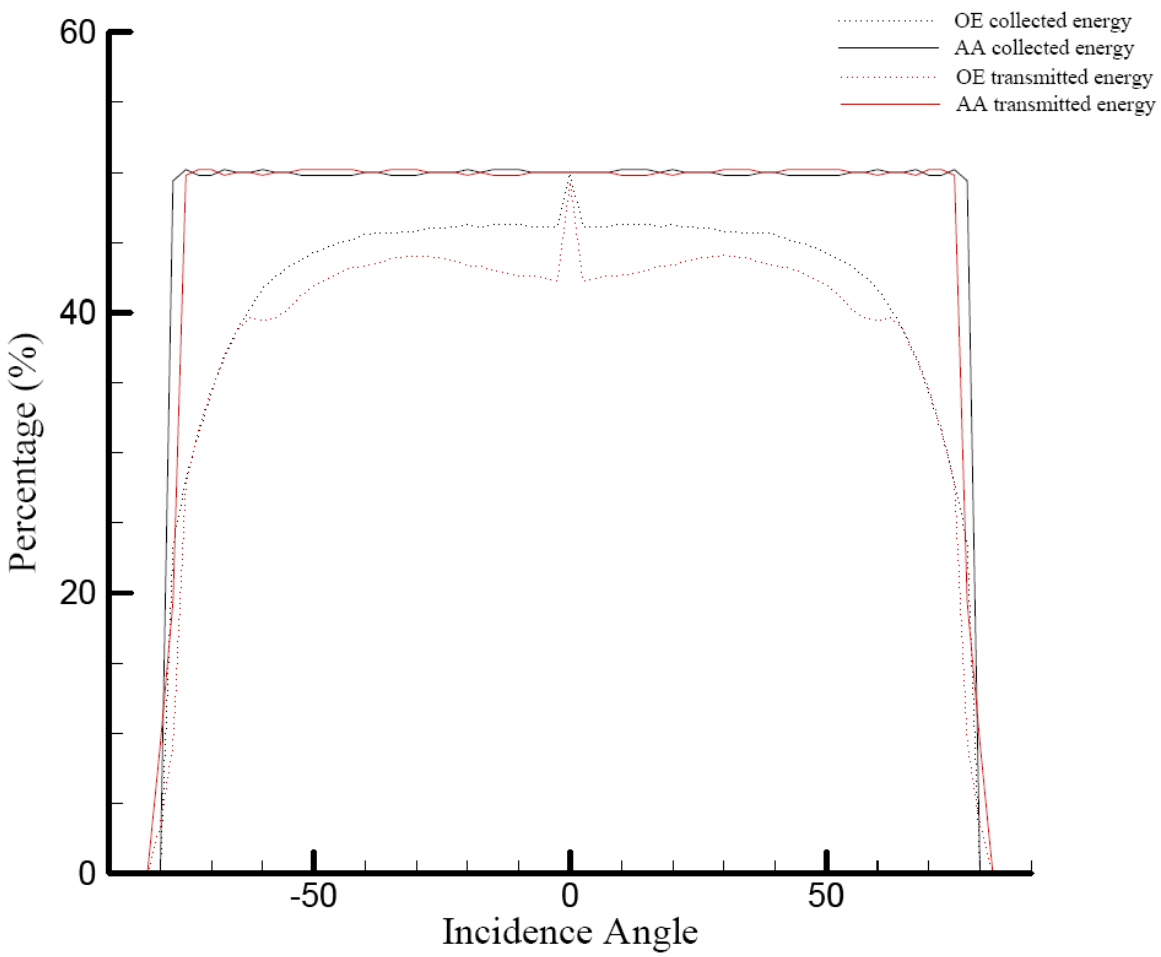

Figure 3-8 – 2-dimensional optical map of the optical efficiency (OE) and angular acceptance (AA) of the baseline collector showing both the percentage of energy reaching the absorber material and the percentage of energy transmitted through the collector.

3.6.2 Conventional fast Fresnel lens augmented baseline design

The next logical step in the design of the system was to augment the baseline design with a conventional Fresnel lens. Given that the lens was being designed for a building integrated collector, the overall thickness of the system in development was a major limiting factor and as such a 'fast' Fresnel lens was designed with an f-number (aspect ratio) of 0.5. A 240000 x 1000000 x 750 micron lens comprised of 640 prisms with a constant width of 375 microns and a maximum prism height of 339 microns was designed in Microsoft excel using the following relationship presented by Leutz and Suzuki (2001) for a "grooves in" simple Fresnel lens:

$$tan\alpha = \frac{R}{n\sqrt{R^2 + f^2} - f}$$ Equation 3-16

Where: R represents the maximum distance from the optical axis, n denotes the refractive index of the material and f is the focal length of the system (Figure 3-9).

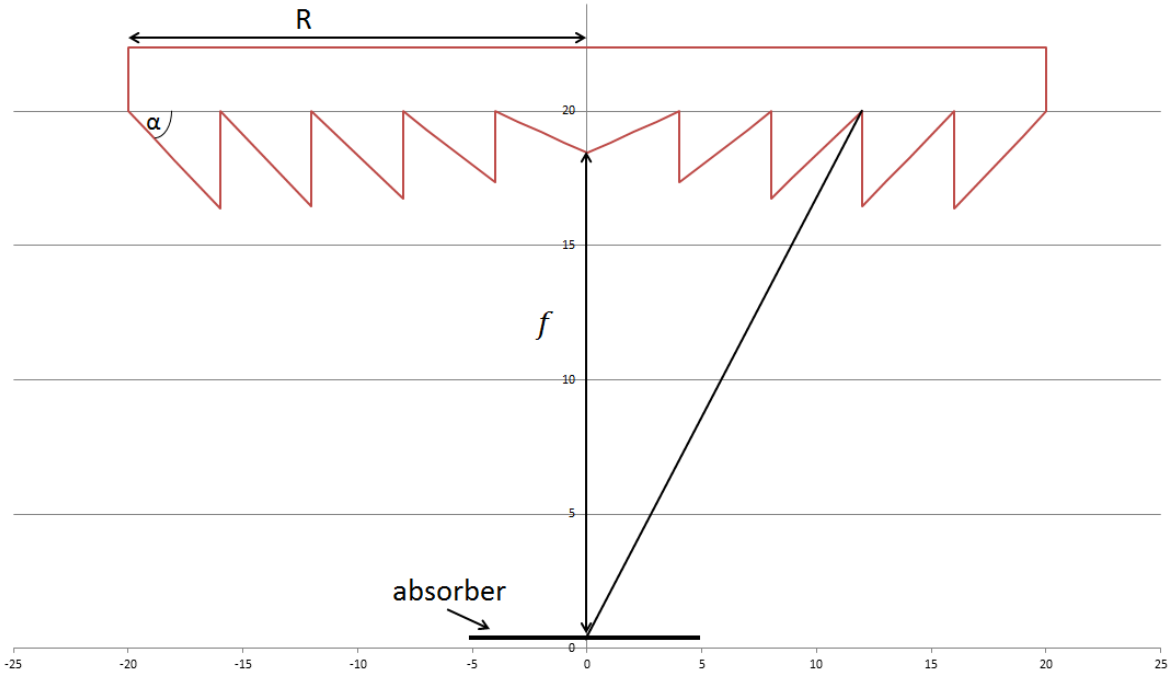

Figure 3-9 - Schematic detailing the variables used in the lens design

In order to ensure that the maximum prism height stayed within the 375 micron maximum limit set by the eventual manufacturer of the lens and that an inbuilt buffer was established between the design specifications and the limit of the manufacturer's abilities, the prism width was set at a constant 375 microns across the lens. The reasoning for this was purely mathematical and came down to simple geometry. If the height of the lens and the distance of the furthest prism from the lens were constant (12 cm for this design) as is true for any fast Fresnel lens, then the subtended angle (α) at the furthest point along the lens (R_{max}) must equal 45^o. This means that, for a lens comprised of prisms of a constant width, the subtended angle α in the furthest prism from the optical axis must always be less than 45^o and as a result the prism height must always be less than the prism width. In the case of the lens dimensions described above the maximum slope angle was 42.09^o, 0.07^o inside the upper limit where total internal refraction begins to take effect (42.16^o).

Figure 3-10 shows a perpendicular 2-dimensional trace of the lens described above and, as with the baseline collector, a 2-dimensional optical map was created to examine the performance of the conventional fast Fresnel lens augmented baseline (CFFLAB) collector (Figure 3-11). The 2-dimensional performance of this collector design shows that the optical performance of the augmented collector increases the amount of energy incident on the absorber between the angles -20^o to $+20^o$ or in terms of time harvesting solar energy and shading the interior of a building; 1 hour and 20 minutes either side of solar noon. However, the performance of the lens rapidly deteriorates either side of perpendicular and the performance of the CFFLAB collector results in a much lower quantity of energy becoming available to the absorber outside of this collection window, when compared with the baseline collector. In addition, the optical efficiency of the CFFLAB collector is relatively low (~ 80%) during the perpendicular ray trace despite relatively low absorption within the lens itself, indicating a high percentage of reflective losses from the sloped prism surface.

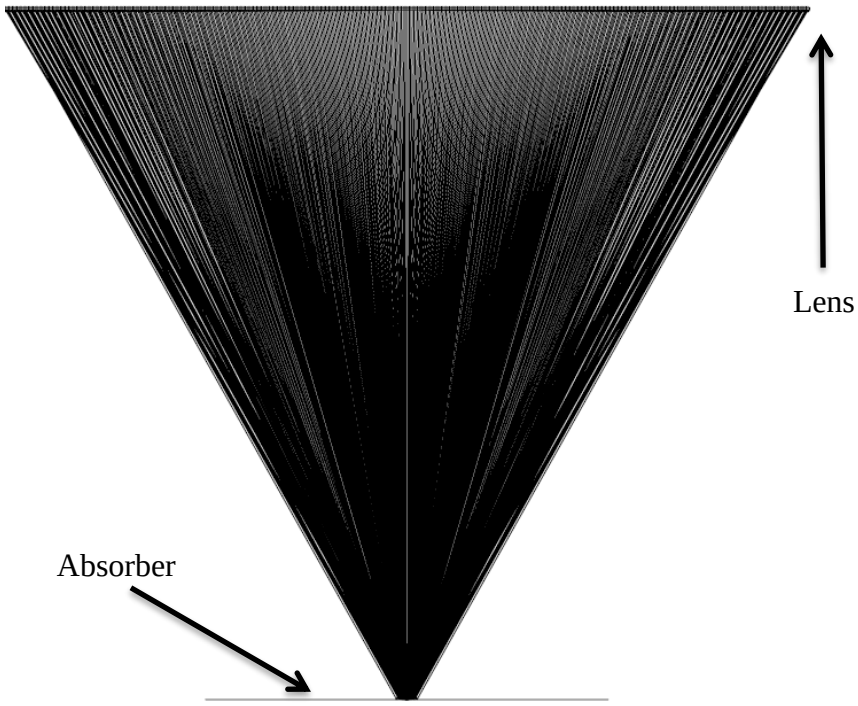

Figure 3-10 - 2-dimensional perpendicular ray trace of a 24 cm conventional fast Fresnel lens with a constant prism width of 375 microns

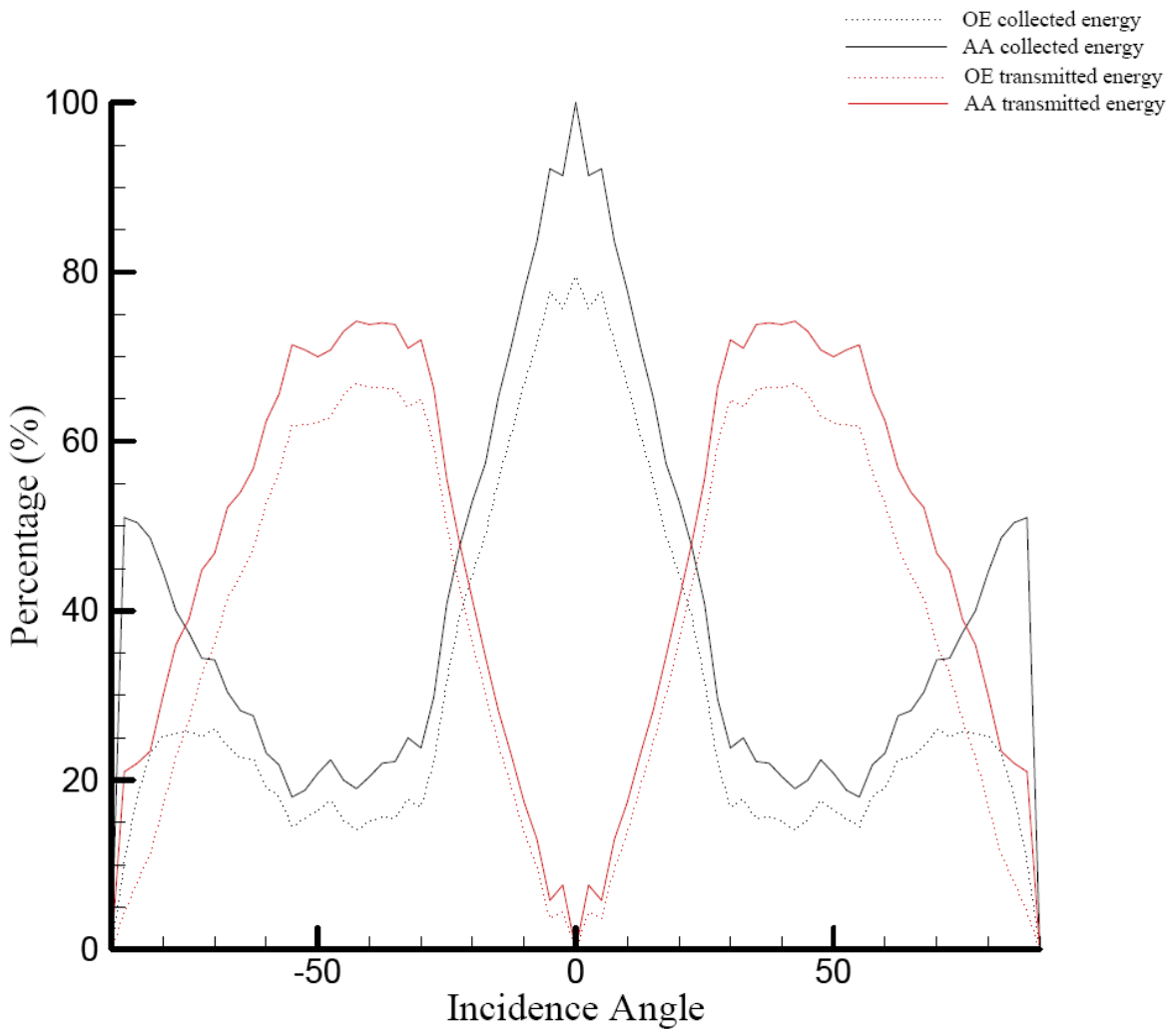

Figure 3-11 - 2-dimensional optical map of the optical efficiency (OE) and angular acceptance (AA) of the CFFLAB collector showing the percentage of energy reaching the absorber material and the percentage of energy transmitted through the collector.

In order to identify the reason for this rapid drop off in angular acceptance, a series of 2-dimensional ray traces were carried out at 1° intervals extending from perpendicular (0° ray trace shown in Figure 3-10) to +10°. Due to the axisymmetric nature of the lens this evaluation is also representative of the range 0° to -10°.

Figure 3-12 shows an immediate transition of the prisms furthest away from the optical axis (with the larger slope angles) to totally internally reflecting the incident rays from the sloped face of the prisms as the incidence angle exceeds the 42.16°, the upper limit of total internal reflection (TIR) for PMMA. As the incidence angle increases from 2° in Figure 3-13 to 10° in Figure 3-17 a

gradual increase in the number of prisms affected by the TIR limit is noticed, which subsequently reduces the area of the lens which can viably transform the incident rays of light.

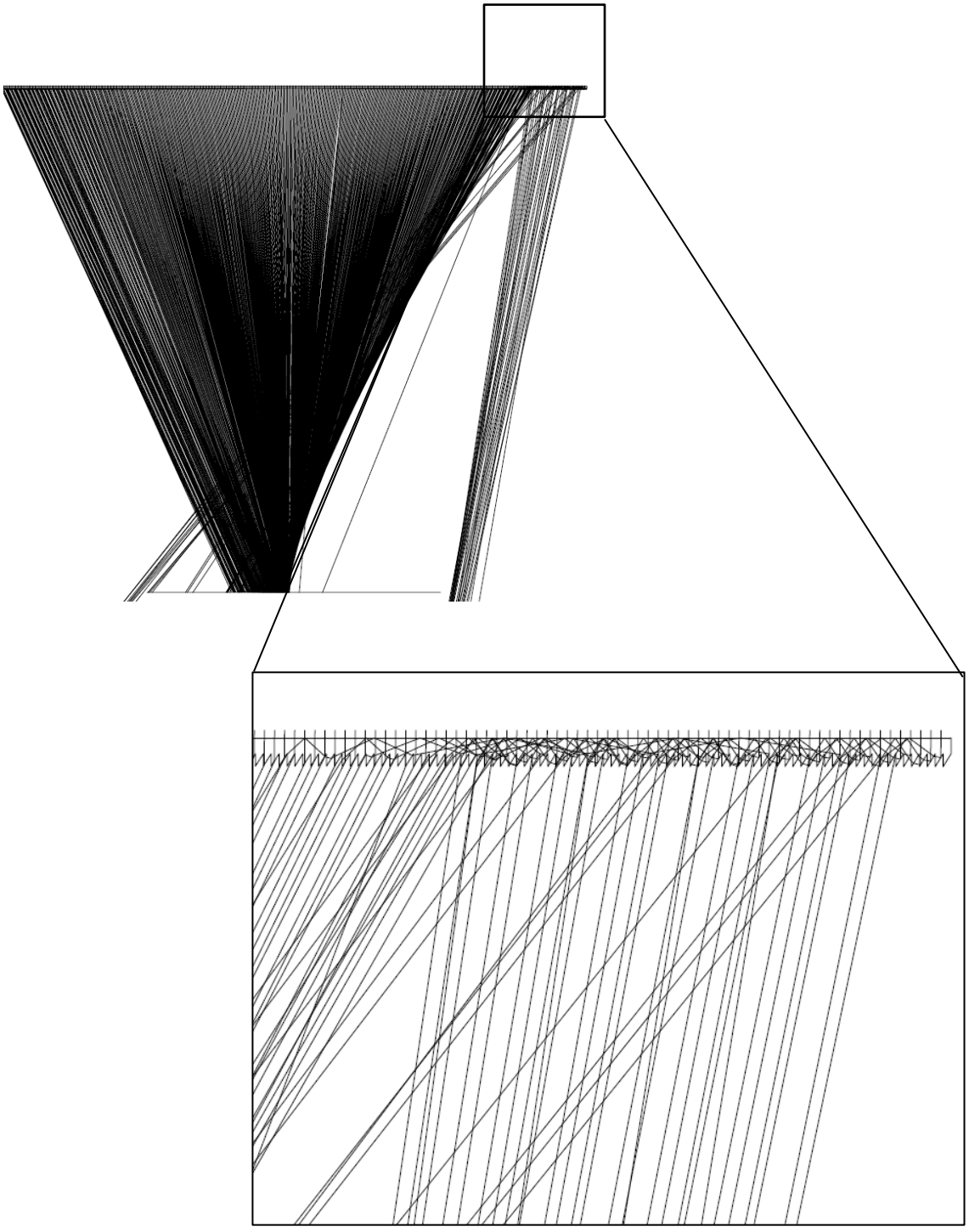

Figure 3-12 - 1º incidence angle 2-dimensional ray trace of the CFFLAB collector and close-up of an area of total internal reflection.

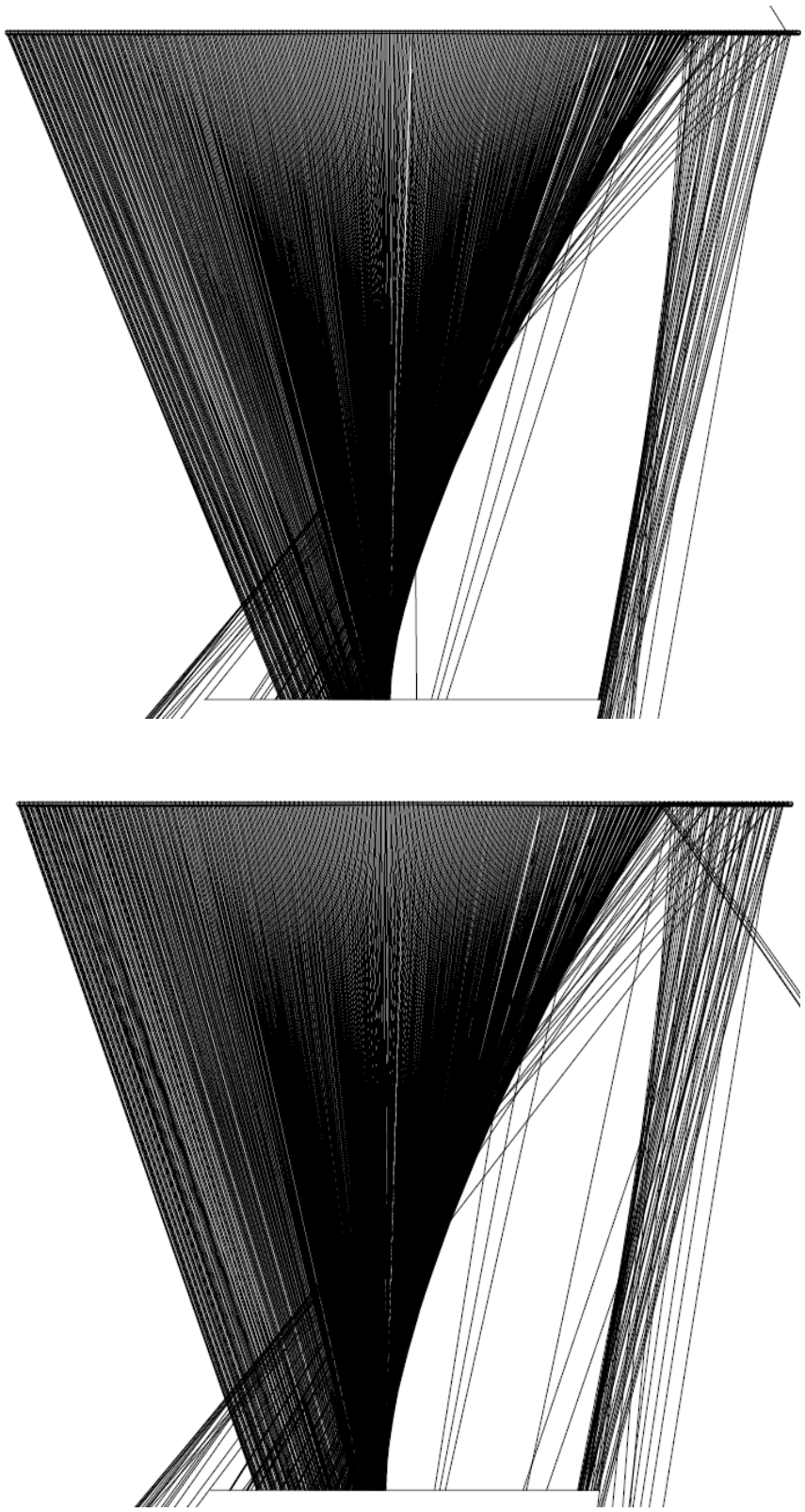

Figure 3-13 - Top: 2º incidence angle 2-dimensional ray trace of the CFFLAB collector and Bottom: 3º incidence angle 2-dimensional ray trace of the CFFLAB collector.

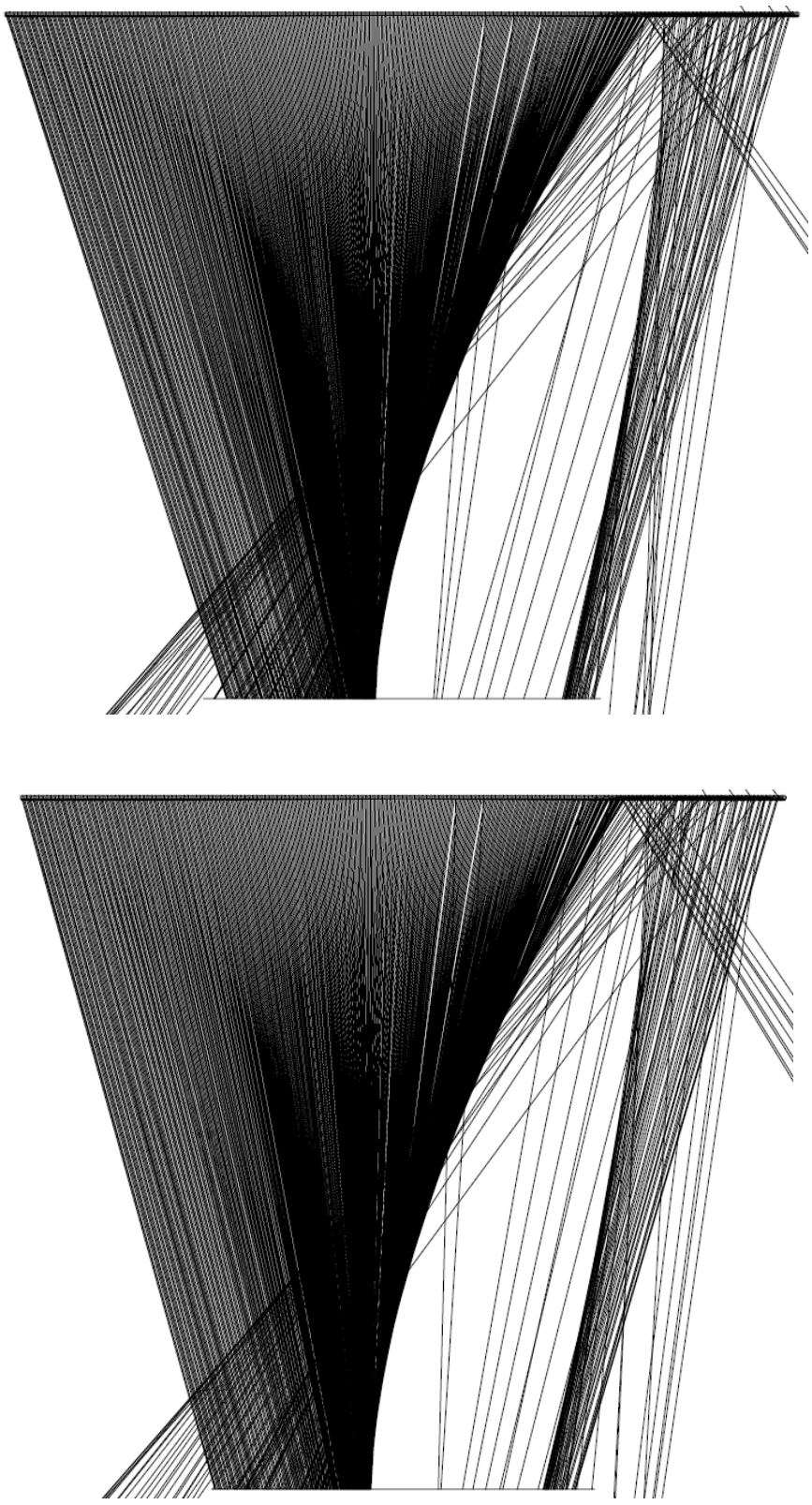

Figure 3-14 - Top: 4º incidence angle 2-dimensional ray trace of the CFFLAB collector and Bottom: 5º incidence angle 2-dimensional ray trace of the CFFLAB collector.

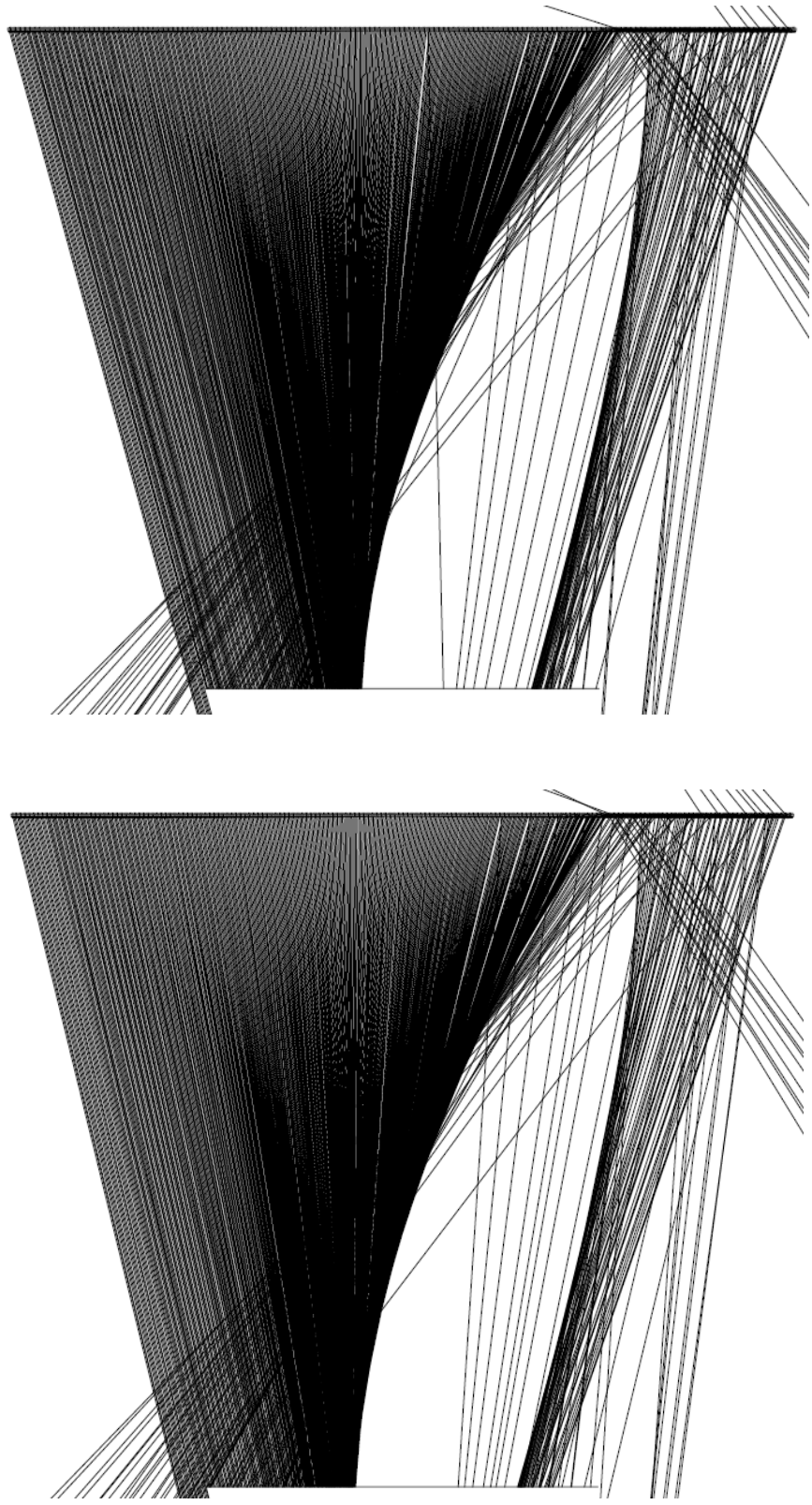

Figure 3-15 - Top: 6º incidence angle 2-dimensional ray trace of the CFFLAB collector and Bottom: 7º incidence angle 2-dimensional ray trace of the CFFLAB collector.

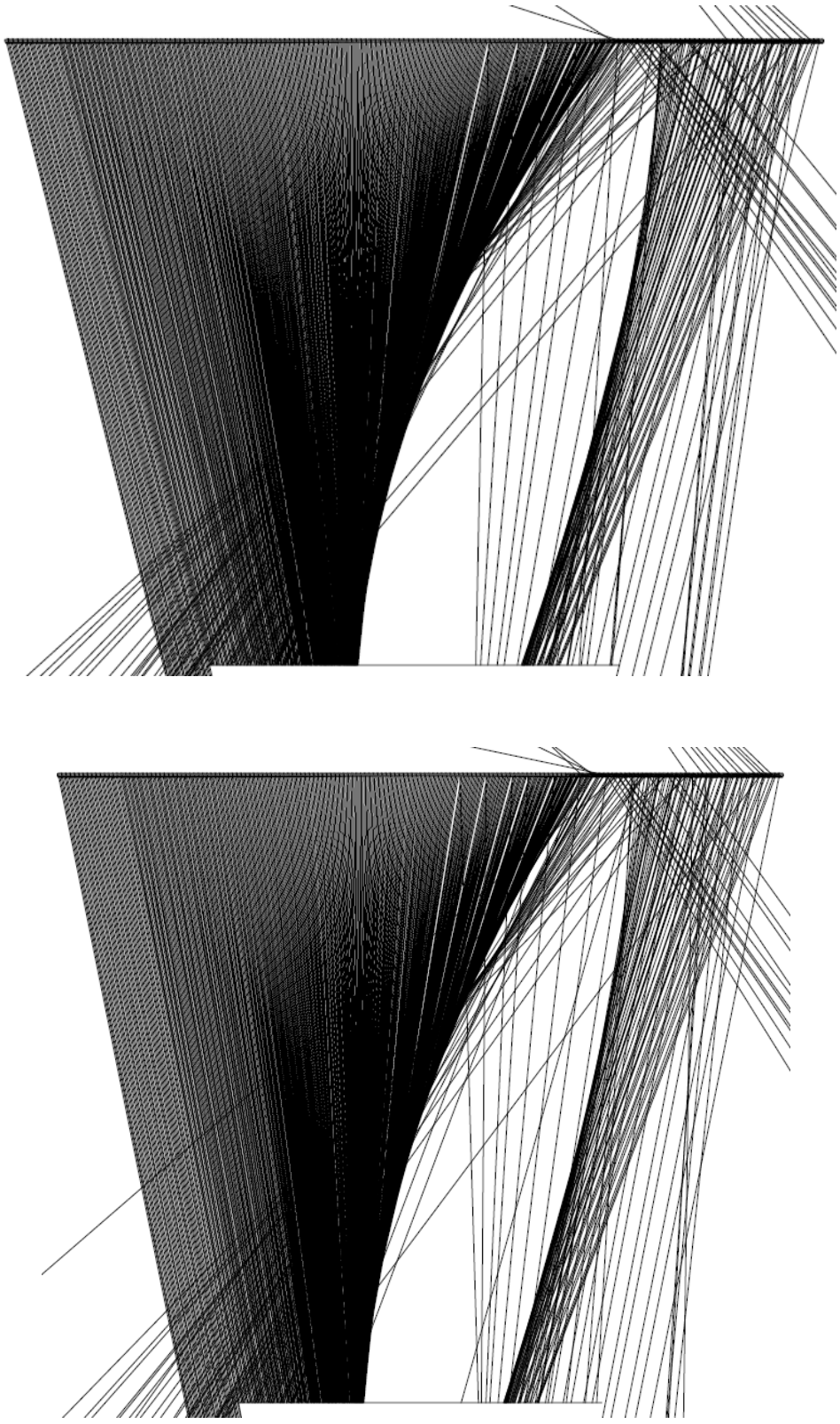

Figure 3-16 - Top: 8º incidence angle 2-dimensional ray trace of the CFFLAB collector and Bottom: 9º incidence angle 2-dimensional ray trace of the CFFLAB collector.

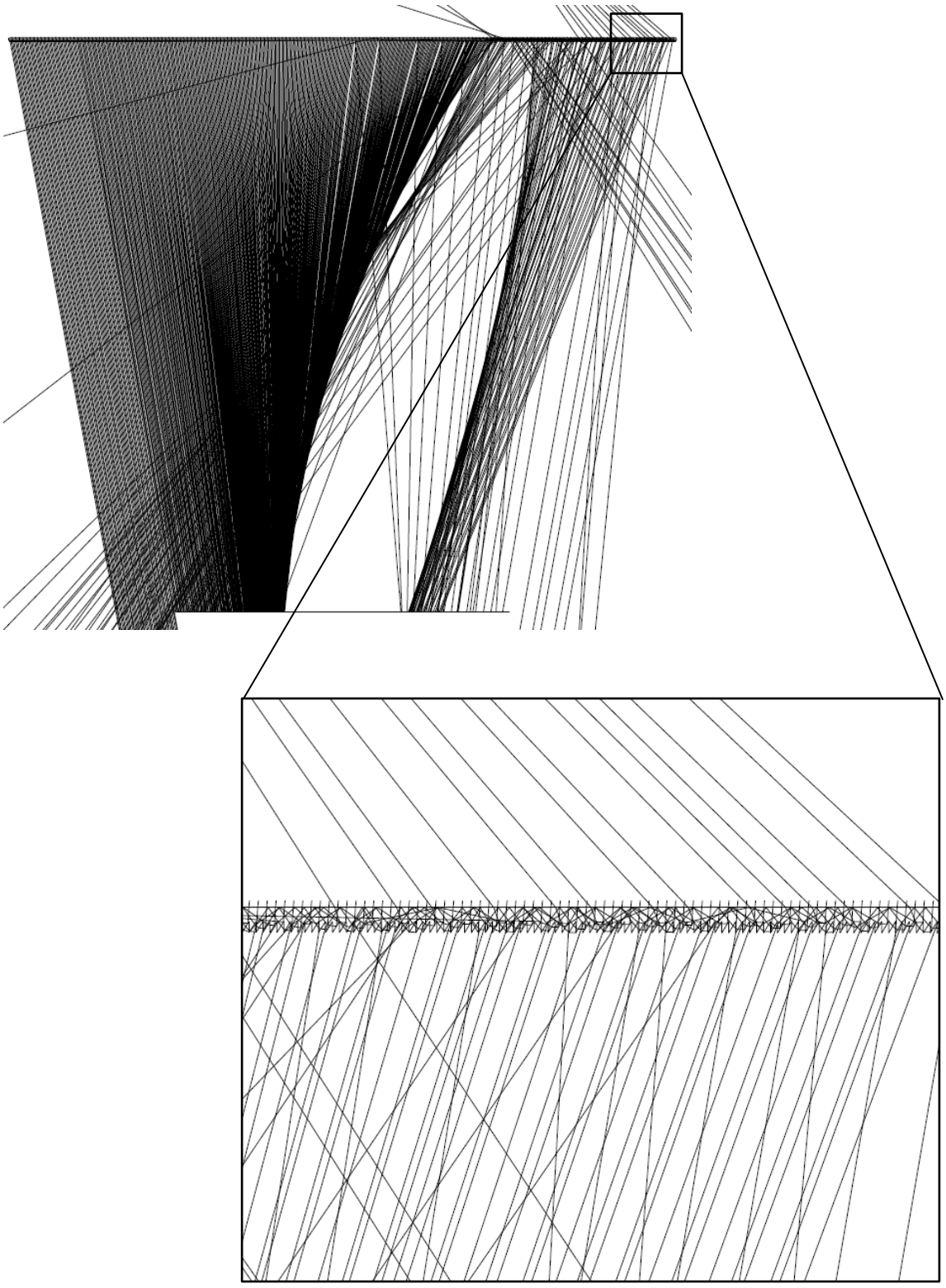

Figure 3-17 - 10º incidence angle 2-dimensional ray trace of the CFFLAB collector and close-up of an area of total internal reflection.

This rapid deterioration of the lens performance as a result of TIR is not unexpected and is a direct consequence of the f-number chosen. As the f-number or aperture ratio of a lens, its overall width divided by its depth, is reduced towards the theoretical maximum of 0.5 the prism slope angles must be increased to create a faster transformation of the incident rays (Figure 3-18). As a direct consequence of this, the 'faster' the lens has to transform light the higher its reflective losses are and the more prone it is to TIR over small changes in incidence angle.

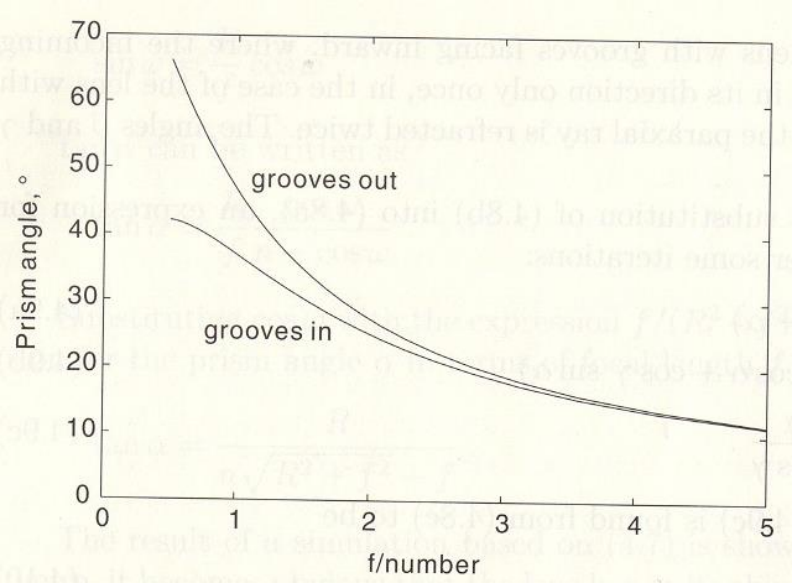

Figure 3-18 - Relationship between prism angle and f-number.

(Leutz and Suzuki, 2001)

In attempting to improve the variable 2-dimensional performance of the CFFLAB collector two questions become apparent for further exploration; can the performance of the CFFLAB collector be improved with a greater lens resolution and/or can the collection window be improved by adjusting the lens profile to reduce reflection losses and delay TIR while maintaining the f-number of the lens over a predefined absorber area?

3.6.2.1 The effect of lens resolution on the CFFLAB collector performance

The first option and most obvious of these questions to examine is how an increase in resolution effects the performance of the CFFLAB collector. Since the purpose of the Fresnel equation is to recreate the performance of a large convex lens by removing the unimportant material between the two refractive interfaces while maintaining the shape of those interfaces it stands to reason that if the curved convex lens is reproduced using progressively more straight edged prisms the resultant lenses will more closely represent the performance of the original convex curve. To examine the effect of an increased lens resolution on the performance of the CFFLAB collector 12 conventional fast Fresnel lenses were created and their performances were evaluated. Table 3-3 identifies the 12 resolutions examined in terms of their prism widths, the maximum prism heights, the number of prisms required to create a lens with the specified prism widths, the remaining unused area of the lens based on the manufacturer's available collector dimensions divided by 5 (to produce a final modular collector comprised of 5 side by side lenses) and the amount of PMMA required to be cut from the sheet during manufacture as a percentage of the overall lens material.

Table 3-3 - Lens resolution in terms of the number of prisms required for a range of prism widths and the resultant unused lens areas.

Prism width (microns)	Number of prisms	Max. prism height (microns)	Unused area (microns)	Cut material (% of lens)
375	506	339	125	32.13
350	542	316	150	29.98
325	584	293	100	27.86
300	632	271	200	25.70
275	690	248	125	23.58
250	760	226	0	21.47
225	844	203	50	19.31
200	950	181	0	17.18
175	1084	158	150	15.01
150	1266	135	50	12.88
125	1520	113	0	10.74
100	1900	90	0	8.60

The cut material was calculated as follows:

$$Total\ Cut\ Area = 2 \times \sum_{R_{max}}^{0} \left(\frac{z \times x}{2}\right)$$

Equation 3-17

Where; z is the height of the prism and x is the prism width. The total cut area was then divided by the total area of the lens material.

Figure 3-19, Figure 3-20 and Figure 3-21 identify some of the practical implications of varying the resolution of the lens in terms of manufacturing consequences encountered. Firstly, Figure 3-19 shows the relationship between an increased lens resolution, in terms of decreasing the width of the prisms, and the number of prisms necessary to create that lens profile. Figure 3-20 identifies that as the lens resolution increases the maximum height of the prisms reduce and perhaps most significant consequence is the relationship between the increase in lens resolution and the reduction in the percentage of material which needs to be removed (Figure 3-21). All of these factors directly affect the prototype manufacturing time for the lens and as a consequence the cost of producing the prototype for the proof of concept testing.

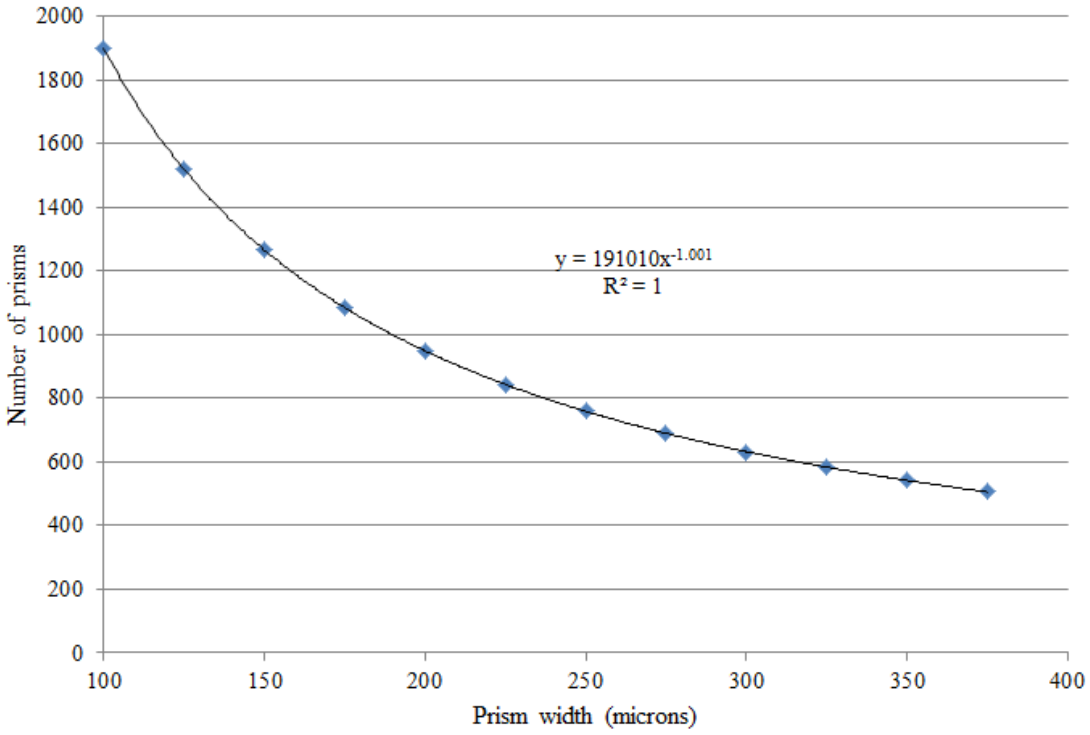

Figure 3-19 - Graphic representation of the relationship between the numbers of prisms required for the range of prism widths investigated.

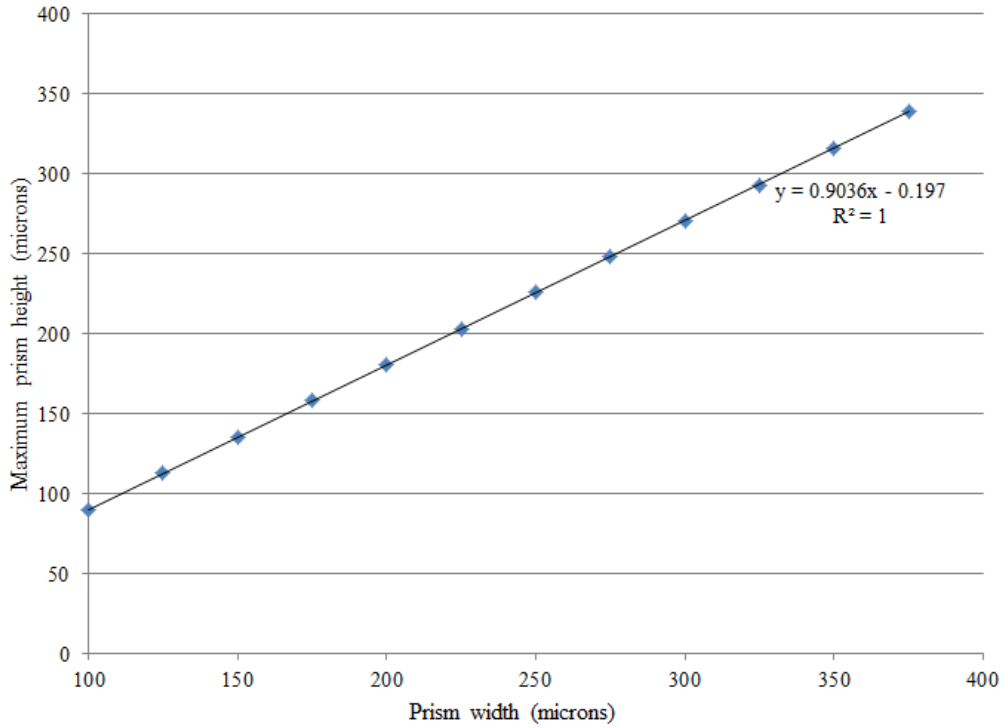

Figure 3-20 - Graphic representation of the relationship between maximum prism heights across the range of prism widths investigated.

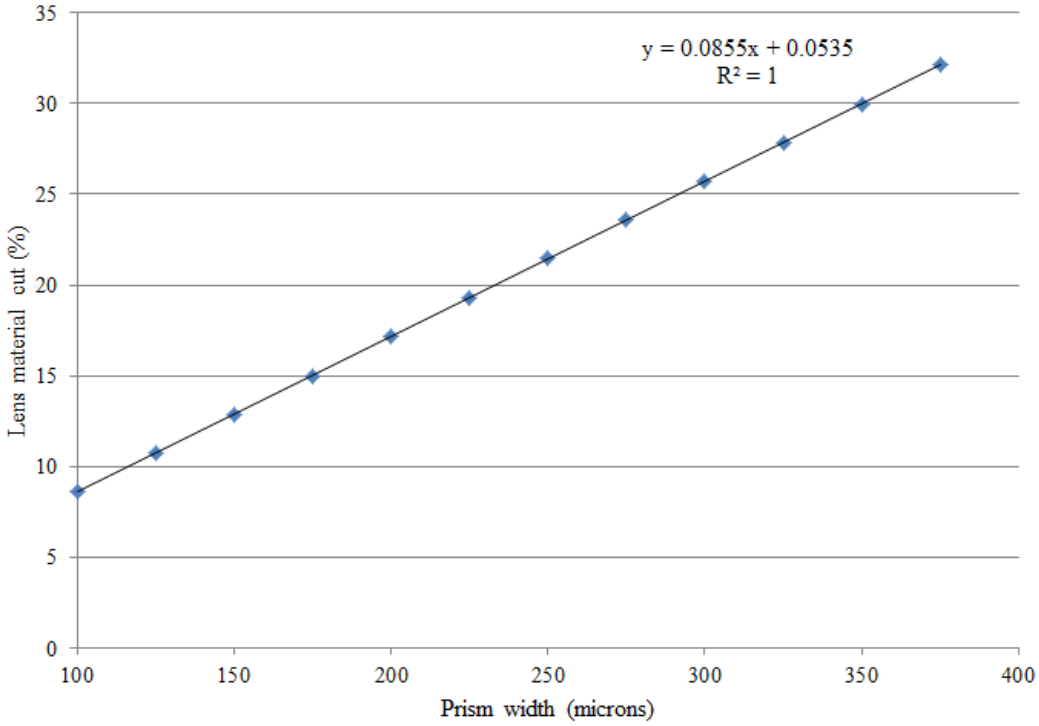

Figure 3-21 - Graphic representation of the relationship between the quantities of lens material which needs to be removed across the range of prism widths investigated.

The following 2-dimensional optical maps show the performance of the CFFLAB collector across the full range of resolutions investigated, from a constant prism width of 375 microns which approaches the maximum prism height achievable as a result of the manufacturing constraints, to a constant prism width of 100 microns where the accuracy necessary to produce the smaller inner prisms of the lens begins to exceed the minimum tolerances of the machining process used. Figure 3-22 and Figure 3-23 show the relative parity in the performance of the CFFLAB collector in terms of energy collected between the resolution ranges of 100 microns to 275 microns. However, with the decreased resolution of prism widths in excess of 300 microns (Figure 3-24) the lens performance begins to deviate from the prescribed profiles with increasingly erratic behaviour noticed in both angular acceptance and optical efficiency outside the $\pm 30^{o}$ collection spike. Although in terms of energy collection this is not a major issue, it does identify an additional small instability within the transmitted energy profile. Therefore, in terms of this CFFLAB collector, there is no perceived benefit in the additional cost and machining time required for removing the extra material in the creation of the 300 micron to 375 micron lenses.

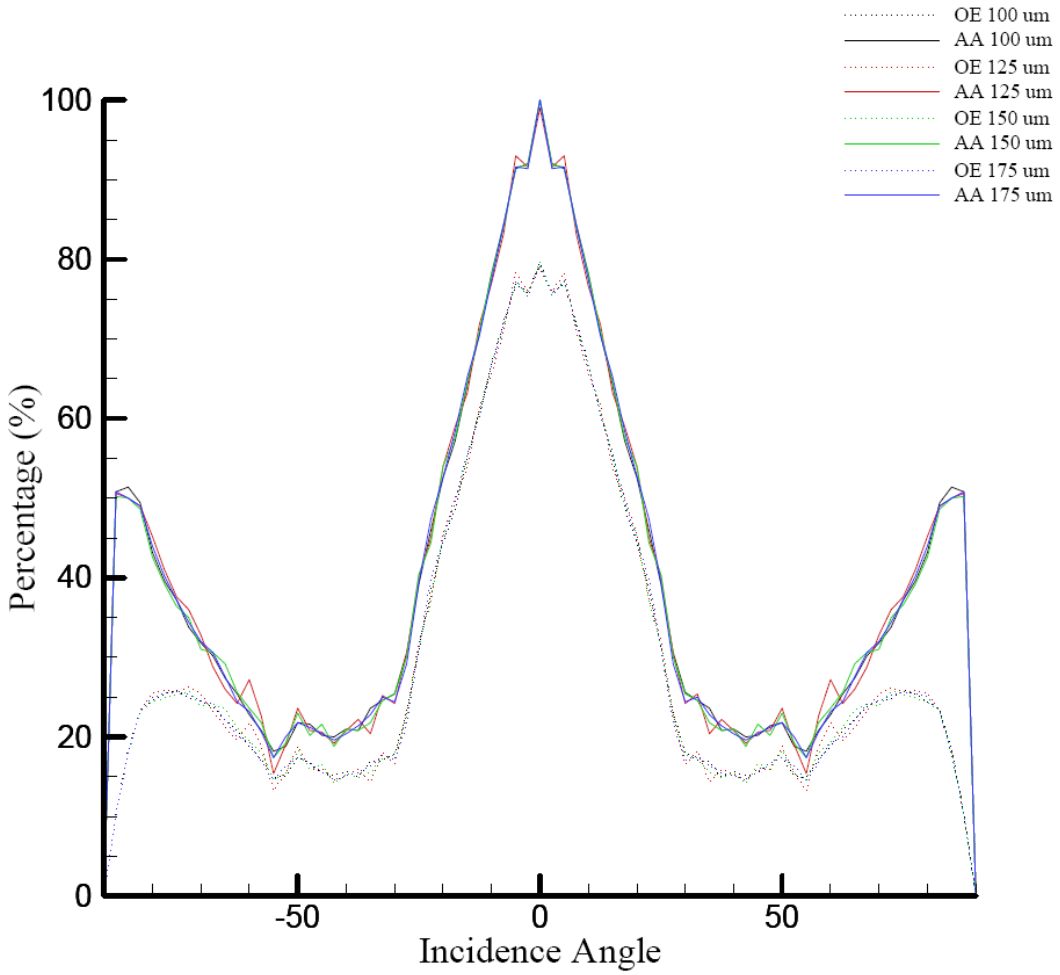

Figure 3-22 – Compiled 2-dimensional optical maps of the optical efficiency (OE) and angular acceptance (AA) of the CFFLAB collector resolutions ranging from 100 microns to 175 microns showing the percentage of energy reaching the absorber material.

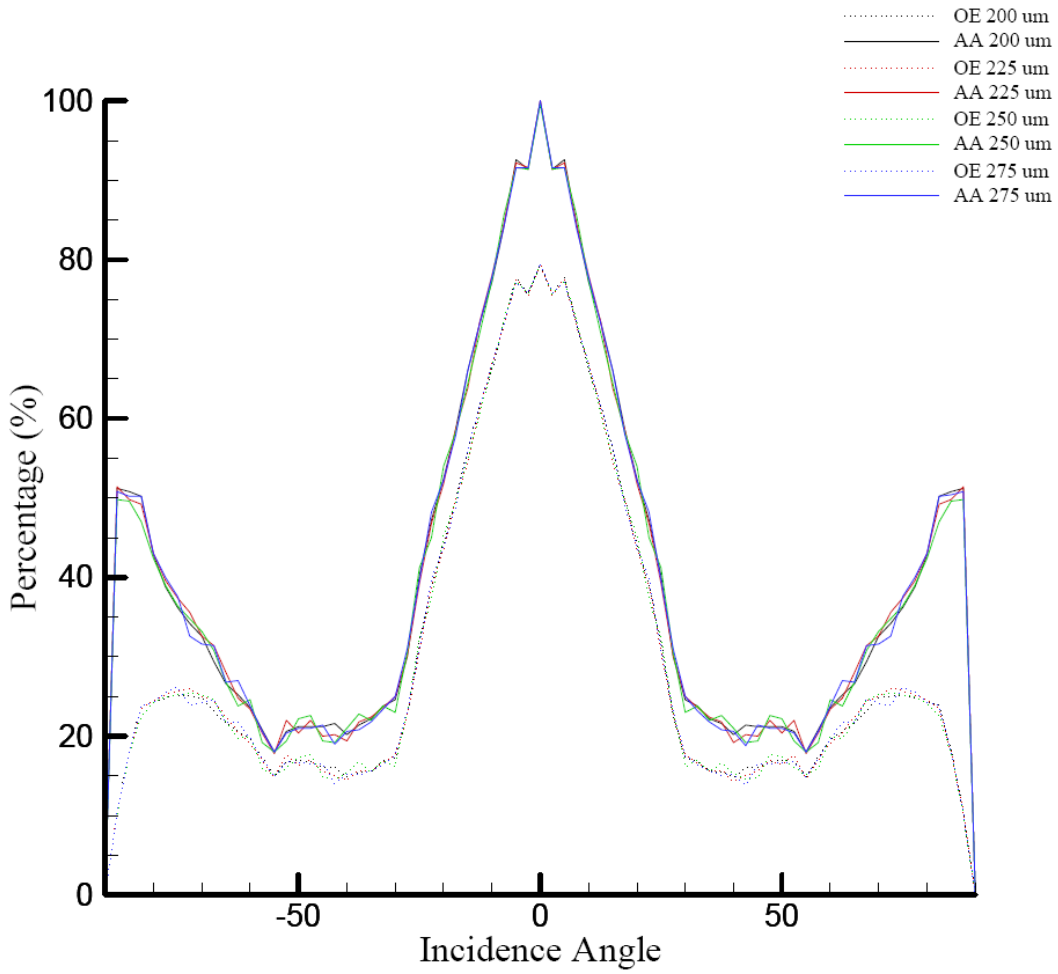

Figure 3-23 - Compiled 2-dimensional optical maps of the optical efficiency (OE) and angular acceptance (AA) of the CFFLAB collector resolutions ranging from 200 microns to 275 microns showing the percentage of energy reaching the absorber material.

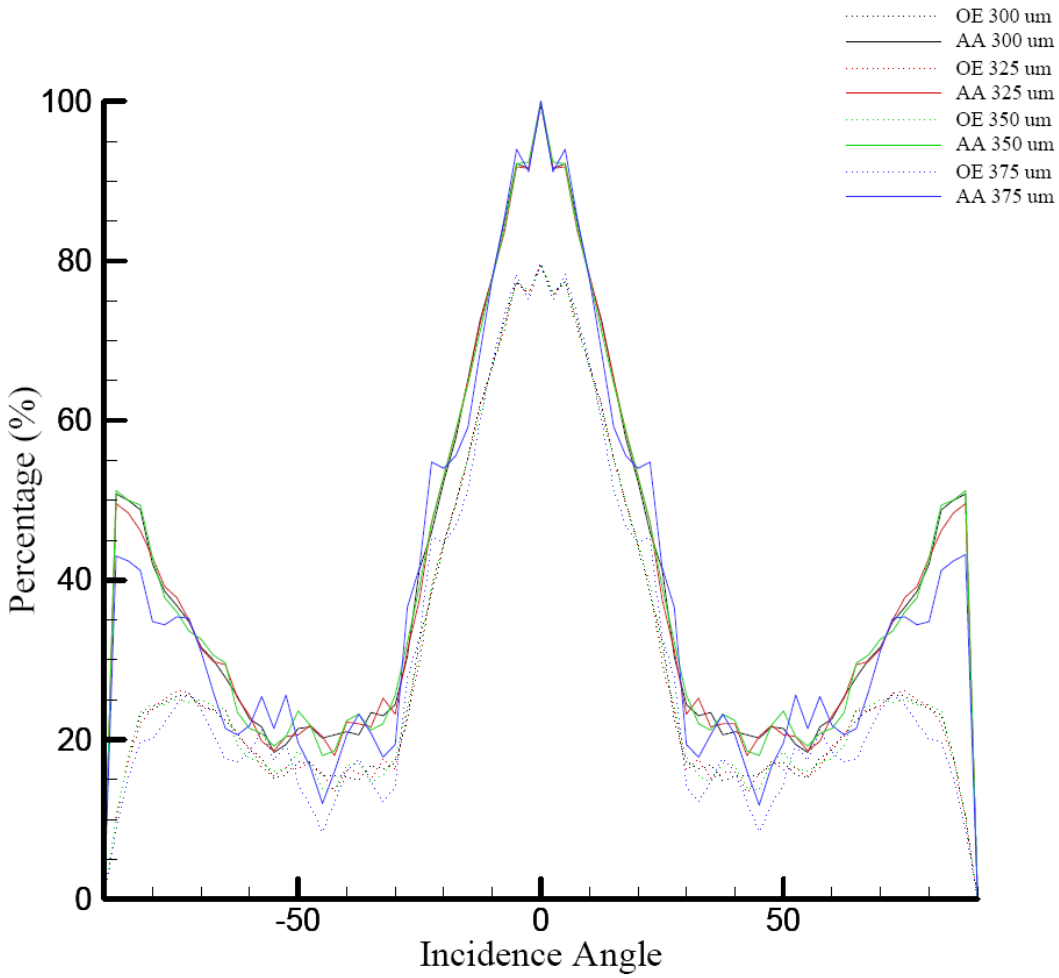

Figure 3-24 - Compiled 2-dimensional optical maps of the optical efficiency (OE) and angular acceptance (AA) of the CFFLAB collector resolutions ranging from 300 microns to 375 microns showing the percentage of energy reaching the absorber material.

Table 3-4 examines the performance of the various CFFLAB collector resolutions in terms of the amount of energy they collect over three distinct phases in their operation; ±15°, ±30° and ±90°. These three phases represent the collection phase (±1 hour either side of solar noon), the transition phase between energy transmission and energy collection and the full 2-dimensional energy collection characteristics of the CFFLAB collector.

Table 3-4 clearly shows that varying the resolution in and of itself doesn't provide any real benefit in improving the performance of the CFFLAB collector. Of specific note is the relatively small variation in optical efficiency (0.65%) as a result of resolution across the ±15° collection phase which indicates, as previously discussed, that the biggest optical losses from the system are still reflective losses from the sloped prism faces.

In order to address this problem more directly the second of the design questions, “can the collection window be improved by adjusting the lens profile to reduce reflection losses and delay TIR while maintaining the f-number of the lens?” will now be addressed.

Table 3-4 – Variations in predicted energy collection in terms of angular acceptance (AA) and optical efficiency (OE) at each resolution across three collection intervals; (a) ±15°, (b) ±30° and (c) ±90° of solar noon

Lens	AA (%)	OE (%)	Lens	AA (%)	OE (%)
100	81.66	68.80	100	62.55	52.07
125	81.40	68.56	125	62.55	52.00
150	81.69	68.82	150	62.62	52.05
175	81.57	68.72	175	62.54	52.05
200	82.09	69.06	200	62.93	52.28
225	81.89	68.77	225	62.71	51.97
250	81.69	68.79	250	62.64	52.05
275	82.02	69.14	275	62.96	52.29
300	82.22	69.18	300	62.94	52.32
325	81.92	68.96	325	62.66	52.07
350	81.91	68.92	350	63.07	52.39
375	80.95	68.53	375	63.06	52.55

(a) (b)

Lens	AA (%)	OE (%)
100	39.90	29.86
125	40.01	29.93
150	39.87	29.88
175	39.88	29.88
200	40.01	29.94
225	40.00	29.87
250	39.75	29.82
275	40.00	29.93
300	39.92	29.92
325	39.77	29.82
350	39.95	29.92
375	38.20	28.94

(c)

3.6.2.2 The effect of lens defocus and resolution on the CFFLAB collector performance

The next step in attempting to improve the performance of the CFFLAB collector was to reduce reflection losses and delay total internal reflection (TIR). The simplest and most obvious way to achieve this was by defocusing the lens. Defocusing the lens does three things to the CFFLAB collector; it spreads the incident energy over a wider area, reduces reflection losses from the sloped prism surfaces and delays TIR by creating an angular 'buffer' between the slope angle and the critical angle.

Figure 3-25 shows a sketch of a typical fast Fresnel lens which highlights the relative ease by which small amendments to the prism angles of the lens can be made with very little effect on the lens as a whole. The sketch, which is a profile of the prism heights in relation to each other, highlights the relative consistency in prism height (and therefore slope angle) until approximately two-thirds of the way from the outer lens to the optical axis before rapidly reducing to 0 at the centre of the lens.

Figure 3-25 – Sketch of the profile of a fast Fresnel lens in terms of prism height highlighting the gradual decrease from the outer lens to the optical axis.

This relationship provided the opportunity to investigate the performance of the CFFLAB collector across a number of levels of lens defocus. The predicted 2-dimensional optical performance of the CFFLAB collector over the following levels of defocus was investigated; 1^{o}, 2^{o}, 3^{o}, 4^{o}, 5^{o}, 6^{o}, 10^{o}, 15^{o}, 20^{o}, 23.5^{o} and 25^{o}. The main objectives of the defocus evaluation were to improve energy collection without inhibiting the transmission of light into the building outside the collection phase and as such the focus was on improving the performance of the CFFLAB collector during that collection window.

For consistency and succinctness, the following sections only provide ray trace diagrams of a CFFLAB collector with a lens resolution of 150 micron and lens dimensions of 189900 x 1000000 x 750 microns subjected to various degrees of defocus. However, since there is no available information in academic, commercial or industrial literature about the effects of defocus and/or

fast Fresnel lens resolution the predicted 2-dimensional optical performance of CFFLAB collectors with the resolutions investigated above at each of the levels of defocus will also be presented and summarise in the Appendix for completeness.

Figure 3-26 effectively shows the drop-off in performance for lenses defocused beyond 10° and Table 3-5 presented a full breakdown of the lens performance alongside the averaged angular acceptance and optical efficiency across the collection window.

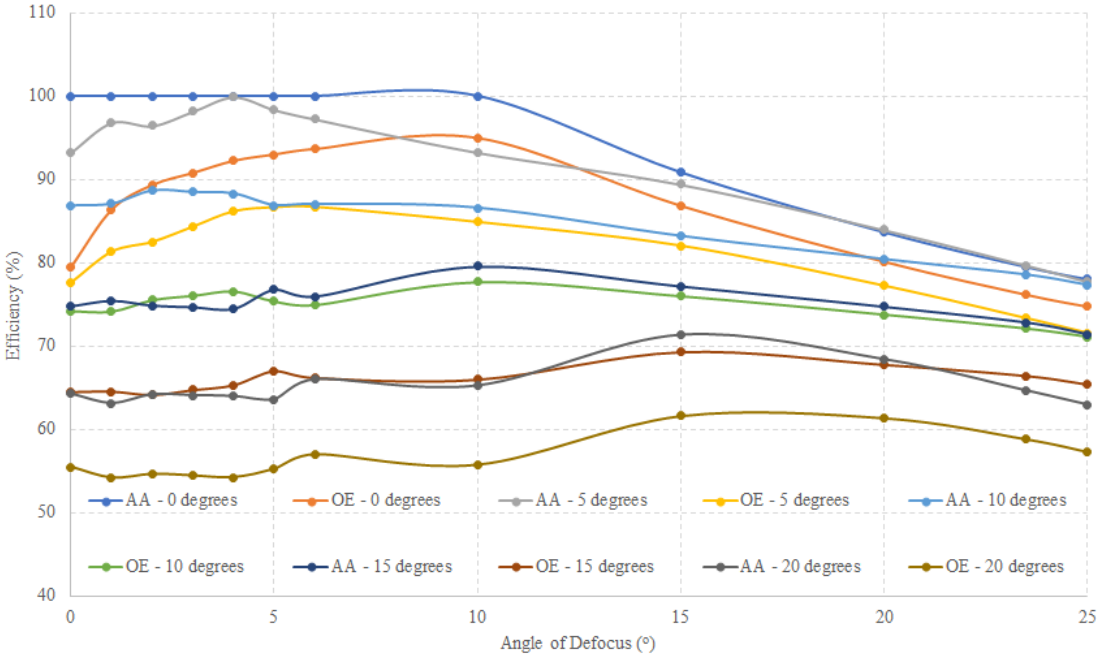

Figure 3-26 – Angular acceptance (AA) and optical efficiency (OE) of the 150 micron lens resolution across varying levels of lens defocus at incremental incident angles up to and including the design limit.

Table 3-5 – Simulated optical performance of the 150 micron lens resolution across varying levels of lens defocus at incremental incident angles up to and including the design limit with averaged optical efficiency (OE) and angular acceptance (AA).

Incidence Angle	Efficiency (%)	Angle of Defocus (°)											
		0	1	2	3	4	5	6	10	15	20	23.5	25
0	AA	100.00	100.00	100.00	100.00	100.00	100.00	100.00	100.00	90.84	83.68	79.52	78.04
	OE	79.57	86.41	89.35	90.80	92.24	93.00	93.66	94.96	86.84	80.16	76.20	74.78
5	AA	93.28	96.84	96.46	98.19	99.92	98.38	97.26	93.26	89.42	83.96	79.70	77.76
	OE	77.65	81.35	82.52	84.36	86.19	86.67	86.71	84.90	82.06	77.26	73.36	71.60
10	AA	86.86	87.08	88.66	88.48	88.30	86.90	87.06	86.60	83.22	80.44	78.58	77.36
	OE	74.20	74.15	75.54	76.07	76.59	75.38	74.95	77.72	76.02	73.79	72.10	71.11
15	AA	74.80	75.46	74.88	74.69	74.50	76.82	75.98	79.58	77.20	74.74	72.84	71.44
	OE	64.50	64.56	64.15	64.75	65.34	67.06	66.21	66.00	69.35	67.81	66.45	65.42
20	AA	64.28	63.16	64.20	64.10	64.00	63.64	66.02	65.28	71.40	68.44	64.66	62.96
	OE	55.50	54.19	54.64	54.45	54.25	55.27	57.02	55.74	61.65	61.38	58.81	57.28
Average Efficiency AA		83.84	84.51	84.84	85.09	85.34	85.15	85.26	84.94	82.42	78.25	75.06	73.51
Average Efficiency OE		70.28	72.13	73.24	74.08	74.92	75.48	75.71	75.86	75.18	72.08	69.38	68.04

3.7 Defocusing a fast Fresnel lens and the introduction of accretion

One of the practical considerations when defocusing a fast Fresnel lens is the necessity to accrete the lens to counteract the profile tending to zero away from the optical axis. Figure 3-27 clearly shows this tendency and how, as the level of defocus increases, it creates a more pronounced area which needs to be filled or accreted by one (or potential multiple) additional lens profile. The default lens profile used to build the defocused lenses back to the optical axis on all of the lenses designed and presented in this thesis is the 0 degree defocused (the conventional) fast Fresnel lens profile at each resolution. This decision was made to limit the amount of variability between designs and allow for the lenses to be as comparable as was reasonably practicable.

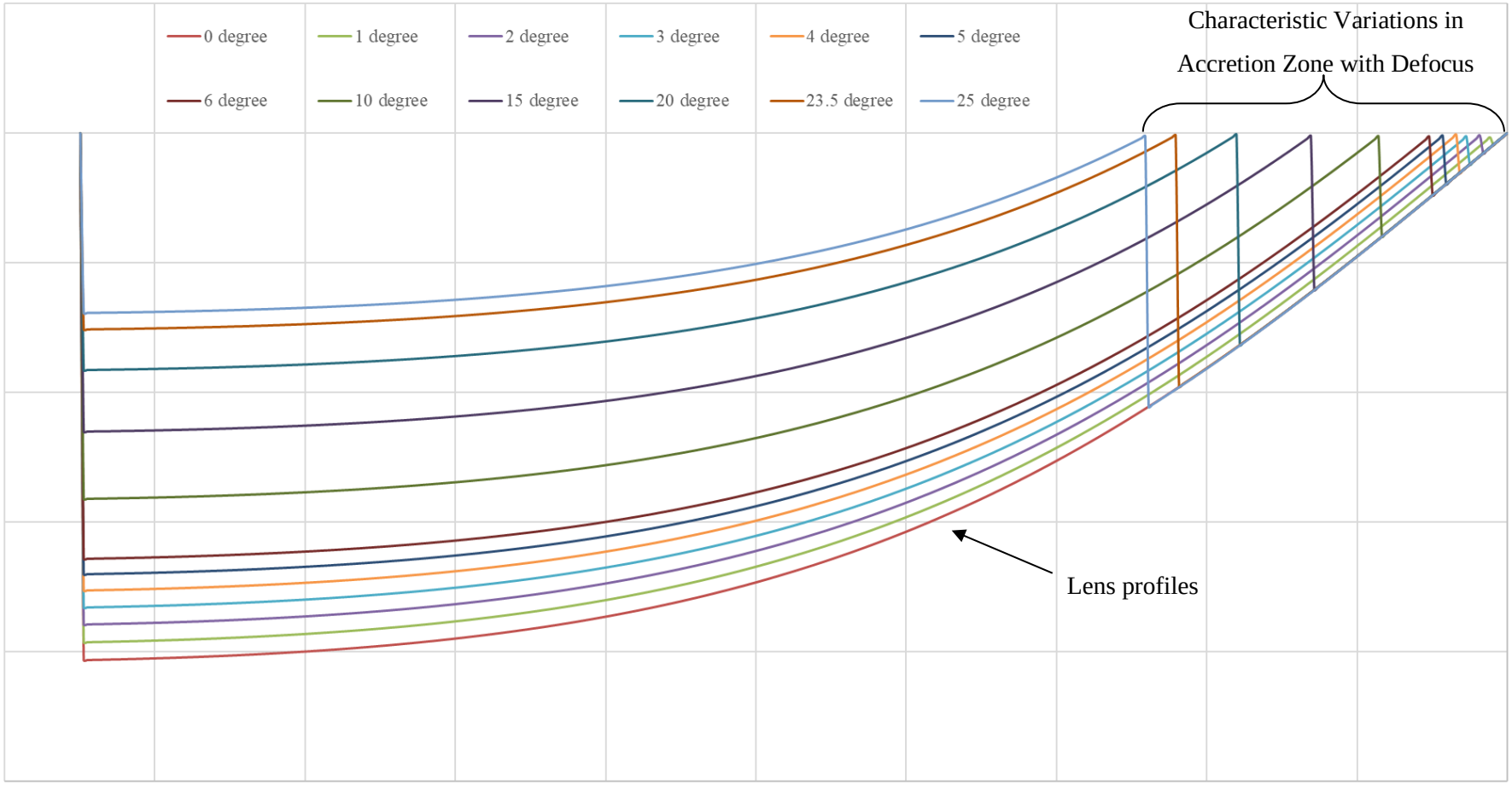

Figure 3-27 – Variation in the length of the accretion zone with varying levels of lens defocus

3.8 Design for prototype manufacture

The final stage in the optical design phase was to choose a lens profile which could be readily manufactured for the experimental proof of concept prototype. Given the overall dimensions required, the resolution of the lens profiles and the specified material requirements, this stage proved to be a challenge. The lens with the greatest improvement over the CFFLAB design was the 6^{o} defocussed fast Fresnel lens however complications around the design of the accretion zone, the transition from the defocussed lens back to the conventional lens, caused some practical issues. Essentially, as a fast Fresnel lens is defocussed the prism height towards the centre of the lens reduced below the minimum value which could be manufactured. In order to prevent a central area of the lens (about the optical axis) becoming non-active, once the prism height dropped below the minimum threshold that section was replaced by the equivalent CFFLAB span. This accretion process was crude but effective and optimising that transition is an interesting area for future study but in the case of the 6^{o} defocussed fast Fresnel lens the transition from low prism height as it tended to zero back to the conventional profile proved surprisingly difficult. After an extended period of communication with Glyndŵr Innovations Ltd, the manufacturer of the prototype lens, a compromise was reach and the profile most suited to the high precision milling machine's tolerance and within the optimal range for investigation was the 5^{o} defocused fast Fresnel lens.

3.8.1 Energy flux distribution profile of the 5º defocused fast Fresnel lens augmented baseline design

With the design finalised it was possible to generate a detailed comparison of the energy flux distribution profile between the CFFLAB and the 5º defocused fast Fresnel lens augmented baseline (DFFLAB) across the designed collection window. The energy flux distribution across the absorber plane was modelled using 5000 incident rays with an absorber resolution of 100 components. The profiles presented from Figure 3-28 to Figure 3-33 provide a clear visualisation of how the energy flux migrates across the absorber plane for both the CFFLAB and the 5º DFFLAB at 1º increments up to and including the design limit of 20º. Of particular note within the first 5 degrees is the reduction in peak energy flux at a relatively small focal point for the defocused lens. Although not within the remit of this thesis, an evaluation into cell performance as a direct consequence of hot spot reductions may have some merit.

In terms of overall energy flux distribution, the benefits of defocusing the lens reduce significantly as the incidence angle increases towards the design limit due in part to the increasing influence of the accreted region, which generates more unpredictable behaviour within the design.

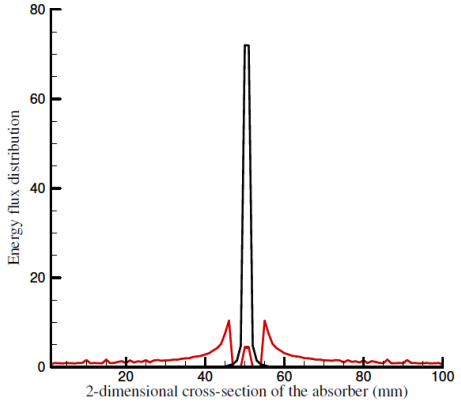

(a)

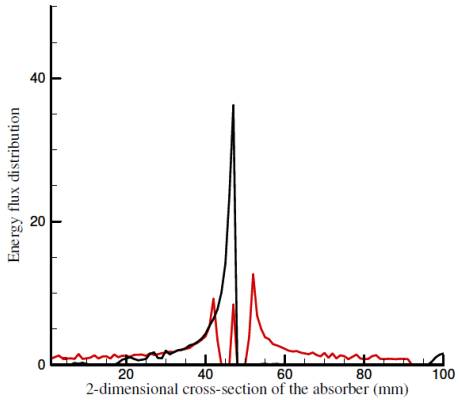

(c)

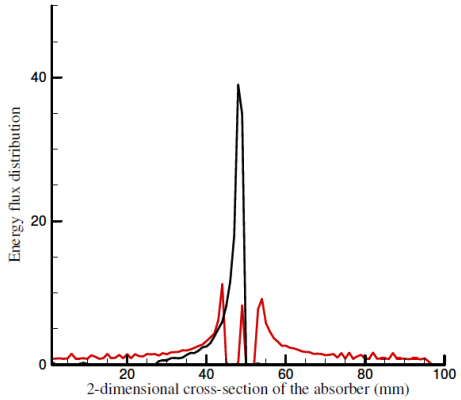

(b)

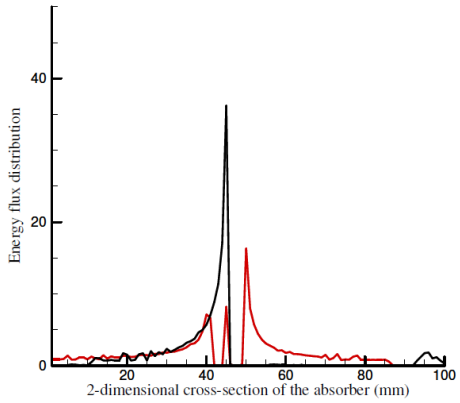

(d)

Figure 3-28 – 2-Dimensional energy flux distribution across the absorber for the CFFLAB (black) and the 5º DFFLAB (red) collectors at varying degrees of incidence angle: (a) 0º, (b) 1º, (c) 2º, (d) 3º

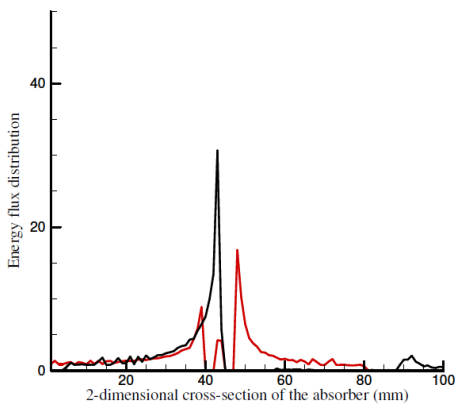

(e)

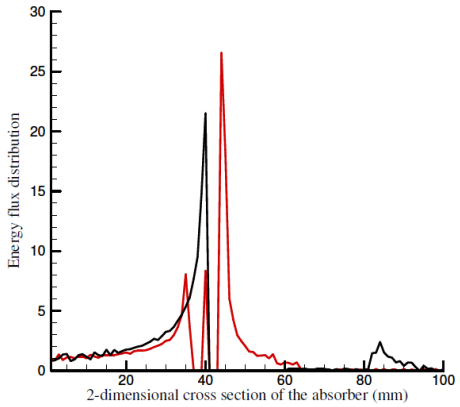

(g)

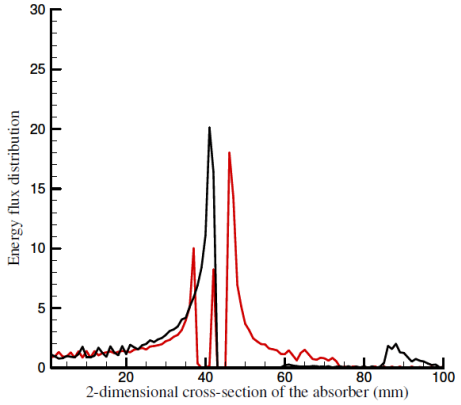

(f)

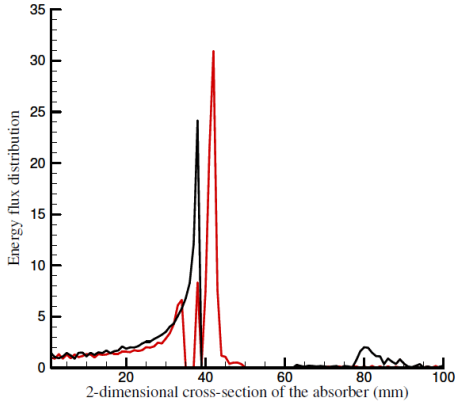

(h)

Figure 3-29 – 2-Dimensional energy flux distribution across the absorber for the CFFLAB (black) and the 5º DFFLAB (red) collectors at varying degrees of incidence angle: (e) 4º, (f) 5º, (g) 6º, (h) 7º

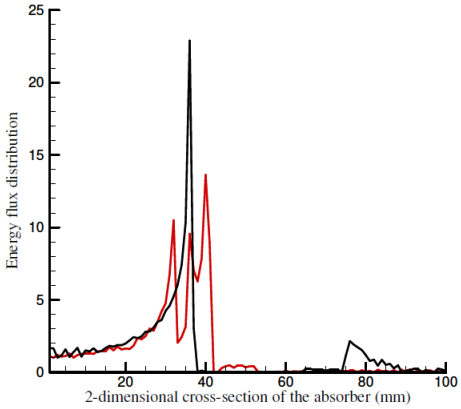

(i)

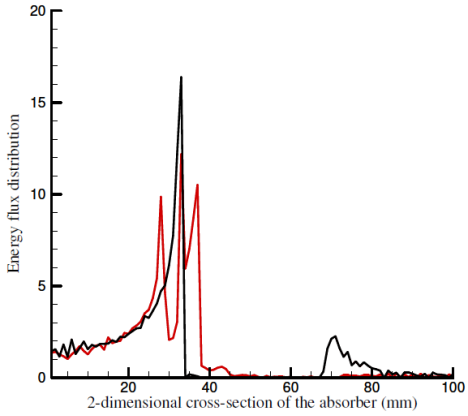

(k)

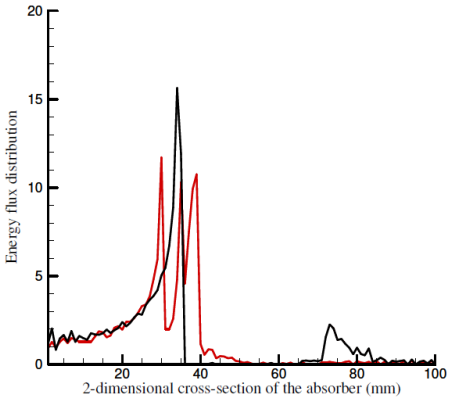

(j)

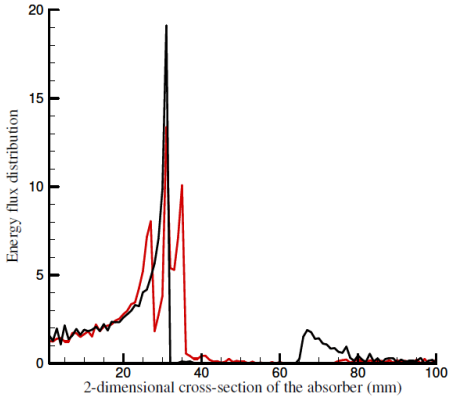

(l)

Figure 3-30 - 2-Dimensional energy flux distribution across the absorber for the CFFLAB (black) and the 5º DFFLAB (red) collectors at varying degrees of incidence angle: (i) 8º, (j) 9º, (k) 10º, (l) 11º

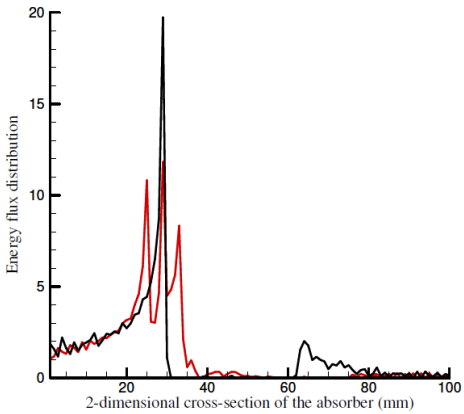

(m)

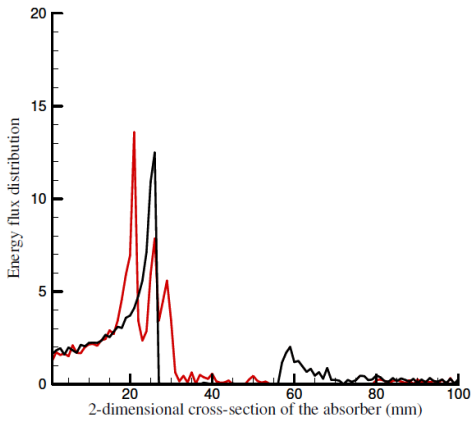

(o)

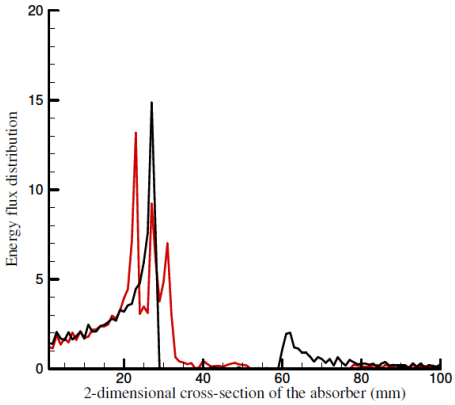

(n)

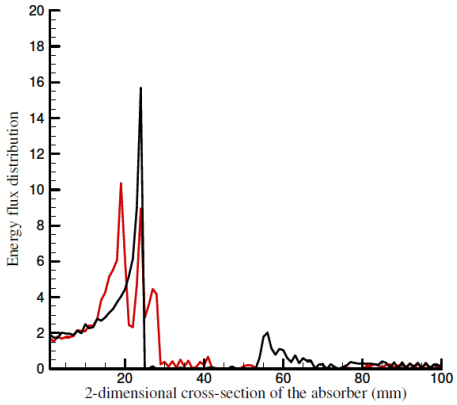

(p)

Figure 3-31 - 2-Dimensional energy flux distribution across the absorber for the CFFLAB (black) and the 5º DFFLAB (red) collectors at varying degrees of incidence angle: (m) 12º, (n) 13º, (o) 14º, (p) 15º

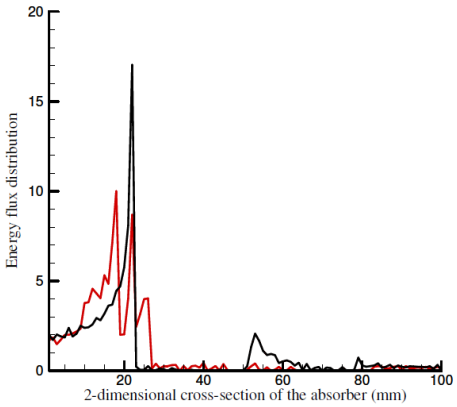

(q)

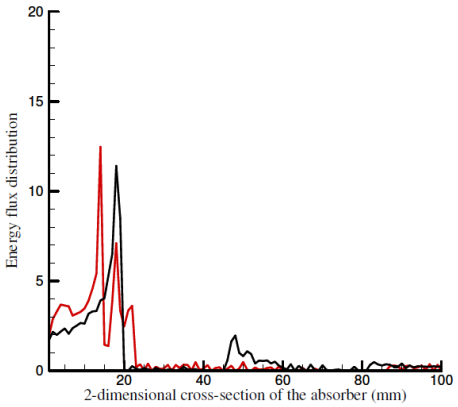

(s)

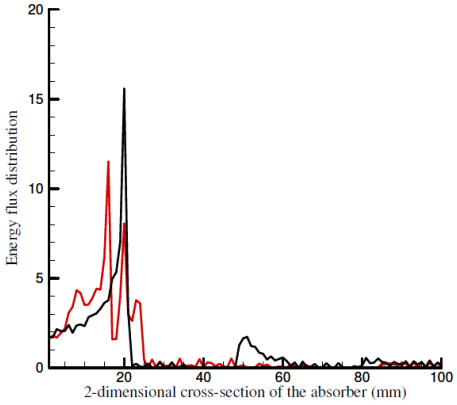

(r)

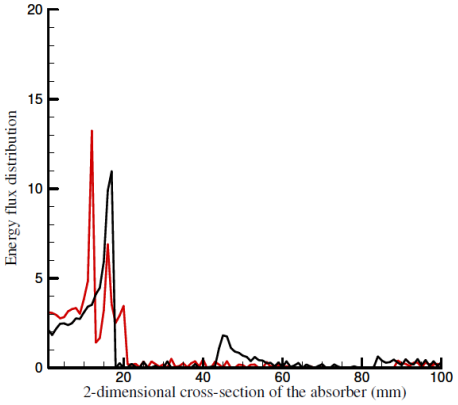

(t)

Figure 3-32 - 2-Dimensional energy flux distribution across the absorber for the CFFLAB (black) and the 5º DFFLAB (red) collectors at varying degrees of incidence angle: (q) 16º, (r) 17º, (s) 18º (t) 19º

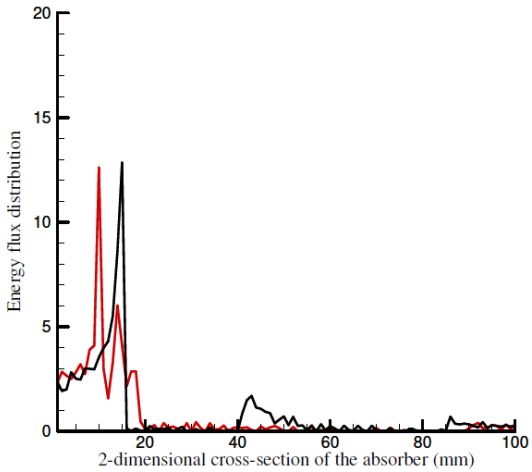

(u)

Figure 3-33 - 2-Dimensional energy flux distribution across the absorber for the CFFLAB (black) and the 5° DFFLAB (red) collectors at varying degrees of incidence angle: (u) 20°

3.9 The effect multiple absorbers

A detailed analysis of the effect of multiple absorbers was also carried out as part of the optical simulation phase of the design. The optical model was expanded to encompass five side-by-side lens profiles and five absorber planes in an attempt to expand the modular system up to the dimensions of a typical double-glazed window. This system was then modelled using 5000 rays of incident light to evaluate whether any increase in performance could be attributed to the presence of adjacent cells i.e. a modularity efficiency. However, the results of those simulations have been excluded from the modelling analysis for two reasons:

1. Additional energy collection was incidental and not a consequence of the optical design intent and as such had limited value.
2. Although improvements in overall optical efficiency and angular acceptance were seen when the number of absorbers was increased the gains were marginal (1-3% across the incident range) and detracted from the overall objective of the lens design.

3.10 Chapter Summary

This chapter has introduced the basic concepts in applied nonimaging optical design and the evaluation of refractive elements using both first principle methodologies and ray tracing software. The design criteria for the developed system was then outlined and the performance of a conventional fast Fresnel lens augmented collector, in terms of angular acceptance and optical efficiency, was presented against a baseline design. The comparison clearly demonstrated that by adding the fast Fresnel to the baseline design, energy collection during the design window for this system was greatly increased. The baseline comparison also identified a number of potential areas of improvement for the developed system which prompted the examination of two additional avenues of investigation; can the performance of the CFFLAB collector be improved with a greater lens resolution and/or can the collection window be improved by adjusting the lens profile to reduce reflection losses and delay TIR while maintaining the f-number of the lens over a predefined absorber area.

There was relative parity in the optical performance of the CFFLAB collector in terms of energy collected between the resolution ranges of 100 microns to 275 microns. However, with the decreased resolution of prism widths in excess of 300 microns the behaviour of the lens became less stable and as such didn't justify the additional manufacturing costs associated with the excess material removal. At the other extreme of the lens designs the rapid reduction in prism height made the manufacture of the 100 micron and 125 micron lenses unfeasible. Those practical consideration in combination with the prototype manufacturing process, number of prisms required and percentage of cut material led to the selection of a 150 micron lens resolution.

The 150 micron lens was then defocused in an attempt to improve the performance of the CFFLAB collector by reducing reflection losses and delaying the onset of total internal reflection (TIR). The following levels of defocus were investigated; 1^o, 2^o, 3^o, 4^o, 5^o, 6^o, 10^o, 15^o, 20^o, 23.5^o and 25^o with 0 defocus representing the CFFLAB collector. At a 0^o incidence angle the optical efficiency of the collector increased by 19% at a defocus of 10^o primarily as a result of; a reduction in TIR losses from the outer limit of the lens, reductions in the material attenuation (reductions in prism height) and rounding errors in the prism design. This value is somewhat suspicious as the expected optical efficiency at a perpendicular plane of incidence shouldn't be heavily impacted by these issues. The remaining 5-degree stepwise changes in incidence angle up to and including the design limit presented a variable increase in lens performance both in terms of optical efficiency and angular acceptance however the trend for the lenses with a defocus of less than 10

degrees was an improvement on the CFFLAB's performance. Overall, the design with the maximum improvement in performance, averaged across the collection range, was the 6° defocussed fast Fresnel lens with a 4.44% increase. This design was taken forward to a prototype manufacturer but ultimately the modifications required to produce this lens prevented the design from being used and the 5° defocused fast Fresnel lens with a 4.21% increase in efficiency was selected instead.

The practicalities associated with the manufacture of the proof of concept prototype lens have also been included at various points through the design process and have heavily influenced the final lens design. These practical considerations were a useful means of keeping the optical modelling focused on a practical final design, the 5° defocused fast Fresnel lens.

After the final decision had been made on the lens design being brought forward to manufacture, it was possible to delve into the simulated performance more deeply. The absorber flux mapping was carried out at 1 degree increments up to and include the design limit (an acceptance half angle equal to ±20°). The developed system shows a reduction in the peak energy flux on the absorber, compared to a conventional fast Fresnel lens, for incidence angles from 0 to 4°. The significance of this finding is relatively arbitrary given the variations in energy distribution over the subsequent range of 5 to 20°. However, the optical mapping graphs provide a clear understanding of the expected energy distribution across the physical solar cells in the prototype collector (about the optical axis) and serve as a means to identify an area for further refinement in the evolution of defocused fast Fresnel lens design.

Finally, the effect of adding multiple absorbers was briefly discussed and the reasons for excluding the results from this piece of work were explained.

Collector Design and Fabrication

4 Collector Design and Fabrication

4.1 Introduction

This chapter describes the design, component selection, fabrication and assembly of both the baseline and the accreted 5º defocused fast Fresnel lens augmented baseline (DFFLAB) prototype modular, building integrated solar collectors and the temperature sensor array used during the experimental phase. The design focuses on the functionality and flexibility of the collectors to enable a full range of experimental testing to be carried out to both validate and refine the predicted optical performance of the systems described in chapter 3.

4.1.1 Manufacture of the accreted 5º defocused fast Fresnel lens

The finalised accreted 5º defocused fast Fresnel lens design, as described in chapter 3, was manufactured by Glyndŵr Innovations Ltd, Wales using their high precision diamond cutting Computer Numerical Control (CNC) facilities (Figure 4-1). Due to the sensitive nature of the technology and control processes involved only a brief overview of the manufacturing process can be provided in this thesis with the permission of Glyndŵr Innovations Ltd.

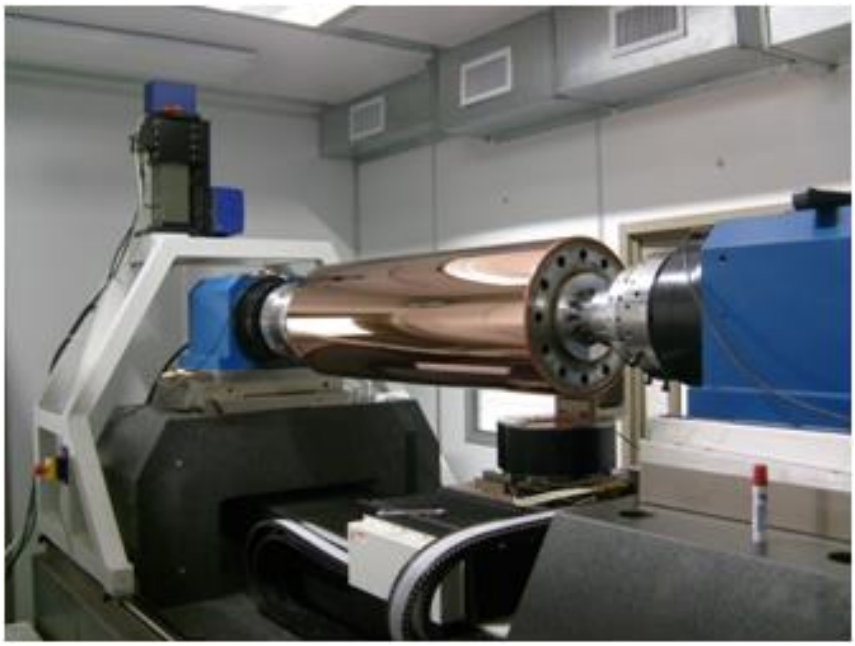

Figure 4-1 – High precision diamond cutting CNC machine in its climate controlled and vibration isolated protective environment.

The 5 axis CNC machine was located in a High-Efficiency Particulate Air (HEPA) filtered, climate controlled, class 10,000 clean room. Where the particulate matter suspended in the air, equal to or greater than 0.5 microns in length, was limited to 10,000 per ft^2 and the temperature within the space was maintained to within ±0.1 ^oC. The clean room itself was situated in a temperature-controlled laboratory (±1 ^oC) and isolated from the room, the building and the external environment using a series of anti-vibration mountings. All of these precautions allowed the machine to cut the five consecutive, side by side accreted 5^o defocused fast Fresnel lenses directly into one sheet of 0.75 mm thick PMMA of dimensions 1 m x 0.5 m at an accuracy of less than 1 micron, a typical resolution of less than 1 nm and a repeatability of less than 75 nm. The PMMA sheet was mounted on a rotating cylindrical drum with a length of 1 m and a circumference of 0.5 m by gluing both longitudinal ends of the PMMA sheet to the drum along its length at a fixed point ensuring a tight fit around the rest of the drum. Once the PMMA sheet had been properly mounted 1 micron of the PMMA material was removed from the outer surface of the sheet to create a clean, uniform optical surface on which to begin the lens manufacture.

As previously mentioned the lenses in chapter 3 were designed using practical constraints of this manufacturing process and although this hi-tec high precision manufacturing system sounds ideal some issues were experienced during the prototype manufacture. Figure 4-2 shows how the experimental nature of this prototyping procedure can affect the quality of the final product. In this case one of two manufacturing errors led to the failure in the successful production of an optical grade lens either separately or in combination. It is possible that the seal between the sheet of PMMA and the mounting drum was not fully tight throughout its entire length or that there was a fluctuation in the temperature regulation system during the cutting process allowing the PMMA sheet to expand and warp while the diamond cutter was still removing material.

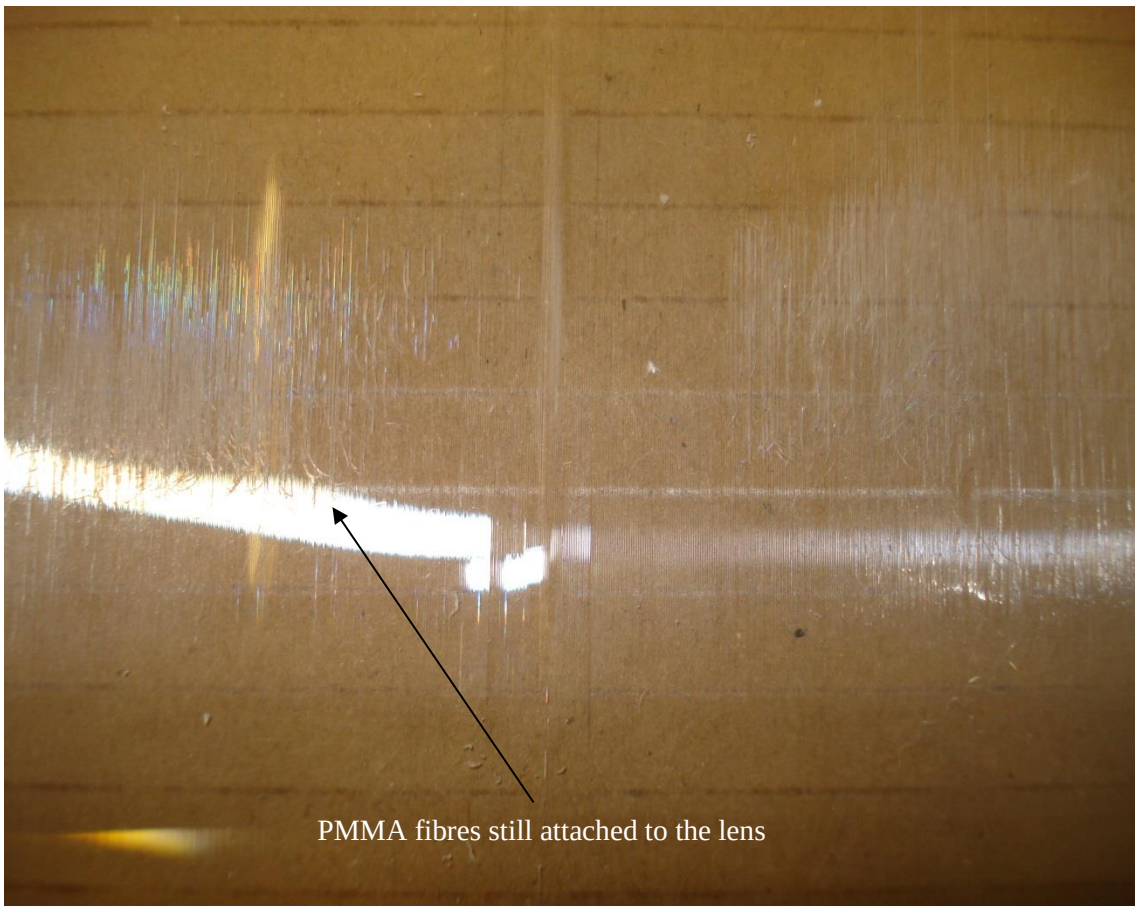

Figure 4-2 – Defective Fresnel lens after the cutting process with strands of PMMA still attached to the surface of the lens

Once the lens was successfully manufactured it was bonded to a 3 mm pane of Perspex Clear using Tensol 70, a thixotropic two stage PMMA cement with a refractive index of 1.49. Due to the large surface area of the lens and the inherent difficulties associated (entrapped bubbles etc) with bonding a Fresnel lens to Perspex at this scale it was decided to bond the full 1 m x 0.5 m Fresnel lens to the outer glazing pane only around the edges of the lens where the supporting frame would act to hide the bonded areas. This approach has both positive and negative consequences. The fact that the lens was not in direct contact with the outer glazing introduced a small PMMA-air-PMMA interface which affected the optical performance of the system creating an additional optical loss at each of the interfaces of approximately 4%. This was however the preferred option as it could be adequately anticipated and calculated whereas the alternative option of coating the entire 1 m x 0.5 m area with a bonding solution could have led to two additional problems which couldn't be readily accounted for: an unevenness in the bonding solution which could alter the designed ray path through the system and the aforementioned bubbling leading to an speckled finish on the lens and additional assumptions about how much light was subjected to the losses associated with the PMMA-air-PMMA interface.

4.1.2 Manufacture of the absorber arrays

The collector's absorber plane consisted of 5 series connected PV arrays each consisting of 3 series connected Sunways monocrystalline 156 (AH50-H) Solar Cells. The dimensions of the solar cells, as bought from the manufacturer, were too big for the designed collector (156 mm x 156 mm) and were in a pseudo-square format with a combined area of 4.41 cm^2 cut from the corners (Anon, 2013a) In order to facilitate the absorber requirements of the designed system and create a uniform absorber area the cells were cut into 95 mm x 156 mm strips using the Universitat de Lleida's custom-built manual feed PV cell cutter. This was achieved by cutting the cells twice along their longitudinal axis as show in Figure 4-3.

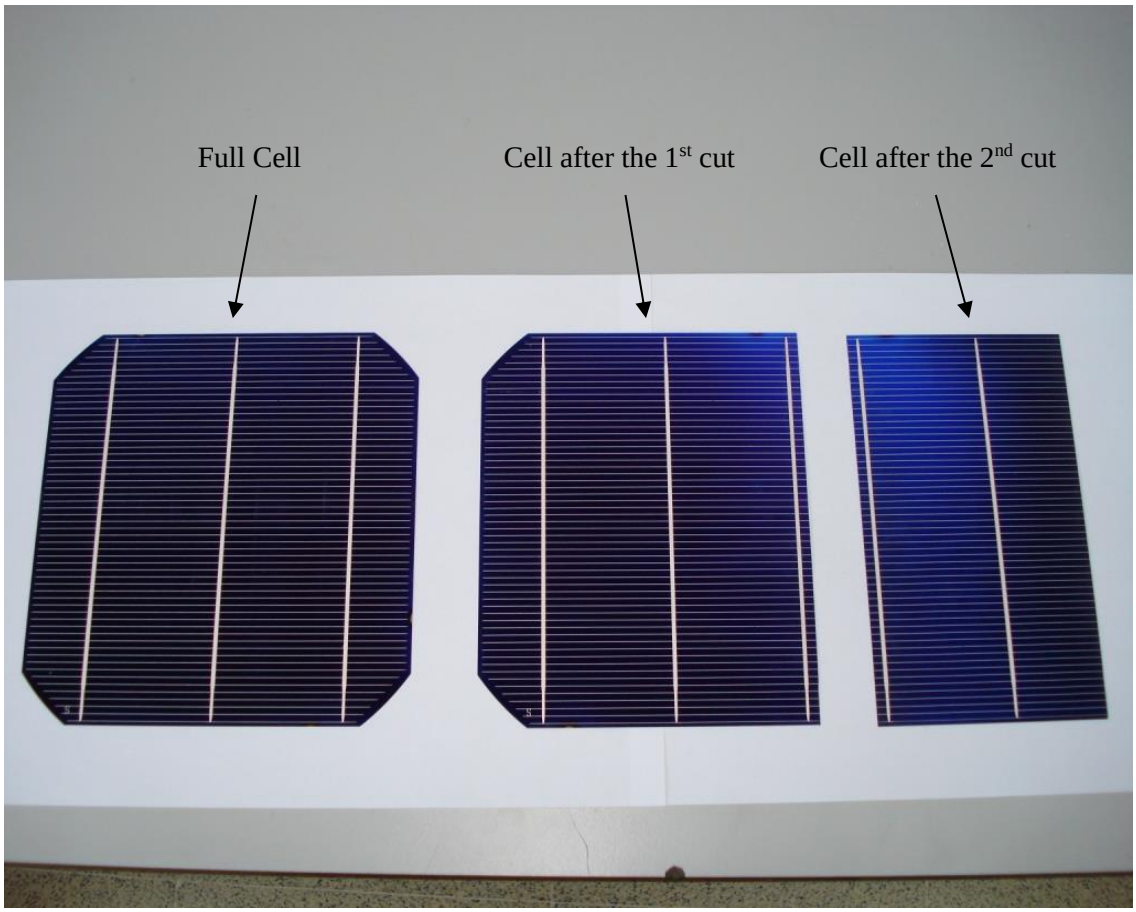

Figure 4-3 – Phases in the PV cell cutting procedure: full cell (left), 1st cut (centre) and 2nd cut (right)

The PV cell cutter (Figure 4-4) used a 0.3 mm thick diamond cutting blade propelled by a pressurised air motor to 25,000 revolutions per minute. The PV cell mounting bed utilized a manually adjustable guide for accurate and repeatable cutting and the PV cells were held in place

by creating a partial vacuum underneath both sides of the mounting bed throughout the cutting process. Once a PV cell was fixed in place on the mounting bed the motor was initiated and allowed to attain full speed before the PV cell was manually pushed through the diamond cutting blade at a slow and steady pace to ensure that the cutting process produced repeatable high quality results (Figure 4-5).

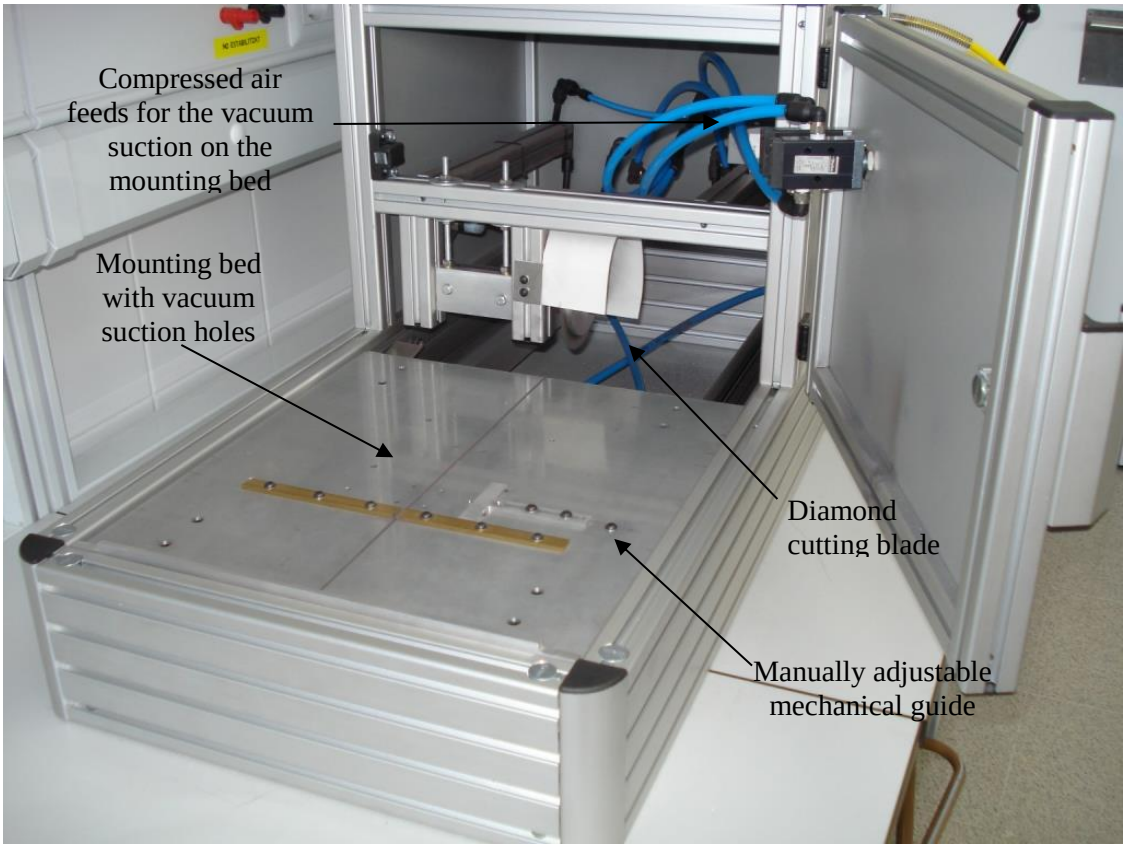

Figure 4-4 – Universitat de Lleida's manual feed Cell Cutter 210

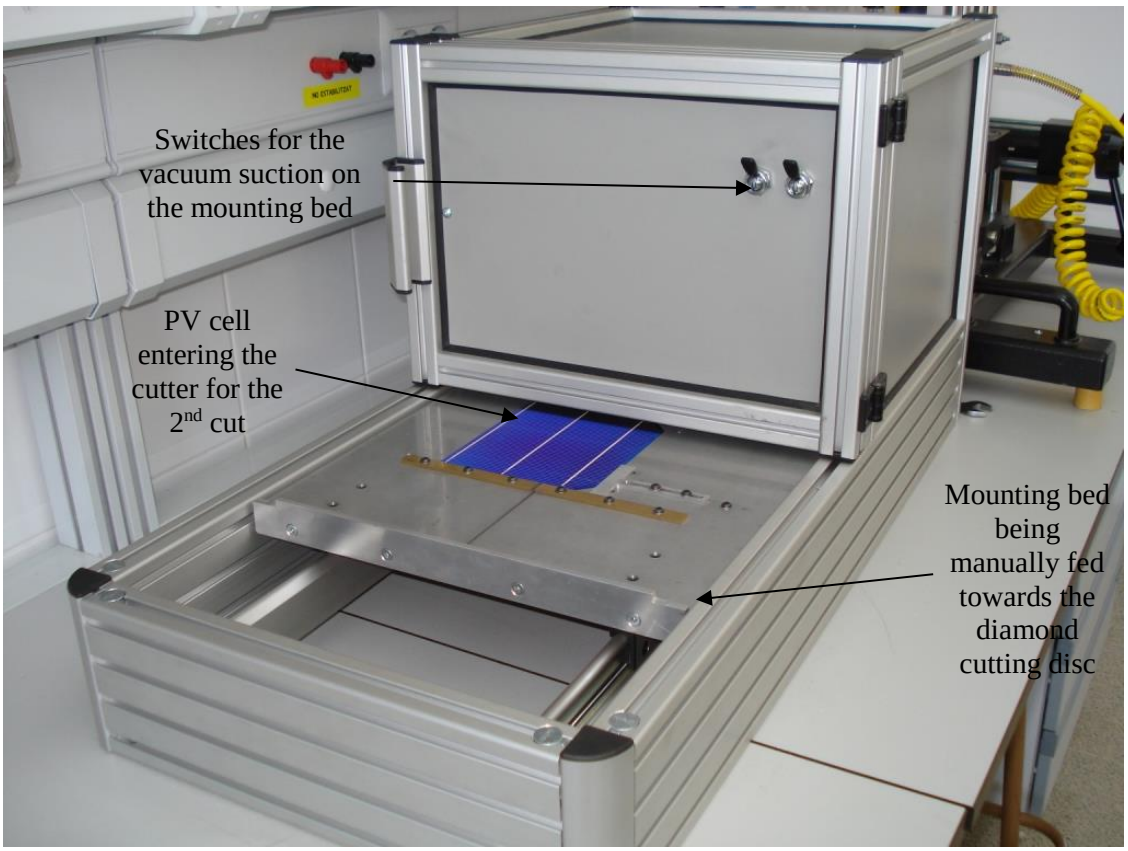

Figure 4-5 – PV cell fixed on the mounting bed and being advanced towards the diamond cutting blade

Figure 4-6 shows a typical example of the high quality achieved by the Cell Cutter 210. Each of the cuts produced a uniform edge with negligible visible or detectable damage to the PV cells providing an absorber of the required dimension with an asymmetric busbar configuration (Figure 4-3, right).

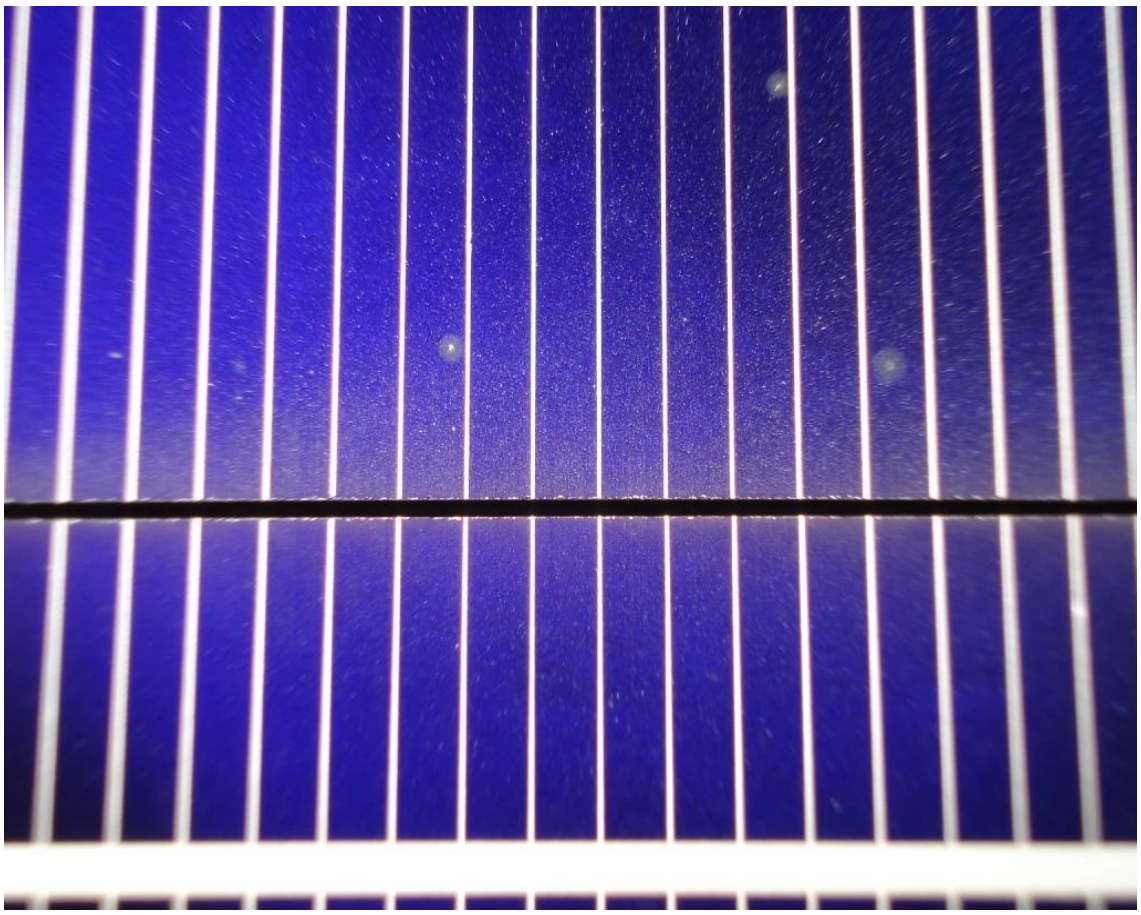

Figure 4-6 – A generic example of the cut quality achieved by the Universitat de Lleida's manual feed Cell Cutter 210 (busbar dimensions = 1.54 mm for comparison).

Once cut to the appropriate size for the designed system the PV cells were then soldered together in series to form the 5 absorber arrays (Figure 4-7). The electrical interconnections were formed using a copper-based soldering ribbon 2 mm wide and 0.25 mm thick designed specifically for joining PV cells which was attached along the length of the busbars, front and back, to ensure there was a constant electrical resistance throughout the system.

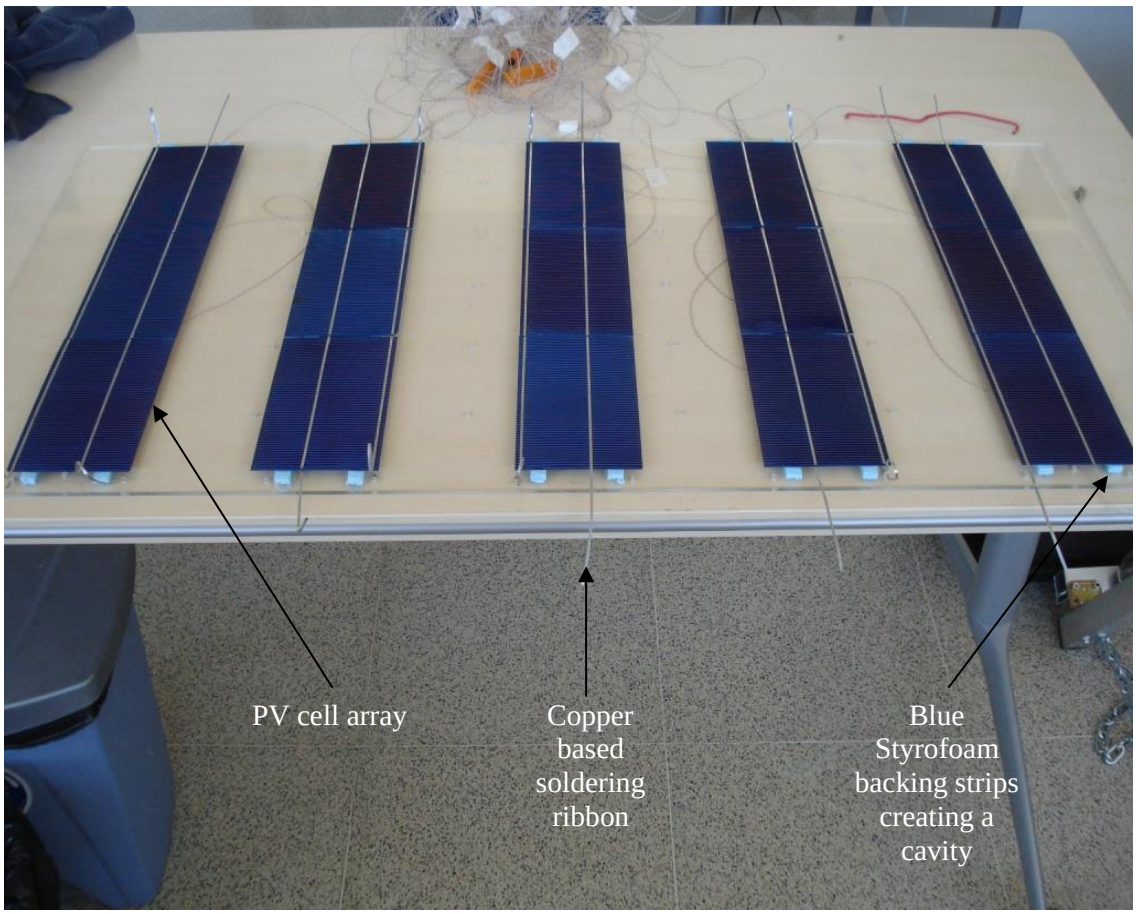

Figure 4-7 – The 5 absorber arrays connected with soldering ribbon and mounted on blue Styrofoam backing strips

4.1.3 Manufacture of the PV convective cavity backing support

The potential for the PV cells to overheat in an enclosed module was an obvious concern early on in the conception of this design and has led to both potential diversifications in the application of the system and allowed for innovative solutions to be explored. In order to encourage the development of convective heat transfer cells to prevent damage to the PV absorber array and assist in cooling the PV cells between tests two 1 cm wide and 0.5 cm thick Styrofoam backing strips were mounted between the PV arrays and the backing pane of Perspex (Figure 4-7). The Styrofoam was bonded to the Perspex backing pane using Loctite® 595, a thermally conductive electrically insulating thixotropic paste, so that the electrical properties of the cells were not impeded as a result of maintaining a characteristic heat transfer environment. The incorporation of the backing strips was also intended to act as a buffer to protect the cells from the structural flexing which is encountered as the relatively thin sheet of Perspex responds to an increase in temperature and to provide a small amount of room to connect the temperature sensors.

4.1.4 Manufacture of the supporting frame

The collector was constructed from 3 mm Perspex Clear and supported in place by 6 mm cavity 20 mm x 20 mm Bosch Rexroth Aluminium strut framing cut to length. Although BK7 glass would have been the material of choice for the collector panes it was discounted for two practical reason: the slightly difference in the refractive index of BK7 glass could not have been built into the ray trace simulations and cutting small holes in glass for the thermocouples is more difficult than cutting into Perspex. Figure 4-8 shows the basic structure of the supporting frame. The white backing pane, although not part of the collector design, was inserted to highlight the holes cut into the PMMA to facilitate the thermocouple temperature sensors and the release of excess heat within the cavity.

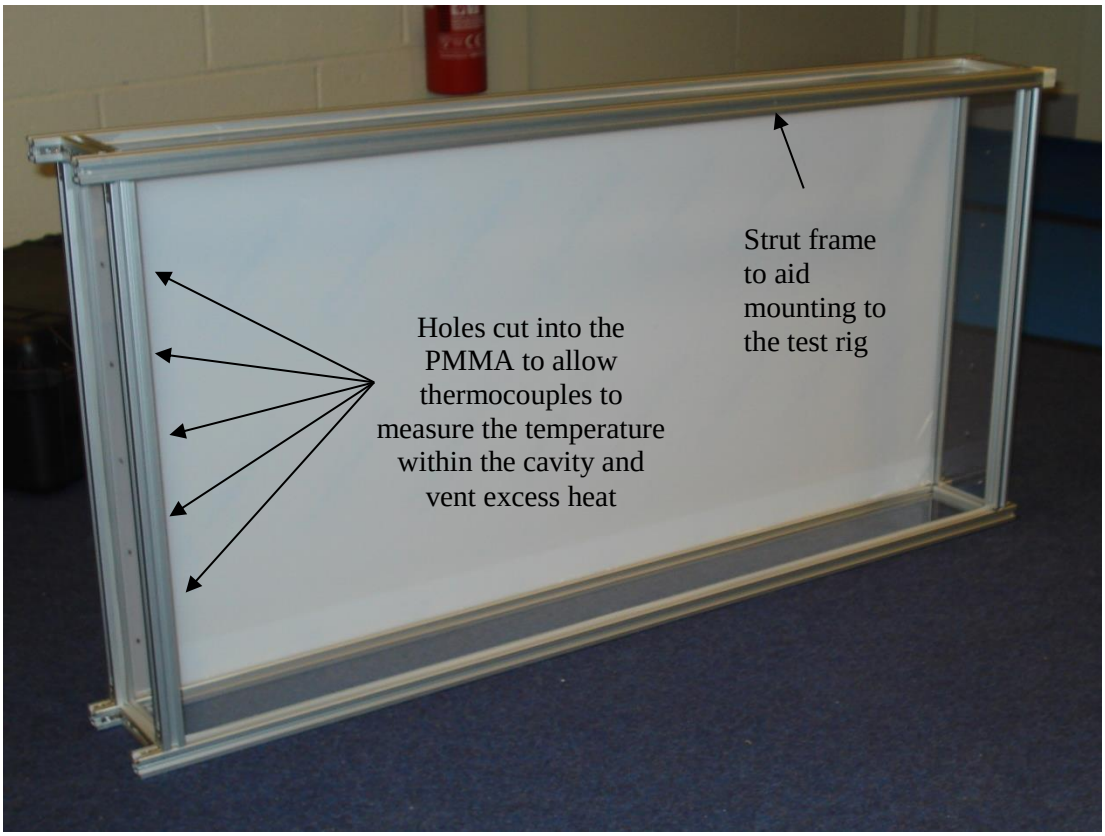

Figure 4-8 – The collector's supporting frame

Once installed into the Aluminium strut framing the panes were secured in place using angled bracket and the system was sealed using rubber seals inserts.

4.1.5 Thermocouple array

The array of temperature sensors was manufactured in-house from two different diameters of class 1 Type TX (Copper/Constantan) thermocouple extension cables encased in Pulverised Fuel Ash (PFA) insulation: 0.2 mm and 0.5 mm. The finer 0.2 mm sensors were used to measure the back temperature at the centre of each of the 15 individual PV cells in the absorber array and the larger, more robust, 0.5 mm were encased in a metallic block and used as the primary and backup ambient temperature sensors. The type TX thermocouple extension cables (properties presented in Table 4-1) were cut to size, the PFA insulation was stripped back slightly at either end and a temperature sensing junction was made by welding the negative Constantan cable to the positive Copper cable using a foot pedal operated L60+ thermocouple and fine wire welder.

Table 4-1 – Type TX thermocouple cable properties

Type	Tolerance Class		Cable Temperature Range	Measuring Junction Temperature
	1	2		
TX	± 30 µV (± 0.5 ºC)	± 60 µV (± 1.0 ºC)	-25 ºC to + 100 ºC	300 ºC

(Adapted from Anon, 1993)

The thermocouples were then visually inspected to ensure a clean weld had been achieved before the junctions were encased in a thin film of Araldite® Precision, a two-stage adhesive comprised of a resin and a hardener, to protect the thermocouples during handling and the evaluation process. At this point the thermocouples were labelled and connected to a portable Delta-T DL2e data logger fitted with 4 LAC1 15-channel multiplexer cards giving a capacity of 60 channels with an additional two in-build digital channels. The data logger was programmed to record the output of each of the thermocouples (2 x 0.5 mm sensors and 15 x 0.2 mm sensors) every minute at a typical capture rate of 10 channels per second. The output from each of the thermocouples was then referenced against the output of a cold junction and the digital electrical impulse from each of the thermocouples was converted into its corresponding temperature in degrees Celsius (ºC) using a conversion table built in to the data logger software. Finally, the cells were fixed to the centre of the underside of each of the PV cells using additional Araldite® resin.

4.1.6 Physical appearance of the baseline and DFFLAB collectors

The physical appearance of the completed baseline and DFFLAB collector configurations are shown from the front in Figure 4-9 and the appearance of the DFFLAB collector configuration is shown, from two non-perpendicular viewpoints, in Figure 4-10. In relation to the criteria outlined by Luque and Hegedus (2011) in chapter 1 for the judgement of the aesthetic qualities of building integrated photovoltaic systems the developed DFFLAB collector has been designed to be as inconspicuous as is reasonably practicable while still being functional as both a solar collector and passive solar shade. To be constructed using the materials, and mimicking the aesthetics of, an ordinary window. The modular design of the collector is designed to be gridular by nature allowing the collector to be easily integrated and altered to match the building grid lines. The collector design has, by consideration of the previous factors and the definition by Luque and Hegedus (2011), been well engineered and is innovative.

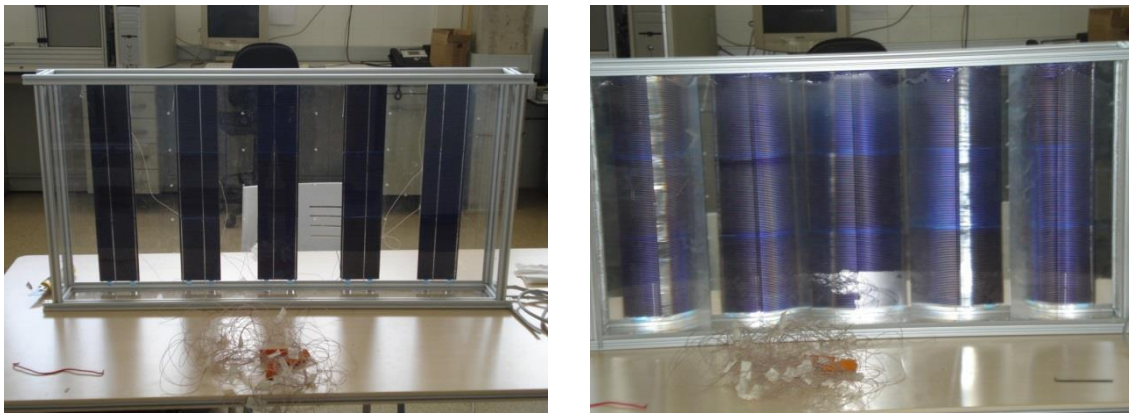

Figure 4-9 – Comparison between Baseline (left) and DFFLAB (right) collector configurations at a perpendicular viewpoint

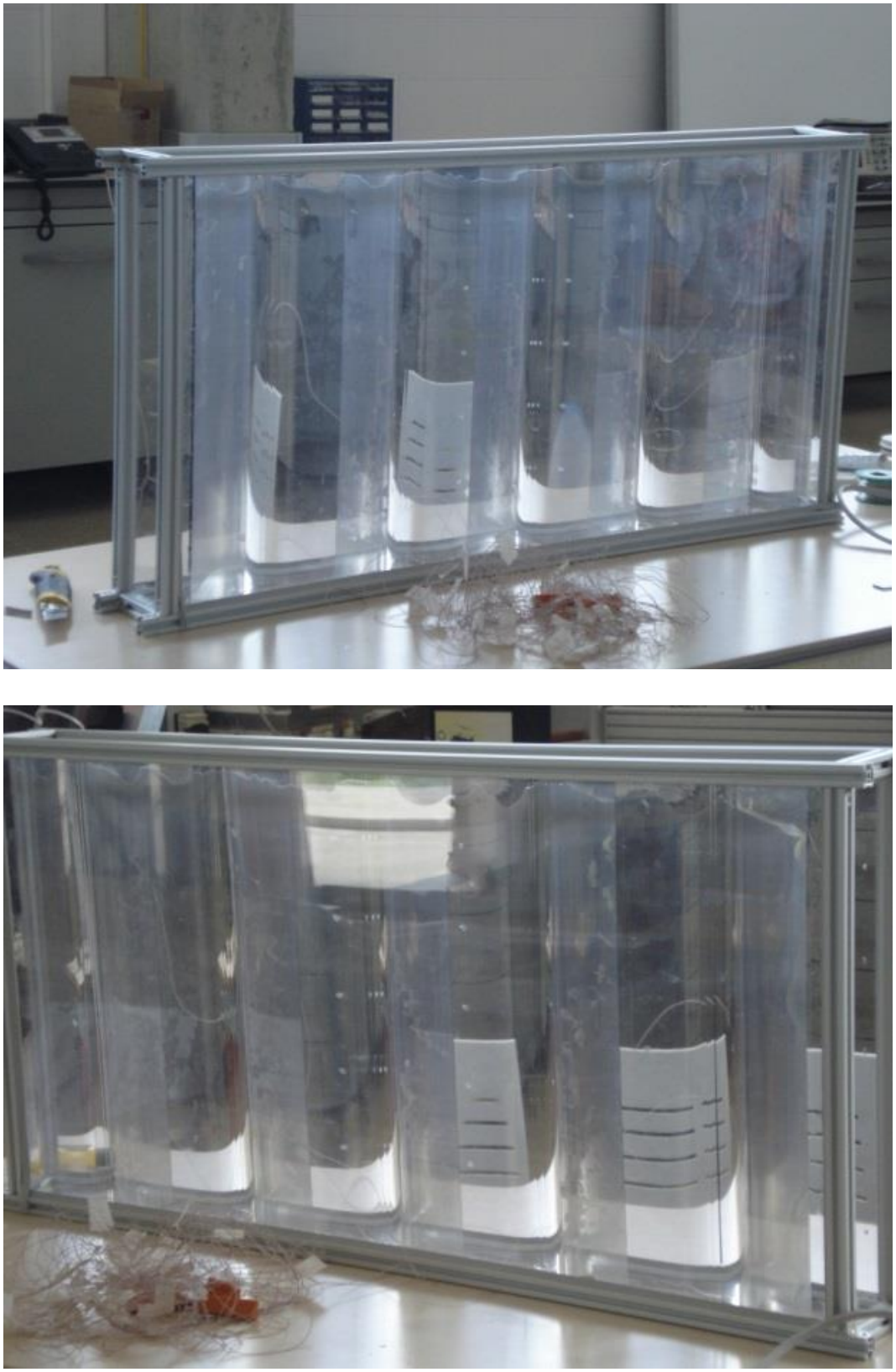

Figure 4-10 – DFFLAB collector at non-perpendicular viewpoints completely obscuring the absorber array

4.2 Assembly of the complete test platform

The completed collector module was then fixed to a 2-dimensional solar tracker at the Universitat de Lleida's rooftop test facility in Catalunya, Spain (described in chapter 5) using angular mounting brackets at each of the corners with a nut and washer inserted into the strut framing cavity and tightened in place. The collector was mounted with the PV cells orientated in an east-west alignment because of greater accuracy and speed in the control of the vertical motor.

4.2.1 Experimental test facility

The experimental testing of all three collector configurations (uncovered, covered with the Perspex sheet (baseline) and finally with the 5º Defocused fast Fresnel Lens (DFFL)) was carried out using the 2-axis solar tracker at the Universitat de Lleida's rooftop testing facility (Figure 4-11) in Cataluña, Spain (Latitude 41.6167º N, Longitude 0.6333º E) from March to June 2012.

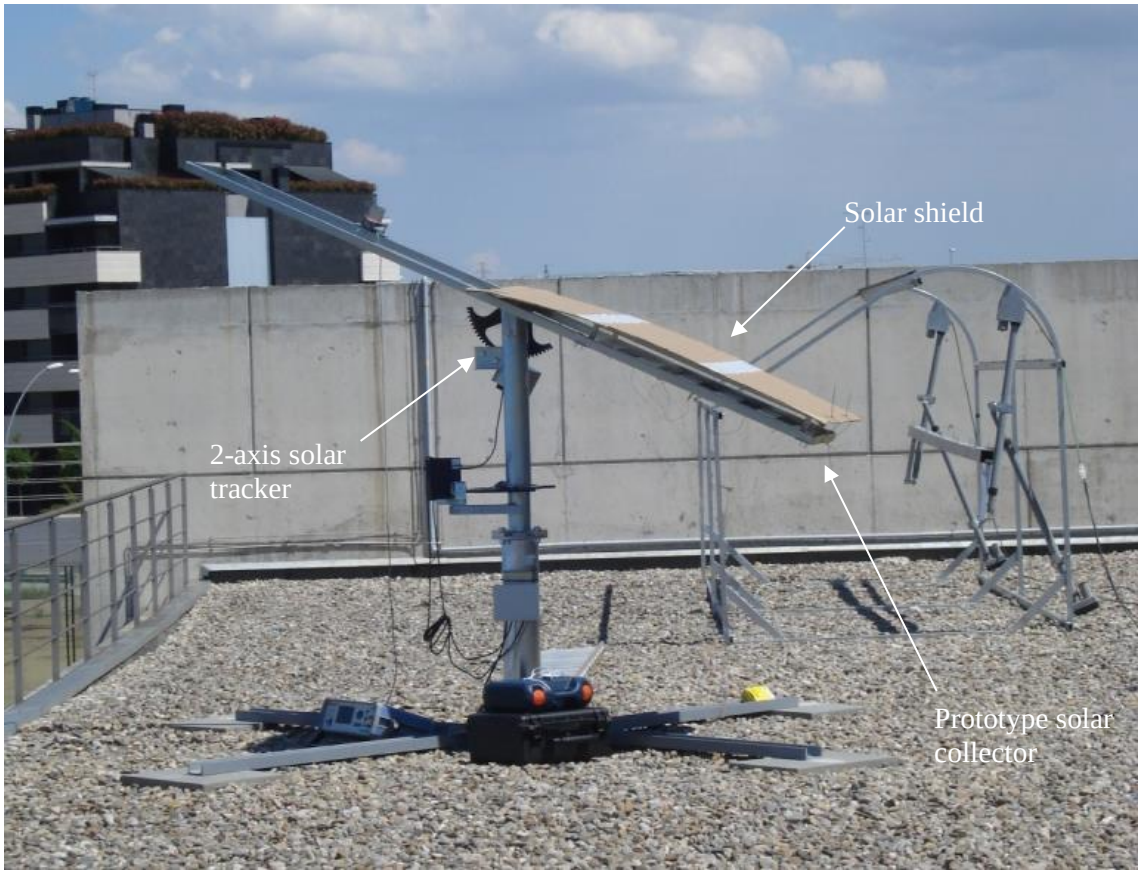

Figure 4-11– Rooftop testing facility at the Universitat de Lleida

4.2.2 2-axis solar tracker

A 2-axis solar tracker (Figure 4-12 (a) and (b)) is an electronically controlled mechanically driven mounting platform for a solar energy collector. Its function is to keep a solar collector in a plane perpendicular to the angle of the sun by tracking the position of the sun in the sky using a combination of incident solar radiation data (captured by a PV feedback sensor) and a few input parameters (latitude, longitude etc). The inputs are interpreted by a controller module with a user interface (Figure 4-12 (c)) which drives two electric motors controlling the position of the collector mounting plane. The accuracy of the tracker shown in Figure 4-12 allowed for accurate measurements of both perpendicular and repeatable non-perpendicular collector orientations.

(a)

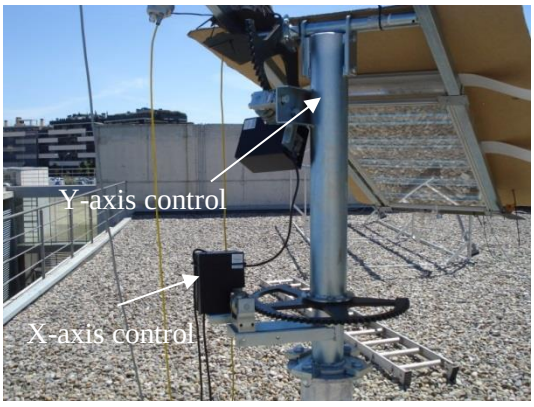

(b)

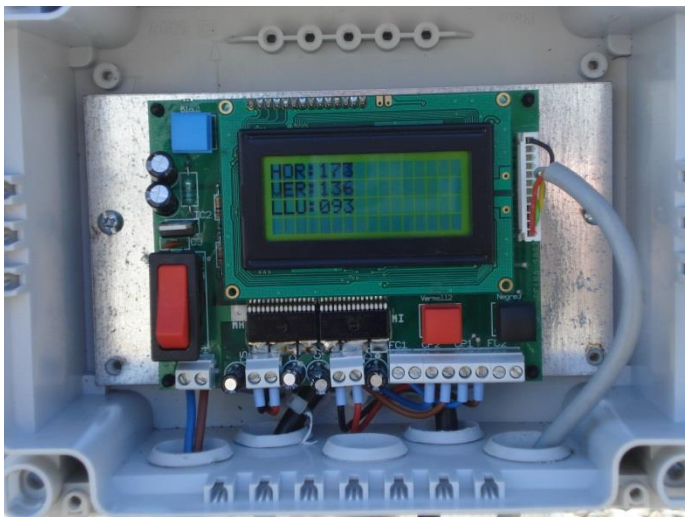

(c)

Figure 4-12 - Two axis solar tracker: (a) 2-D tracker, (b) X and Y axis gearing and motor arrangements and (c) control interface

4.2.3 Data logging equipment

In total three data loggers were used during the outdoor experimental testing. Each of the standalone loggers was programmed and assigned to a different specific task. The time clocks on all of the loggers were then synchronised to allow for accurate data management.

4.2.3.1 Delta-T DL2e data logger

The DL2e data logger (Figure 4-13) manufactured by Delta-T Devices is a versatile, programmable and weatherproof field data logger which can be power by battery and left exposed to the elements. During the outdoor experimental testing the prototype collector was mounted on a 2-dimensional tracker. The 15 thermocouples attached to the cells of the collector's PV array and the ambient temperature sensor were connected to the weatherproof logger and remained outside for the duration of the test period. Before and after the experimental tests the logger was connected to a laptop computer and the acquisition of data was started and stopped, respectively. The collected data, stored as a compressed .dat file was then exported to the laptop, converted to a .csv file using Delta-T Devices' Dataset Import Wizard software and finally the .csv file was imported into Microsoft Excel for analysis.

Figure 4-13 – DL2e data logger

4.2.3.2 Campbell CR1000 data logger

Campbell Scientific describes the CR1000 data logger as *"a rugged instrument with research-grade performance"* (Anon, 2013b). During the outdoor testing programme the CR1000 was used to record the data from the pyranometer, pyrheliometer and secondary ambient temperature sensor (Figure 4-14). Once all of the connections were made and the unit was programmed it was covered to shield the connections from any interference as a result of ambient temperature and irradiance fluctuations around the logger.

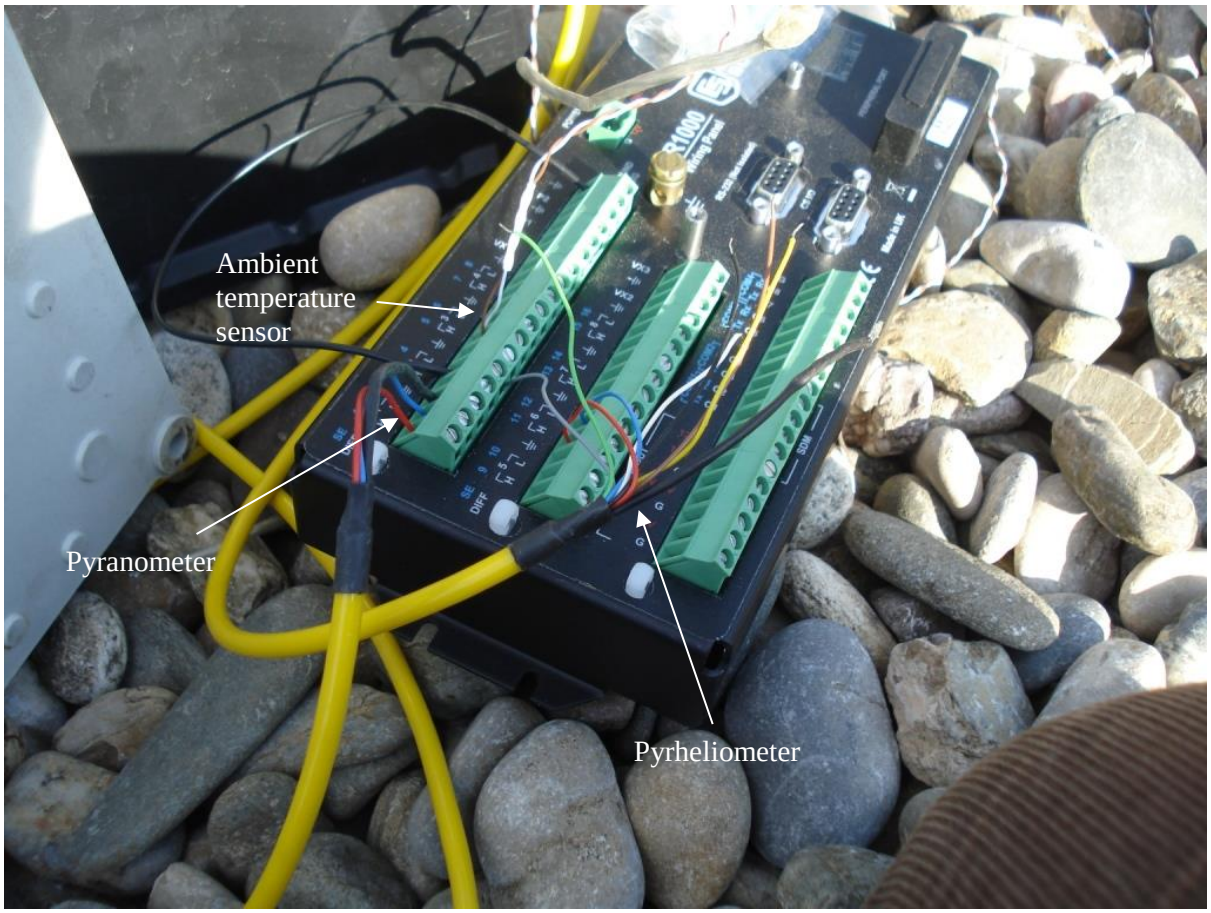

Figure 4-14 – Campbell Scientific CR1000 (sensor connections shown)

4.2.3.3 Campbell CR3000 data logger

The CR1000 data logger was sufficient for the initial testing. However, due to a series of technical difficulties described later in this chapter, additional logging capacity was required to allow for a bespoke resistance-capacitance circuit (described in section 4.2.4.4.3) to be incorporated into the data logging platform. To accommodate these additional input channels a Campbell CR3000 was used to capture the data generated during the latter experimental tests.

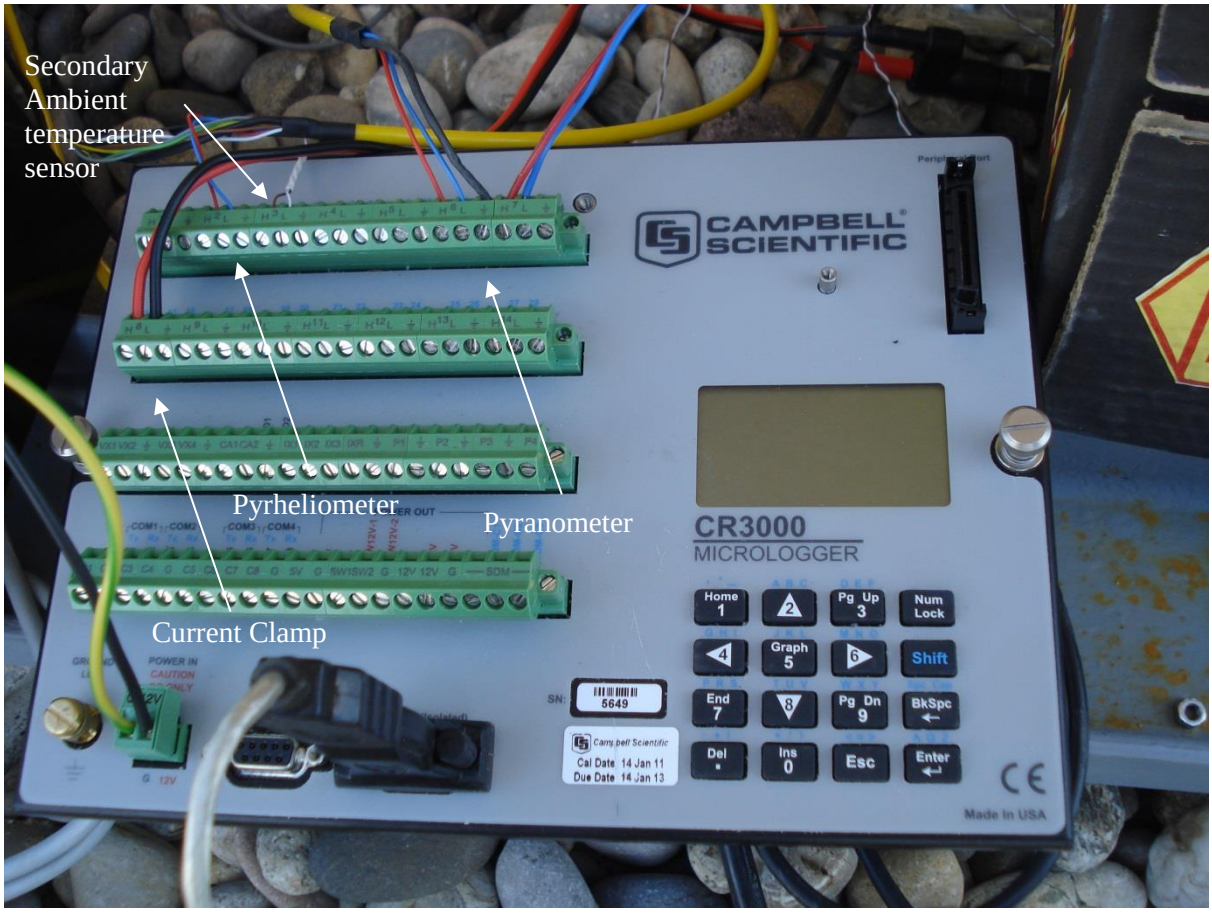

Figure 4-15 – Campbell scientific CR3000 logger (sensor connections shown)

4.2.4 Sensor Equipment

The following sub-sections provide a brief description and summary of the sensor equipment installed and used during the experimental phase of the lens and collector validation. This section also includes a brief description of the logging equipment used. Throughout these descriptions it should be noted that all of the equipment used was fully calibrated, where appropriate, to ensure the accuracy of the data acquired.

4.2.4.1 Pyranometer

The global irradiance on the collector was continuously measured using a Kipp and Zonen CM4 pyranometer. Global irradiance is the sum of the direct and diffuse irradiance on the collector (Duffie and Beckman, 2006). The pryanometer produces a voltage output (mV) which is converted to a Wm^{-2} by a conversion factor supplied by the sensor calibration process. The pyranometer was carefully sited on the 2-D tracker to remain parallel with the plane of collection whilst ensuring that there was no potential for shading. When installed in line with the manufacturer's guidance the CM4 pyranometer has a field of view of 180^{o} and an experimental error of $7\mu VW^{-1}m^{-2}$ (Kipp and Zonen(a), 2013).

4.2.4.2 Pyrheliometer

Throughout the optical design and modelling chapter (chapter 3) the importance of direct or beam radiation on the optical system has been enforced. The vector components of the incident energy have a direct impact on the performance of a concentrating solar collector, in this case a line axial refractive lens. To differentiate between beam and diffuse radiation a Kipp and Zonen CHP1 pyrheliometer was used. Like the CM4 pyranometer, the CHP1 requires a conversion factor and an accurate installation with the sensor's aperture un-shaded and parallel with the collection plane however unlike the CM4 the CHP1 limits the field of collection to a solid angle of 5^{o}. This provides a means to experimentally approximate the amount of light incident on the collector plane which hasn't been deflected through the atmosphere. The CHP1 has a manufacturer's stated sensitivity of 7 to 14 $7\mu VW^{-1}m^{-2}$ (Kipp and Zonen(b), 2013).

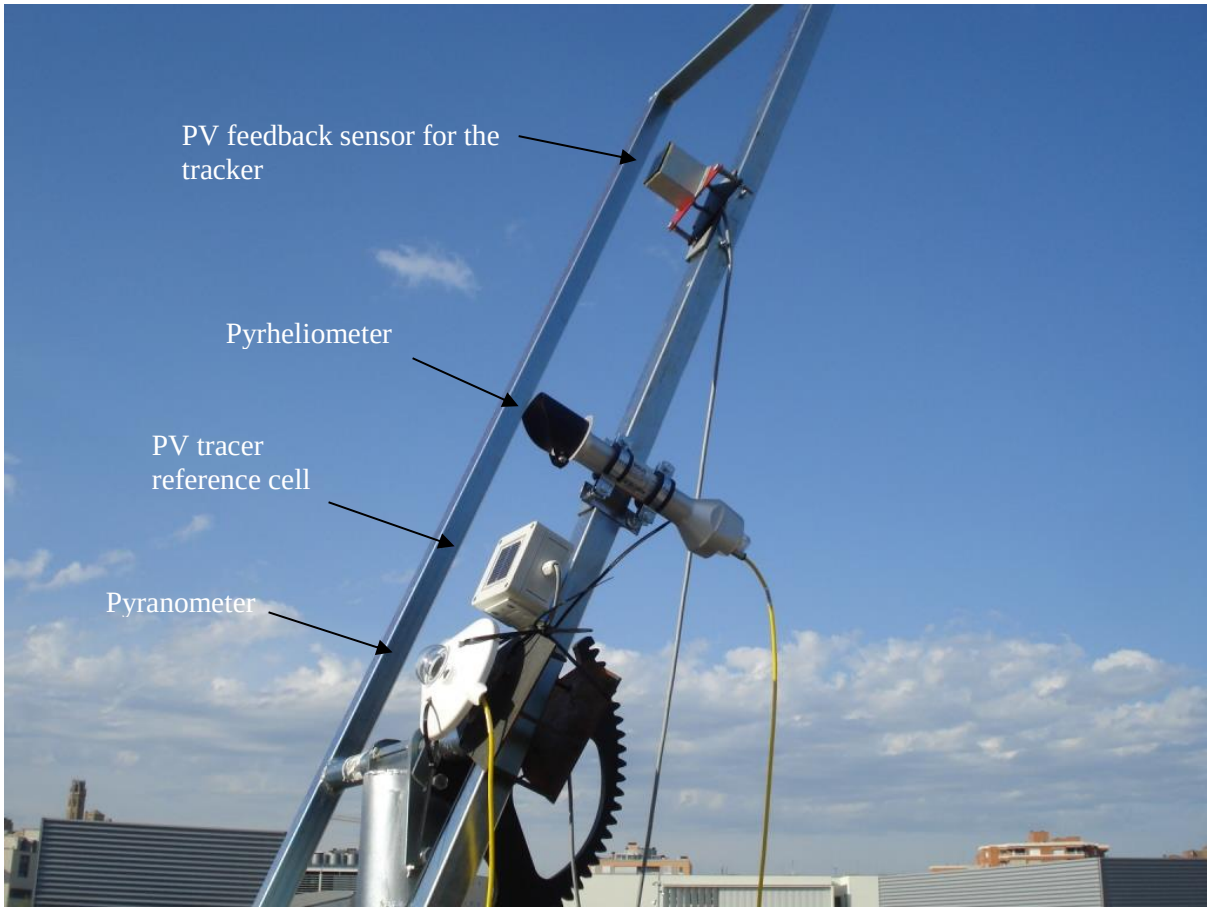

Figure 4-16 – Solar energy sensor array

4.2.4.3 Inclinometer

In order to accurately approximate the offset angle required during the various non-perpendicular experiments a manual spirit level inclinometer was used to control the necessary vertical adjustments. The 2-dimensional tracker was continuously moving to maintain the test rig's perpendicular orientation relative to the sun's position. The inclinometer was mounted to the collectors' supporting frame as shown in Figure 4-17. For accurate control of the offset angle required the inclinometer was levelled before each experiment, offset by the required angle and then the vertical control motor was used to re-level the inclinometer seconds before the array was exposed to solar radiation.

Figure 4-17 – Frame mounted manual inclinometer

4.2.4.4 I-V Tracing Equipment

Before leaving Northern Ireland the individual cells of the collector array were characterised under controlled indoor simulated conditions using a Keithley 2400 SourceMeter and the entire array was assembled to ensure all of the cells were performing as predicted. Unfortunately, during transit the cells were damaged beyond repair and the array was rebuilt using cells gratefully supplied by Dr Daniel Chemisana at the University of Lleida. The specification of those cells has been presented in Section 4.1.2.

An additional issue was then encountered when using the University of Lleida's I-V tracer a PVPM 2540C I-V tracer. The tracer used to characterise the initial cells had no issue with the cell output however the Universitat de Lleida's I-V tracer could not provide an accurate I-V curve due to an insufficient range in the voltage produced relative to the current output from the array. As a result, the graphs produced from the collected data, although accurate, were of limited use and the problem became more pronounced as the intensity incident upon the cells increased (Figure 4-18). Ideally, for the I-V tracer to function constructively the PV array would have been constructed of a larger number of smaller cells but due to time constraints this was not possible.

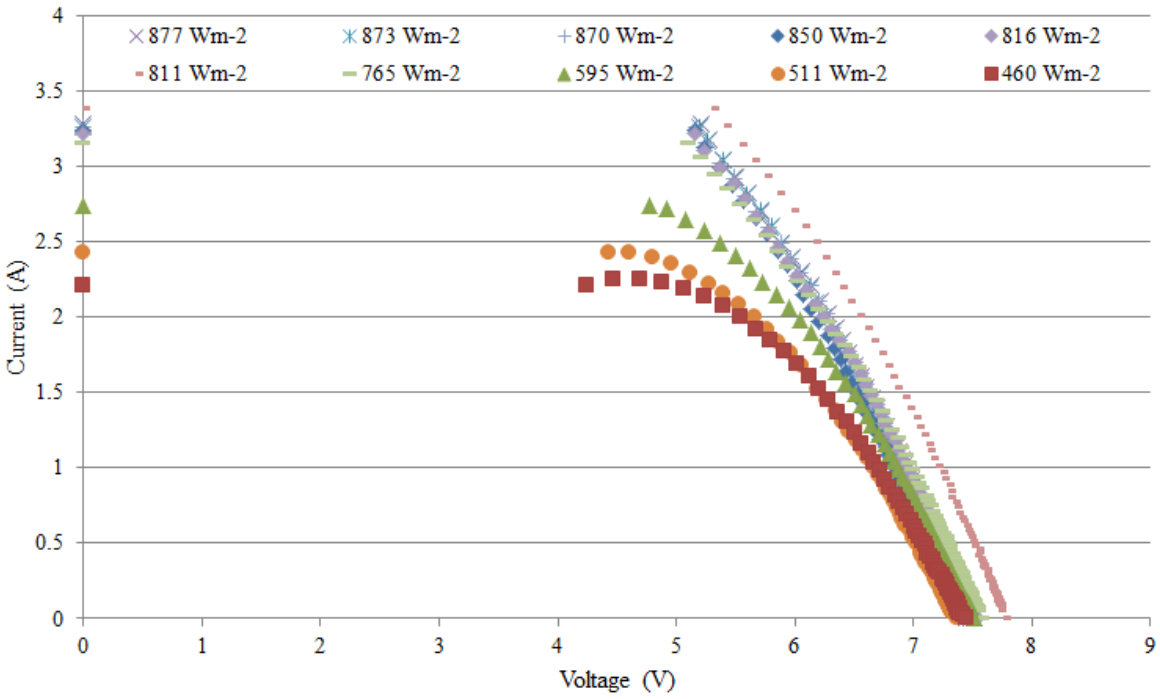

Figure 4-18 – I-V curves generated using the PVPM I-V tracer

To counteract the issues encountered a number of potential solutions were investigated; testing during periods of lower intensity, a reduction in the number of cells connected to the array and finally the design and fabrication of a resistance-capacitance (RC) circuit to create the I-V curves in place of an I-V tracer. Each of those potential solutions is briefly described in the following subsections.

4.2.4.4.1 Testing during periods of reduced insolation

The first approach was to carry out the experimental programme during periods when the solar insolation was 'off-peak' during clear sky early morning and late afternoon sessions. However, as demonstrated in Figure 4-18, despite accurate values for I_{sc} and V_{oc} the PVPM tracer was unable to create a complete I-V curve even at relatively low irradiation levels of 460 Wm^{-2}.

4.2.4.4.2 Reducing the number of cells in the array

The number of cells connected in series was reduced from 15 to 9 in an attempt to compensate for the PVPM tracer's auto-scaling function by lowering the overall collector voltage output however this failed to resolve the issue and resulted in a similar output to that shown in Figure 4-18.

4.2.4.4.3 The design and fabrication of a custom-built resistance-capacitance circuit

Finally, in order to characterise the I-V curves for the array cells a resistance-capacitance circuit was designed (Figure 4-19) and the data was captured using the Campbell CR3000 data logger described in section 4.2.3.3. The 9-cell array was connected to the RC circuit. When the collector array was exposed to solar insolation the voltage generated by the collector array charged a 1 Farrad capacitor providing the open circuit voltage (V_{OC}). The charge/discharge switch was then flipped to discharge, and the current was recorded using a current clamp connected to the CR3000 data logger as the capacitor was discharged through the resistors. The accuracy of the current measurement was increased by coiling the output cable through the clamp 5 times. The current value was then divided by 5 to accurately describe the I-V curve until short circuit current (I_{SC}) was reached. The resolution of the collected data was refined by varying the resistance of the circuit and the voltage was measured simultaneously by a direct connection to the logger.

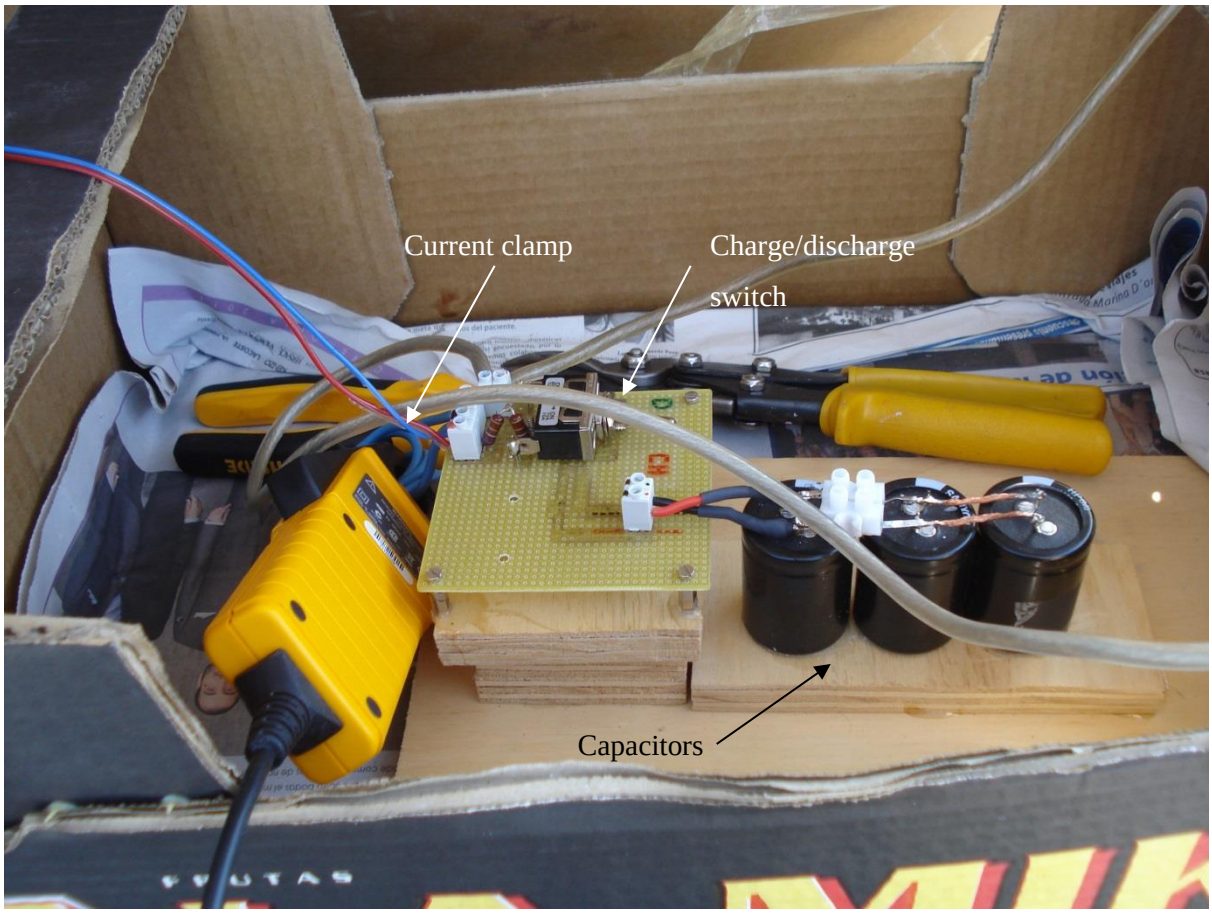

Figure 4-19 – Custom built resistance-capacitance circuit to capture the collectors' I-V curves

4.3 Summary

The manufacture of the accreted 5^{o} defocused fast Fresnel lens, the collector's supporting frame, the module's absorber arrays, the convective backing support system and the temperature sensor array have been presented, discussed and their physical properties have been identified and evaluated where appropriate. The physical appearance of both the baseline and DFFLAB collectors has also been documented and discussed in relation to the criteria for the assessment of building integrated photovoltaic systems and the objectives of this thesis.

The main issue encountered during the manufacture of the complete experimental collector prototype was the process of bonding the relatively large Fresnel lens area to the backing PMMA pane and the advantages and disadvantages of the bonding method used have been highlight accordingly. Further work on this bonding method has the potential to improve the optical performance of the DFFLAB collector, as a result of reducing reflection losses, by between 4 and 8 % based on PMMA-air-PMMA boundary interface assumptions.

Finally, a full breakdown of all of the experimental equipment used has been presented and described.

Experimental Results and Analysis

5 Results and Analysis

5.1 Introduction

The results obtained using the experimental test rig described in chapter 4 are presented in the following format. The short circuit current under varying levels of incident solar radiation for each of the collector configurations is characterised by presenting $I_{SC}G$ curves for the absorber array uncovered, covered with the Perspex sheet (baseline) and finally with the 5° Defocused fast Fresnel Lens (DFFL). The second phase quantifies collector performance in terms of both I-V and P-V characteristic curves for each of the three configurations along with the effect of a series of one-dimensional off-axis variations (5°, 10°, 15°) for the 5° DFFLAB collector to establish whether the Maximum Power Point (P_{MPP}), voltage and current at P_{MPP} (V_{MPP} and I_{MPP}, respectively), Fill Factor (FF) and finally efficiency (η) of the absorber array validates the performance predicted by the optical models. The efficiencies of all three systems are then identified, including the effects of the Perspex lens and 5° DFFL on the overall performance of the array. Finally, the 5° DFFLAB collector is characterised under constant exposure, various off-axis orientations (a typical real world half angle acceptance period) to examine whether or not the transient absorber flux creates any major issues, primarily with V_{OC} and cell temperature, which could be used to inform future refinements of the optical design.

To aid in understanding the significance of the information presented in the results and analysis phase of the experimental testing process, across a variety of the collector configurations, the following analogy describing PV cell operation by Gray and Schwartz cited by Luque and Hedges (2003) has been included:

> *Imagine a funnel that has a variety of holes of different shapes and sizes in it. It also has a stopcock at the bottom for controlling the flow of liquid through the bottom of the funnel. Water, representing the incident sunlight, is poured into the top of the funnel. Water flowing out of the funnel through the stopcock represents the current delivered by the solar cell. Since the funnel is full of holes, some of the water leaks out instead of flowing through the stopcock. This leakage represents the recombination of minority carriers in the solar cell. The different-shaped holes represent different sources of recombination. For instance, square holes might represent recombination in the base region, round holes might be recombination in the space-charge region, triangular holes might be surface recombination at the back contact, and so on. The rate at which water pours in is proportional to the light intensity. At steady state, the water will find a height such that the flow of water in, I_{GEN}, is equal to the flow through the stopcock (I) plus the water that leaks through the holes (I_{RECOMB}). This height represents the solar cell voltage (V). When the stopcock is fully open, the water flows out through the*

stopcock at its maximum rate (I_{SC}), although some water will leak out through the holes so that $I_{SC} < I_{GEN}$. This is analogous to the collection efficiency, η_C, of a solar cell – the objective being to minimize the amount of leakage (recombination) so that η_C is as close to unity as possible. Smaller holes mean less recombination and $I_{SC} \rightarrow I_{GEN}$. As the stopcock is slowly closed, the level of liquid in the funnel rises – just as the solar cell voltage increases as the current decreases. When the stopcock is completely closed, the height of the water is representative of the open-circuit voltage (V_{OC}). At open circuit all the minority carriers must recombine just as all the water must leak out of the funnel in this analogy. If the holes are all big, the height of the water will be low. This is equivalent to short minority-carrier lifetimes and large surface recombination velocities that result in a low V_{OC}. By reducing the size of the holes (i.e. increasing the minority-carrier lifetimes and reducing the surface recombination velocities), the height of the water in the funnel (i.e. V_{OC}) is increased. Reducing the size of only the square holes (by increasing the minority-carrier lifetime in the base) will not increase the height of the water as much as might be expected since the round holes (recombination in the depletion region) are still large. All leaks (recombination sources) must be plugged (recombination rates minimized) before the height of the water (V_{OC}) increases substantially.

5.2 Issues encountered during experimental testing

After the manufacture of the absorber array and subsequent attachment of the collector to the 2-dimensional tracker (described in chapter 4) two issues were noted during preliminary testing; a broken temperature sensor junction on one of the thermocouples (Figure 5-1) and sagging of the Perspex sheets as a result of the temperature increase during exposure (Figure 5-2). The results from a series of preliminary setup tests identified that the sensor junction on thermocouple 8, the temperature sensor attached to the back surface of the most central cell in the array, had broken sometime during the manufacturing process. At this point in the experimental programme the sensor could not be fixed or replaced without completely destroying the cells of the absorber array during disassembly. It was therefore decided to continue with the experimental programme using the additional 14 thermocouples connected to the back of the remaining cells in the array. Although, as discussed in chapter 3, the use of Perspex is common for the refractive collector components. However, the physical span of the developed module led to an unexpected amount of sagging in the inner Perspex sheets, which was more pronounced towards the centre of the collector. Figure 5-2 shows the bow or sag in the absorber plane created as a result of the thermal expansion in the Perspex backing sheet. This is a definite area where simple improvements to the system design could be made.

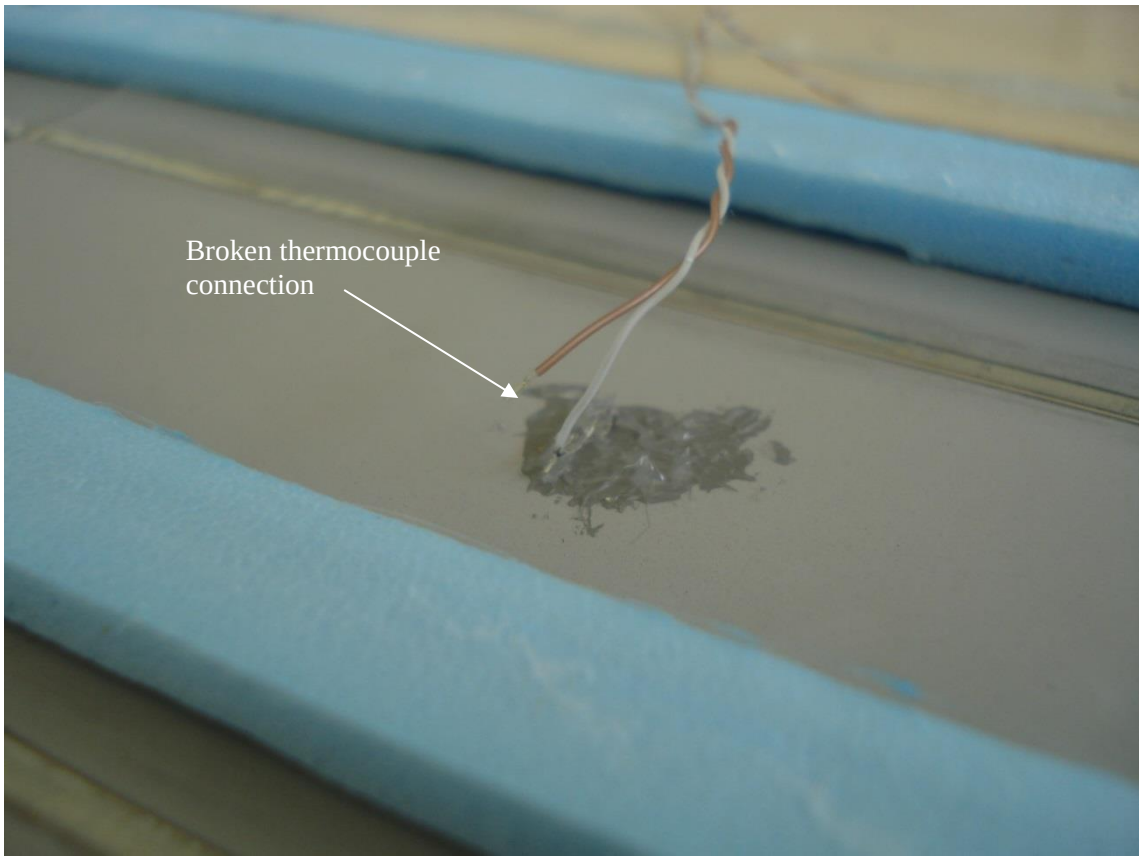

Figure 5-1 – Broken thermocouple sensor junction on cell 8 (centre cell) of the array

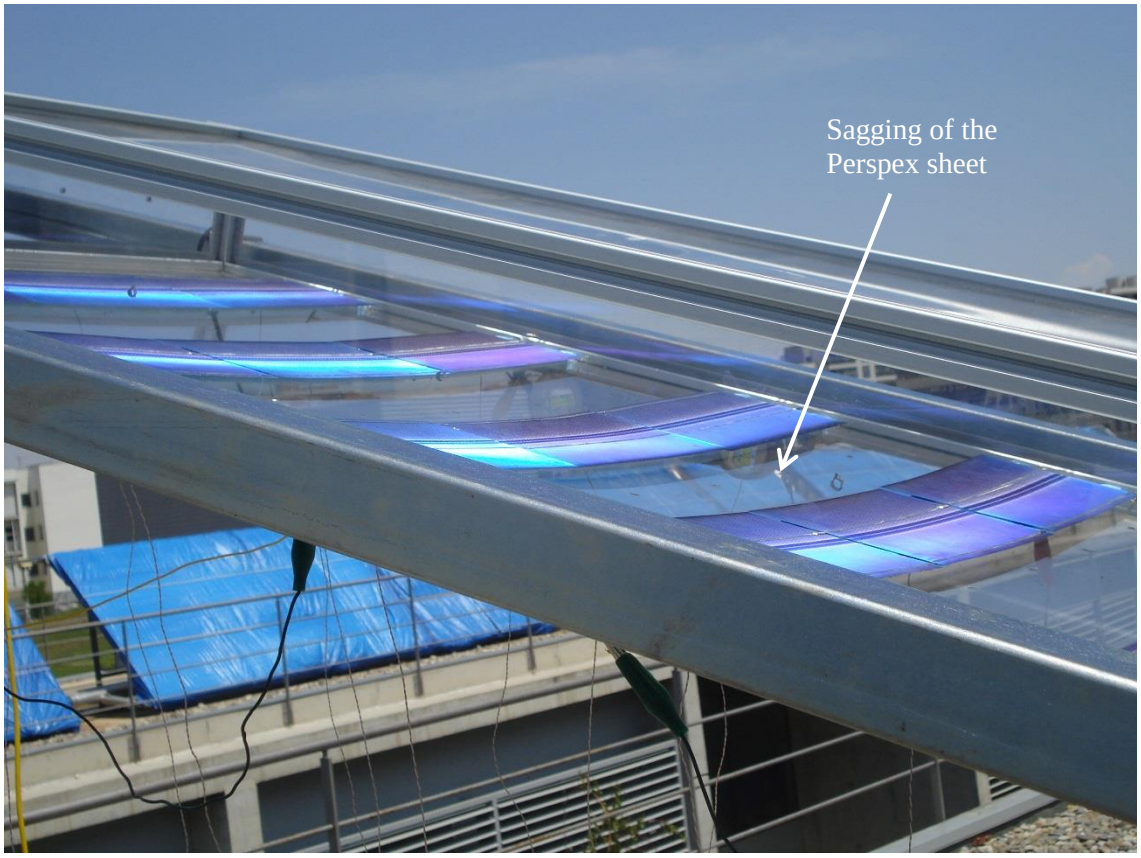

Figure 5-2 – Temperature related sagging in the Perspex sheet during exposure

5.3 Manufacturer's specified cell performance

In order to add additional context to the results presented in this chapter, Figure 5-3 shows the manufacturer's specified cell performance derived under standard test conditions. The standard test conditions are: Light spectrum AM = 1.5, irradiation intensity E = 1000 Wm^{-2} and cell temperature T_c = 25 °C.

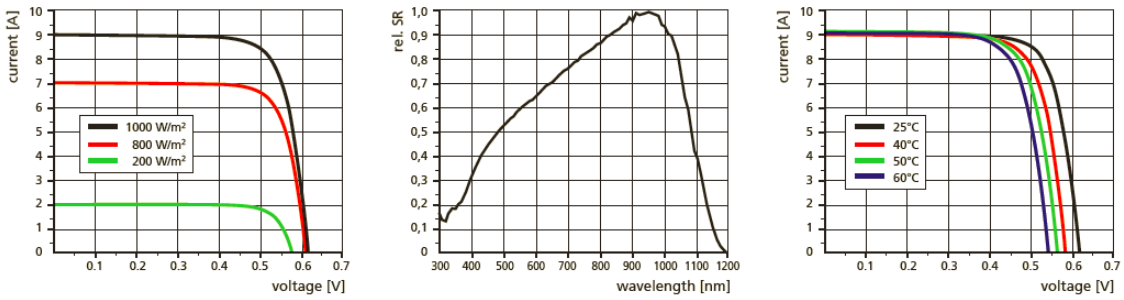

(a) (b) (c)

Figure 5-3 - Manufacturer's stated cell performance; (a) variations in I-V behaviour with irradiation intensity, (b) cell spectral sensitivity curve and (c) variations in I-V behaviour at different cell temperatures (Anon, 2013)

The information presented in Figure 5-3 shows how the full individual cells perform under controlled indoor conditions. By cutting the cells to meet the absorber criteria the overall current output of the cells was reduced by 62 % in proportion to the area of cell removed. The effect of connecting these cells, cut to purpose, in series is an increase in the voltage delivered by the array with a minimal variation in the current output. This allows for a prediction on the performance of the 9-cell array tested, with an effective collection area of 0.6 m x 0.5 m. The uncovered baseline collector is anticipated to have a short circuit current of approximately 5.58 A (9 A x 62 %) at an incident radiation level of 1000 Wm^{-2} and a voltage of approximately 5.4 V (9 x 0.6 V) during the short exposure characterisation tests at an ambient temperature of 30 °C. These predicted values allow for the performance of the fabricated absorber array to be linked back to the standard test conditions, ensuring that any damage to the cells as a result of cutting or losses as a result of the circuit design can be quantified.

5.4 Short Circuit Current –Intensity ($I_{SC}G$) collector characterisation

The amount of current generated by a solar cell is proportional to the intensity and distribution of the solar radiation incident on the absorber array and the current losses due to recombination. The maximum current available for any given level of irradiance is the short circuit current (I_{SC}) for that level of incident radiation (G). This section investigates the effect of the clear Perspex sheet and the 5º DFFL on the current generated by the absorber array based on the amount of global, direct and diffuse radiation incident on the individual collector configurations. The $I_{SC}G$ characterisation experiments were carried out on days with transient solar conditions which, due to intermittent cloud cover, varied both the intensity of the incident solar radiation and the percentage of direct irradiance available in relation to the overall global irradiance. This scenario was used to evaluate the optical efficiencies of the systems and the filtration characteristics of the 5º DFFLAB collector's incident angle tolerances by examining the electrical performance of the absorber array.

5.4.1 Methodology for $I_{SC}G$ characterisation

Using the experimental setup described in chapter 4 the collector base was fixed to the 2-axis solar tracker and the individual collector configurations were created by removing or changing the covering pane between the clear Perspex sheet and the 5º DFFL. The tracker was aligned to a position where the light incident on the absorber was perpendicular to the absorber array and the 2-axis tracker was allowed to track the position of the sun relative to the position of the absorber plane, using its autonomous control mechanism, during continuous exposure to transient solar conditions. Since I_{SC} is independent of cell temperature the $I_{SC}G$ curves were then created by operating the custom built IV tracer, described in chapter 4, in its discharge 'continuous free flow' mode i.e. removing the stop cock in the funnel analogy by Gray and Schwartz (Luque and Hedges, 2003) by reducing electrical impedance. The data from the experimental sensors were collected by the three data loggers and the results were compiled and analysed in Microsoft Excel. The ambient temperature conditions and global irradiance during each of the $I_{SC}G$ experiments are presented in Figure 5-4.

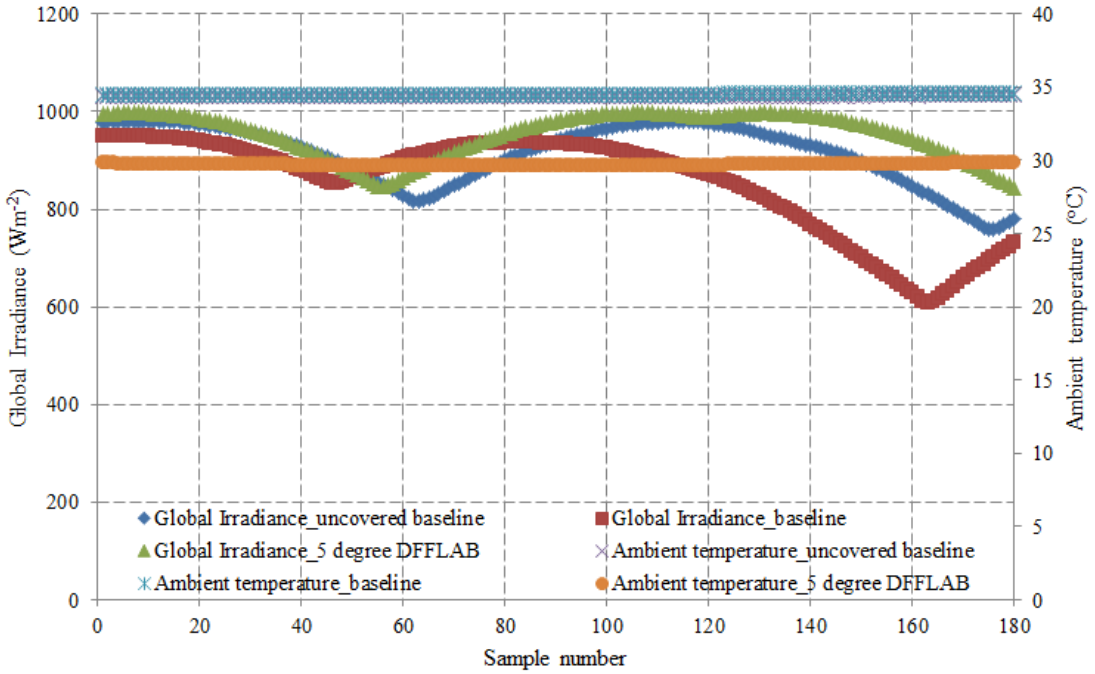

Figure 5-4 – Ambient temperature and global irradiance variations during the $I_{SC}G$ experiments

5.4.2 $I_{SC}G$ characterisation curves

The results from the $I_{SC}G$ characterisation experiments are presented in Figure 5-5 to Figure 5-7. The graphs show how short circuit current for the uncovered baseline collector, baseline collector and the 5° DFFLAB collector vary with both the intensity and composition of global irradiance. Dark current was negligible in all cases.

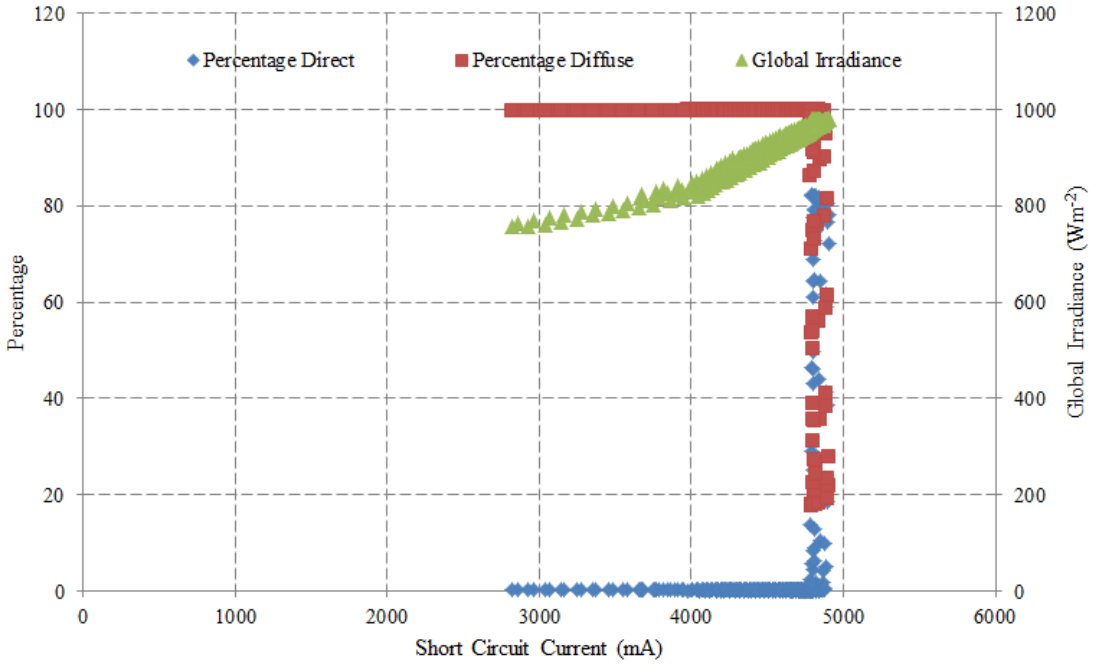

Figure 5-5 – Relationship between short circuit current, Global irradiance and the composition of the incident solar radiation for the uncovered baseline collector

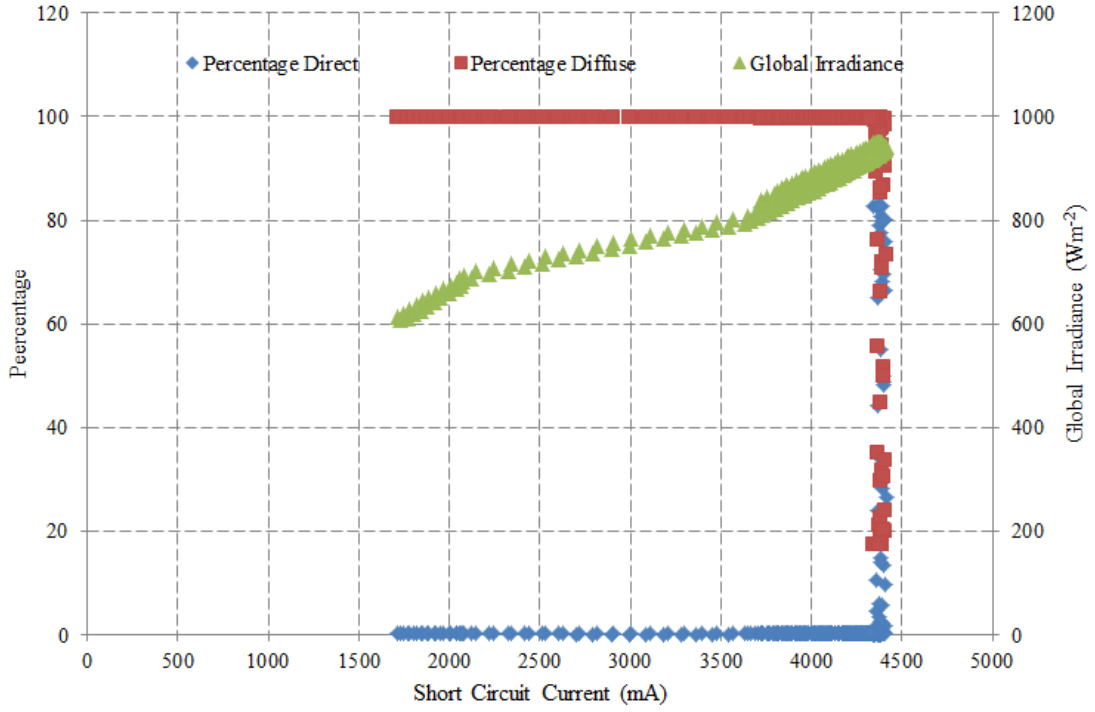

Figure 5-6 - Relationship between short circuit current, Global irradiance and the composition of the incident solar radiation for the baseline collector

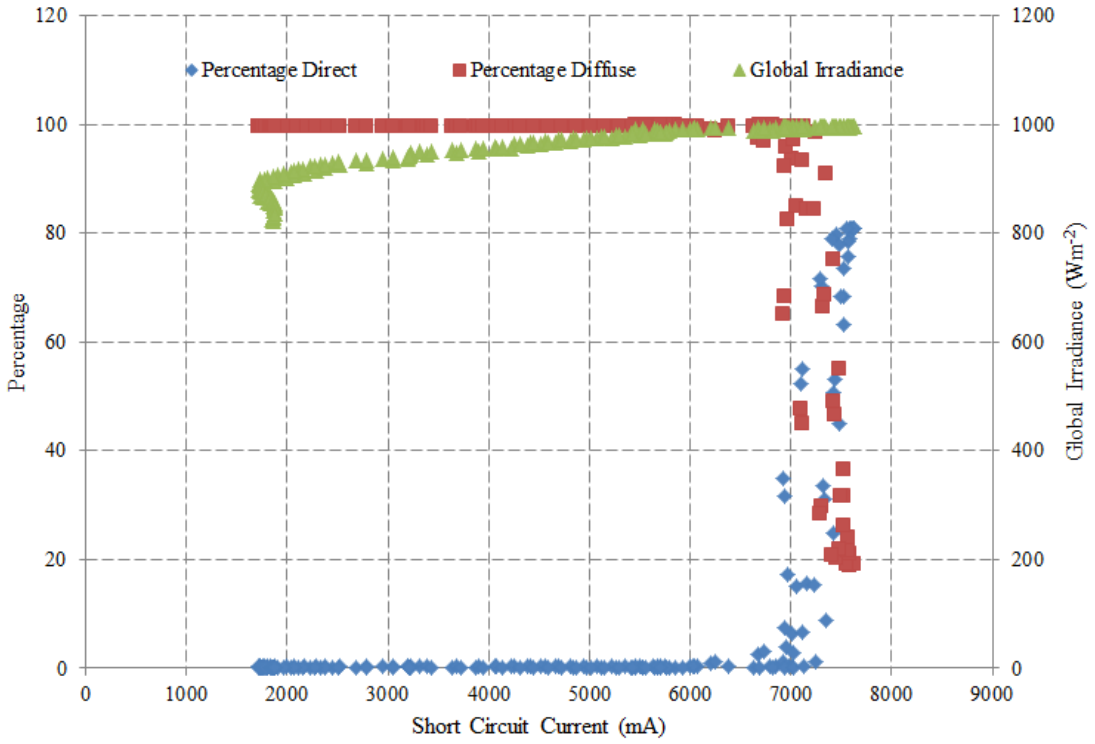

Figure 5-7 - Relationship between short circuit current, Global irradiance and the composition of the incident solar radiation for the 5° DFFLAB collector

5.4.3 Summary of $I_{SC}G$ characteristics

The analysis of the results from the $I_{SC}G$ experiments presented in Figure 5-5 to Figure 5-7 allows the effects of a number of collector components to be quantified. The short circuit current of the absorber array has been summarised in Table 5-1. The addition of the 3 mm thick clear Perspex sheet to the collector base resulted in a decrease in the maximum short circuit current generated of 9 %. The addition of the 5° DFFL created a 74 % increase in the maximum short circuit current recorded at similar levels of solar irradiation when compared with the performance of the baseline collector.

As previously mentioned, the variations in incident solar radiation were achieved by carrying out the experiments during periods of transient and variable cloud cover which, shown in Figure 5-4, created an undulating pattern of incident radiation. This undulation in incident radiation also varied the composition of the insolation. As direct rays encountered moisture in the atmosphere they were scattered increasing the proportion of diffuse radiation and decreasing the proportion of direct radiation in the overall global radiation value, with higher levels of incident radiation primarily composed of a greater percentage of direct rays. The 5° DFFLAB collector, being more sensitive to the angle of incident radiation was affected by this shift in global radiation

composition. This can be noted in Figure 5-7 as the range of short circuit current measurements recorded vary when global irradiance plateaus around 1000 Wm^{-2} and the composition of direct and diffuse irradiation changes.

The graphs presented in Figure 5-5 and Figure 5-6 show that, despite varying compositions of direct and diffuse radiation, the short circuit current increases linearly with increasing levels of solar radiation evidenced by the linearity of results at the point of maximum short circuit current encountered in each case. By contrast the short circuit current for the 5° DFFLAB collector (Figure 5-7) remains relatively stable as global insolation increases, albeit over a smaller range than the other configurations, with the highest values recorded corresponding to periods when direct radiation was the dominant component of the global radiation.

Table 5-1 – Summary of $I_{SC}G$ experiments

Collector configuration	$I_{SC\ (MAX)}$	G at $I_{SC\ (MAX)}$	% G direct	% G diffuse	G_{MAX}
	(mA)	(Wm^{-2})	(-)	(-)	(Wm^{-2})
Uncovered baseline	4905	981	72.17	27.83	981
Baseline	4412	941	73.43	26.57	951
5° DFFLAB	7628	997	80.99	19.01	997

From Figure 5-3 it can be noted that the uncovered baseline cell output should be between 4960 mA for an incident radiation of 900 Wm^{-2} and 5580 for 1000 Wm^{-2} under single cell controlled indoor test conditions. The difference between the short circuit current recorded experimentally and the predicted value, derived from the manufacturer's data sheet, was a result of an increase in the relative electrical losses within the absorber array namely a combination of series resistance losses in connecting the cells of the array and current mismatch in individual cell output. The energy incident on the absorber array in the 5° DFFLAB collector configuration, when perpendicular to the sun, was double that of the energy incident on the uncovered collector minus optical losses from the system. However, the corresponding increase in short circuit current was 74 %. Since I_{SC} is directly proportional to incident radiation the 26 % difference in expected output can be attributed to the following; optical losses through the 3 mm Perspex pane, optical losses through the lens and optical losses as a result of non-specular incident radiation. The

variation in I_{SC} between the uncovered and covered baseline collector suggest that a 9 % loss can be attributed to the presence of the 3 mm Perspex pane the lens was bonded too.

The remaining collector losses were a result of the combined effect of the optical losses from the 5º DFFL and the uneven distribution of the incident light on the cells of the absorber. The difference in the magnitude of losses through the 5º DFFL and the Perspex pane suggest that, when the incident angle is perpendicular, attenuation losses in the thicker Perspex pane were a larger contributor to optical losses in the system than the 5º DFFL. This identifies the potential for improvements to the collector's performance can be made by changing material of, or reducing the thickness of, the bonded pane.

5.5 I-V and P-V curve characterisation

Current-Voltage (I-V) and Power-Voltage (P-V) curves are staples in analysing the performance of PV cells and collectors. The two curves are frequently presented independently but within this section the two sets of characteristic curves for each experiment have been superimposed onto the same graphs for clarity during the discussion, as the position of the Maximum Power Point (P_{MPP}) on the P-V curve is important in deriving the Fill Factor (FF) and electrical efficiency (η) of the absorber array. Again, as with the previous section, the primary purpose of these experiments is to use a set of electrical analysis tools to validate the predicted behaviour of the lens derived from the optical models.

5.5.1 I-V and P-V curve perpendicular methodology

As with the $I_{SC}G$ characterisation, the I-V and P-V curve characterisation was conducted using the experimental setup described in chapter 4. The collector base was fixed to the 2-axis solar tracker and the individual collector configurations were created by interchanging the covering pane between no cover, the clear Perspex sheet and the 5º DFFL. The tracker was again aligned to a tracking position where the light incident on the absorber was perpendicular to the absorber array and the 2-axis tracker was allowed to track the position of the sun relative to the position of the absorber plane during the experiments. However, unlike the $I_{SC}G$ experiments, the I-V and P-V curve experiments were carried out under instantaneous characterisation conditions in order to capture the performance of the absorber array while limiting increases in cell temperature (where reasonably practicable under outdoor experimental conditions) which would result in an intrinsic decrease of V_{OC}. The data were then captured by the three independent data loggers and

the results were compiled and analysed in Microsoft Excel. The ambient temperature conditions and irradiance profile during each of the I-V and P-V experiments are presented in Figure 5-8.

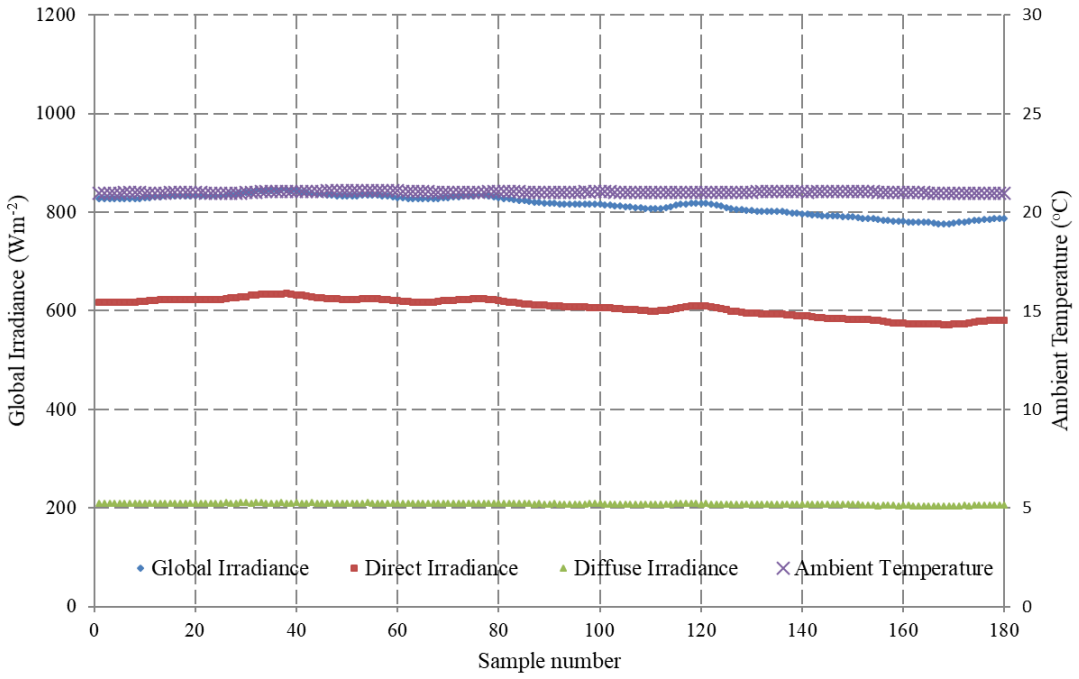

Figure 5-8 – Ambient Temperature and Irradiance Profile during the I-V and P-V experiments

5.5.2 I-V and P-V curves for the collector configuration at perpendicular incidence angles

The results from the I-V and P-V characterisation experiments are presented in Figure 5-9 to 5-11. The graphs show how both short circuit current and power output for the uncovered baseline collector, baseline collector and the 5° DFFLAB collector vary with both the intensity and composition of global irradiance. As with the $I_{SC}G$ experiments the effects of dark current was negligible in all cases.

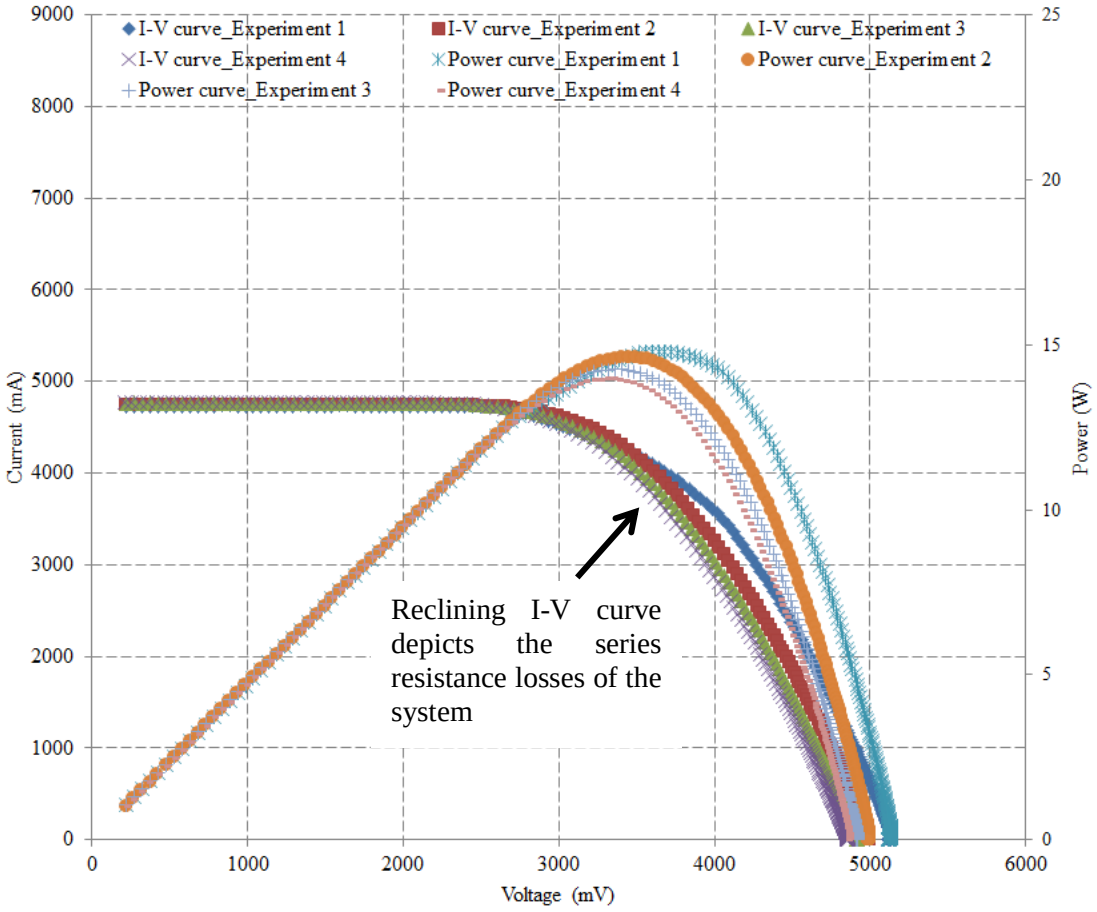

Figure 5-9 – I-V and P-V curves for the uncovered baseline collector

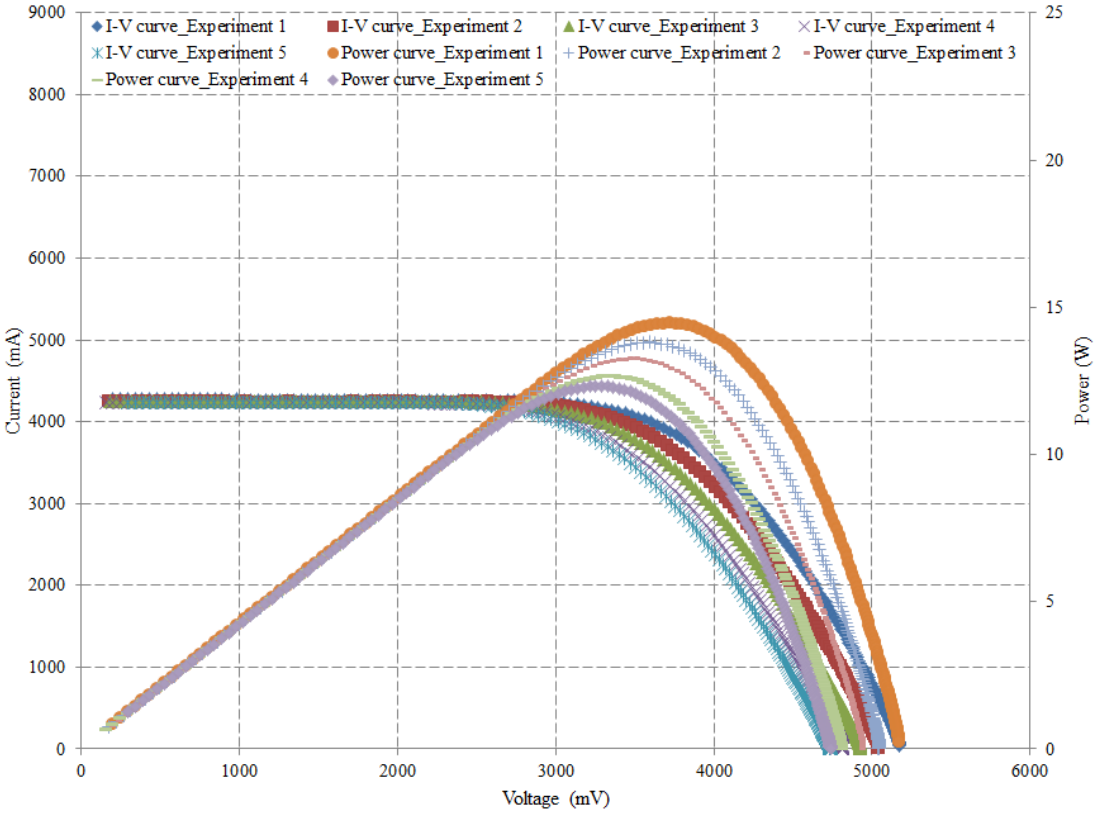

Figure 5-10 - I-V and P-V curves for the baseline collector

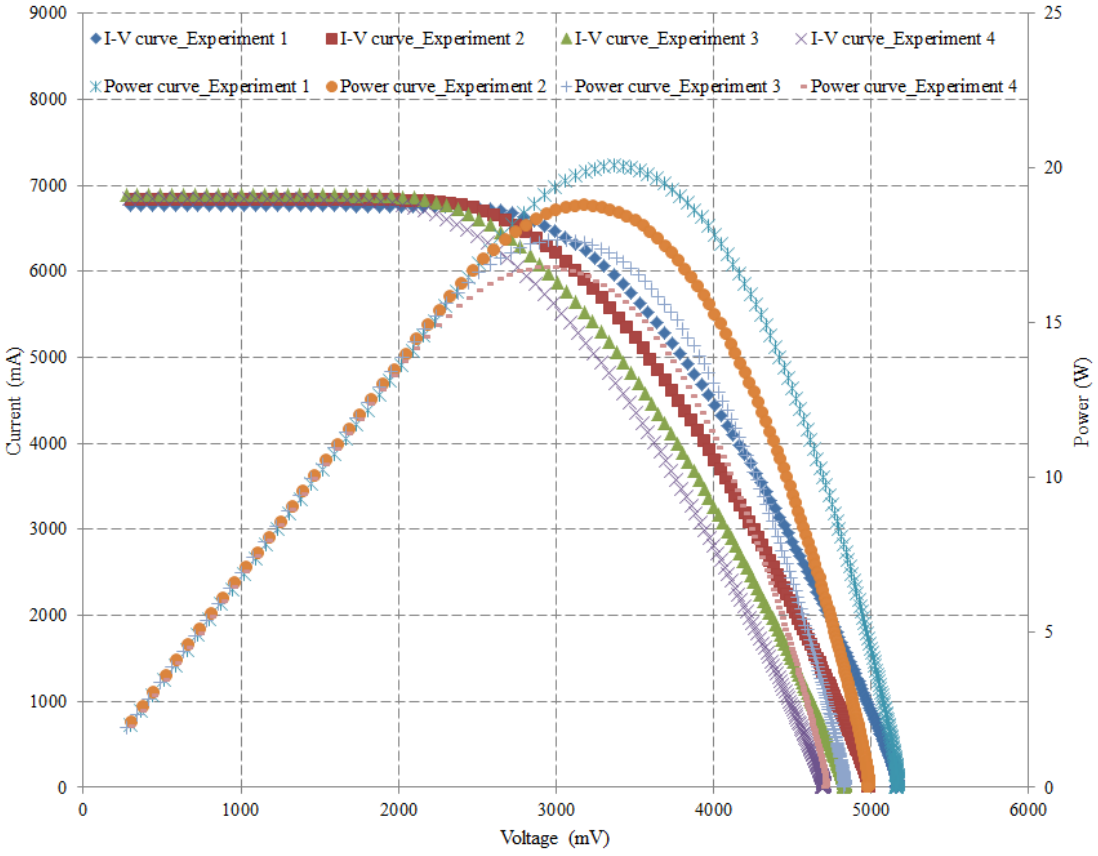

Figure 5-11 - I-V and P-V curves for the 5º DFFLAB collector

5.5.3 Summary of I-V and P-V curves for perpendicular incident angles

The effect of the various collector configurations on the overall absorber array at relatively constant levels of insolation and perpendicular incidence angles has been summarised in Table 5-2. The following equations, presented in the review of solar cells in chapter 2, were used calculate Fill Factor (FF) and cell efficiency (ɳ).

$$FF = \frac{P_{MPP}}{V_{OC}I_{SC}} = \frac{V_{MPP}I_{MPP}}{V_{OC}I_{SC}} \qquad \text{Equation 5-1}$$

$$\eta = \frac{P_{MPP}}{P_{in}} = \frac{FFV_{OC}I_{SC}}{GA_{eff}} \qquad \text{Equation 5-2}$$

Where; GA_{eff} is the global incident radiation (G) multiplied by the effective absorber area (A_{eff}) power input (P_{in}) to the cell. The sensitivity of the solar cells to specific wavelengths of light (Figure 5-3) is incorporated into the cell collector efficiency in each case but not elaborated on further.

A number of important points can be extracted from the information presented in the figures and summary table for these experiments. The first of which is the impact on individual cell performance as a result of connecting the cells into a module. A note has been added to Figure 5-9 which draws attention to the impact of series resistance on the I-V curves when compared to the I-V curve for the single cell under standard test conditions (Figure 5-3 (a)). The relaxation of the I-V curve indicates that resistive losses have been introduced to the system and that those losses have impacted on the collector's performance. The extent of that impact can be quantified by examining the change in fill factor from the cell to the collector module. From the information presented in Figure 5-3 it is possible to calculate that the fill factor for the single cell should be between 0.813 and 0.787 under 800 and 1000 Wm^{-2}, respectively. The fill factor calculated for the uncovered baseline collector varied slightly under the transient conditions but was on average 0.609 at an average global irradiance of 939 Wm^{-2} which attributes a reduction in fill factor of 0.122 to the electrical connections between the cells. Since fill factor is also a determining factor in the position of the maximum power point on an I-V curve it is apparent that the increases in electrical resistance also had a detrimental impact on power output, however this is an expected outcome in the manufacture of PV modules and can be reduced by using a more sophisticated assembly process but not eliminated completely.

Also of interest are the variations in cell efficiency. As Equation 5-2 states, cell efficiency is also affected by fill factor. From the information on a single cell's performance presented in Figure 5-3 it is possible to calculate the nominal cell efficiency under standard test conditions. That information implies that the cell's efficiency should vary between 17.53 and 17.46% at incidence radiation levels of 800 and 1000 Wm^{-2}, respectively. The calculated cell efficiencies under transient test conditions were lower than expected due to the impacts of series resistance on fill factor mentioned previously plus one additional factor; the proportional reduction in absorber area as a consequence of cutting the solar cells to size for the proof of concept design. In reducing the overall area of the cell to match the design criteria from the optical design chapter (chapter 3) the ratio of collector area to grid area for the cell was changed. The proportional area of the busbar was inadvertently increased which resulted in an additional reduction in cell efficiency.

It should be noted however that the advantage of carrying out a comparative analysis of the three collector designs allows for variations in fill factor and cell efficiency to be normalised for these experiments because any non-idealities in the base collector performance is experienced across all configurations equally.

This commonality in the underlying absorber material behaviour leads to some general observations on the impact of the optical components used in the various collector configurations and allows for some validation of the optical simulations. Beginning with a comparison between the uncovered and covered baseline design it is clear what impact the 3 mm Perspex sheet had on the PV cells. During the collection period global irradiance was relatively consistent between the uncovered and covered collectors (3 % difference in average intensity) and, when corrected for the 3% variation in average intensity, the uncovered collector reaffirmed the 9% losses in I_{SC} associated with the inclusion of the Perspex sheet. The 5° DFFLAB again demonstrated a significant increase in short circuit current (62.2 %) and an increase in power output of 73.6 %. These real-world comparative findings are in line with what was predicted during the optical modelling of the developed system which demonstrated a 75 % increase in optical efficiency at a perpendicular incident angle.

Table 5-2 – Summary of the performance of the three collector configurations under perpendicular exposure to incident solar radiation

Collector configuration	Experiment number	Global Irradiance (Wm^{-2})	Direct Irradiance (Wm^{-2})	P_{MPP} (W)	I_{MPP} (mA)	V_{MPP} (mV)	I_{SC} (mA)	V_{OC} (mV)	FF (-)	η (%)	T_{VOC} (^oC)
Uncovered baseline	1	937	700	14.81	4021	3682	4738	5134	0.609	11.85	39.11
	2	939	700	14.63	4300	3403	4748	4997	0.617	11.68	39.79
	3	940	701	14.25	4190	3402	4761	4918	0.609	11.37	44.46
	4	941	703	13.97	4233	3300	4775	4857	0.602	11.13	47.80
Baseline	1	911	680	14.46	3884	3722	4285	5175	0.652	11.90	35.82
	2	910	680	13.81	3844	3592	4246	5046	0.644	11.38	36.50
	3	909	679	13.26	3788	3501	4252	4928	0.633	10.94	39.50
	4	904	675	12.67	3840	3300	4239	4812	0.621	10.51	44.92
	5	905	675	12.32	3788	3252	4242	4737	0.613	10.21	52.00
5^o DFFLAB	1	894	634	20.08	5965	3366	6770	5168	0.574	16.84	37.60
	2	898	634	18.79	5906	3181	6834	4989	0.551	15.69	39.88
	3	906	642	17.69	5871	3013	6895	4832	0.531	14.64	42.62
	4	902	638	16.79	5851	2871	6851	4702	0.521	13.96	49.38

5.5.4 I-V and P-V curve off-axis methodology

Having completed the validation of the optical model at a perpendicular angle the next logical step was to confirm the lens' behaviour across the range of design acceptance angles. To achieve this the 5º DFFL was attached to the collector base, fixed to the 2-axis solar tracker and covered with a solar shield. The tracker was aligned to a tracking position where the light incident on the absorber was perpendicular to the absorber array and the 2-axis tracker was allowed to track the position of the sun relative to the position of the absorber plane during the experiments. However, unlike the perpendicular I-V and P-V curve experiments, the inclinometer shown in chapter 4 was offset to the required angle and the tracker's y-axis motor was used to quickly rotate the collector into the desired off-axis orientation for each of the experiments. The system was instantaneously characterised by removing the solar shield, capturing the data and replacing the solar shield again in order to capture the performance of the absorber array while limiting increases in cell temperature (where reasonably practicable under outdoor experimental conditions) which, as previously mentioned, would result in an intrinsic decrease in V_{OC}. The data were captured by the 3 independent data loggers and the results were compiled and analysed in Microsoft Excel. A small laptop explosion during one of the experiments meant that the data for the 20º experiments were corrupted and couldn't be transferred into Excel and the dependency for ideal experimental conditions during this analysis meant that the data series could be completed during the experimental window in Lleida. Thankfully, the quality of the data captured for the four remaining incidence angles was sufficiently high to provide validation of the optical modelling. The ambient temperature conditions and global irradiance relative to the orientation of the collector during each of the off axis I-V and P-V experiments are presented in Figure 5-8.

5.5.5 I-V and P-V curves for the 5º DFFLAB collector configuration at off-axis incidence angles

The results from the off-axis I-V and P-V characterisation experiments are presented in Figure 5-12 to 5-14. The graphs show how current, voltage and power for the DFFLAB collector vary across a range of discrete incidence angles. The effects of dark current were negligible in all cases.

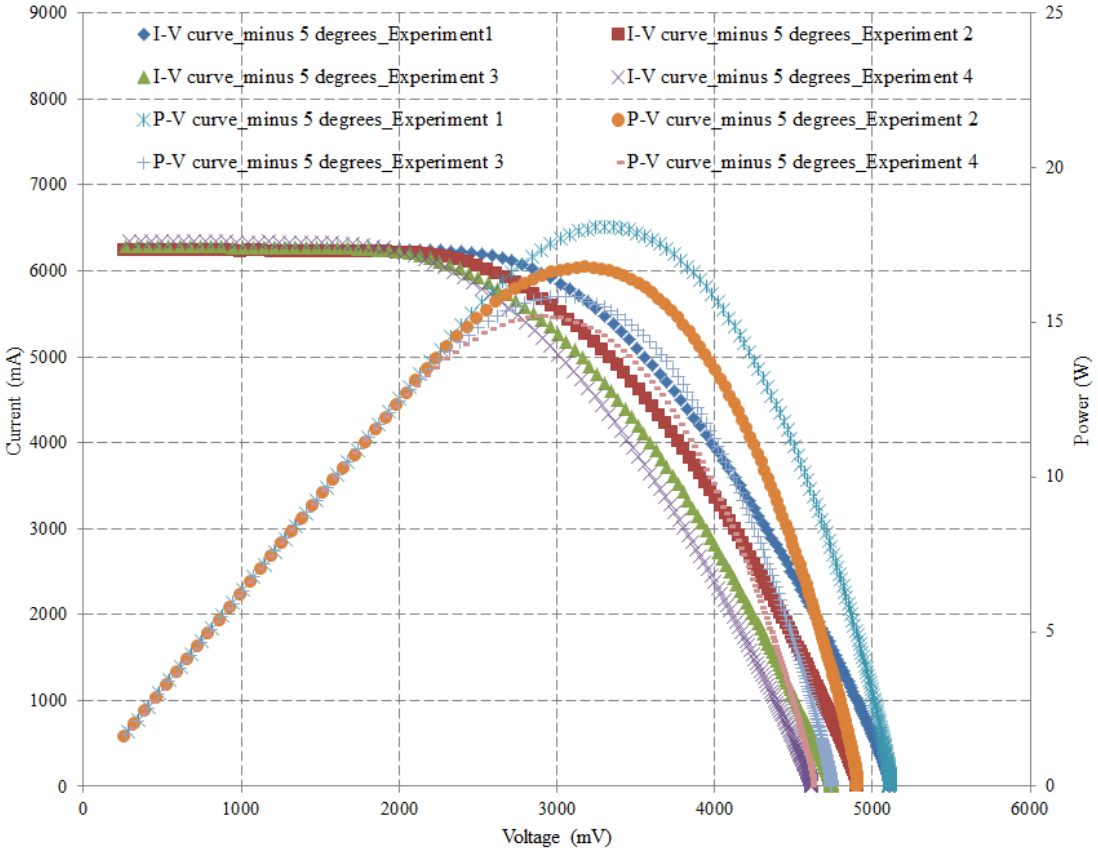

Figure 5-12 – I-V and P-V curves for the 5º DFFLAB collector at a 5º off-axis inclination

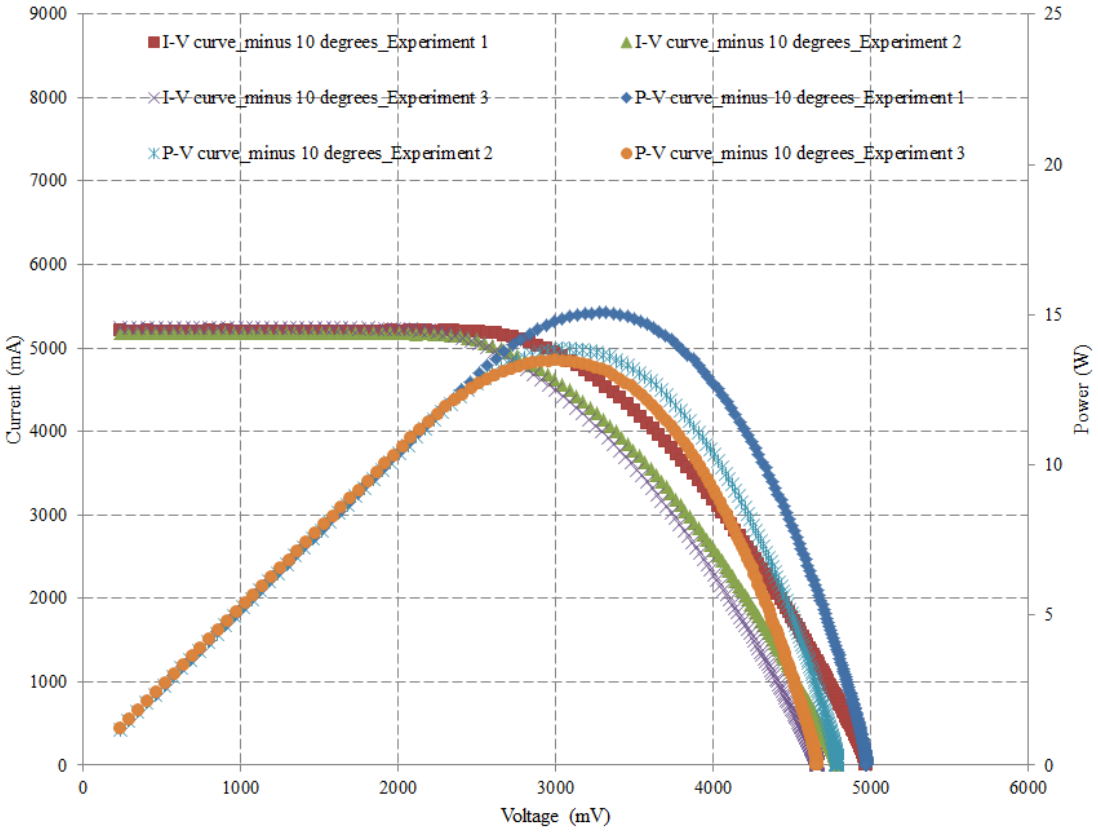

Figure 5-13 - I-V and P-V curves for the 5º DFFLAB collector at a 10º off-axis inclination

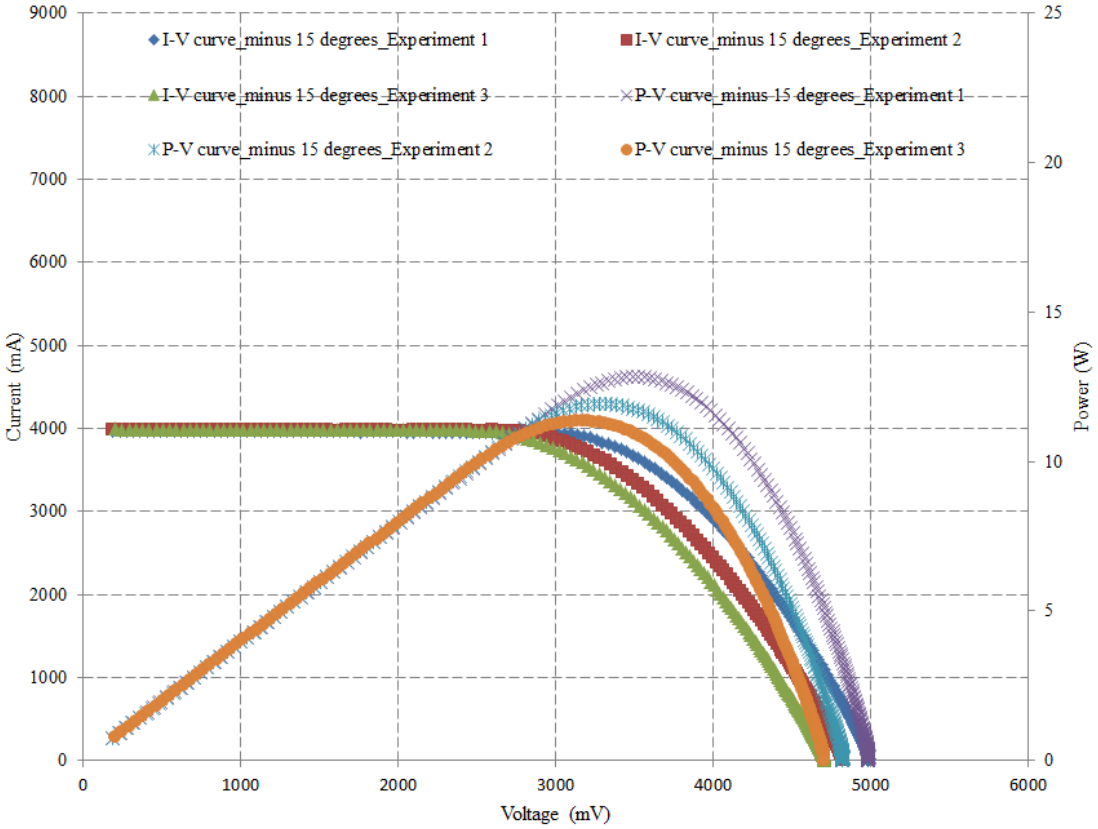

Figure 5-14 - I-V and P-V curves for the 5º DFFLAB collector at a 15º off-axis inclination

5.5.6 Summary of I-V and P-V curves for the 5º DFFLAB collector at non-perpendicular incident angles

The effect of the varying incidence angles on the 5º DFFLAB collector has been summarised in Table 5-3. The focus of this series of experiments is around comparatively evaluating the performance of the collector at the various off-axis tilt angles in conjunction with the predicted energy collection compiled in the optical design chapter (Table 3-5). When normalised against the optical efficiencies presented in Table 3-5, the average power output of the collector at each of the off-axis tilt angles does mirror the modelled relationship and corroborates the decay in power generation from the optical axis to a representative incidence angle of 15º albeit with a 1 W error which is likely to be a combined result of error in the tracker alignment (i.e. the pause between the tracker moving) and the transient solar conditions during the test period. A side-by-side comparison has been included in Table 5-4. Of specific note in Table 5-3 is the significant decrease in direct irradiance measured by the pyrheliometer, this doesn't suggest that there was no direct component to the incident radiation but does confirm that incident angle had moved far enough from perpendicular to no longer register as direct.

Table 5-3 - Summary of the performance of the 5º DFFLAB collector under off-axis incident solar radiation

Collector configuration	Experiment number	Global Irradiance (Wm^{-2})	Direct Irradiance (Wm^{-2})	P_{MPP} (W)	I_{MPP} (mA)	V_{MPP} (mV)	I_{SC} (mA)	V_{OC} (mV)	FF (-)	η (%)	T_{VOC} (ºC)
0 degrees	1	894	634	20.08	5965	3366	6770	5168	0.574	16.84	37.60
	2	898	634	18.79	5906	3181	6834	4989	0.551	15.69	39.88
	3	906	642	17.69	5871	3013	6895	4832	0.531	14.64	42.62
	4	902	638	16.79	5851	2871	6851	4702	0.521	13.96	49.38
5 degrees	1	910	6	18.09	5479	3303	6260	5110	0.566	14.90	38.84
	2	910	6	16.78	5271	3184	6240	4909	0.548	13.82	39.20
	3	908	6	15.83	5171	3061	6283	4740	0.531	13.07	46.46
	4	914	6	15.20	5220	2911	6341	4614	0.519	12.47	52.31
10 degrees	1	900	4	15.07	4601	3275	5206	4971	0.582	12.55	40.01
	2	897	4	13.85	4559	3039	5185	4786	0.558	11.58	42.30
	3	903	4	13.48	4494	2999	5242	4659	0.552	11.19	46.18
15 degrees	1	925	3	12.83	3640	3525	3970	4986	0.648	10.40	39.11
	2	923	3	11.94	3604	3313	3986	4822	0.621	9.70	42.09
	3	923	3	11.36	3588	3166	3991	4705	0.605	9.23	44.32

Table 5-4 – Comparison between the 5º DFFLAB's modelled optical efficiency and the experimental power generation for off-axis tilt angles

Tilt angle (degrees)	Optical Efficiency (%)	Normalised Power (%)
0	93	93
5	86.67	83.55
10	75.38	71.68
15	67.06	61.07

5.5.7 I-V and P-V curves for the 5º DFFLAB collector configuration during continuous exposure and various off-axis incidence angles methodology

A final series of experiments were carried out to characterise the 5º DFFLAB during continuous exposure across the collection half angle to evaluate the cumulative impact of variations in absorber flux on the temperature of the cells. Although the actual performance of the PV cells over a varying temperature range is outside of scope for this investigation it is logical to make an assessment of the impact the transient peaks in absorber flux are likely to have on the absorber material, primarily to inform further refinements of the lens design.

As with the previous experiments, the 5º DFFL was attached to the collector base, fixed to the 2-axis solar tracker and covered with a solar shield. The tracker was aligned to a tracking position where the light incident on the absorber was perpendicular to the absorber array and the 2-axis tracker was allowed to track the position of the sun relative to the position of the absorber plane until the experiment started. Once in position, the tracker was fixed in place and the solar shield was removed. The system was characterised at discrete intervals as the collector experienced a transition through the designed collection period.

The data were captured by the 3 independent data loggers and the results were compiled and analysed in Microsoft Excel. The ambient temperature conditions and global irradiance relative to the orientation of the collector during the constant exposure and continuous off-axis experiments are presented in Figure 5-8.

5.5.8 I-V and P-V curves for the 5° DFFLAB collector configuration during continuous exposure and various off-axis incidence angles

The results from the constant exposure and continuous off-axis experiments are presented in Figure 5-15 and Figure 5-16. The graphs show how the I-V and P-V characteristics of the collector varies across the selected half angle, respectively. For clarity the two curves have been presented separately in this section. The discrete sample period wasn't exact but was consistent at approximately one capture every 5 minutes (~1.25°). The effects of dark current were negligible in all cases.

5.5.9 Summary of I-V and P-V characterisation curves for the 5° DFFLAB collector under constant exposure and continuous off-axis variations

When compared to the controlled off-axis results presented in Table 5-3, it was observed from Figure 5-15 that the transient and localised peaks in absorber flux had no real impact on overall cell temperature. This is important to note because concentrating systems, particularly those with high concentration ratios, generally lead to either overheating (as seen in SMS lenses, particularly the TIR-R designs) over the absorber material or an accelerated decrease in V_{OC}. The dominant force is the reduction of V_{OC} was the absorber plane tending towards thermal equilibrium, once thermal equilibrium for the cells had been reached no further degradation in open circuit voltage was observed. In fact, as the direction of incident light moved towards the edge of the collection window V_{OC} began to increase again from its minimum value during experiment 11 (~14°).

Overall, the impacts of the angular variations in the direction of incident light can be summed up in the notes added to Figure 5-15. As the direction of the sun moved from perpendicular the level of incident radiation arriving at the absorber decreased and this decrease in available energy is mirrored in the drop in I_{SC}. In parallel, the impact of absorber temperature on V_{OC} increased with time, reducing the value of V_{OC} until the incident radiation reached a level low enough to allow the absorber array to stabilise at a lower level of thermal equilibrium.

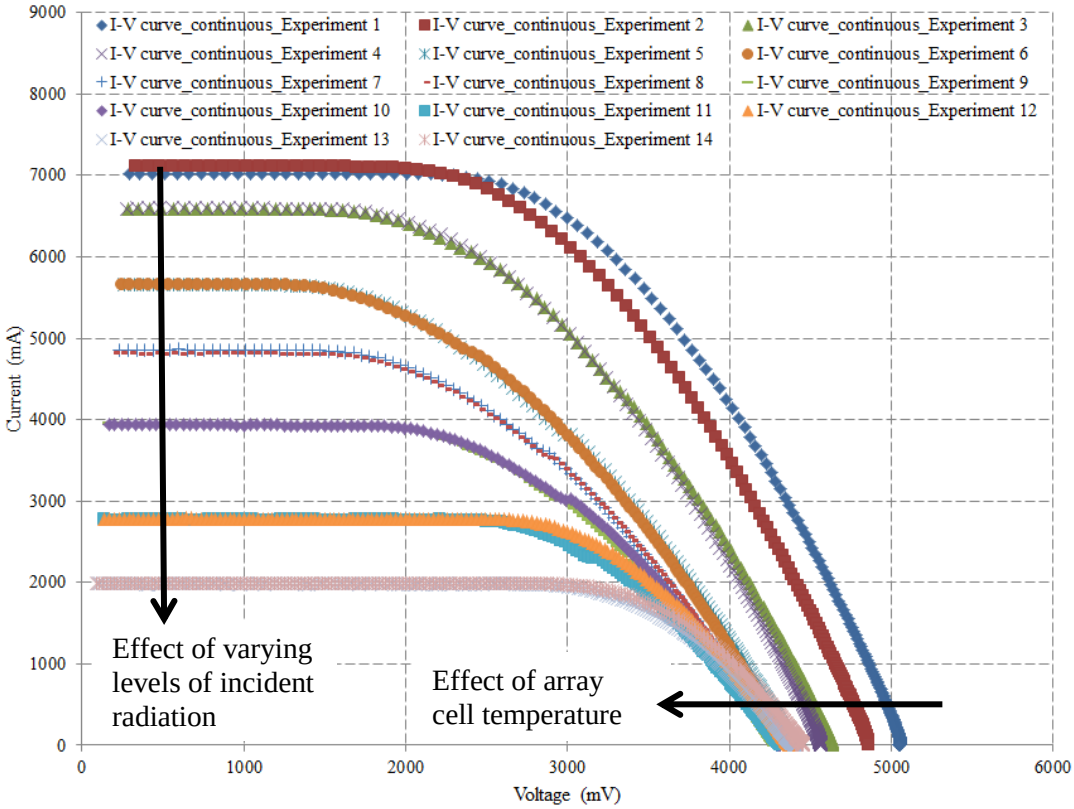

Figure 5-15 – I-V curves for the 5º DFFLAB collector under constant exposure and continuous off-axis variations

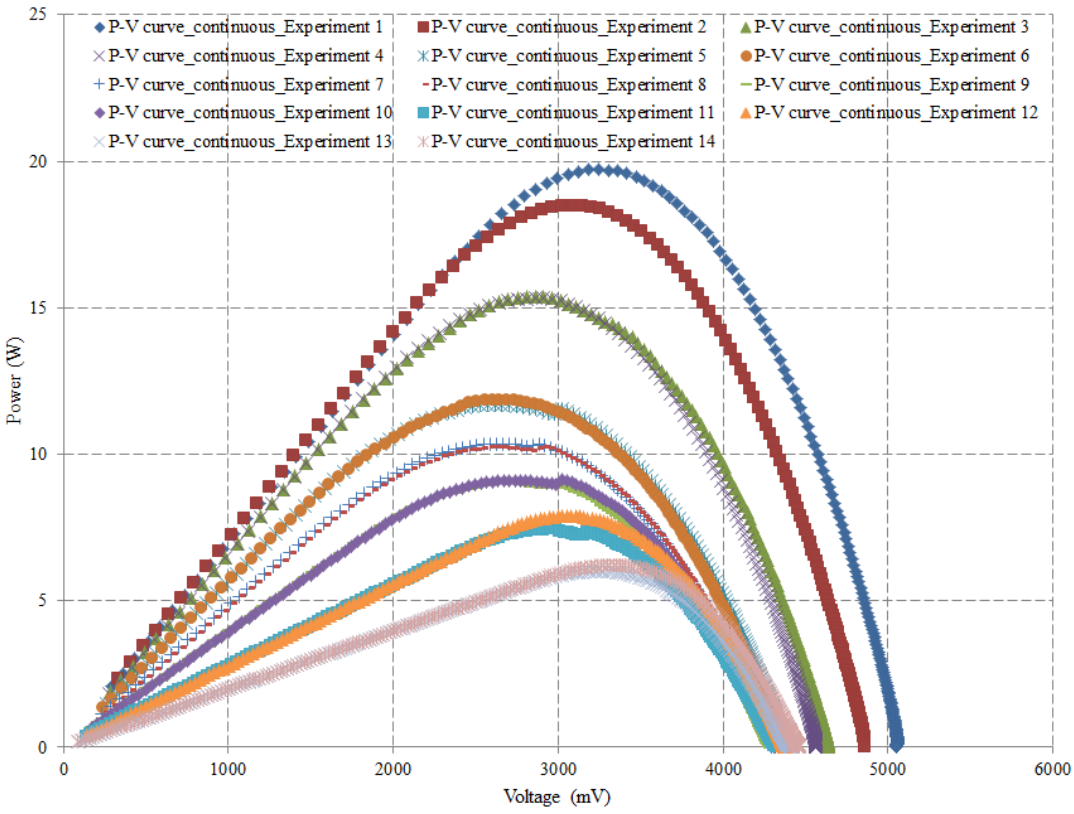

Figure 5-16 - P-V curves for the 5º DFFLAB collector under constant exposure and continuous off-axis variations

5.6 Conclusions

Despite the practical challenges encountered, the experimental programme was successful in validating the optical modelling presented in Chapter 3 and allowed the comparative analysis of the three collector configurations to characterise the various collector elements; absorber plane, Perspex cover and 5º DFFL. The following section draws a number of conclusions from the analysis carried out on the data obtained during the experimental programme.:

- From the evidence presented in Figure 5-2, it is clear that Perspex is not suitable for use as a component in a large spanning, refractive solar collectors due to the level of thermal sagging at relatively low temperatures.
- The uncovered baseline collector performed within the expected parameters of the information provided in the manufacturer's data sheet with variations in fill factor and cell efficiency attributed to the resistive losses associated with connecting the individual cells in series for the collector design.
- As an optical component, the addition of the clear Perspex sheet to the baseline collector produced an overall decrease in short circuit current of 9 % during both the $I_{SC}G$ and the I-V experiments. It is assumed this loss is primarily due to high levels of absorption within the lens.
- The addition of the 5º DFFLAB led to a theoretical increase of direct incident energy of 100 % compared to the baseline collector but only resulted in an increase in short circuit current of 74 % during the $I_{SC}G$ experiments and 62.2 % increase during the perpendicular I-V experiments.
- Optical losses from the 5º DFFLAB component were lower than the losses from the clear 3 mm Perspex sheet.
- The impacts of junction quality and series resistance on collector's performance was quantified as a function of degradation in fill factor. Overall, the fill factor for the individual cells decreased by 0.122.
- Overall cell efficiency was also reduced from ~17.5 % to ~11.5 % as a result of the decreased fill factor in conjunction with cutting the individual cells to size for the prototype design.
- The 5º DFFLAB collector demonstrated an increase in average power output during the P-V experiments of 73.6 % compared to the baseline collector.
- During the discretised off-axis experiments the normalised power output from the 5º DFFLAB mirrored the variations in optical efficiency seen during the optical modelling exercises, validating that the lens' angular performance matched the experimental output from the collector.

- Finally, during the constant exposure and continuous off-axis variations experiment it was observed that the transient and localised peaks in absorber flux had no significant impact on overall cell temperature.

Projected Performance of the validated collector Module

6 Projected Performance of the validate collector module

6.1 Introduction

The purpose of this chapter is to project the performance of the developed 5° DFFLAB collector, validated during the experimental phase, into the two building integrated environments outlined in the design brief; façade and atrium integration. The chapter begins by visually reaffirming and reinforcing the validation of the optical modelling and then briefly introduces the software programme used before presenting the modelled annual energy collection at a number of integration angles and collector orientations. Finally, a brief summary is presented describing the outcomes of the simulations and drawing conclusions on the most effective methods of integrating the developed collector into the built environment.

6.2 Verification of the Eazee optical model

Figure 6-1 presents a photo taken during the experimental phase of the project directly below a simulated energy flux distribution map of the CFFLAB collector (black) and the 5° DFFLAB collector (red). The photograph of the observed lens performance during the outdoor trials very clearly shows the same variations in intensity of the incident light on the absorber surface along with the relative position of the concentrated peaks in collection. It should be noted that the "peaking" seen during the optical modelling and the outdoor experimental testing is a direct consequence of the lens accretion method and is an area which can be improved. Figure 6-2 and Figure 6-3 show a thermal image in image photograph of the absorber plane and a close up of the thermal image with a cross sectional temperature profile, respectively. The images verify that, despite large localised peaks in energy flux along the absorbers surface, the temperature distribution across the cells during periods of illumination were relatively stable. The maximum 'spot' temperature encountered along the cell was 78.3 °C with a reduction in temperature towards the edges of the cell.

In conjunction with the detailed experimental analysis presented in the previous chapter this visual confirmation of the optical modelling is sufficient to confirm the validity of the optical models generated. Now validated the optical models can be used to extrapolate the annual predicted performance of the collector using historic meteorological data when it has been integrated into the build environment.

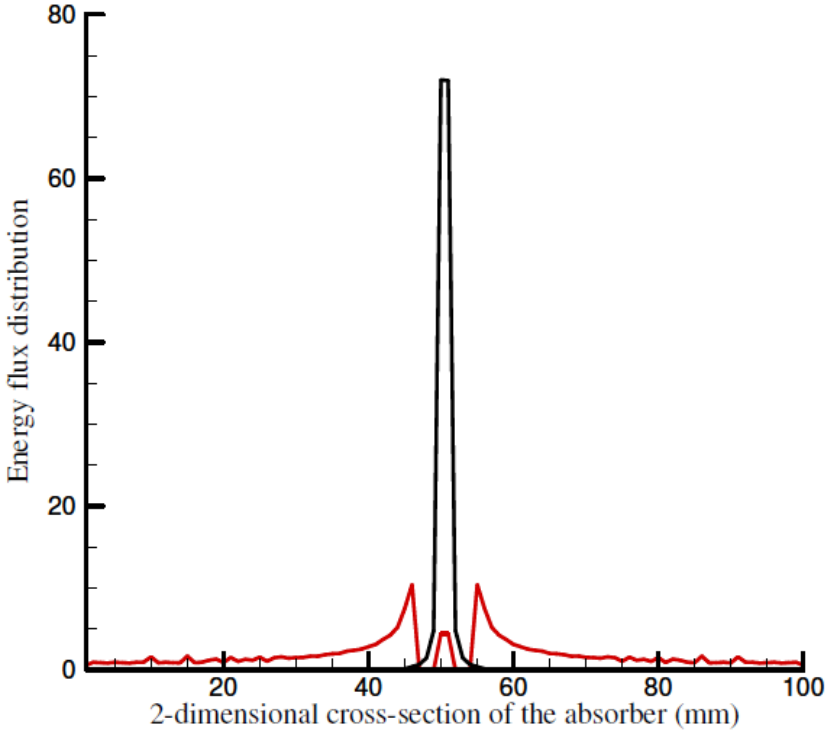

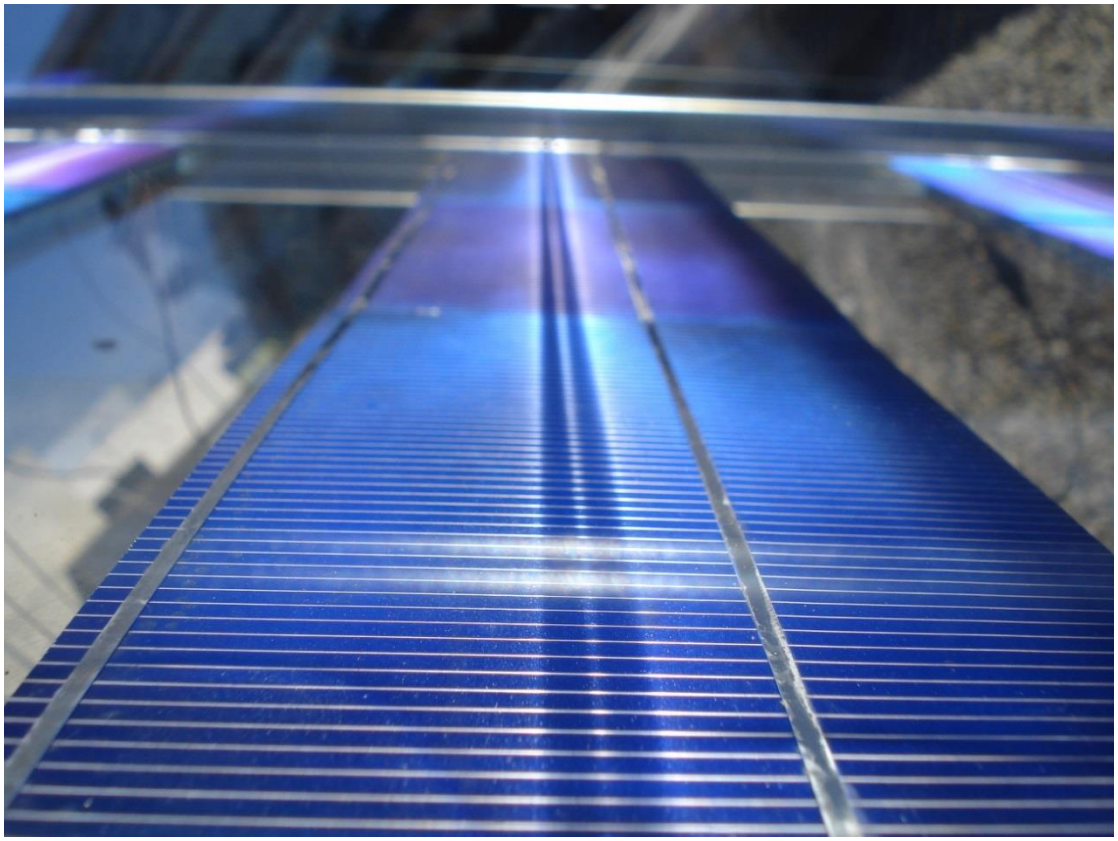

Figure 6-1 - Modelled energy flux across the absorber (red profile, top) and observed energy flux across the absorber during the outdoor experimental characterisation of the module (bottom)

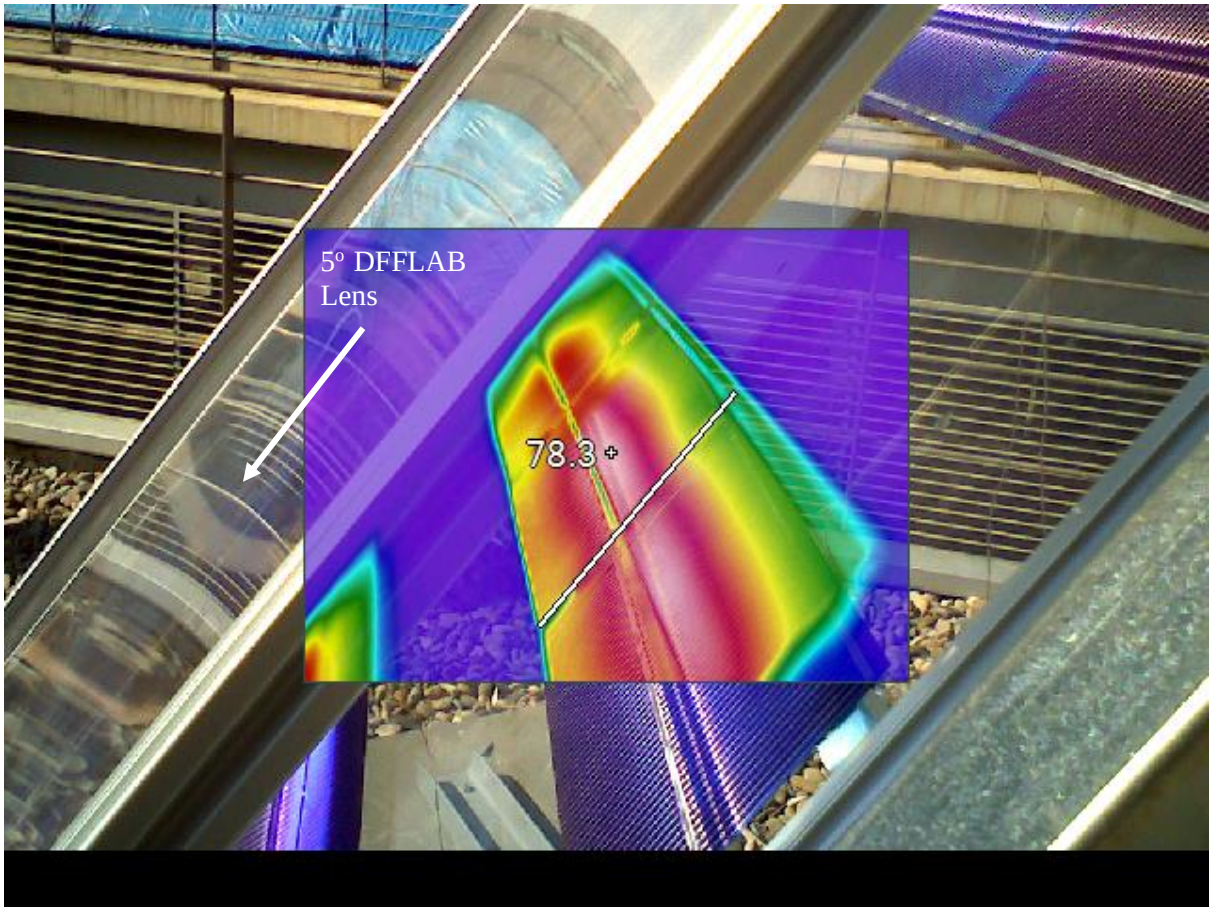

Figure 6-2 - Thermal image in image photograph of the 5º DFFLAB collector under test

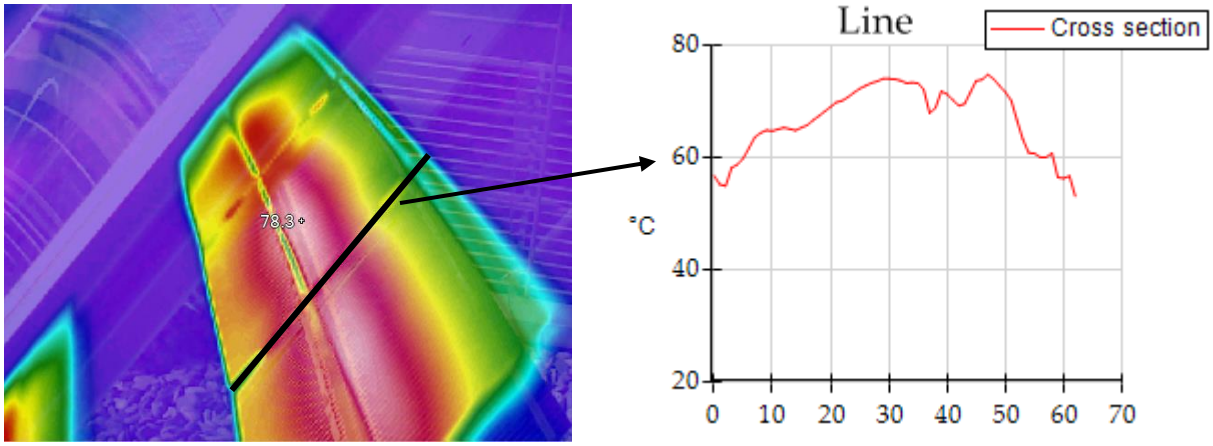

(a) (b)

Figure 6-3 - Thermal image of the absorber showing a peak surface temperature of 78.3 ºC (a) and cross-sectional temperature profile parallel to the PV cell join line (b)

6.3 Prediction of a building integrated 5° DFFLAB collector's annual performance

The designed and modelled 5° DFFLAB collector was analysed in a 3-dimensional simulation to examine the collector's annual performance by incorporating more realistic variations in both azimuth and incidence angles to determine the performance of the collector in a number of typical installations. These installations were linked to the most likely scenarios given in the design brief; atrium roofs and façades. These characteristic profiles were then combined with historic meteorological for Athens, Greece during 2005 to identify how each of the collectors would perform when integrated into either a south-facing 38° sloped atrium roof or a building façade in both East-West and North-South orientations (Figure 6-4). The main constraint encountered using the historic dataset was that the data was only available at 1-hour intervals which equates to a set of discrete 15 degree intervals. In terms of optics associated with the 5° DFFLAB design this is likely result in additional errors due to the angular dependence of the lens performance, thus affecting the predicted energy collection. However, this exercise serves to provide some context into the collector's output when installed as part of a Building Integrated Photovoltaic (BIPV) system. All profiles were plotted against the same axis for ease of comparison.

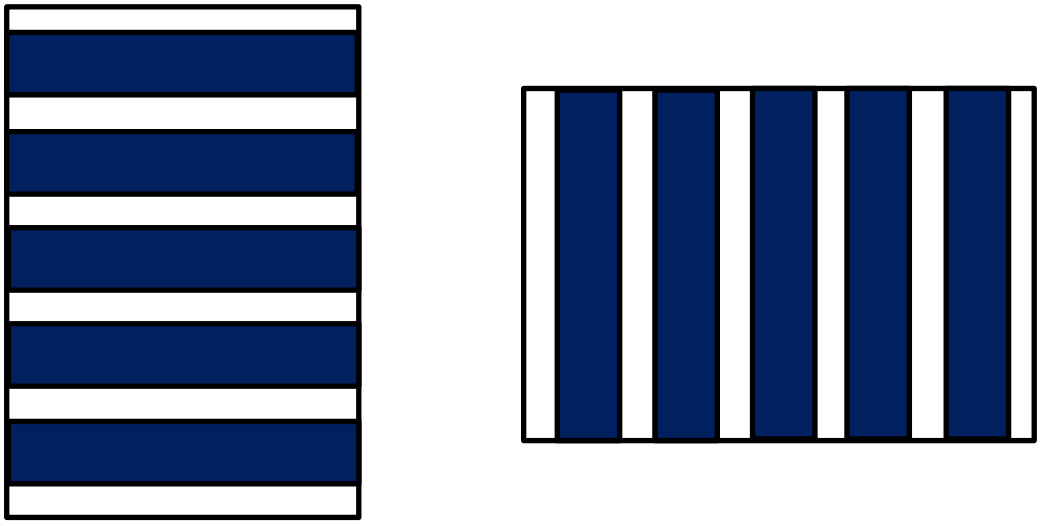

(a) (b)

Figure 6-4 - Collector configurations: East-West (a) and North-South (b)

6.3.1 Atrium Roof Integration

Atrium roof integration was the first system integration method investigated. Figure 2-30 has been reproduced from the literature review for clarity (Figure 6-5).

Figure 6-5 – PV cells integrated into atrium glazing

(Thomas, 2003)

Figure 6-6 and Figure 6-7 show the daily energy collection per meter squared for the 5º DFFLAB collector for each day in Athens, Greece during 2005 in their North-South and East-West collector orientations, respectively.

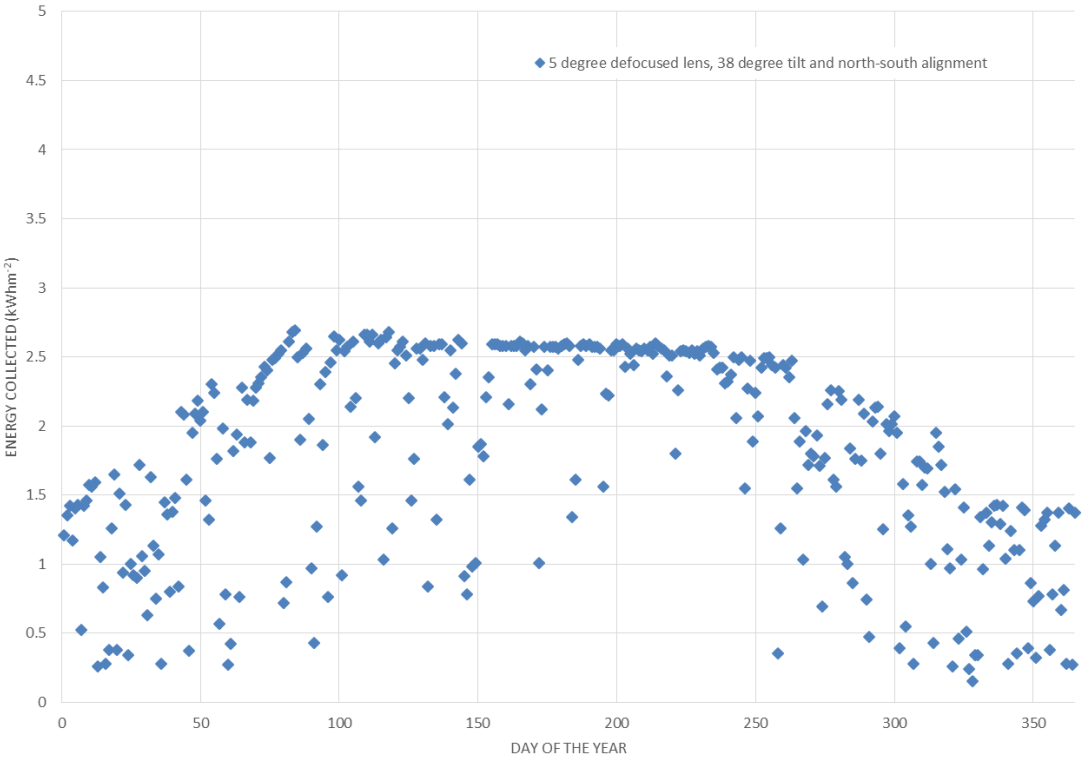

Figure 6-6 - Atrium integration with a North-South collector orientation

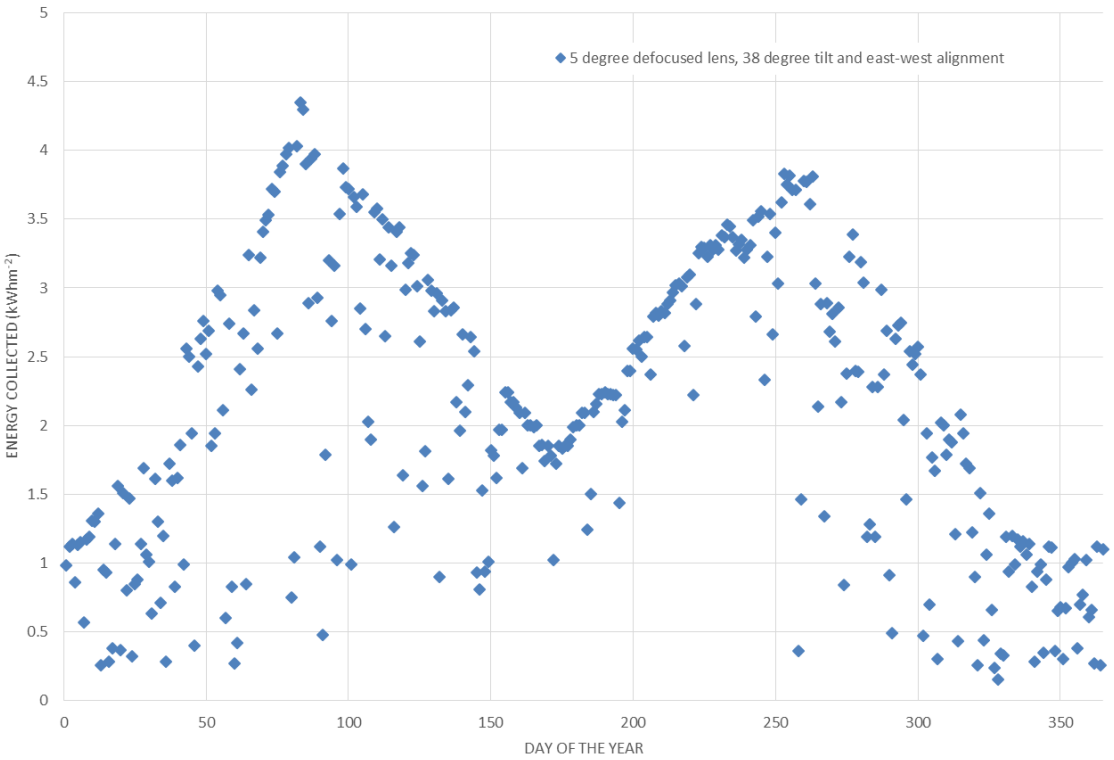

Figure 6-7 - Atrium integration with an East-West collector orientation

6.3.2 Façade integrated

A façade integrated solar collector (with a β angle of 90° i.e. vertically mounted) was the second type of system highlighted in the design brief for the developed 5° DFFLAB collector. Figure 2-32 has been reproduced from the literature review for clarity (Figure 6-8).

Figure 6-8 – Vertical building integrated PV modules

(Thomas, 2003)

Figure 6-9 and Figure 6-10 show the daily energy collection per meter squared for the 5° DFFLAB collector for each day in Athens, Greece during 2005 in their North-South and East-West collector orientations, respectively.

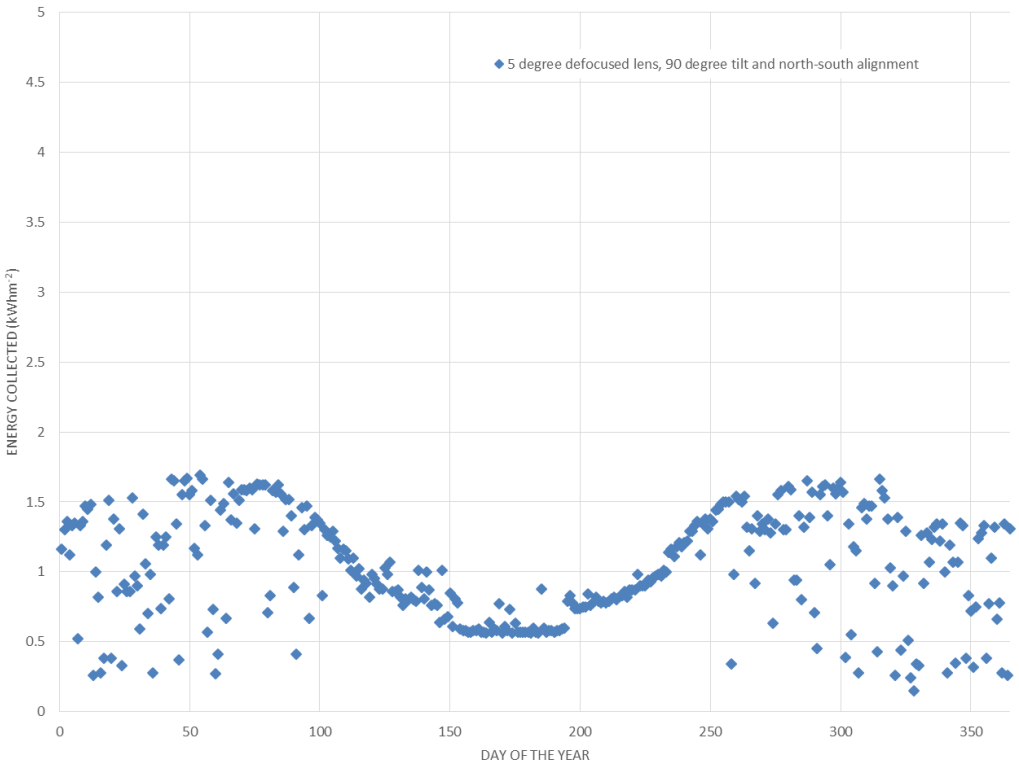

Figure 6-9 - Façade integration with a North-South collector orientation

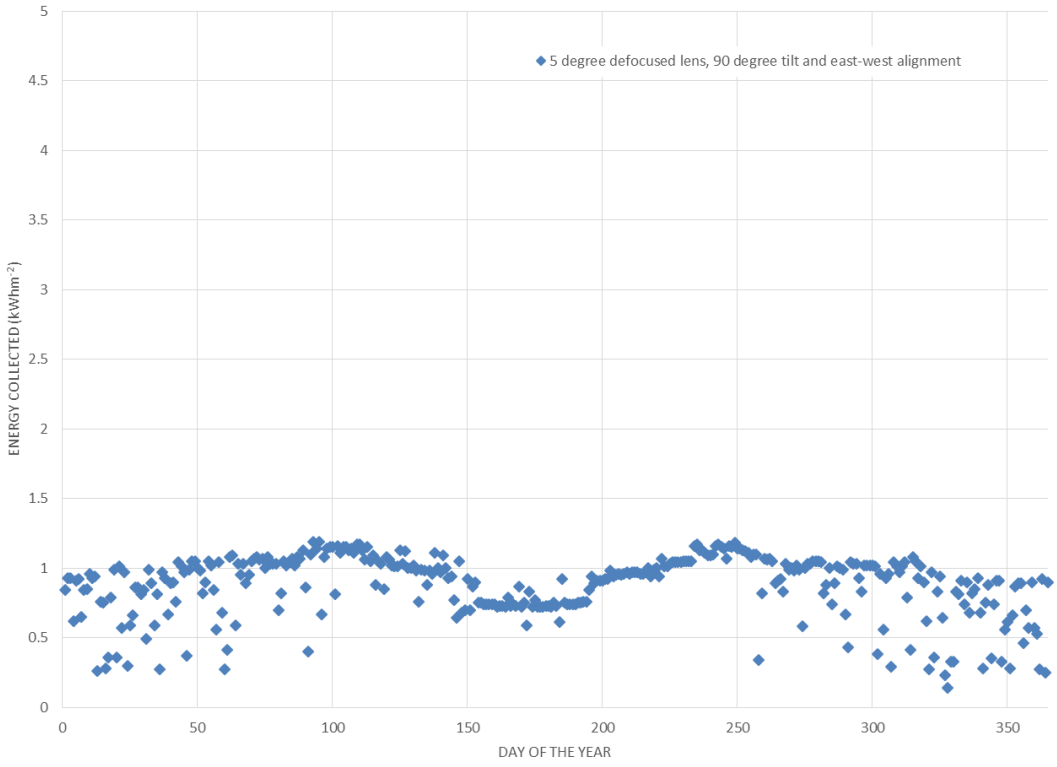

Figure 6-10 - Façade integration with an East-West collector orientation

6.3.3 Summary of annual performance models

The monthly data generated from the annual energy collection models has been compiled and presented in Table 6-1 and Figure 6-11.

From the information presented, the building integration method with the most significant potential is clearly atrium integration. Figure 6-11 shows that the two atrium integrated collectors performed consistently higher than the façade collectors for 10 of the 12 months of the year. The annual energy collection totals presented in Table 6-1 show the extent of gap in collection efficiencies between the two systems with the atrium integrated models generating over twice the annual energy collected by the façade integrated systems. This disparity in performance is a direct outcome of the optical design methodology used. In designing a line axial Fresnel lens for this application, an atrium integrated system was unintentionally favoured because of the more optimal transient geometric variations in incident range seen by the tilted collector and a reduction in end losses.

In comparing the performance as a consequence of absorber orientation, the results were a little unexpected. Aligning the absorbers in their East-West orientation for the atrium integrated system yielded an increase in collection efficiency of 16% with significant improvements in performance noted during the shoulder months (Figure 6-7). In contrast, the East-West orientation of the façade integrated system performed better than the North-South orientation during May to August with an overall efficiency deficit of 14.5% over the year. This can again be attributed to the line axial design methodology used and raises an interesting area for further study; can a line axial design be augmented with a secondary refractive profile at right angles to the first to increase the performance of a façade integrated solar window?

It is clear that in integrating the collector's lens at 38^{o} for the atrium collectors the absorber is exposed for longer durations maximising both solar energy capture for electrical generation and reducing the peak solar loading within the building's envelope.

Table 6-1 – Summary of the simulated annual energy collection

	Atrium		Façade	
Month	North-South	East-West	North-South	East-West
January	33.6	30.51	31.53	22.83
February	41.08	50.13	33.67	24.05
March	61.28	90.22	41.94	29.64
April	63.12	84.46	33.3	31.67
May	63.86	69.61	26.21	29.44
June	72.91	57.47	18.17	22.47
July	75.35	71.96	21.92	26.59
August	76.16	98.12	30.97	32.54
September	60.95	89.92	39.56	30.74
October	50.1	65.68	39.56	28.11
November	32.94	35.21	29.78	22.35
December	30.26	24.69	29.14	20.83
Annual Energy Collection	661.61	767.98	375.75	321.26
Units	$kWhm^{-2}$	$kWhm^{-2}$	$kWhm^{-2}$	$kWhm^{-2}$

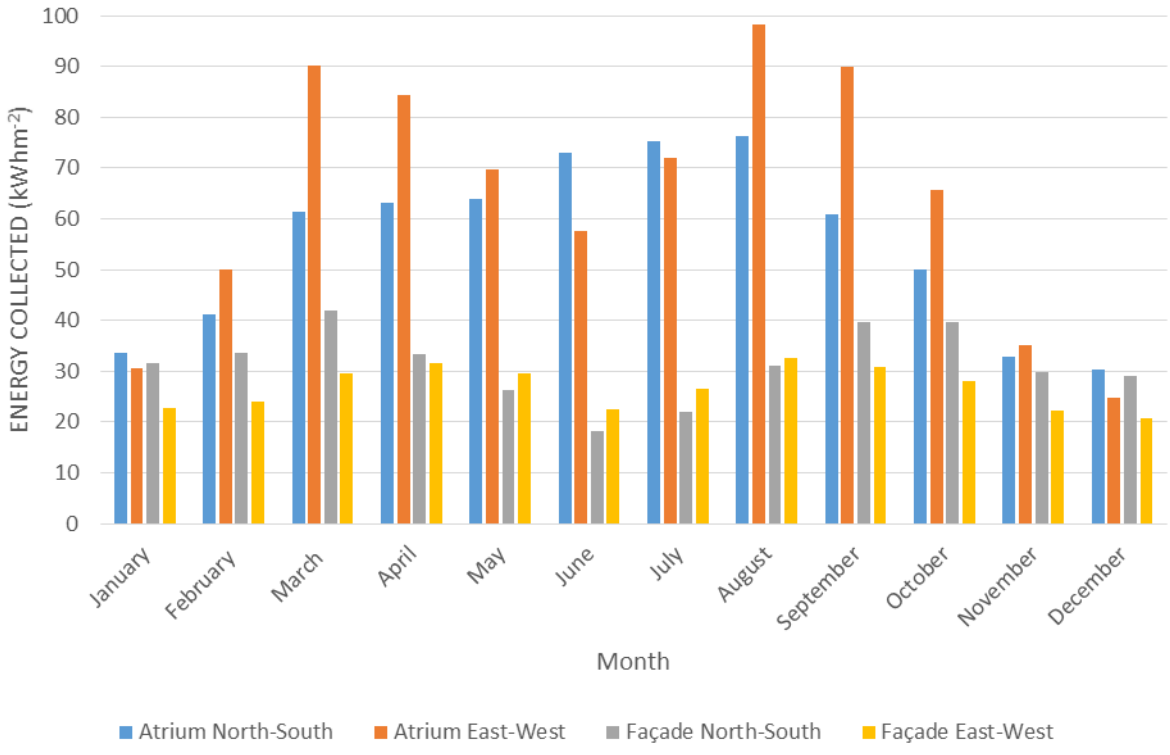

Figure 6-11 – Projected monthly energy collection for the four building integration methods

The information presented in Table 6-1 and Figure 6-11 provide a valuable insight into the 5° DFFLAB collector but the final test for the novel system design is; how does it compare to the baseline system across the full collection period, annually? That comparison is presented in Table 6-2 and provides some interesting areas for discussion.

Given that the collection period of the 5° DFFLAB collector was one hour and 20 minutes either side of solar noon, and that the baseline design wasn't constrained by the same limit, the difference in energy collection was not as pronounced as expected. Atrium integration was again the highest performing building integration method with the North-South integrated module collecting 94 % of the energy collected by the baseline design and East-West integration collecting an additional 9 % above the baseline collector's performance. The comparison for façade integration was not as favourable with North-South and East-West integration performing at 88 % and 76 % of the baseline collector's energy collection, respectively. This indicates that further refinement for façade integration is necessary.

Table 6-2 – Comparison of Baseline and 5° DFFLAB annual collector performance for the four building integration methods

Collector	Alignment	BIPV configuration	Annual Energy Collected ($kWhm^{-2}yr^{-1}$)
Baseline	N/S	Façade	425
		Atrium	706
	E/W	Façade	425
		Atrium	707
5° DFFLAB	N/S	Façade	375
		Atrium	661
	E/W	Façade	321
		Atrium	768

6.4 Chapter Summary

This chapter has addressed the final component of the design brief outlined at the end of the literature review. It has extended the simulation of the developed lens within the context of atrium and façade building integrated systems and, in using real world historic data, has projected the performance of the lens in operation. The projections have shown that the most effective collector orientation produced an annual energy collection of 768 $kWhm^{-2}yr^{-1}$ for an atrium roof (38^{o} slope) and an East-West absorber alignment, providing a 9 % increase in energy collection above the baseline design.

The results presented in this chapter have confirmed that, by replacing a building element (window), a building integrated solar collector utilising a 5^{o} defocused fast Fresnel lens is capable of providing quantifiable benefits to a building in terms of electrical energy collection. It is also important to note that the energy generated is a by-product of passive solar shading which produces a further energy saving by lowering solar gains across the collection period either side of solar noon.

Conclusions and Recommendations

7 Conclusions and Recommendations

In bringing this thesis to a close the following section detailing the main conclusions from the work carried out herein has been presented. The conclusions are then followed by a series of recommendations for further study which have been direct outcomes of the proof of concept design and characterisation process.

7.1 Conclusions

This thesis has taken a broad approach into building integrated solar energy collection and has presented a novel solution which attempts to address as many of the physical, technical and aesthetic barriers to these technologies as possible. The literature review led to the design of a novel, modular, solar window for building integration applications. Comparable in scale to a double-glazed window, the design conceals the dark absorber material from non-perpendicular viewpoints, provides solar shading and electrical energy generation either side of solar noon while at the same time allowing natural lighting to be conveyed into the building's interior outside of the selective collection period (solar noon ±20 degrees). The subsections which follow highlight the main conclusions drawn from the each of the areas of original work presented throughout this thesis.

7.1.1 Conclusions from the optical design

A comprehensive investigation into the design and optimisation of a series of fast Fresnel lenses for solar energy collection was carried out, including varying levels of defocus. The developed lenses were then modelled using Eazee, a ray tracing program and the results were analysed in detail. That analysis led to the following conclusions:

- The addition of a conventional fast Fresnel lens to the baseline collector led to a significant increase in energy collection of up to 75% when the direction of the incident light was perpendicular to the collector plane. However, the optical performance rapidly deteriorated as the incidence angle increased and the impact of total internal reflections within the lens became more pronounced.
- The resolution of prism width on a conventional fast Fresnel lens within the range of 100 to 275 microns has little effect on the performance of the lens. Increasing the prism width

between 300 and 375 microns resulted in a more erratic optical performance of the conventional lens design.

- Defocusing a conventional fast Fresnel lens spreads the incident energy over a wider area, reduces reflection losses from the prism surfaces and delays total internal reflection by creating a buffer between the slope angle and the critical angle of total internal reflection.
- Defocusing a conventional fast Fresnel lens by more than 10 degrees leads to a significant drop-off in performance. In contrast the trend in performance for lenses with a defocus of less than 10 degrees was an increase in performance compared to a conventional fast Fresnel lens.
- Defocusing a conventional fast Fresnel lens by 6 degrees resulted in a 4.44% increase in the optical efficiency of the collector, 4.21% for the 5 degree defocused lens manufactured for the proof of concept prototype.
- An improvement in the energy flux distribution was observed between the 5 degree defocused fast Fresnel lens and the conventional fast Fresnel lens.

7.1.2 Conclusions from the experimental characterisation of the system

A detailed programme of comparative real world, outdoor experiments was carried out to validate the performance of the optical design and modelling of the 5^{o} defocused fast Fresnel lens against a series of baseline designs. The use of the baseline designs allowed for a very clear understanding of the impact each refractive element of the novel collector design was having on solar energy collection. This detailed experimental programme resulted in the collection and subsequent analysis of real-world data and the following conclusions are an output of that process:

- From the evidence presented in Figure 5-2, it is clear that Perspex is not suitable for use as a component in a large spanning, refractive solar collector due to the level of thermal sagging at relatively low temperatures.
- The uncovered baseline collector performed within the expected parameters of the information provided in the manufacturer's data sheet with variations in fill factor and cell efficiency attributed to the resistive losses associated with connecting the individual cells in series for the collector design.
- As an optical component, the addition of the clear Perspex sheet to the baseline collector produced an overall decrease in short circuit current of 9 % during both the $I_{SC}G$ and the I-V experiments. It is assumed this loss is primarily due to high levels of absorption within the lens.

- The addition of the 5º DFFLAB led to a theoretical increase of direct incident energy of 100 % compared to the baseline collector but only resulted in an increase in short circuit current of 74 % during the $I_{SC}G$ experiments and 62.2 % increase during the perpendicular I-V experiments.
- Optical losses from the 5º DFFLAB component were lower than the losses from the clear 3 mm Perspex sheet.
- The impacts of junction quality and series resistance on collector's performance was quantified as a function of degradation in fill factor. Overall, the fill factor for the individual cells decreased by 0.122.
- Overall cell efficiency was also reduced from ~17.5 % to ~11.5 % as a result of the decreased fill factor in conjunction with cutting the individual cells to size for the prototype design.
- The 5º DFFLAB collector demonstrated an increase in average power output during the P-V experiments of 73.6 % compared to the baseline collector.
- During the discretised off-axis experiments the normalised power output from the 5º DFFLAB mirrored the variations in optical efficiency seen during the optical modelling exercises, validating that the lens' angular performance matched the experimental output from the collector.
- Finally, during the constant exposure and continuous off-axis variations experiment it was observed that the transient and localised peaks in absorber flux had no significant impact on overall cell temperature.

7.1.3 Conclusions from the projected annual performance on a building integrated collector

After the optical model of the 5º defocused fast Fresnel lens had been validated through both experimental data and visual observation it could be used to predict the annual performance of the novel design, integrated into the build environment, in four separate orientations. That prediction of installed performance using historical meteorological data produced the following conclusions:

- The observed distribution of light across the absorber plane clearly showed the same variations in intensity described by the absorber flux maps created during the optical modelling.
- The developed collector performed significantly better when integrated within an atrium roof.

- The orientation of the absorber plane had an impact on the overall energy collected with an East-West alignment of the collector resulting in an additional energy collection of ~106 $kWhm^{-2}$ over a North-South alignment for an atrium integrated panel. Conversely, for a façade mounted collector a North-South alignment collected ~55 $kWhm^{-2}$ more than the East-West orientation.
- When compared against the annual performance of the baseline collector the atrium integrated 5^{o} DFFLAB module collected an additional 9 % of incident energy annually.

7.2 Recommendations for further study

Despite the detailed optical and experimental analysis of the proof of concept prototype, the designs presented in this thesis are still at a relatively immature stage in development. The eventual end goal for this type of innovation should be to shrink the cavity back down to the dimensions of a double-glazed window pane, allowing both active energy collection and passive solar shading throughout the year. To achieve this goal further research is required into:

- the most effective way of managing the accretion region between the defocussed and conventional lens profiles. It may be possible to create a much more stable absorber flux, within the constraints of both aspect ratio and managing refractive losses, by actively designing around the accretion point across the entire lens. Including the potential of developing an aspheric region of the lens at the accretion point,
- augmentation with a secondary refractive profile at right angles to the first to increase the performance of a façade integrated solar window,
- the potential of using the SMS technique to improve uniformity over the absorber area,
- the most appropriate material(s) and thickness to use for both the refractive elements and the structural window pane,
- the most effective way(s) to bond the refractive element to the structural window material,
- the most effective way(s) to bond the PV cells to the structural window material,
- a comprehensive optical and thermal modelling of the reduced depth unit,
- the potential of managing PV cell working temperature by controlling the gaseous cavity between the inner and outer window panes,
- an optimised system for replacing an existing window with a Fresnel augmented solar collector,
- managing modular integration within the architectural, aesthetic and technical barriers outlined in this thesis,
- evaluating the consequences on PV cell performance of recurring peaks in transient energy flux across the absorber plane,
- evaluating the quality and distribution of the natural light transmitted into the building outside of the collection window,
- Finally, the practical challenges around converting the design to a hard tool for cost effectively moulding cheap refractive lenses at scale should be examined as part of a design for manufacture activity.

The recommendations presented above are not fully comprehensive, but they do encompass the most significant research challenges derived from the work carried out in this thesis.

References

8 References

ALVAREZ, J.L., HERNÁNDEZ, M., BENÍTEZ, P., MIÑANO, J.C., (2001), TIR-R concentrator: A new compact high-gain SMS, In Proceedings of the 2001 SPIE conference: nonimaging optics: maximum efficiency light transfer VI, **4446**, pp 32 – 42

ANON, (1993), BS 4937-30: International thermocouple reference tables. Extension and compensating cables. Tolerances and identification system, BSI, UK

ANON, (2008), Climate Change Act, The Stationary Office Ltd, London, UK

ANON, (2011), DIRECTIVE 2011/65/EU OF THE EUROPEAN PARLIAMENT AND OF THE COUNCIL of 8 June 2011 on the restriction of the use of certain hazardous substances in electrical and electronic equipment (recast), Available online: https://eur-lex.europa.eu/legal-content/EN/TXT/?uri=CELEX%3A32011L0065 [Accessed: January 2020]

ANON, (2013a), Sunways Solar Cells Mono 156 (AH50-H): Datasheet, Available online at: https://www.enfsolar.com/Product/pdf/Cell/517cc317dd81c.pdf [Accessed: January 2020]

ANON, (2013b), CR1000 product brochure, Campbell Scientific, Available online: http://s.campbellsci.com/documents/us/product-brochures/b_cr1000.pdf [Accessed: January 2020]

ANON., (2015a), Conference of the Parties (COP21): Adoption of the Paris Agreement. Available online: https://unfccc.int/files/essential_background/convention/application/pdf/english_paris_agreement.pdf [Accessed: 13/5/2020]

ANON, (2015b), Transforming our world: the 2030 Agenda for Sustainable Development, Available online at: http://www.un.org/ga/search/view_doc.asp?symbol=A/RES/70/1&Lang=E [Accessed January 2020]

ANON., (2016), Paris Agreement: Entry into force communication., Available online: https://treaties.un.org/doc/Publication/CN/2016/CN.735.2016-Eng.pdf [Accessed: 13/5/2020]

ANON., (2017), Global Market Outlook for Solar Power: 2017 – 2021, SolarPower Europe, Brussels, Belgium

ANON., (2018a), Directive (EU) 2018/844, Available online: https://eur-lex.europa.eu/legal-content/EN/TXT/HTML/?uri=CELEX:32018L0844&from=EN [Accessed: 13/5/2020]

ANON, (2018b), PV module/panel and PV array, Samlexsolar, Available online: http://www.samlexsolar.com/learning-center/solar-cell-module-array.aspx [Accessed: January 2020]

ANON., (2019a), Net Zero – The UK's contribution to stopping global warming., Available online: https://www.theccc.org.uk/publication/net-zero-the-uks-contribution-to-stopping-global-warming/ [Accessed: 13/5/2020]

ANON., (2019b), The Climate Change Act 2008 (2050 Target Amendment) Order 2019 Available online:

https://www.legislation.gov.uk/ukdsi/2019/9780111187654/pdfs/ukdsi_9780111187654_en.pdf [Accessed: 13/5/2020]

ASTM, (2003), G 173-03 – Standard tables for reference solar spectral irradiances: direct normal and hemispherical on 37º tilted surface, American society for testing and materials, West Conshohocken, PA, USA

BENFORD, F., BOCK, J.E., (1939), A time analysis of sunshine, Trans. Am. Illumin. Eng. Soc., **34**, 200

BENÍTEZ, P., MIÑANO, J.C., BLEN, J., MOHEDANO, R., CHAVES, J., DROSS, O., HERNÁNDEZ, M., ALVAREZ, J.L., FALICOFF, W., (2004), SMS design method in 3D geometry: examples and applications, In Proceedings of the 2004 SPIE conference: nonimaging optics: maximum efficiency light transfer VII, **5185**, pp 18 – 29

BERGER, V., (2003), The method of optimization for illumination optical systems with application of Total Internal Reflection, In Proceedings of the 2003 SPIE conference: design of efficient illumination systems, pp 166 – 174

BOETTNER, E.A., BARNETT, N.E., (1951), Design and construction of Fresnel optics for photoelectric receivers, Journal of the optical society of America, **41**(11), pp 849 – 857

BORN, M., WOLF, E., (2002), Principles of Optics (7th Edition), Cambridge University Press, Cambridge, UK

BUTTI, K., PERLIN, J., (1981), A Golden Thread – 2500 years of solar architecture and technology, Marion Boyars Publisher Ltd, London, UK

CALERO, D.P., MIÑANO, J.C., BENÍTEZ, P., HERNANDEZ, M., CVETKOVIC, A., (2006), Design and modelling of a measuring device for a TIR-R concentrator, In Proceedings of the 2006 SPIE conference: High and low concentration for solar electrical applications, **6339**, pp 63390H: 1 – 11

CHEMISANA VILLEGAS, D., (2009), Diseño y characterization de un concentrador térmico – fotovoltaico cuasiestacionario para integración arquitectónica, PhD Thesis, University of Lleida, Lleida, Spain *In Spanish

CHEMISANA VILLEGAS, D., ROSELL, J.L., (2011), Design and optical performance of a nonimaging Fresnel transmissive concentrator for building integration applications, Energy Conversion and Management, **52**, 3241-3248

CHOW, T.T., (2009), A review on photovoltaic/thermal hybrid solar technology, Applied Energy, **87**, pp 365-379

CIBSE, (2009), KS15: Capturing solar energy, CIBSE Publications, London, UK

COLLARES-PEREIRA, M., (1979), High temperature solar collector with optimal concentration: non-focusing Fresnel with secondary concentrator, Solar Energy, 23, pp 409 – 420

COLLARES-PEREIRA, M., RABL, A., WINSTON, R., (1977), Lens mirror combinations with maximal concentration, Applied Optics, **16**(10), pp 2677 - 2683

DROSS, O., MOHEDANO, R., BENÍTEZ, P., MIÑANO, J.C., CHAVES, J., BLEN, J., HERNÁNDEZ, M., MUÑOZ, F., (2004), Review of SMS design methods and real world applications, In Proceedings of the 2004 SPIE conference: nonimaging optics: Design of efficient illumination systems, **5529**, pp 35 – 47

DUFFIE, J.A., BECKMAN, W.A., (2006), Solar Engineering of Thermal Processes, 3rd Edition, Wiley-Interscience, New York, USA

DUPONT, E., KOPPELAAR, R., JEANMART, HERVÉ., (2020), Global available solar energy under physical and energy return on investment constraints, Applied Energy, 257, 113968

EREC, (2010), RE-thinking 2050: A 100% Renewable Energy Vision for the European Union, European Renewable Energy Council, Brussels, Belgium

EU, (2009), European Renewable Directive (directive 2009/28/EC of the European parliament and of the council), Official Journal of the European Union, Brussels, Belgium

GAUR, M.K., (2018), Recent development and applications of evacuated tube solar collectors. In proceedings of the 2018 conference on Smart Technologies for Green and Sustainable Future

GOSWAMI, D.Y., KREITH, F., KREIDER, J.F., (2000), Principles of solar engineering, Taylor and Francis, Philadelphia, USA

GRABOVIČKIC, D., MIÑANO, J.C., BENÍTEZ, P., (2009), Free form V-groove reflector design with the SMS method" In Proceedings of the 2009 SPIE conference: nonimaging optics: Efficient design for illumination and solar concentration VI, **7423**, pp 742303: 1 – 11

GRAY, J.L., (2011), Handbook of photovoltaic science and engineering, Chapter 3 – The physics of solar cells, Edited by Luque, A., Hegedus, S., John Wiley and Sons Ltd, UK

HINTERBERGER, H., WINSTON, R., (1966), Efficient Light Coupler for Threshold Čerenkov Counters, Review of Scientific Instruments, **37**, pp. 1094 – 1095

HOWELL, J., SIEGEL, R., MENGÜÇ, M.P., (2010), Thermal Radiation Heat Transfer (4th Edition), Taylor & Francis Group, USA

JAMES, L.W., WILLIAMS, J.K., (1978), Fresnel optics for solar concentration on photovoltaic cells, In Proceedings of the 13th IEEE photovoltaic specialists conference, pp 673 – 679

JOHNSON, B.K., (1942), Recent optical materials and their possible applications, In Proceeding of the symposium on recent optical materials, 1942, pp 291 – 300

KAAN, H. and REIJENGA, T., (2004), Photovoltaics in an architectural context, Progress in Photovoltaics: research and applications, **12**, pp 395 - 408

KALOGIROU, S.A., (2004), Solar thermal collectors and applications, Progress in Energy and Combustion Science, 30, pp 231 – 295

KIPP AND ZONEN, (2013a), CM4 High Temperature Pyranometer Specification Sheet, Available online: https://www.kippzonen.com/Product/10/CM4-Pyranometer#.XinRtGj7SUk [Accessed: January 2020]

KIPP AND ZONEN, (2013b), CHP1 Pyrheliometer Specification Sheet, Available online: https://www.kippzonen.com/Product/18/CHP1-Pyrheliometer#.XinSzmj7SUk [Accessed: January 2020]

KRITCHMAN, E.M., (1984), Two stage linear Fresnel lens, Solar Energy, **33**(1), pp 35 – 39

KRITCHMAN, E.M., FRIESEM, A.A., YEKUTIELI, G., (1979a), Efficient Fresnel lens for solar concentration, Solar Energy, **22**, pp 119 – 123

KRITCHMAN, E.M., FRIESEM, A.A., YEKUTIELI, G., (1979b), Highly concentrating Fresnel lenses, Applied Optics, **18**(15), pp 2688 – 2695

LEUTZ, R., FU, L., ANNEN, H.P., (2009), Stress in large area optics for solar concentrators, In Proceedings of the 2009 SPIE conference: reliability of photocells, modules, components and systems II., **7412**, pp 741206: 1 – 7

LEUTZ, R., RIES, H., (2003a), Tailored Fresnel optics 2 – The facets, In Proceedings of the 2003 SPIE conference: design of efficient illumination systems, pp 159 – 165

LEUTZ, R., RIES, H., (2003b), Squaring the circle – the use of microstructures for converting and homogenizing beam patterns, In Proceedings of the 2003 SPIE conference: design of efficient illumination systems, pp 106 – 112

LEUTZ, R., SUZUKI, A., (2001), Nonimaging Fresnel Lenses – Design and performance of solar concentrators, Springer-Verlag, Berlin, Germany

LEUTZ, R., SUZUKI, A., AKISAWA, A., KASHIWAGI, T., (1999), Design of a nonimaging Fresnel lens for solar concentrators, Solar Energy, **65**(6), pp 379 – 387

LEUTZ, R., SUZUKI, A., AKISAWA, A., KASHIWAGI, T., (2000a), Shaped nonimaging Fresnel lenses, Journal of optics A: Pure and applied optics, **2**, pp 112 – 116

LEUTZ, R., SUZUKI, A., AKISAWA, A., KASHIWAGI, T., (2000b), Flux densities in optimum nonimaging Fresnel lens solar concentrators for space, In Proceedings of the 2000 Photovoltaic specialists conference, pp 1146 – 1149

LIN, J.S., HUANG, W.C., HSU, H.C., CHANG, M.W., LIU, C.P., (2005), A study for special Fresnel lens for high efficiency solar concentrators, In Proceedings of the 2005 SPIE conference: design of efficient illumination systems, **5942**, pp 59420: 1 – 9

LORENZO, E., (1981), Chromatic aberration effect on solar energy systems using Fresnel lenses, Applied Optics, **20**(21), pp 3729 – 3732

LORENZO, E., LUQUE, A., (1981), Fresnel lens analysis for solar energy applications, Applied Optics, **20**(17), pp 2941 – 2945

LORENZO, E., LUQUE, A., (1982), Comparison of Fresnel lenses and parabolic mirrors as solar energy concentrators, Applied Optics, **21**(10), pp 1851 – 1853

LUCERA, L., MACHUI, F., SCHMIDT, H.D., AHMAD, T., KUBIS, P., STROHM, S., (2017), Printed semi-transparent large area organic photovoltaic modules with power conversion efficiencies of close to 5 %, Organ. Electronics, **45**, pp 209-214

LUI, C.P., LIN, H.Y., HSIAO, C.T., (2009), Optical design of a new combo solar concentrator, In Proceedings of the 2009 SPIE conference: nonimaging optics: Efficient design for illumination and solar concentration VI, **7423**, pp 74230X: 1 – 11

LUQUE, A., (1989), Solar cells and optics for photovoltaic concentration. Adam Hilger, Bristol, UK

LUQUE, A., HEGEDUS, S. (2011), Handbook of photovoltaic science and engineering (2nd Edition), John Wiley and Sons Ltd, London, UK

MARKVART, T., (1994), Solar Electricity, John Wiley and Sons Ltd, UK

MCCANDLESS, B.E., SITES, J.R., (2011), Handbook of photovoltaic science and engineering, Chapter 14 – Cadmium Telluride Solar Cells, Edited by Luque, A., Hegedus, S., John Wiley and Sons Ltd, UK

MERTENS, K., (2014), Photovoltaics: Fundamentals, Technology and Practice, John Wiley and Sons Ltd, London, UK

MILLER, O.E., MCLEOD, J.H., SHERWOOD, W.T., (1951) Thin sheet plastic Fresnel lenses of high aperture" Journal of the optical society of America, **41**(11), pp 807 – 815

MIÑANO, J.C., BENÍTEZ, P., GONZÁLEZ, J.C., (1995a), RX: a nonimaging concentrator, Applied Optics, **34**(13), pp 2226 – 2235

MIÑANO, J.C., BENITEZ, P., GONZALEZ, J.C., FALICOFF, W., CAULFIELD, H.J., (2003), U.S. Patent No. 6639733 B2

MIÑANO, J.C., BENÍTEZ, P., LIN, W., MUÑOZ, F., INFANTE, J., SANTAMARÍA, A., (2009), Overview of the SMS design method applied to imaging optics, In Proceedings of the 2009 SPIE conference: Novel optical systems design and optimization XII, **7429**, pp 74290C: 1 – 9

MIÑANO, J.C., GONZÁLEZ, J.C., (1991), Design of nonimaging lenses and lens-mirror combinations, In Proceedings of the 1991 SPIE conference: nonimaging optics: maximum efficiency light transfer, **1528**, pp 104 – 116

MIÑANO, J.C., GONZÁLEZ, J.C., (1992), New method of design of nonimaging concentrators, Applied Optics, **31**, pp 3051 – 3060

MIÑANO, J.C., GONZÁLEZ, J.C., BENÍTEZ, P., (1995b), RXI: a high-gain, compact, nonimaging concentrator, Applied Optics, **34**(34), pp 7850 – 7856

MIÑANO, J.C., GONZÁLEZ, J.C., BENITEZ, P., (2005), A high-gain, compact, nonimaging concentrator: RXI, Applied Optics, **34**(34), pp 7850 – 7856

MORENO, A., CHEMISANA, D., VAILLON, R., RIVEROLA, A., SOLANS, A., (2019), Energy and Luminous Performance Investigation of an OPV/ETFE Glazing Element for Building Integration, Energies, **12**(10), pp 1870

MULLIGAN, W.P., TERAO, A., DAROCZI, S.G., PUJOL, O.C., CUDZINOVIC, M.J., VERLINDEN, P.J., SWANSON, R.M., BENÍTEZ, P., MIÑANO, J.C., (2000), A flat-plate concentrator: Micro-concentrator design overview, In Proceedings of the 28th IEEE photovoltaic specialists conference, pp 1495 – 1497

MUÑOZ, F., BENÍTEZ, P., MIÑANO, J.C., (2008), High-order aspherics: The SMS nonimaging design method applied to imaging optics, In Proceedings of the 2008 SPIE conference: optical design and engineering III, **7100**, pp 71000K: 1 – 9

NACHMIAS, T., OHAYON, A., MELZER, S.E., KABLA, M., LOUZON, E., LEVY, U., (2009), Shallow Fresnel lens fabrication using grey scale lithography made by high energy beam sensitive mask (HEBS) technology and reactive ion etching, In Proceedings of the 2009 SPIE conference: advanced fabrication technologies for micro/nano optics and photonics II., **7205**, pp 72050B: 1 – 12

NASA, (2020), Anatomy of the Sun, Available Online: https://www.nasa.gov/mission_pages/sunearth/science/solar-anatomy.html [Accessed: January 2020]

NORTON, B., (1992), Solar Energy Thermal Technology, Springer-Verlag, London, UK

NREL, (2020), Best research-cell efficiencies, National Renewable Energy Laboratory, Available online: https://www.nrel.gov/pv/cell-efficiency.html [Accessed: January 2020]

O'GALLAGHER, J., WINSTON, R., (1983), Development of compound parabolic concentrators for solar energy, International Journal of Ambient Energy, **4**, pp 171-186

O'NEILL, M.J., (1978), Solar concentrator and energy collection systems, U.S, Patent No. 4069812

O'NEILL, M.J., (2000a), Color-mixing lens for solar concentrating system and methods of manufacture and operation thereof, U.S. Patent No. 6031179

O'NEILL, M.J., (2000b), Stretched Fresnel lens solar concentrator for space power, U.S. Patent No. 6075200

OSHIDA, I., (1961), Step Lenses and Step Prisms for utilization of Solar Energy, New Sources of Energy, Proceedings of the Conference, pp 598-603

PARKYN, B., FALICOFF, W., MIÑANO, J.C., BENÍTEZ, P., CHAVES, J., SUN, Y., (2003), Off-axis TIR lens for conformal luminaries, In Proceedings of the 2003 SPIE conference: nonimaging optics: Design of efficient illumination systems, **5186**, pp 56 – 59

RABL, A., (1985), Active solar collectors and their applications, Oxford University Press, New York, USA

RAINHART, L.G., SCHIMMEL, W.P., (1974), Effect of outdoor aging on acrylic sheet, Solar Energy, **17**, pp 259 – 264

REIJENGA, T., (2000), Photovoltaic Building Integration Concepts – What do Architects need?, Proc. IEA PVPS Task7 Workshop Lausanne Featuring A Review of PV Products, IEA PVPS Task7, Halcrow Gilbert, Swindon (2000)

RIES, H., LEUTZ, R., (2003), Tailored Fresnel optics 1 – Global shape, In Proceedings of the 2003 SPIE conference: design of efficient illumination systems, pp 154 – 158

ROBERTS, S., GUARIENTO, N., (2009), Building integrated photovoltaics: A handbook, Birkhäuser, Basel, Switzerland

SALVESEN, F., (2015), Energy Upgrade of Non-Residential Buildings, Available online at: https://www.iea-shc.org/Data/Sites/1/publications/Position-Paper--Task47-Solar-Renovation-NonResidential-Buildings-Position-Paper-2015-09.pdf [Accessed: January 2020]

SHAFARMAN, W.N., STOLT, L., (2011), Handbook of photovoltaic science and engineering, Chapter 13 – Cu(InGa)Se2 Solar Cells, Edited by Luque, A., Hegedus, S., John Wiley and Sons Ltd, UK

SHOCKLEY, W., QUEISSER, H.J., (1961), Detailed Balance Limit of Efficiency of p-n Junction Solar Cells, Journal of Applied Physics, **32**, pp 510-519

SLOTBOOM, J.W., DE GRAAFF, H.C., (1976), Measurements of bandgap narrowing in Si bipolar transistors, Solid State Electronics, **19**, pp 857-862

STEFFEN, W., ROCKSTRÖM, J., RICHARDSON, K., LENTON, T.M., FOLKE, C., LIVERMAN, D., SUMMERHAYES, C.P., BARNOSKY, A.D., CORNELL, S.E., CRUCIFIX, M., DONGES, J.F., FETZER, I., LADE, S.J, SCHEFFER, M, WINKELMANN, R., SCHELLNHUBER, H.J., (2018), Trajectories of the Earth System in the Anthropocene, Proceedings of the National Academy of Sciences, **115**(33), pp 8252-8259

STRONG, S., LLOYD JONES, D., (2001) A Renewable Future, IEA PVPS Task7, Final Task

TERAO, A., MULLIGAN, P., DAROCZI, S.G., PUJOL, O.C., VERLINDEN, P.J., SWANSON, R.M., (2000), A mirror-less design for micro-concentrator modules, In Proceedings of the 28th IEEE photovoltaic specialists conference, pp 1416 – 1419

THOMAS, R., (2003), Photovoltaics and Architecture, Spon Press, London, UK

THOMAS, R., GRAINGER, T., GETHING, B., KEYS, M., (1999), Photovoltaics in Buildings – A Design Guide, Report S/P2/00282/REP, ETSU, DTI, London

TRIPANAGNOSTOPOULOS, Y., (2014), New Designs of Building Integrated Solar Energy Systems, Energy Procedia, **57**, pp 2186-2194

TRIPANAGNOSTOPOULOS, Y., SIABEKOU, CH., TONUI, J.K., (2007), The Fresnel lens concept for solar control of buildings, Solar Energy, **81**, 661 – 675

TVER'YANOVICH, E.V., (1984), Profiles of solar engineering Fresnel lenses, Geliotekhnika, 1984, **19**(9), pp 31 – 34

VAN MIERLO, B., OUDSHOFF. B., (1999), Literature survey and analysis of nontechnical problems for the introduction of building integrated photovoltaic systems, IVAM Environmental Research, Universiteit van Amsterdam, Amsterdam

VÁZQUEZ-MOLINI, D., FERNÁNDEZ-BALBUENA, A.A., BERNABEU, E., MUÑOZ DE LUNA CLEMENTE, J., DOMINGO-MANRIQUE, A., GARCÍA-BOTTELA, A., (2009), New concentrator multifocal Fresnel lens for improved uniformity: design and characterisation, In Proceedings of the 2009 SPIE conference: High and low concentration for solar electrical applications IV, **7407**, pp 74070I: 1 – 11

WEISS, W., MAUTHNER, F., (2015), Solar heat worldwide – Markets and contribution to the energy supply 2013, AEE INTEC, Gleisdorf, Austria

WEISS, W., SPÖRK-DÜR, M., (2019), Solar heat worldwide: Global market development and trends in 2017, AEE INTEC, Gleisdorf, Austria

WENHAM, S.R., GREEN, M.A., WATT, M.E., CORKISH, R., (2007), Applied Photovoltaics, (2nd Edition), Earthscan, London, UK

WINSTON, R., (1974), Principles of solar concentrators of a novel design, Solar Energy, **16**, pp. 89 – 95.

WINSTON, R., MINANO, J.C., BENÍTEZ, P., (2005), Nonimaging Optics, Elsevier Academic Press, London, UK

YAN, F., NOBLE, J., PELTOLA, J.,WICKS, S., BALASUBRAMANIAN, S., (2013), Semitransparent OPV modules pass environmental chamber test requirements, Solar Energy Mater. Solar Cell, **114,** pp 214-218

YOSHIOKA, K., ENDOH, K., KOBAYASHI, M., SUZUKI, A., SAITOH, T., (1994b), Design and properties of a refractive concentrator module, Solar energy materials and solar cells, **34**, pp 125 – 131

YOSHIOKA, K., KOBAYASHI, M., SUZUKI, A., ENDOH, K., OHE, N., SAITOH, T., (1994a), Optimum design and properties of a static concentrator with a nonimaging lens, In Proceedings of the 1994 world conference on photovoltaic energy conversion, pp 1119 – 1122

ZACHAROPOULOS, A., (2001), Optical Design Modelling and Experimental Characterisation of Line-axis Concentrators for Solar Photovoltaic and Thermal Applications, PhD Thesis, Ulster University, UK

ZHAI, H., DAI, Y.J., WU, J.Y., WANG, R.Z., ZHANG, L.Y., (2010), Experimental investigation and analysis on a concentrating solar collector using linear Fresnel lens, Energy Conversion and Management, **51**, 48 – 55

Appendix

9 Appendix

Additional information generated as part of the optical design phase of this thesis is presented here. It includes a series of tables comprehensively detailing the optical modelling carried out on the range of lens resolutions and levels of defocus discussed during the design of the 150 micron lens in the main body of the thesis. Each lens resolution and level of defocus was examined across a number of discrete angles of incidence. The intention of presenting this information is to aide any further work carried out on this topic, not to provide a detailed analysis of the information generated.

The data generated from the optical modelling for all lens resolutions and degrees of defocus is presented in Table 9-1 to Table 9-5, covering the range from 0 degrees defocused (perpendicular incident light) up to the half angle design limit of 20 degrees, respectively. The coloured scheme, using the legend provided in Figure 9-1, is intended to identify the lens resolution with the highest and lowest angular acceptance and optical efficiency at each level of defocus.

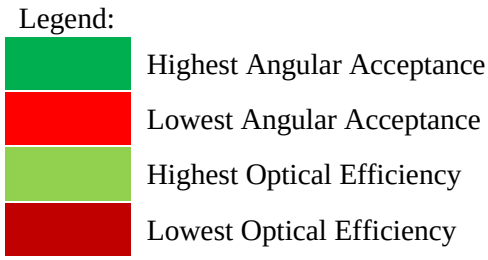

Figure 9-1 – Legend for the incidence angle overview summary tables

Table 9-1 – Comparative lens performance at an incidence angle of 0 degrees (perpendicular insolation)

Lens Design	Efficiency (%)	Angle of Defocus (°)											
		0	1	2	3	4	5	6	10	15	20	23.5	25
100 micron	AA	100.00	100.00	100.00	100.00	100.00	100.00	100.00	100.00	91.08	84.04	79.48	77.84
	OE	79.46	86.39	89.32	91.06	92.23	93.05	93.64	94.95	87.06	80.50	76.16	74.58
125 micron	AA	99.10	100.00	100.00	100.00	100.00	100.00	100.00	99.76	90.64	83.56	79.48	77.72
	OE	78.75	86.39	89.34	91.08	92.22	93.06	93.65	94.73	86.65	80.04	76.16	74.47
150 micron	AA	100.00	100.00	100.00	100.00	100.00	100.00	100.00	100.00	90.84	83.68	79.52	78.04
	OE	79.57	86.41	89.35	90.80	92.24	93.00	93.66	94.96	86.84	80.16	76.20	74.78
175 micron	AA	99.82	100.00	100.00	100.00	100.00	100.00	100.00	100.00	91.04	83.80	79.56	78.04
	OE	79.20	86.45	89.35	91.08	92.24	93.06	93.66	94.96	87.03	80.27	76.24	74.78
200 micron	AA	99.56	100.00	100.00	100.00	100.00	100.00	100.00	99.84	90.72	83.76	79.48	77.84
	OE	79.28	86.46	89.36	91.10	92.24	93.06	93.67	94.82	86.73	80.23	76.16	74.59
225 micron	AA	100.00	100.00	100.00	100.00	100.00	100.00	100.00	100.00	90.84	83.84	79.52	77.88
	OE	79.39	86.44	89.37	91.09	92.25	93.05	93.67	94.97	86.85	80.31	76.20	74.63
250 micron	AA	99.64	100.00	100.00	100.00	100.00	100.00	100.00	100.00	90.92	83.80	79.48	77.96
	OE	79.24	86.46	89.38	91.10	92.26	93.08	93.68	94.98	86.93	80.28	76.17	74.72
275 micron	AA	100.00	100.00	100.00	100.00	100.00	100.00	100.00	100.00	90.80	83.92	79.76	77.96
	OE	79.50	86.47	89.39	91.11	92.27	93.08	93.69	94.98	86.82	80.40	76.44	74.72
300 micron	AA	99.82	100.00	100.00	100.00	100.00	100.00	100.00	100.00	90.96	83.96	79.80	77.96
	OE	79.34	86.48	89.40	91.12	92.27	93.09	93.69	94.99	86.98	80.44	76.48	74.72
325 micron	AA	100.00	100.00	100.00	100.00	100.00	100.00	100.00	100.00	90.96	83.92	79.72	78.04
	OE	79.55	86.50	89.40	91.13	92.28	93.10	93.70	94.99	86.98	80.40	76.41	74.80
350 micron	AA	99.86	100.00	100.00	100.00	100.00	100.00	100.00	100.00	90.84	83.96	79.72	78.00
	OE	79.40	86.50	89.41	91.14	92.29	93.10	93.70	95.00	86.87	80.44	76.41	74.77
375 micron	AA	99.92	100.00	100.00	100.00	100.00	100.00	100.00	100.00	90.92	83.80	79.72	77.96
	OE	79.50	86.52	89.42	91.14	92.29	93.11	93.71	95.00	86.95	80.29	76.42	74.73
Perspex	AA	63.20	-	-	-	-	-	-	-	-	-	-	-
	OE	62.26	-	-	-	-	-	-	-	-	-	-	-

Table 9-2 – Comparative lens performance at an incidence angle of 5 degrees

Lens Design	Efficiency (%)	Angle of Defocus (°)											
		0	1	2	3	4	5	6	10	15	20	23.5	25
100 micron	AA	93.50	97.02	96.44	99.76	99.60	98.22	97.36	93.26	89.42	83.64	79.42	77.68
	OE	77.71	81.49	82.37	84.25	85.91	86.51	86.78	84.87	82.05	76.96	73.12	71.52
125 micron	AA	93.40	96.84	96.84	99.72	99.76	98.32	97.28	93.10	89.44	83.86	79.38	77.84
	OE	77.74	81.39	82.76	84.47	86.00	86.61	86.72	84.73	82.07	77.15	73.08	71.67
150 micron	AA	93.28	96.84	96.46	98.19	99.92	98.38	97.26	93.26	89.42	83.96	79.70	77.76
	OE	77.65	81.35	82.52	84.36	86.19	86.67	86.71	84.90	82.06	77.26	73.36	71.60
175 micron	AA	93.48	97.18	97.16	99.76	99.78	98.46	97.22	93.16	89.50	84.00	79.58	78.00
	OE	77.84	81.78	83.12	84.74	86.06	86.74	86.69	84.81	82.10	77.29	73.27	71.80
200 micron	AA	93.34	97.04	97.34	99.74	99.80	98.44	97.14	93.22	89.36	83.84	79.48	77.82
	OE	77.80	81.67	83.31	84.78	86.08	86.73	86.60	84.87	82.01	77.15	73.18	71.64
225 micron	AA	93.12	96.72	97.34	99.72	99.68	98.44	97.16	93.18	89.38	83.92	79.68	77.78
	OE	77.75	81.51	83.36	84.82	85.99	86.74	86.64	84.84	82.03	77.23	73.37	71.62
250 micron	AA	93.18	97.30	96.84	98.98	99.76	98.46	97.24	93.24	89.42	83.78	79.48	77.74
	OE	77.68	81.58	82.80	83.63	86.06	86.75	86.72	84.90	82.07	77.10	73.19	71.59
275 micron	AA	93.70	97.42	97.20	99.40	99.72	98.42	97.30	93.18	89.04	83.98	79.52	77.82
	OE	77.94	81.75	83.00	84.00	86.05	86.73	86.78	84.85	82.04	77.27	73.21	71.67
300 micron	AA	93.14	97.12	97.04	99.40	99.78	98.44	97.26	93.28	89.50	83.92	79.68	78.04
	OE	77.68	81.57	83.05	84.05	86.08	86.75	86.75	84.94	82.15	77.21	73.38	71.87
325 micron	AA	94.10	97.48	97.44	99.40	99.80	98.38	97.20	93.24	89.40	83.88	79.58	77.92
	OE	78.27	81.86	83.31	84.23	86.13	86.68	86.70	84.91	82.10	77.20	73.29	71.76
350 micron	AA	93.80	97.54	97.68	99.62	99.78	98.42	97.20	93.22	89.38	83.90	79.62	77.98
	OE	78.18	81.85	83.39	84.31	86.11	86.75	86.70	84.89	82.04	77.22	73.33	71.80
375 micron	AA	93.74	97.32	96.90	99.58	99.78	98.46	97.20	93.24	89.42	83.90	79.52	77.86
	OE	78.03	81.70	82.90	84.40	86.12	86.79	86.71	84.92	82.08	77.22	73.24	71.71
Perspex	AA	63.20	-	-	-	-	-	-	-	-	-	-	-
	OE	57.53	-	-	-	-	-	-	-	-	-	-	-

Table 9-3 – Comparative lens performance at an incidence angle of 10 degrees

Lens Design	Efficiency (%)	Angle of Defocus (^{o})											
		0	1	2	3	4	5	6	10	15	20	23.5	25
100 micron	AA	85.90	86.84	88.06	85.82	87.78	87.04	87.28	86.52	83.14	80.48	78.74	77.48
	OE	73.65	74.06	75.14	74.86	76.15	75.03	74.33	77.68	75.92	73.83	72.26	71.21
125 micron	AA	85.92	86.50	89.08	86.24	87.64	86.58	86.70	86.54	83.14	80.40	78.74	77.26
	OE	73.55	73.69	75.62	74.89	75.99	75.02	73.94	77.69	75.95	73.77	72.24	71.03
150 micron	AA	86.86	87.08	88.66	88.48	88.30	86.90	87.06	86.60	83.22	80.44	78.58	77.36
	OE	74.20	74.15	75.54	76.07	76.59	75.38	74.95	77.72	76.02	73.79	72.10	71.11
175 micron	AA	86.22	86.96	89.00	85.96	87.92	86.88	87.16	86.56	83.32	80.42	78.74	77.60
	OE	73.90	74.11	75.77	74.99	76.24	75.22	74.85	77.71	76.10	73.77	72.19	71.35
200 micron	AA	86.24	86.80	88.64	86.44	87.78	87.02	87.02	86.56	83.32	80.44	78.64	77.36
	OE	73.89	73.88	75.63	75.19	76.16	75.24	74.56	77.69	76.10	73.79	72.17	71.10
225 micron	AA	86.08	86.56	88.54	86.60	88.04	87.01	86.96	86.60	83.32	80.50	78.74	77.50
	OE	73.78	73.98	75.54	75.28	76.49	75.18	74.48	77.70	76.12	73.83	72.26	71.26
250 micron	AA	86.24	87.06	89.08	86.18	88.08	86.96	86.70	86.50	83.20	80.42	78.64	77.50
	OE	73.89	74.08	75.96	74.95	76.34	75.32	74.34	77.67	75.99	73.77	72.17	71.24
275 micron	AA	86.58	87.16	89.22	86.28	88.16	86.82	87.08	86.58	83.32	80.40	78.74	77.38
	OE	74.16	74.19	75.98	75.07	76.48	75.34	74.95	77.72	76.14	73.84	72.26	71.15
300 micron	AA	85.98	86.94	89.04	85.70	87.78	87.18	87.14	86.66	83.32	80.44	78.74	77.60
	OE	73.92	74.20	76.06	74.73	76.22	75.43	74.86	77.83	76.11	73.79	72.26	71.36
325 micron	AA	86.54	87.12	89.66	87.24	88.22	87.16	87.12	86.60	83.28	80.50	78.70	77.52
	OE	74.07	74.22	76.39	75.80	76.63	75.42	74.78	77.76	76.06	73.84	72.23	71.27
350 micron	AA	86.28	87.02	89.76	86.62	87.88	87.14	87.04	86.58	83.26	80.40	78.76	77.52
	OE	73.96	74.12	76.35	75.34	76.25	75.26	74.64	77.76	76.07	73.77	72.29	71.26
375 micron	AA	86.36	86.52	89.52	86.56	87.50	86.76	86.88	86.56	83.28	80.44	78.66	77.48
	OE	74.00	73.90	76.36	75.21	76.05	75.15	74.53	77.73	76.11	73.83	72.20	71.24
Perspex	AA	63.20	-	-	-	-	-	-	-	-	-	-	-
	OE	57.20	-	-	-	-	-	-	-	-	-	-	-

Table 9-4 – Comparative lens performance at an incidence angle of 15 degrees

Lens Design	Efficiency (%)	Angle of Defocus (^{o})											
		0	1	2	3	4	5	6	10	15	20	23.5	25
100 micron	AA	74.94	75.04	75.10	75.60	75.72	77.34	76.34	79.40	77.12	74.80	72.80	71.50
	OE	64.94	64.54	64.42	64.82	66.23	67.45	66.45	66.87	69.28	67.84	66.39	65.46
125 micron	AA	74.30	75.26	75.32	75.36	74.88	77.14	76.14	79.86	77.16	74.76	72.74	71.58
	OE	64.24	64.64	64.51	64.56	65.60	67.32	66.29	66.27	69.29	67.81	66.36	65.53
150 micron	AA	74.80	75.46	74.88	74.69	74.50	76.82	75.98	79.58	77.20	74.74	72.84	71.44
	OE	64.50	64.56	64.15	64.75	65.34	67.06	66.21	66.00	69.35	67.81	66.45	65.42
175 micron	AA	74.66	75.24	72.26	75.38	74.84	77.44	76.22	79.52	77.26	74.88	72.78	71.56
	OE	64.54	64.64	64.43	64.57	65.68	67.45	66.36	66.64	69.40	67.93	66.40	65.52
200 micron	AA	74.74	75.40	75.16	75.68	75.62	76.98	75.90	79.76	77.16	74.84	72.74	71.58
	OE	64.47	64.68	64.31	64.66	65.99	67.15	66.11	66.17	69.31	67.89	66.35	65.52
225 micron	AA	74.66	75.32	75.12	75.50	74.84	75.89	76.02	79.74	77.10	74.84	72.80	71.52
	OE	64.51	64.55	64.37	64.54	65.59	67.05	66.22	66.14	69.30	67.90	66.42	65.50
250 micron	AA	74.50	74.96	75.24	74.86	74.44	76.60	75.78	79.52	77.14	74.68	72.76	71.44
	OE	64.31	64.31	64.33	64.26	65.20	66.94	68.02	66.09	69.30	67.79	66.37	65.42
275 micron	AA	64.56	75.06	75.24	75.72	75.38	77.10	75.98	79.84	77.14	75.00	72.72	71.44
	OE	74.84	64.53	64.46	64.73	65.85	67.27	66.34	66.33	69.35	68.03	66.30	65.41
300 micron	AA	74.68	75.02	74.96	75.40	74.66	77.00	76.02	79.90	77.22	74.84	72.84	71.62
	OE	64.53	64.49	64.32	64.71	65.42	67.19	66.25	66.26	69.36	67.91	66.44	65.58
325 micron	AA	74.84	75.82	75.72	75.96	75.32	77.90	76.40	79.74	77.18	74.80	72.74	71.54
	OE	64.57	64.85	64.60	64.89	65.86	67.72	66.48	66.24	69.32	67.88	66.37	65.52
350 micron	AA	74.86	75.56	75.48	76.30	75.06	77.34	76.20	79.86	77.18	74.90	72.86	71.56
	OE	64.66	64.88	64.62	65.22	65.63	67.37	66.37	66.27	69.35	67.94	66.47	65.54
375 micron	AA	74.72	74.88	75.36	75.74	74.52	76.98	75.78	79.80	77.22	74.82	72.82	71.56
	OE	62.47	64.35	64.55	64.80	65.38	67.04	66.16	66.24	69.37	67.90	66.39	65.56
Perspex	AA	63.20	-	-	-	-	-	-	-	-	-	-	-
	OE	57.51	-	-	-	-	-	-	-	-	-	-	-

Table 9-5 – Comparative lens performance at an incidence angle of 20 degrees

Lens Design	Efficiency (%)	Angle of Defocus (^{o})											
		0	1	2	3	4	5	6	10	15	20	23.5	25
100 micron	AA	63.66	62.92	64.04	63.84	63.86	64.24	66.32	65.42	71.38	68.40	64.58	62.70
	OE	55.04	54.15	54.39	54.21	54.30	55.73	57.21	55.76	61.68	61.36	58.73	57.07
125 micron	AA	64.92	63.32	63.92	64.02	63.70	63.32	65.78	65.66	71.26	68.40	64.48	62.64
	OE	55.98	54.26	54.39	54.25	54.02	55.07	55.80	56.05	61.58	61.35	58.68	57.04
150 micron	AA	64.28	63.16	64.20	64.10	64.00	63.64	66.02	65.28	71.40	68.44	64.66	62.96
	OE	55.50	54.19	54.64	54.45	54.25	55.27	57.02	55.74	61.65	61.38	58.81	57.28
175 micron	AA	64.38	63.26	63.68	63.82	64.14	63.80	66.40	65.90	71.44	68.54	64.66	62.96
	OE	55.63	54.34	54.24	54.14	54.32	55.34	57.30	56.23	61.76	61.49	58.84	57.27
200 micron	AA	63.86	63.12	63.94	63.88	63.86	63.98	66.10	65.62	71.22	68.36	64.48	62.66
	OE	55.16	54.24	54.47	54.29	54.15	55.54	57.13	56.06	61.59	61.34	58.67	57.05
225 micron	AA	64.10	63.52	63.82	63.68	64.02	63.75	66.34	65.66	71.26	68.42	64.58	62.86
	OE	55.33	54.40	54.39	54.19	54.12	55.60	57.21	55.98	61.59	61.37	58.76	57.22
250 micron	AA	64.50	63.32	64.00	64.18	63.76	63.56	66.08	65.58	71.32	68.46	64.60	62.64
	OE	55.60	54.35	54.48	54.36	54.09	55.25	57.00	56.03	61.66	61.42	58.79	57.03
275 micron	AA	64.06	63.38	63.74	64.14	63.76	63.70	65.98	65.64	71.38	68.48	64.68	62.80
	OE	55.36	54.40	54.44	54.37	54.32	55.31	57.25	56.04	61.71	61.41	58.88	57.18
300 micron	AA	64.62	63.38	63.42	64.16	64.48	63.86	66.48	65.66	71.38	68.54	64.52	62.86
	OE	55.82	54.47	54.18	54.54	54.51	55.35	57.27	56.15	61.72	61.51	58.74	57.24
325 micron	AA	64.12	63.32	63.98	64.14	64.16	63.94	66.46	65.88	71.28	68.32	64.50	62.90
	OE	55.40	54.37	54.49	54.42	54.40	55.56	57.22	56.18	61.64	61.33	58.72	57.26
350 micron	AA	64.00	63.28	63.78	64.30	64.36	63.60	66.52	65.74	71.42	68.44	64.72	62.82
	OE	55.36	54.35	54.35	54.50	54.48	55.30	57.26	56.06	61.74	61.40	58.92	57.21
375 micron	AA	64.56	63.14	63.98	63.78	63.88	63.72	66.04	66.08	71.30	68.46	64.56	62.84
	OE	55.68	54.29	54.60	54.28	54.31	55.43	57.08	56.37	61.66	61.45	58.78	57.23
Perspex	AA	63.18	-	-	-	-	-	-	-	-	-	-	-
	OE	57.46	-	-	-	-	-	-	-	-	-	-	-